

# Spectroscopic Studies on Semiconducting Interfaces with Giant Spin Splitting

THÈSE N° 4870 (2010)

PRÉSENTÉE LE 18 NOVEMBRE 2010

À LA FACULTÉ SCIENCES DE BASE

LABORATOIRE DE SPECTROSCOPIE ÉLECTRONIQUE

PROGRAMME DOCTORAL EN PHYSIQUE

ÉCOLE POLYTECHNIQUE FÉDÉRALE DE LAUSANNE

POUR L'OBTENTION DU GRADE DE DOCTEUR ÈS SCIENCES

PAR

Emmanouil FRANTZESKAKIS

acceptée sur proposition du jury:

Prof. G. Meylan, président du jury

Prof. M. Grioni, directeur de thèse

Prof. Ph. Aebi, rapporteur

Prof. H. Brune, rapporteur

Prof. M. Golden, rapporteur



ÉCOLE POLYTECHNIQUE  
FÉDÉRALE DE LAUSANNE

Suisse  
2010



---

## Abstract

---

The application of an external magnetic field can lift the spin degeneracy of electronic states through its interaction with the electronic magnetic moment. A closely-related phenomenon is the Rashba-Bychkov (RB) effect where symmetry breaking at surfaces or interfaces gives rise to an electric field which is in turn seen as an effective magnetic field in the electrons' rest frame. The resulting  $k$ -dependent energy splitting of spin-polarized electronic states has been observed on various metal surfaces but the effect is much larger in artificially-grown surface alloys; such as the  $\text{BiAg}_2$  grown at the surface of  $\text{Ag}(111)$ . The spin splitting magnitude observed in these systems might be very useful in spintronics applications since it could decrease the spin precession time in a spin transistor and distinguish between the extrinsic and intrinsic spin Hall effects. Nevertheless, their metallic character poses serious obstacles in the exploitation of the RB effect due to the presence of spin-degenerate electronic states at the Fermi level which would dominate transport experiments.

We have used angle-resolved photoelectron spectroscopy (ARPES) to explore the RB effects on various artificially grown structures, formed on semiconducting substrates. The interplay of quantum confinement and giant RB splitting on a trilayer  $\text{Si}(111)\text{-Ag-BiAg}_2$  system reveals the formation of a complex spin-dependent structure, which can be externally tuned by varying the Ag layer thickness. This provides a means to tailor the electronic structure and spin polarization near the Fermi level, with potential applications on Si-compatible spintronic devices. Moreover, we have discovered a giant spin splitting in a true semiconducting system, namely the  $\text{Si}(111)\text{-Bi}$  trimer phase. The size of the RB parameters is comparable to those of metallic surface alloys. Using theoretical models we have identified the peculiar band topology as the origin of the giant spin splitting on the  $\text{Bi/Si}(111)$  system. All our findings are supported by relativistic first-principles calculations. Finally, a chapter of this thesis manuscript is devoted to the description of phenomenological theoretical simulation, which can capture the experimental results related to the RB effect on low-dimensional systems.

A parallel experimental project is discussed in a separate chapter. It has been focused on the band topology of the novel  $p(2 \times 2)$  reconstruction of the  $\text{Pt}(111)\text{-Ag-Bi}$  trilayer. We investigated the symmetry properties of the interface states by varying the amount of Ag. ARPES results present the electronic signature of a strain-related structural transition.

**Keywords:** angle-resolved photoelectron spectroscopy, spin-orbit splitting, low-dimensional systems, spintronics



---

## Résumé

---

L'interaction d'un champ magnétique avec le moment magnétique des électrons peut mener à la levée de la dégénérescence de spin des états électroniques. Dans le cas de l'effet Rashba-Bychkov (RB), c'est le champ électrique produit par la rupture de la symétrie de translation à la surface (ou à l'interface) qui est perçu comme un champ magnétique effectif dans le référentiel propre des électrons. L'effet RB mène à la séparation en énergie des états électroniques de spins opposés en fonction de  $k$ . Bien qu'il ait été observé pour différents métaux, l'effet est beaucoup plus important pour des alliages de surface artificiels comme  $\text{BiAg}_2$  élaboré à la surface  $\text{Ag}(111)$ . L'amplitude de la séparation en spin observée dans ces systèmes peut avoir des répercussions pour la spintronique car une forte séparation des bandes électroniques de spins opposés pourrait être associée à un temps de précession très court dans un transistor de spin et permettrait de dissocier les effets de spin hall intrinsèque et extrinsèque. Cependant la nature métallique de ces alliages est un obstacle sérieux pour les applications à cause de la présence à l'énergie de Fermi d'états électroniques non polarisés dont la contribution serait dominante dans les expériences de transport.

Nous avons étudié par spectroscopie de photoélectrons résolue en angle (ARPES) l'effet RB dans différentes structures artificielles élaborées sur un substrat semiconducteur. L'interaction entre le confinement quantique et l'effet RB géant dans un film tricouche  $\text{Si}(111)\text{-Ag-AgBi}_2$  induit une structure électronique dont le diagramme de bande et la polarisation en spin sont complexes et dont les propriétés peuvent être contrôlées par l'épaisseur du film d'argent. Ceci nous offre un moyen de concevoir spécialement la structure électronique et la polarisation en spin près du niveau de Fermi pour des systèmes étant compatibles avec la technologie silicium. Nous avons aussi découvert une séparation géante des bandes de spins opposés dans le système semiconducteur composé d'une monocouche de Bi déposée sur  $\text{Si}(111)$ . Dans la phase trimère  $\text{Bi/Si}(111)$ , l'amplitude du paramètre RB est comparable à celui des alliages de surface métallique. En comparant différents modèles théoriques, nous avons identifié la particularité de la topologie des bandes qui conduit à la séparation géante des bandes de  $\text{Bi/Si}(111)$ . Tous nos résultats sont en accord avec des calculs ab-initio relativistes. Finalement, un chapitre de cette thèse est dédié aux descriptions théoriques phénoménologiques que nous avons utilisées pour comprendre les résultats expérimentaux liés à l'effet RB dans des systèmes de basse dimension.

Un projet parallèle est discuté dans un chapitre séparé. Celui-ci qui est consacré à la topologie des bandes pour le système tricouches  $\text{Pt}(111)\text{-Ag-Bi}$ . Ce système présente une reconstruction

originale  $p(2 \times 2)$ . Nous avons étudié les propriétés de symétrie de l'état d'interface en changeant l'épaisseur d'argent. Les expériences d'ARPES montrent la signature d'une transition liées à la contrainte structurale d'épitaxie.

**Mots clés:** spectroscopie de photoélectrons résolue en angle, séparation de spin-orbite, systèmes de basse dimension, spintronique

---

## Acknowledgements

---

The work for this thesis would be impossible without the help of many different people. My thesis supervisor Marco Grioni supported my work from the first day. His ideas about the thesis projects were very interesting and at the same time they fitted in an excellent manner to the experimental setup. Most importantly, he continued being enthusiastic about my progress until the last day (and I think he will not stop being). I was very lucky to have many conversations about physics with him and I feel proud that I managed to win his trust and respect. Moreover, he gave me an example about a professor who can do everything himself from the beginning to the end (yes, he can also run the lab alone) and at the same time he is more modest than he should. In a more personal level, I would like to thank him for understanding in some (not so funny) moments.

I feel also that I should say a few words about each group member separately.

Stéphane Pons: we went through many different projects, most of them quite successfully. I believe that we both learned from each other (at least I learned a lot) and our complementary skills were the key ingredient for the results. A special acknowledgment goes for the construction of the home-made Ag evaporator which was one of the main reasons for the nice results we acquired.

Luca Moreschini: as my predecessor in the PhD position, he eagerly shared with me many tips and advices. His outstanding Igor skills were the basis for a lot of data treatment presented in this thesis.

Tony (Peng Xu): we started our theses more or less at the same time. He was always there to give me hand in the lab, especially during the time that we were both inexperienced newcomers.

Alberto Crepaldi: a very good friend and talented colleague. Speaking about physics at 4 am normally should make one go to bed as fast as possible; not when speaking with Alberto. I thank him a lot for his help during our time overlap and I am sure that he is the right person to continue the work.

Joy (Ping-Hui Lin), Xiaoqiang Wang, Marco Guarise, Miguel Valbuena: everyone was ready to help when problems arised or when I was in need of some advice. A special acknowledgement to Joy as a very nice office-mate.

Harald Brune was the reason that I came to Switzerland and he supervised the first year of my work. He was always very interested in my later progress. For the same period of time, I would like to thank R. Decker and S. Rusponi.

I gratefully acknowledge the M.Sc. students who worked with me from time to time and contributed to this thesis work: Roberto Mastrangelo, Laura Casanellas, Julliete Audet and Filippo Rossi.

Collaborations were important for the acquired results. Complementary experimental support came from the group of K. Kern in Stuttgart, while state-of-the-art theoretical calculations were made by the research team of J. Henk in Halle. Calculations by A. P. Seitsonen will be also a nice complement to yet unfinished projects.

Prof. A. Baldereschi eagerly checked the validity of the general ideas presented in the theoretical part of this thesis and the corresponding publications. His positive comments and support boosted my confidence and enthusiasm for further theoretical work within my experimental surroundings. Marco Papagno and Daniela Pacilé shared with me two different beamtimes at ELETTRA. The first (the winter-one) as coworkers and the second (the summer-one) as beamline staff. I really appreciate their help and the nice time we had together.

The Institute mechanical workshop led by G. Grandjean provided us with high-quality technical support, vital for every experimental group. M. Doy saved a couple of times my sick PC from the recycle bin, while P. Locatelli and S. Grioni set up a powerful server, which was absolutely necessary for the realization of the described theoretical models. An important acknowledgement goes to the secretaries (C. Roulin, F. Choulat and A. Nguyen) for their kindness and administrative help. Many friends at EPFL and Lausanne provided the necessary equilibrium between work and grills by the lake. Due to the certainty that I will forget someone, I will stay with just an indicative list: Yannis, Marilena, Simos and Evren.

Without the advice and support of my parents and brother, I would never be able to come and stay 5 years in Switzerland. I also thank my parents for many visits at our place, which were important for both sides. Since 28.05.2009, I started understanding how hard it must be for them to have my news mainly by phone.

The same day marked the arrival of Iliana. It is the only person in the so far list that i thank just because she exists. Related to the present thesis, her arrival taught me how to be more effective in my work. Finishing the daily work a few minutes faster started being a matter of ultimate importance. Iwona, thank you for coming with me to Switzerland. Your support either as a listener or as a talker was (and still is) crucial for my work and our life together. We went through many nice and hard moments but the successful realization of our own project (see the date above), will always mark Lausanne as an important place in our long track. Thank you for filling up my life with happiness and for being there every time when I need someone.

Last but not least, I would like to thank the Onassis Public Benefit Foundation for the award of a prestigious scholarship related to this thesis.

---

# Contents

---

<b>Abstract</b>	<b>i</b>
<b>Résumé</b>	<b>iii</b>
<b>Acknowledgements</b>	<b>v</b>
<b>Contents</b>	<b>vii</b>
<b>1 Modern angle-resolved photoelectron spectroscopy: Theory and experiment</b>	<b>1</b>
1.1 The UHV environment . . . . .	1
1.2 Theoretical background on photoelectron spectroscopy . . . . .	5
1.2.1 Introduction to PES - energy conservation . . . . .	5
1.2.2 3-step model . . . . .	6
1.2.3 1-step model . . . . .	8
1.2.4 Theoretical concepts . . . . .	12
1.3 Experimental details of modern photoelectron spectroscopy . . . . .	13
1.4 Complementary characterization techniques . . . . .	16
1.4.1 Low-energy electron diffraction . . . . .	16
1.4.2 Auger electron spectroscopy . . . . .	18
<b>2 Spin splitting on 2D electronic states: Experiment, theory, implications</b>	<b>21</b>
2.1 Theoretical background on the Rashba-Bychkov effect . . . . .	21
2.1.1 Approximating the Dirac equation . . . . .	21
2.1.2 Atomic spin-orbit coupling . . . . .	22
2.1.3 From Dirac to Rashba . . . . .	23
2.1.4 The role of time-reversal symmetry . . . . .	27
2.2 Unveiling the mechanism of the isotropic Rashba-Bychkov effect . . . . .	29
2.2.1 Spin splitting of noble metal surface states - early results . . . . .	29
2.2.2 A combination of theory and experiment towards a better understanding . . . . .	29
2.2.3 A quest to enhance the splitting . . . . .	35
2.3 The breakthrough of surface alloys and its implications . . . . .	36

2.3.1	Experimental discovery and relativistic calculations . . . . .	36
2.3.2	Nearly-free electron approximations of the results . . . . .	39
2.3.3	An alternative view . . . . .	41
2.3.4	Tuning the spin-orbit splitting parameters . . . . .	42
2.4	A flavor of spintronics . . . . .	46
<b>3</b>	<b>Giant spin-orbit effects on 2D systems with semiconducting substrates</b>	<b>51</b>
3.1	Metallic surface alloys on Si(111) and thin buffer layers . . . . .	51
3.1.1	PbAg <sub>2</sub> /Ag/Si(111): An ARPES study . . . . .	51
3.1.2	BiAg <sub>2</sub> /Ag/Si(111): An ARPES study and a NFE model . . . . .	52
3.1.3	Tunable spin-gaps in a quantum-confined geometry (Phys. Rev. Lett. 101, 196805 (2008)) . . . . .	56
3.1.4	BiAg <sub>2</sub> /Ag/Si(111): A parallel ARPES study . . . . .	64
3.1.5	BiAg <sub>2</sub> /Ag/Si(111): A spin-resolved ARPES experiment . . . . .	65
3.2	SO effects on semiconducting interfaces . . . . .	66
3.2.1	Bi/Si(111): Structural characteristics . . . . .	66
3.2.2	Bi/Si(111): Early ARPES studies . . . . .	67
3.2.3	Bi/Si(111): Silicon surface with giant spin splitting (full text published at Phys. Rev. Lett. 103, 046803 (2009)) . . . . .	68
3.2.4	Bi/Si(111): A combined angle- and spin-resolved photoemission study . . . . .	72
3.2.5	Band structure scenario for the giant spin-orbit splitting observed at the Bi/Si(111) interface (Phys. Rev. B 82, 085440) . . . . .	73
3.2.6	RB effects on Bi and Pb thin films . . . . .	91
3.2.7	RB effects on Ge-based systems . . . . .	92
<b>4</b>	<b>The Pt(111)-Ag-Bi interface: Band topology by ARPES</b>	<b>93</b>
4.1	Pt(111)-Ag-Bi: Surface alloying on stressed monolayers . . . . .	93
4.1.1	A structural transition reflected into the band topology of the Pt(111)-Ag-Bi interface (to be submitted to Phys. Rev. B) . . . . .	94
<b>5</b>	<b>Phenomenological simulations of the Rashba-Bychkov splitting</b>	<b>105</b>
5.1	Introduction . . . . .	105
5.2	Simulations based on the NFE approximation . . . . .	106
5.2.1	The nearly-free electron approximation . . . . .	106
5.2.2	NFE simulation - results . . . . .	107
5.2.3	NFE simulation - conclusions . . . . .	111
5.3	Simulations based on the TB approximation . . . . .	112
5.3.1	The tight-binding approximation . . . . .	112
5.3.2	TB simulation - results . . . . .	114
5.3.3	TB simulation - conclusions . . . . .	119
5.4	A comparison of the two approaches . . . . .	120

5.4.1	The Au(111) surface state as a case study . . . . .	120
<b>6</b>	<b>Concluding remarks</b>	<b>123</b>
	<b>Bibliography</b>	<b>125</b>
	<b>Curriculum Vitae</b>	<b>i</b>





# Chapter 1

---

## Modern angle-resolved photoelectron spectroscopy: Theory and experiment

---

### 1.1 The UHV environment

The incident flux ( $F$ ) of a gas on a clean surface is related to the molecular mass ( $m$ ), the temperature ( $T$ ) and the gas pressure ( $P$ ):

$$F = \frac{P}{2\pi kT} \quad \text{in gas molecules}/(\text{m}^2\text{s}) \quad (1.1)$$

where  $k$  is the Boltzmann constant. This is the Hertz-Knudsen-Langmuir equation which arises from a combination of the ideal gas equation and Maxwell-Boltzmann statistics. Moreover, a simple hard-sphere collision model can yield an equation for the mean-free path ( $\lambda$ ) of the gas particles; i.e. the average distance that a particle can travel without suffering any collision:

$$\lambda = \frac{kT}{P\sqrt{2}\pi\sigma^2} \quad (1.2)$$

where  $\sigma$  is the particle radius. For the same temperature and molecular mass (typical average values for residual gases), Table 1.1 reveals the dramatic effect of pressure on the mean free path and the deposition rate of the particles. In the following table, the sticking coefficient of the gas particles is assumed to be unity and the monolayer (ML) coverage around  $10^{15}$  per  $\text{cm}^2$ .

There are three main reasons for the necessity of a vacuum environment during spectroscopic studies:

1. The mean free path of the detected particles (i.e. electrons in the case of photoemission spectroscopy) must be significantly larger than the sample-spectrometer distance and the dimensions of

**Table 1.1** — Mean free path of the gas particles and monolayer deposition time at different levels of background pressure.

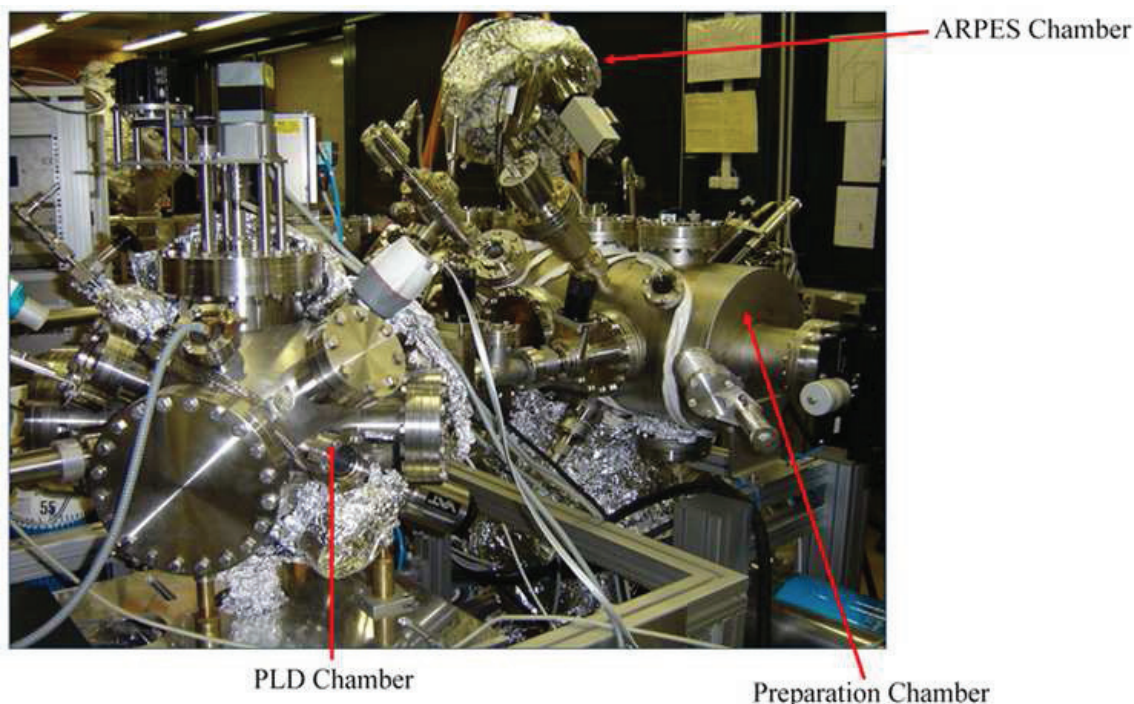
Degree of vacuum	Pressure (Torr)	Mean Free Path (m)	Time/monolayer (s)
Atmospheric	760	$7 \times 10^{-8}$	$10^{-9}$
Low	1	$5 \times 10^{-5}$	$10^{-6}$
Medium	$10^{-3}$	$5 \times 10^{-2}$	$10^{-3}$
High	$10^{-6}$	50	1
Ultra-High	$10^{-9}$	$5 \times 10^5$	$10^4$

the apparatus, in order to ensure a collision-free trajectory until the detection system. This requires pressures lower than  $10^{-4}$  Torr.

2. Pressures higher than  $10^{-6}$  Torr can cause serious damage to channeltron and multiplier detectors used for charged particles.

3. ARPES is very surface sensitive, therefore it demands keeping a clean sample for an amount of time which is larger than the required experimental time. In general, only pressures lower than  $10^{-9}$  Torr satisfy this condition.

In order to achieve a UHV environment, experiments are performed in closed stainless steel chambers, where different pieces are welded or bolted together using leak-tight connections (Fig.

**Figure 1.1** — The UHV multichamber setup at LSE-Lausanne. The preparation chamber is separated from the pulsed laser deposition (PLD) and high-resolution ARPES chambers. Pressures in the order of  $10^{-10}$  mbar are achieved at each part of the setup (photo courtesy of Xu Peng).

1.1). Two stages of pumping are necessary. Primary pumps are used to achieve pressures up to  $10^{-3}$  mbar. Typically, these are either conventional oil-sealed rotary or oil-free membrane pumps. They are connected to turbomolecular pumps which achieve the second-stage pumping. A fast moving rotor collides with the incoming gas particles and pushes them to the direction of the primary pump. Once the UHV range of pressures has been attained, it can be maintained and improved with different ways of pumping; an ionic pump ionizes the residual gas atoms and binds them in such a way so that they do not contribute to the background pressure, while a cryopump traps the gas atoms by condensing them on a very cold surface.

Pressure measurement is achieved by different kinds of sensors. A pirani gauge can give an accurate measurement during the first pumping stage. It is composed of a hot wire whose temperature and therefore resistance varies depending on the number of collisions with the molecules of the residual gas. Therefore, resistivity measurements can be translated into the amount of gas

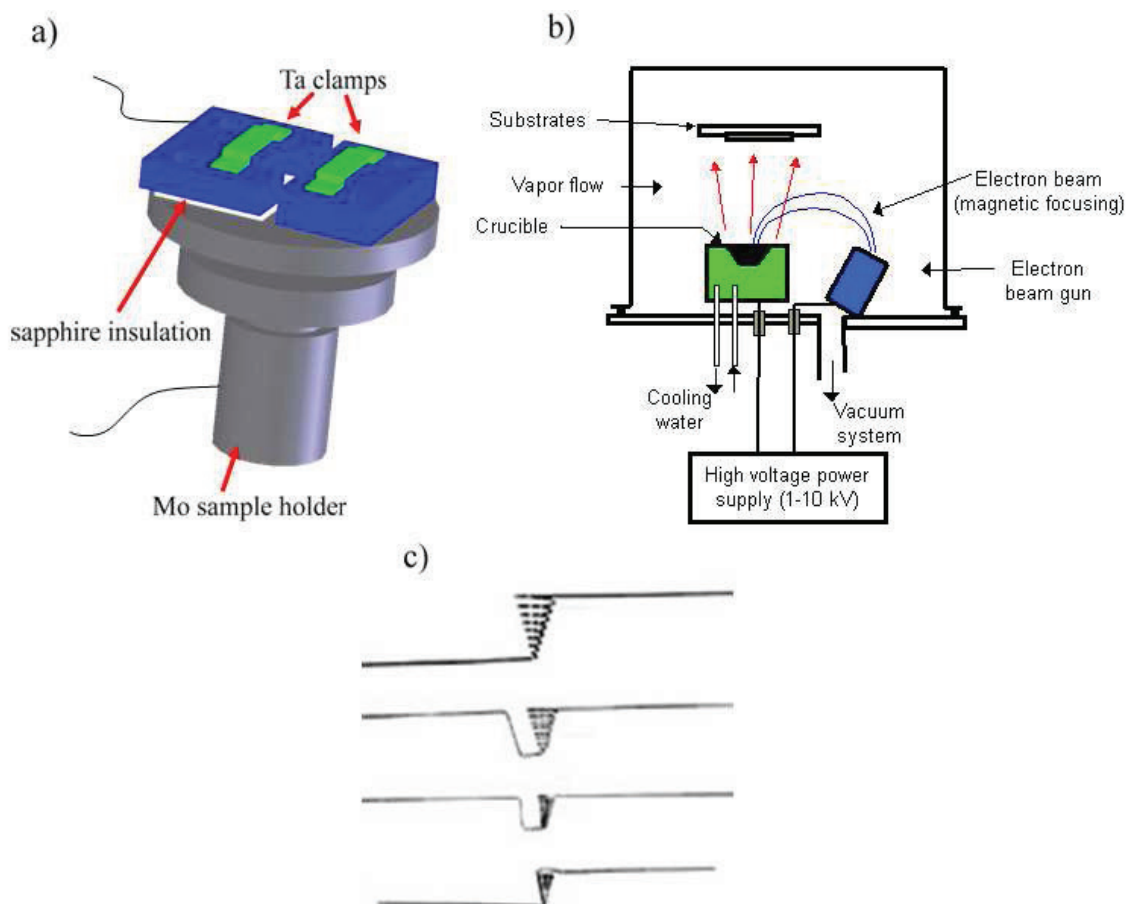


**Figure 1.2** — (a) Si sample holder for direct current injection. The black curves denote the contact wires. The sample is entered under the Ta clamps. The left part of the sample holder is insulated leaving the Si specimen as the only conducting path. (b) Schematic representation of an electron-beam evaporation system. The evaporant is kept into the crucible. Evaporation is effectuated by thermal heating due to the high potential difference between the gun and the crucible (image from CSIC-ICMM, Madrid). (c) Tungsten baskets used for evaporation by resistive heating.

molecules (i.e. gas pressure) after the necessary calibrations.  $P$  in the UHV range can be measured with ion gauges. Electrons emitted by a hot filament are accelerated by a potential difference and ionize the rest gas molecules. The resulting ion current provides a measure of the gas pressure. Under a similar principle of operation, cold cathode gauges are broad-range pressure sensors ( $P < 10^{-3}$  mbar), where ionization of the rest gas is achieved not from a thermionic cathode but by circulating electron plasma trapped in crossed electric and magnetic fields. Chemical analysis of the background pressure is achieved by a quadrupole mass spectrometer. In such an apparatus, ionized gas particles are focused into a mass filter. The ions are separated according to the ratio  $m/q$  and are finally collected by an ion detector.

It is evident that not only experimental measurements but also sample preparation and manipulation should be accomplished under UHV conditions (Table 1.1). The main methods for producing a clean substrate in vacuum are sputtering (i.e. bombardment with noble gas ions), annealing and cleaving. Simple metal surfaces are usually cleaned by many cycles of  $\text{Ar}^+$  sputtering and high-temperature annealing. The sputtering process produces a very clean but rough surface, which can be then repaired by heating. This in turn, might result into surface segregation of bulk impurities and repeated cycles of sputtering may be necessary. Silicon substrates used in this thesis have been cleaned by high-temperature annealing using direct current injection. A specially-designed sample holder leaves the silicon sample as the only path for current circulation (Fig. 1.2 (a)). Resistive heating removes the native oxide layer and carbon impurities. Direct current injection permits the achievement of higher temperatures in comparison to electron bombardment widely used for metals. As a result, sputtering is not necessary for Si substrates. Cleaving can be used in layered materials such as the high-temperature superconductors (cuprates, pnictides), related transition metal oxide systems (e.g. magnanites, cobaltates) and, topological insulator materials (e.g.  $\text{Bi}_2\text{Se}_3$ ,  $\text{Bi}_2\text{Te}_3$ ).

Once the single crystal substrate has been cleaned by sputtering and/or annealing, more complex interfaces can be obtained by the deposition of different atomic species. Electron beam evaporation has been extensively used in this thesis for the deposition of Bi (e.g. Fig. 1.2 (b)). Electrons emitted by a filament are accelerated towards an anode due to high potential difference. The anode is a rod or a crucible containing the evaporant (as in the case of Bi). Atoms from the heated target evaporate and are finally deposited on the substrate depending on their sticking coefficients. A commercial three-cell Omicron evaporator has been used during this thesis work. On the other hand, Ag has been deposited by resistive heating using a home-made tungsten basket, as those depicted in Fig. 1.2 (c). The basket is in thermal contact with the evaporant and there is no need for a high-voltage power supply. Refractory metals (W, Mo and Ta) are widely used for this kind of evaporation sources because they have a low vapor pressure and low reactivity with the evaporant.

UHV sample manipulation (i.e. translation and rotation) is achieved by magnetically-coupled rotary-linear motion feedthroughs, transfer tools based on welded bellows and rotation mechanisms with differential pumping. These systems are leak-tight fixed on the ports of the UHV multichamber setup.

## 1.2 Theoretical background on photoelectron spectroscopy

### 1.2.1 Introduction to PES - energy conservation

Photoelectron spectroscopy (PES), or photoemission spectroscopy, is a conceptually simple "photon-in  $\rightarrow$  electron-out" experiment, based on the interaction between a monochromatic beam of light and a target. The target may belong to the liquid or gas phase, albeit a solid is the most common example. If the incoming photon energy ( $h\nu$ ) is high enough, electrons can escape from the material and their kinetic energy ( $E$ ) may be measured by means of an electrostatic analyzer. Due to energy conservation, one can then have direct information about the energy distribution of electrons inside the sample:

$$E = E_B + h\nu - \Phi \quad (1.3)$$

where  $E_B$  is the binding energy of the electrons and  $\Phi$  the work function of the sample. Both  $E_B$  and  $\Phi$  are measured with respect to the Fermi energy ( $E_F$ ) of the studied material. The work function denotes the minimum amount of energy that is necessary to excite an electron out of the metal, i.e. the energy difference between the Fermi level and the vacuum level ( $E_v$ ). PES can reproduce a detailed DOS diagram for the occupied states of the system (Fig. 1.3 (a)). The unoccupied set of states can be accessed by different experimental techniques such as Inverse Photoelectron Spectroscopy (IPES), X-Ray Absorption Spectroscopy (XAS) or Scanning Tunneling Spectroscopy (STS).

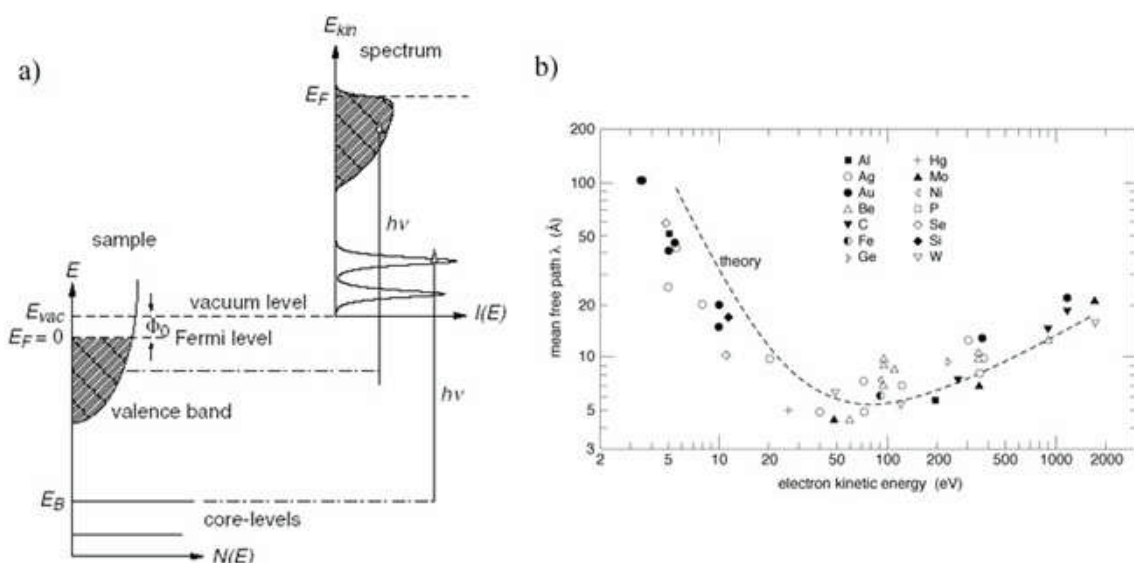


**Figure 1.3** — (a) A photoemission spectrum  $I(E)$  has a direct correspondence to the DOS of the studied material up to  $E_F$ . Peak broadening is due to experimental background and intrinsic finite lifetime effects (see text). (b) The "universal curve" of materials has a global minimum at the UV range. [70, 156]



### 1.2.2 3-step model

A phenomenological three-step model [21, 20] is often applied to describe the underlying physics during a PES experiment. According to this approach, the photoemission process is divided into three sequential steps: (1) optical excitation of the electron in the bulk of the material, (2) propagation of the excited electron to the surface and (3) escape into the vacuum (Fig. 1.4).

The photoexcitation process induces an optical transition inside the solid. Energy and momentum conservation laws must be strictly followed, reducing the number of allowed final states. For UV light, the momentum of the photons is small and can be neglected, so that the acceptable "vertical"  $k$ -space transitions are possible only when the periodic crystal potential is taken into account (Fig. 1.5).

During the second step, the excited electron travels towards the surface and may undergo energy-loss processes due to interactions with other electrons, phonons or impurities. As a result, a large amount of secondary electrons appears superimposed on the intrinsic photoemission signal (Fig. 1.4). Apart from the generation of secondary electrons, inelastic collisions with other particles determine the surface sensitivity of the photoemission process. In principle, only electrons within a few layers under the surface can contribute to the intrinsic signal. Interestingly, all materials follow an approximate "universal curve", which plots the inelastic mean free path (IMFP) of the electrons with respect to their kinetic energy (Fig. 1.3 (a)). IMFP (or  $\lambda$ ) of the electrons is defined as the distance from the surface, where the probability of loss-free emission is decreased by a factor of  $e$ :

$$I(z) = I_0 e^{-z/\lambda \cos \theta} \quad (1.4)$$

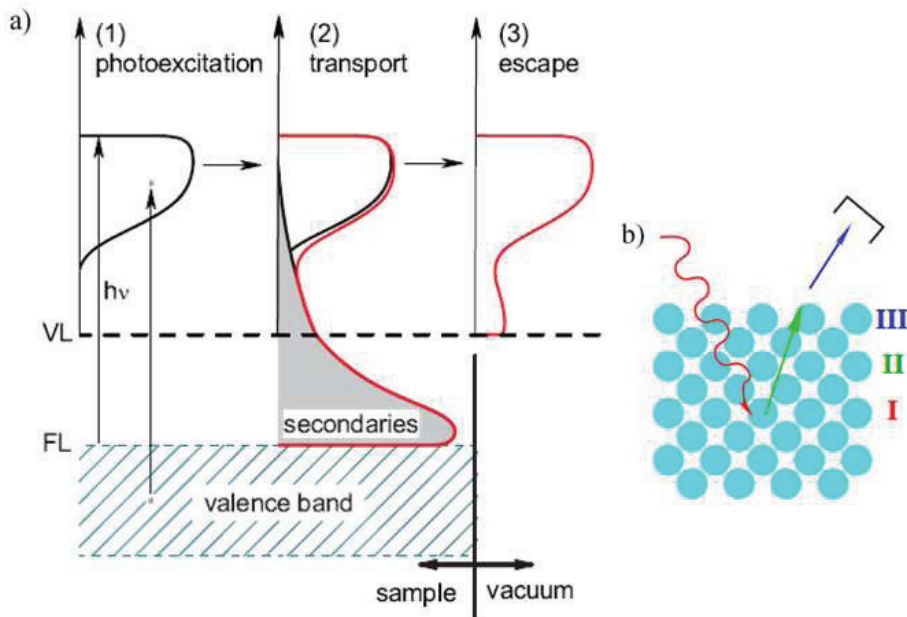


**Figure 1.4** — (a) Modifications of the PES spectrum after each successive step of the 3-step model. (b) A schematic representation of the 3-step model. [70]

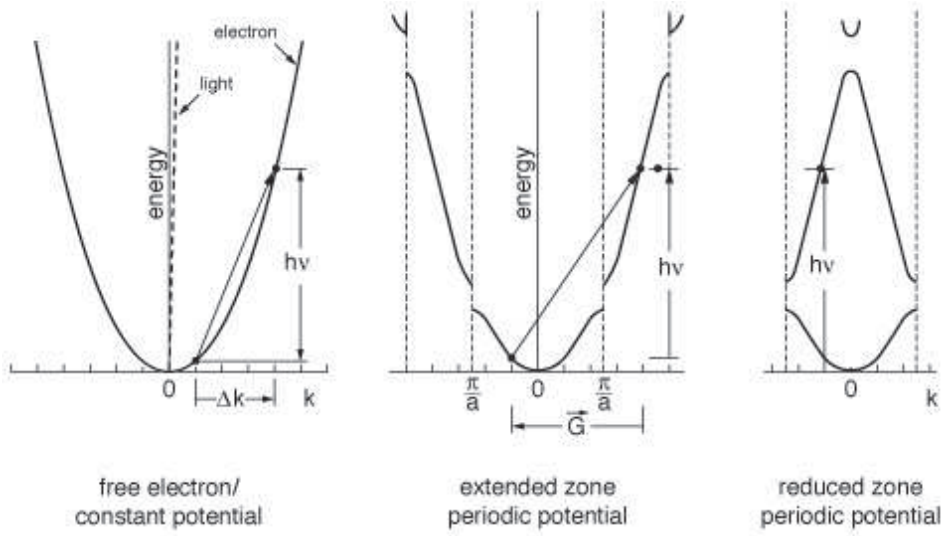


**Figure 1.5** — Simultaneous  $E - k$  conservation implies vertical  $k$ -space transitions because incoming photons carry negligible momentum (tilted dashed line). These requirements are satisfied only if one considers the periodic lattice potential in the reduced zone scheme. [67]

where  $\theta$  is the emission angle of the photoelectron and  $I(z)$  the photoemission intensity at depth  $z$ . Fig. 1.3 (b) exhibits a global minimum at the Ultra-Violet (UV) energy range, revealing that conventional laboratory sources (e.g. He discharge lamps) are ideal if one is interested in the electronic properties of surfaces and interfaces.

During the last step of the phenomenological model, the electrons have to overcome the surface potential barrier. Because of the broken translational symmetry along the  $z$  direction, the perpendicular wavevector of the photoemission process ( $\mathbf{k}_\perp$ ) is not a good quantum number and cannot be conserved during the electron's escape to the vacuum. On the other hand, the momentum conservation law for the parallel component can give us the value of  $k_\parallel$  if one measures  $E$  and  $\theta$  by angle-resolved PES (ARPES):

$$k_\parallel = \frac{\sqrt{2m_e E}}{\hbar} \sin \theta \simeq 0.512 \sqrt{E} \sin \theta \quad (1.5)$$

Escape into the vacuum may be equivalently described as a diffraction phenomenon of bulk electrons on the crystal surface, i.e. their direction of propagation is changed. Therefore, not only the electrons' total energy must be higher than the vacuum energy but also their direction of propagation must lie within a specific angular range determined by the conservation law for  $\mathbf{k}_\parallel$  and the reduction of  $\mathbf{k}_\perp$  due to the surface potential barrier. Otherwise, escape into the vacuum cannot be possible (Fig. 1.6).

For 2D materials like the topics of this thesis, one is interested only in the parallel component of the wavevector. Therefore, ARPES mapping of their electronic structure is generally a straightforward process, which can be experimentally realized by using a fixed excitation energy and measuring the kinetic energy distribution of the emitted photoelectrons as a function of the

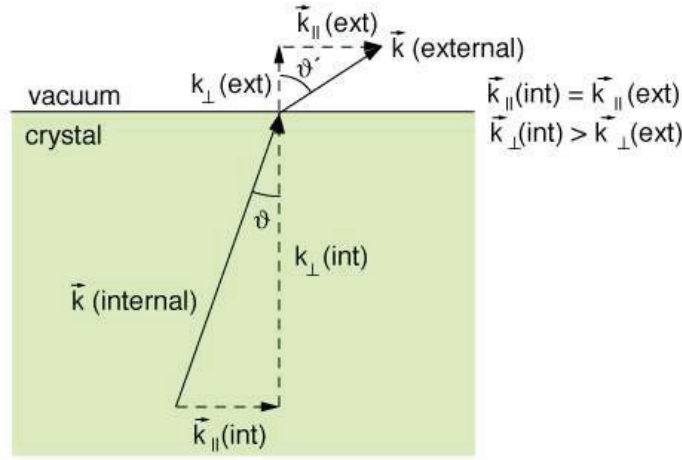


**Figure 1.6** — Only the parallel momentum component is conserved when the photoelectron overcomes the surface potential barrier. If a maximum value for the angle  $\theta$  is overcome, the electron will be reflected into the bulk of the solid. [67]

electron emission angle. On the other hand,  $k_{\perp}$  for 3D systems can be accessed only by making a hypothesis on the dispersion of the excited state. In principle, provided a tunable photon source is available, different modes of PES can be realized where either the initial (constant initial state spectroscopy, CIS) or the final state (constant final state spectroscopy, CFS) is fixed. In this way one can respectively follow the dispersion of the final or the initial state band in the  $z$  direction.

### 1.2.3 1-step model

A more rigorous one-step approach considers the photoemission experiment as a photon-induced excitation of a system in the ground state  $|\psi_i\rangle$  to a final state  $|\psi_f\rangle$  resulting in a photoelectron with momentum  $\mathbf{k}$  and kinetic energy  $E = (\hbar^2 k^2)/(2m_e)$ , and the remaining  $(N - 1)$ -electron system. The Hamiltonian which describes the interaction of the system with the electromagnetic vector potential  $\mathbf{A}$  is given by the transformation  $\mathbf{p} \rightarrow \mathbf{p} - (e/c)\mathbf{A}$  of the momentum operator  $\mathbf{p} = -i\hbar\nabla$  in the unperturbed Hamiltonian  $H_0 = p^2/2m_e + eV$ :

$$\begin{aligned} H &= \frac{1}{2m_e} \left( \mathbf{p} - \frac{e}{c} \mathbf{A} \right)^2 + eV \\ &= \frac{p^2}{2m_e} - \frac{e}{2m_e c} (\mathbf{A} \cdot \mathbf{p} + \mathbf{p} \cdot \mathbf{A} - \frac{e}{c} A^2) + eV \end{aligned} \quad (1.6)$$

At low intensities (e.g. for standard laboratory and even synchrotron sources) the 2<sup>nd</sup> order term in  $\mathbf{A}$  can be neglected. Therefore the interaction Hamiltonian can be written as:

$$\begin{aligned} H_{\text{int}} &= -\frac{e}{2m_e c} (\mathbf{A} \cdot \mathbf{p} + \mathbf{p} \cdot \mathbf{A}) \\ &= -\frac{i\hbar e}{2m_e c} (\mathbf{A} \cdot \nabla + \nabla \cdot \mathbf{A}) \end{aligned} \quad (1.7)$$



If one neglects particular surface effects where  $\mathbf{A}$  can have a strong spatial dependence, the latter can be considered constant over atomic dimensions (dipole approximation) and the second term can be omitted. Under the so-called "dipole approximation" Eq. (1.7) can be further simplified:

$$H_{\text{int}} = -\frac{e}{m_e c} \mathbf{A} \cdot \mathbf{p} \quad (1.8)$$

$H_{\text{int}}$  can be then treated as a periodic perturbation and may be used to calculate the transition probability  $w$  from  $|\psi_i\rangle$  to  $|\psi_f\rangle$  via Fermi's golden rule:

$$w_{i \rightarrow f} = \frac{2\pi}{\hbar} |\langle \psi_f | H_{\text{int}} | \psi_i \rangle|^2 \delta(E_f - E_i - h\nu) \quad (1.9)$$

By neglecting the interaction of the excited photoelectron with the remaining particles (sudden approximation), the  $N$ -electron wavefunction can be written as the product of an one-electron state and the state of remaining electrons:

$$\psi_i(N) = \phi_{i\kappa} \psi_{i\kappa,R}(N-1) \quad \text{and} \quad \psi_f(N) = \phi_{f\mathbf{k}} \psi_{f\mathbf{k},R}(N-1) \quad (1.10)$$

where  $R$  stands for "remaining" and  $\kappa$  ( $\mathbf{k}$ ) represent the momentum of the initial (final) states. The remaining  $(N-1)$  electrons are external spectators but may interact with each other. Using the above considerations, one can write the interaction term as:

$$\langle \psi_f | H_{\text{int}} | \psi_i \rangle = \langle \phi_{f\mathbf{k}} | H_{\text{int}} | \phi_{i\kappa} \rangle \sum_s c_s \quad (1.11)$$

where  $c_s = \langle \psi_{f\mathbf{k},R}(N-1) | \psi_{i\kappa,R}(N-1) \rangle$  and  $\langle \psi_{f\mathbf{k},R}(N-1) |$  are the possible relaxed final states, which are not necessarily eigenstates of the unperturbed  $H_0(N-1)$  Hamiltonian.

The photoemission current will be then:

$$I(\mathbf{k}, E) \propto \sum_{f,i,\kappa} |\langle \phi_{f\mathbf{k}} | H_{\text{int}} | \phi_{i\kappa} \rangle|^2 A(\mathbf{k}, E) \propto \sum_{f,i,\kappa} |M_{i,f}^{\kappa,\mathbf{k}}|^2 A(\mathbf{k}, E) \quad (1.12)$$

with

$$A(\mathbf{k}, E) = \sum_s |c_s|^2 \delta(E_f - E_s(N-1) - E_0(N) - h\nu) \delta(\mathbf{k} - \kappa)$$

where the last term represents the momentum conservation condition.

$I(\mathbf{k}, E)$  therefore depends on the product of the matrix element effects  $M_{i,f}^{\kappa,\mathbf{k}}$  and the spectral function  $A(\mathbf{k}, E)$ .  $A(\mathbf{k}, E)$  is the interesting part of a photoemission spectrum and can be related to fundamental theoretical concepts such as the Green's function (see subsection 1.2.4). It describes the probability to remove (or add) one electron from a many-body system. On the other hand,  $M_{i,f}^{\kappa,\mathbf{k}}$  induces modulations of the photoemission intensity related on the experimental geometry and the polarization of the electromagnetic beam. Equation (1.12) states that simultaneous conservation of

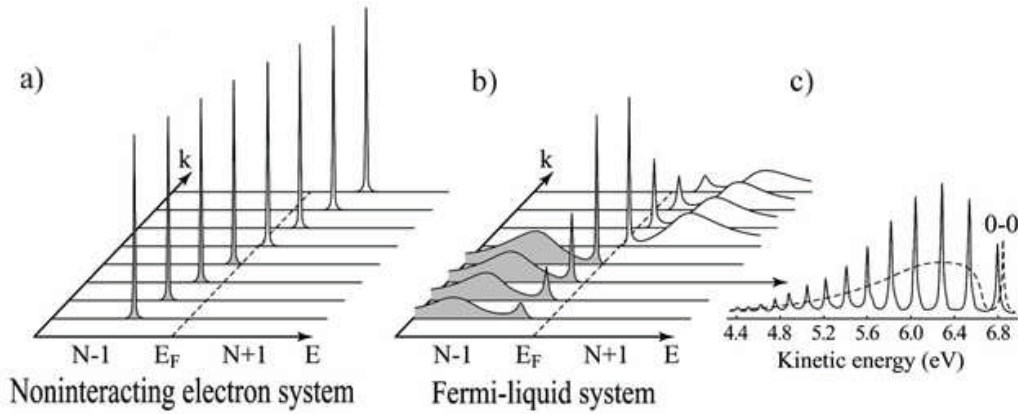


**Figure 1.7** —  $k$ -dependent ARPES spectral function for a free-electron gas (a) and interacting systems (b), (c). (a) The spectrum consists of delta functions at combinations of  $E$  and  $k_{\parallel}$  which satisfy (1.12). (b), (c) Spectral weight is transferred to higher  $E_B$  peaks which correspond to the excited ( $N - 1$ ) states. The latter can appear as sharp photoemission peaks (e.g. molecular hydrogen in (c)) or may be broadened into an incoherent continuum ((b) and solid hydrogen in (c)). [96, 134]

energy and momentum imposes strict restrictions on the combined values of  $\mathbf{k}$  and emission angle, for which a photoelectron can be observed.

ARPES results for  $I(\mathbf{k}, E)$  are usually plotted in the form of band diagrams (i.e.  $E$  vs.  $k_{\parallel}$ ) or constant energy (CE) surfaces (e.g.  $k_x$  vs.  $k_y$  for fixed  $E$ ). In both cases photoemission intensity is determined by a color scale. A more traditional way of presenting the data is by energy or momentum distribution curves (EDC or MDC). In this case, one axis corresponds to photoemission intensity and the other to energy (EDC) or  $k_{\parallel}$  (MDC). Although this approach gives less information about the overall band structure, a careful lineshape analysis of such curves may reveal important correlation effects. The linewidth of an EDC contains information about the lifetime, while that of the MDC is inversely proportional to the coherence length of the particles.

In the limit of non-interacting electrons  $\psi_{f_{s_0,R}}(N - 1) = \psi_{i,R}(N - 1)$  and  $c_{s_0}$  becomes unity while all other  $c_s$  would be equal to zero. The spectral function would therefore consist of delta functions at appropriate  $\mathbf{k}$  and  $E_B$  values which satisfy the conditions imposed by Eq. (1.12) (Fig. 1.7 (a)). Nevertheless, in an interacting many-body system, the "frozen" (unperturbed) ( $N - 1$ ) state will have a significant overlap with the wavefunctions of the excited ( $N - 1$ ) states. From the experimental point of view, the excited ( $N - 1$ ) states will appear as a superposition of "satellite" photoemission peaks at higher  $E_B$  (Fig. 1.7 (c)). The satellites peaks may be broadened into an incoherent continuum (Figs. 1.7 (b) and (c)).

Under certain symmetry considerations  $M_{i,f}^{\mathbf{k}}$  may even suppress the photoemission signal. Each part of the matrix element (Eq. (1.12)) has its own possible symmetry with respect to the sample's mirror planes. Therefore, a transition will be allowed or forbidden depending on a combination of the experimental geometry and the details of the wavefunctions. One can easily analyze the symmetry-imposed conditions when the PES electron analyzer lies within the sample's mirror plane. First of all, the total overlap integral must be an even function with respect to the mirror plane in order to have non-zero signal on the detector. The final state wavefunction  $|\phi_f\rangle$  must be

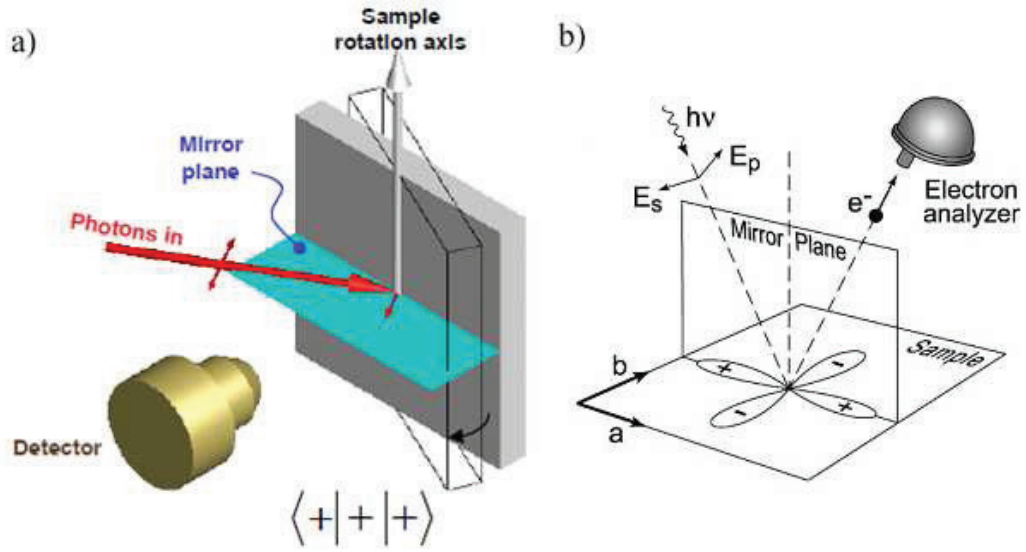


**Figure 1.8** — (a) An experimental geometry following case a) of the matrix elements condition imposed by (1.13). Only even initial states will be probed (Figure from E. Rotenberg). (b) Photoemission from a  $d_{x^2-y^2}$  orbital when the analyzer is located within the sample's mirror plane. Under the depicted geometry, the orbital can be detected only with  $p$ -polarized light ( $E_p$ ). After in-plane rotation of the sample by  $45^\circ$  it would be detected only with  $s$ -polarized light ( $E_s$ ). [35]

also even, since it refers to a plane wave. The parity of  $H_{\text{int}} = \mathbf{A} \cdot \mathbf{p}$  depends on the incoming light polarization, while  $|\phi_i\rangle$  can be even or odd depending on the  $\mathbf{k}$ -vector of the probed final state. Under these considerations  $|M_{i,f}^k|^2$  will be non-zero in the following two cases.

$$|M_{i,f}^k|^2 = |\langle \phi_f | H_{\text{int}} | \phi_i \rangle|^2 \quad \text{non-zero for} \quad \text{a) } \langle + | + | + \rangle \quad \text{or} \quad \text{b) } \langle + | - | - \rangle \quad (1.13)$$

An experimental geometry which would satisfy a) is shown in Fig. 1.8 (a). In Fig. 1.8 (b), one considers a photoemission experiment on a material with a  $d_{x^2-y^2}$  orbital. The choice of  $s$ - or  $p$ -polarized light depends critically on the in-plane sample orientation if one wants to observe non-zero photoemission intensity from this type of orbitals. The situation is more complex when the detector lies out of the sample's mirror plane.

Equation (1.12) is valid only at  $T = 0\text{K}$ . At finite temperatures the product of the spectral function and matrix elements has to be multiplied with the Fermi-Dirac function  $F(E, T)$  to acquire a complete expression for the photoemission intensity:

$$I(\mathbf{k}, E, T) = \sum_{f,i,\mathbf{k}} |M_{i,f}^k|^2 A(\mathbf{k}, E) F(E) \quad (1.14)$$

Thermal excitation of electrons broadens the spectral features but can also give a limited access to the unoccupied states. Observation of the lowest-lying unoccupied states was critical in the experimental observation of the superconducting gap of the BCS-like  $V_3\text{Si}$  compounds [123].

### 1.2.4 Theoretical concepts

The spectral function  $A(\mathbf{k}, \omega)$ , which can be probed by PES, is related to another fundamental theoretical concept; the single particle Green's function  $G(\mathbf{k}, \omega)$ :

$$A(\mathbf{k}, \omega) \equiv -\frac{1}{\pi} |\text{Im}G(\mathbf{k}, \omega)| \quad (1.15)$$

where  $\omega$  is the energy measured from the chemical potential.  $G(\mathbf{k}, \omega)$  is an important tool for the description of interacting many-body systems. The effects of interactions are contained in the self-energy operator  $\Sigma(\mathbf{k}, \omega)$ :

$$G(\mathbf{k}, \omega) = \frac{1}{\omega - E - \Sigma(\mathbf{k}, \omega)} \quad (1.16)$$

$E$  denotes the energy satisfying Eq. (1.12) for non-interacting particles. As explained in the previous subsection, the spectral function is modified in the presence of correlations (Fig. 1.7). For interacting systems, e.g. the so-called Fermi Liquids (FL) represented in Figs. 1.7 (b) and (c),  $A(\mathbf{k}, \omega)$  is given by the following expression of general validity:

$$A(\mathbf{k}, \omega) = \frac{1}{\pi} \frac{|\text{Im} \Sigma(\mathbf{k}, \omega)|}{|\omega - E - \text{Re} \Sigma(\mathbf{k}, \omega)|^2 + |\text{Im} \Sigma(\mathbf{k}, \omega)|^2} \quad (1.17)$$

This equation predicts a non-symmetric line shape with a peak width of  $2\text{Im} \Sigma(\mathbf{k}, \omega)$  and a peak position shift of  $\text{Re} \Sigma(\mathbf{k}, \omega)$ . Under ideal experimental conditions, these quantities can be measured and one can have an indication about the correlations in the studied materials. Equation (1.17) can be approximated by:

$$A(\mathbf{k}, \omega) \approx Z_k \frac{1}{\pi} \frac{|\text{Im} \Sigma(\mathbf{k}, \omega)|}{|\omega - E|^2 + |\text{Im} \Sigma(\mathbf{k}, \omega)|^2} + A_{\text{inc}} \quad (1.18)$$

One can easily identify the first term (Lorentzian) with the sharp peaks of Figs. 1.7 (a) and (b), and the second term with the higher- $E_B$  satellites. Eq. (1.18) and Fig. 1.7 reveal that if the independent electron picture is a good first approximation, electron-electron interactions will not invalidate this picture for levels near  $E_F$ . The self-energy operator  $\Sigma(\mathbf{k}, \omega)$  for a FL system is predicted to have the following asymptotic form:

$$\Sigma = \alpha\omega + i\beta\omega^2 \quad (1.19)$$

Near the Fermi level, the spectrum has an asymmetric Lorentzian shape, and exactly at  $E_F$  it reduces to a *delta* function. A sharp Fermi surface is therefore still present. As a result, one can define "new" weakly interacting particles; i.e. quasiparticles (QP), which obey the Fermi-Dirac statistics and can be considered as bare electrons, "dressed" by a cloud of virtual excitations. The analogy of electrons and quasiparticles reveals the reason of the fundamental similarities between the interacting FL systems and non-interacting Fermi gases.

A detailed QP lifetime analysis using the  $I(E)$  energy distribution curves for the 2D FL system  $\text{TiTe}_2$  revealed that the ARPES spectrum is not only a map of the "hole" spectral function but it also contains information about the photoemitted electron, thus inducing residual broadening of the peaks [116]. It has been nevertheless shown for 2D states that the electron's contribution is negligible and the linewidth reflects the hole lifetime [138]. This is an additional advantage of low-dimensional systems for ARPES investigation.

### 1.3 Experimental details of modern photoelectron spectroscopy

ARPES experiments take place under UHV conditions (see section 1.1) by means of modern spectrometers termed hemispherical analyzers. A hemispherical analyzer can measure the kinetic energy and momentum of the photoemitted electrons, and it thus allows the user to plot the electronic band diagram of the studied material and access the spectral function. It consists of three main parts; an electrostatic lens system, a hemispherical deflector with entrance and (optionally) exit slits and a multichannel detector (Fig. 1.9 (a)).

The most important part of the spectrometer is the hemispherical deflector. In short, the deflector acts as an electron monochromator allowing only electrons within a certain range of energies to pass through the analyzer and arrive at the detector. It consists of two concentric hemispheres with radii  $R_{\text{in}}$  and  $R_{\text{out}}$ , which are kept at a potential difference  $\Delta V$ . These are essentially a pair of electrodes, which acts as a capacitor. Although, different electrode geometries are possible (parallel plates, cylindrical), the hemispherical shape is most widely used for ARPES.

Photoemitted electrons move through the electrostatic field of the two hemispheres and experience a radial electrostatic force. As a result, they are deflected and they can reach the exit slit and

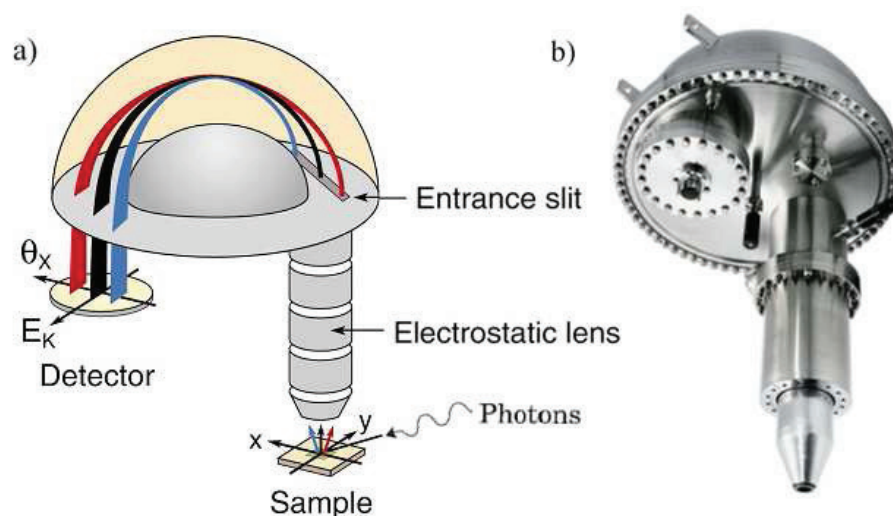


**Figure 1.9** — (a) A schematic view of a modern ARPES hemispherical analyzer. The different components are explained in the text. (b) The Phoibos 150 Specs analyzer used for the data acquired in this thesis. [140]

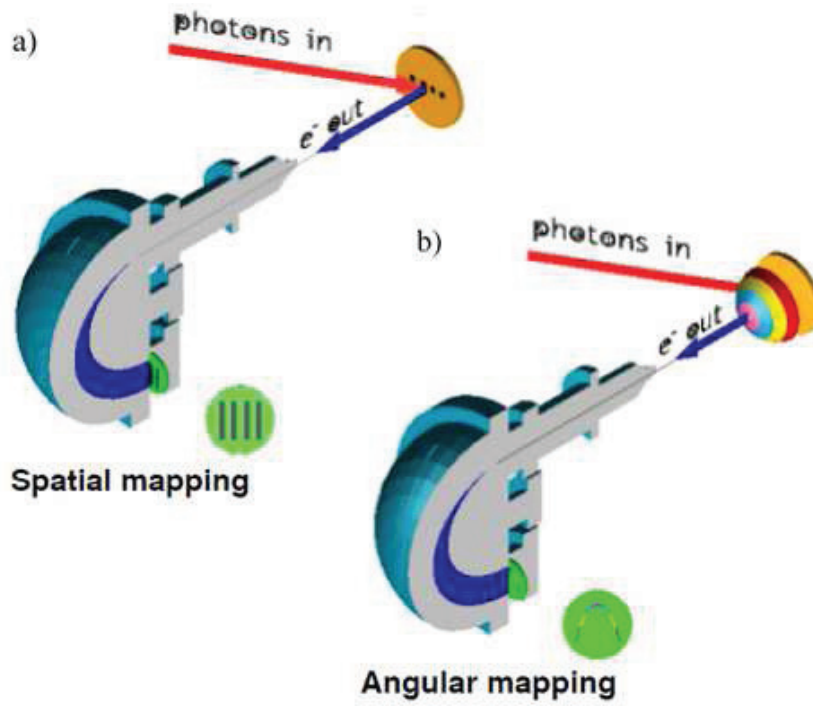


**Figure 1.10** — In the hemispherical deflector, photoelectrons are dispersed not only according to their energy but also their position on the sample (a) or momentum (b). 2D detectors can therefore give spatial (a) or k-dispersion (b) information within a single image (figure from E. Rotenberg).

the detector only if their kinetic energy  $E$  satisfies the following condition:

$$E = \frac{e\Delta V}{\frac{R_{\text{out}}}{R_{\text{in}}} - \frac{R_{\text{in}}}{R_{\text{out}}}} \quad (1.20)$$

In order to measure a spectrum, one would have to start at a specific kinetic energy and stepwise increase it, thus counting the electrons arriving at each potential. However, the energy resolution  $\Delta E$  depends on the kinetic energy. Therefore, in order to work with constant  $\Delta E$  over a large range of energies, modern spectrometers are equipped with an electrostatic lens system just before the entrance slit of the deflector. These lenses collect a portion of the photoemitted electrons defined by those rays, which can be transferred through the apertures and focused onto the slit. Apart from focusing the electron beam, the electrostatic lenses retard or accelerate the electrons to the proper "pass energy" defined by equation (1.20). Thus, the analyzer itself is kept at constant  $\Delta V$  and the lenses potential is swept in order to scan through the energy range of interest (sweep-mode acquisition). The energy resolution depends on the pass energy ( $E_{\text{pass}}$ ), the slit width ( $S$ ) and the acceptance angle ( $\alpha$ ) in the dispersive direction:

$$\Delta E = E_{\text{pass}} \left( \frac{S}{R_o} + \frac{\alpha^2}{4} \right) \quad (1.21)$$

where  $R_o$  is the mean radius of the hemispherical setup (i.e  $R_o = (R_1 + R_2)/2$ ) and  $S$  the mean



value of the slit width ( $S = (S_{\text{entrance}} + S_{\text{exit}})/2$ ). The analyzer can be operated in Fixed Analyzer Transmission (FAT) or Fixed Retarding Ratio (FRR) mode. FAT was introduced in the previous paragraph;  $E_{\text{pass}}$  is held constant and it is entirely the job of the lens system to retard the given kinetic energy to the range accepted by the analyzer. In the alternative FRR mode, a constant value for the  $E_{\text{pass}}/E$  ratio is maintained, while the lens voltages are swept. FAT is typically used for ARPES spectra, while FRR is more useful for Auger spectra 1.4.2. The latter can recover weak Auger peaks at high kinetic energy, while restricting the intense low energy background that can damage the detection system.

Photoelectrons are dispersed through the hemispherical deflector, so that electrons with different energies arrive at different points in the radial (= energy-dispersive) direction (Fig. 1.10). They are also dispersed along the perpendicular direction (i.e. around the circumference of the sphere) according to their emission angle (angular mode) or emission position (transmission or magnification mode). Modern spectrometers exploit this effect by using 2D detectors. A virtual exit slit is defined by the software and the detector structure. A single image can provide a description of the band dispersion or spatial information about the electronic structure.

The detector is essentially a micro-channel plate (MCP) assembly. Each plate is composed of a large number of thin glass tubes (channels) fused together. (Fig. 1.11). The tubes work as independent secondary electron multipliers. Two MCPs are arranged in a chevron (v-like) shape with angled channels rotated  $180^\circ$  with respect to each other. Electrons which exit the first plate start the cascade in the second. The MCP arrangement multiplies each incoming photoelectron about  $10^7$  to  $10^8$  times. The resulting electron beam is accelerated to a phosphor screen, where it produces a light flash, which is in turn detected by a sensitive CCD camera. The position of the light flash corresponds to the position of the initial electron. Such an MCP arrangement shows high detection efficiency for both electrons and ions, but it is also sensitive to other kind of particles (e.g. photons).

Most of the work presented in this thesis was performed with a commercial Phoibos 150 hemispherical analyzer by Specs GmbH (Figs. 1.9 (b) and 1.11 (b)). The mean radius of the deflector  $R_o$  is equal to 150mm. An aperture in the lens system determines the acceptance angle and gives the user the flexibility to eliminate aberration effects. The maximum acceptance angle is  $\pm 13^\circ$  for the angular modes, while the ultimate energy and angular resolutions are 2meV and  $0.05^\circ$  correspondingly. For small spot analysis a lateral resolution down to  $100\mu\text{m}$  is possible using a spatially-resolved mode and the iris aperture of the lens system. All parts of the analyzer are surrounded by 1.5mm thick  $\mu$ -metal to screen the external magnetic fields which may influence the electron trajectories.

ARPES in the UV range can be performed with various excitation sources. High-brightness UV sources based on an electric discharge in a rare gas are a powerful solution for laboratory-based experiments. Synchrotron radiation is an interesting alternative and has important advantages such as the high intensity, the tunable polarization of the incoming beam and the availability of a wide spectral range of photon energies. Recently, laser sources have started being employed for ARPES experiments. Such sources enjoy the advantages of a very intense and polarized light, but on the

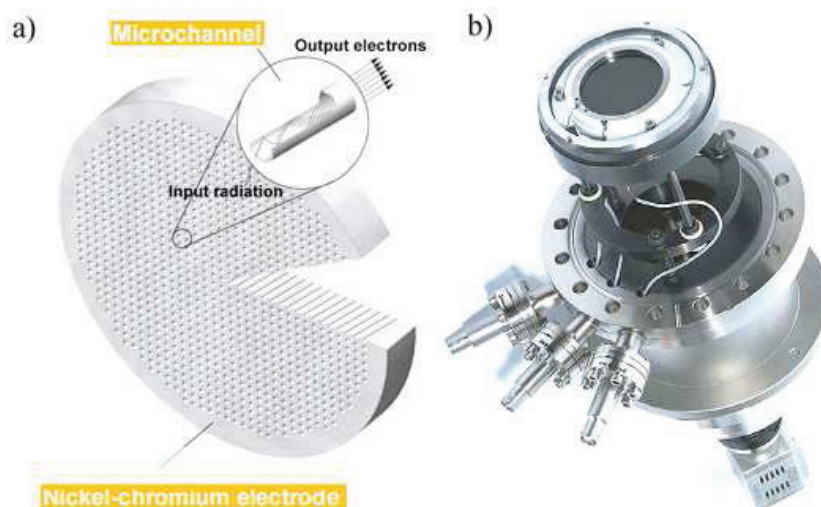


**Figure 1.11** — (a) A micro-channel plate (MCP) consists of a large number of glass capillaries, each one acting as an independent electron multiplier. (b) The MCP detector of the Phoibos 150 Specs analyzer used for the data acquired in this thesis. [139]

other hand the small kinetic energy of the excited photoelectrons means that the available  $k$ -space range is limited (Eq. (1.5)).

During the work for this thesis, ARPES results have been obtained with a Scienta VUV 5000 high-intensity source. A schematic view of the source can be seen in Fig. 1.12. He-plasma is generated with the Electron Cyclotron Resonance technique (ECR). The ECR condition for the discharge is met by the combination of a microwave generator and a magnetic field tuned to the necessary microwave frequency. Radiation is concentrated to HeI (21eV and 23eV) and HeII (41eV and 48eV) lines. The system is coupled to a monochromator where the user can select the incoming photon energy. The 21eV (mainly) and 41eV discharge lines produce photons with high intensity and have been routinely used for the results of this thesis work.

Apart from photoelectron spectroscopy, complementary surface science techniques have been used to provide additional information about the structure and the chemical composition of the studied surfaces and interfaces. In the following section, low-energy electron diffraction and Auger electron spectroscopy will be briefly reviewed.

## 1.4 Complementary characterization techniques

### 1.4.1 Low-energy electron diffraction

Low-energy electron diffraction (LEED) is a surface sensitive technique which can provide information about the size and symmetry of the surface unit cell. It is based on the elastic scattering of a monochromatic electron beam by the surface atoms. The diffraction pattern is recorded and analysis of the spot positions determines the symmetry and atomic order of surface reconstructions.



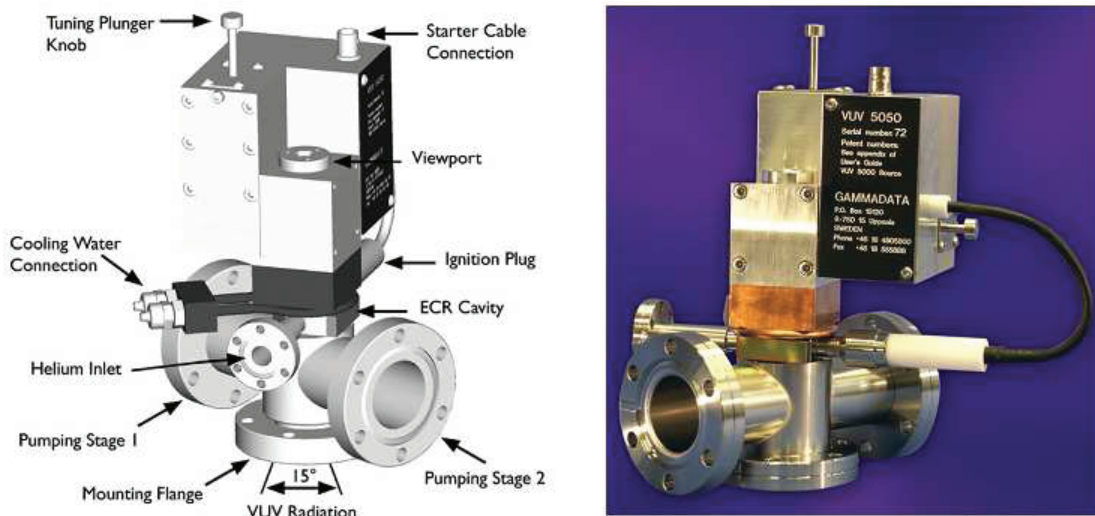


**Figure 1.12** — A schematic representation (left) and a photograph (right) of the high-brightness Scienta VUV 5000 photon source used for the data acquired in this thesis. [149]

The main advantage of LEED is that it is a technique which can give fast information about the studied material and it can be performed routinely before other time-consuming experiments (e.g. ARPES).

LEED is an "electron-in  $\rightarrow$  electron-out" experimental technique. An electron gun generates a monochromatic beam of electrons which is incident normally on the sample. The generated back-scattered electrons pass through a series of hemispherical grids where the inelastically scattered particles are screened out. The elastically scattered electrons arrive at a fluorescent screen, causing a bright diffraction pattern (Fig. 1.13 (a)). The pattern is an image of the reciprocal space unit cell of the studied surface.

From the theoretical point of view, surface atoms can be considered as point scatterers. Bright spots on the fluorescent screen are the result of constructive interference between the scattered beams. In the case of a 1D chain of atoms, the interference maxima appear at angles  $\theta$  which satisfy the Bragg condition:

$$k = G_{\parallel} \quad \text{and} \quad \sin \theta = n\lambda \quad (1.22)$$

where  $n$  is an integer number defining the order of diffraction,  $a$  is the atomic separation and  $\lambda$  the wavelength of the incident electron beam. From the above formula, one can conclude that diffraction effects are possible only if the wavelength range of electrons employed in the LEED experiment is comparable to the atomic spacing. Moreover, the size of the diffraction pattern depends on the incident beam energy. The latter can be easily tuned giving access to more reciprocal lattice points.

Apart from the standard qualitative analysis of the surface symmetry, LEED can be used as a quantitative tool to provide accurate information about the atomic positions. In this experiment, one has to perform a detailed measurement of the intensities of various diffracted beams as a function of

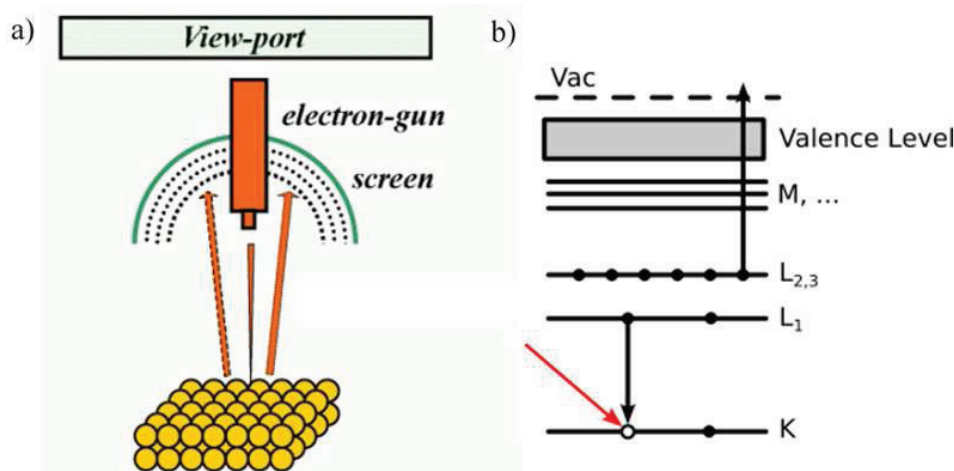


**Figure 1.13** — (a) A simplified schematic representation of a LEED experiment. Elastically back-scattered electrons pass through the hemispherical grids and their interference spots on the phosphor screen are an image of the reciprocal lattice unit cell (image from Department of Metallurgy, Tohoku University, Japan). (b) A schematic diagram of the energy transitions involved in a AES experiment. An incoming electron beam creates a core-hole (K-level) which is subsequently filled by the relaxation of another electron (from the  $L_1$  level). The gained energy is transferred to a third electron, which can be emitted from the solid. A  $KL_1L_{2,3}$  transition is depicted.

the incoming electron beam energy. The obtained  $I - V$  curves must be then compared with theoretically generated  $I - V$  curves for different structural models. In this way, LEED can distinguish between iso-symmetrical surface reconstructions with different atomic arrangement.

LEED has been routinely performed during the work for this thesis to determine the surface symmetry and the quality of the samples before ARPES measurements. LEED images of different surface reconstructions are presented in chapters 3 and 4. In the case of the Bi/Si(111) system, quantitative  $I - V$  LEED measurements allowed the discrimination of two reconstructions with the same reciprocal lattice symmetry and size (section 3.2).

## 1.4.2 Auger electron spectroscopy

Auger electron spectroscopy (AES) is a surface sensitive technique which can give direct information about the chemical composition of the topmost layers of the sample. During the Auger process, the sample is exposed to a beam of high energy electrons (2 – 10keV). Electron impact can result into the removal of a core-level electron. The ionized atom may then relax to a state of lower energy by the filling of the core-hole with a higher-level electron and the simultaneous transfer of the liberated energy to second electron which is emitted. The final state has therefore two core-holes (Fig. 1.13 (b)).

Different Auger transitions are possible depending on the location of the initial and the final two holes. Due to energy conservation, each of them can be tracked after measuring the kinetic energy of the emitted electrons. The transitions are material specific because the energy level positions of core electrons vary between different atoms. As a result, the kinetic energy of the emitted electrons is a signature of the surface chemical composition.

AES has been employed during the work for this thesis to determine the quantity of deposited material and the cleanliness of the studied surfaces. The kinetic energy measurement of the emitted electrons has been performed with the Phoibos 150 Specs analyzer by using a spatial lens mode.



# Chapter 2

---

## Spin splitting on 2D electronic states: Experiment, theory, implications

---

### 2.1 Theoretical background on the Rashba-Bychkov effect

#### 2.1.1 Approximating the Dirac equation

The Schrödinger equation is one of the cornerstones of condensed matter physics. Its predictions for solutions which follow the Bloch theorem have given rise to the most successful approach of solid state physics, the band theory. Despite its successes, the Schrödinger equation does not take into account relativistic effects such as the spin-orbit (SO) interaction. In 1928, the work of Paul Dirac filled the gap by providing a description of spin- $\frac{1}{2}$  particles which is consistent with both the principles of special relativity and quantum mechanics. Assuming a time-independent problem, the Dirac equation can take the following form:

$$(c\boldsymbol{\alpha} \cdot \mathbf{p} + \beta mc^2 + V)\psi = E\psi \quad (2.1)$$

where  $\boldsymbol{\alpha} = \begin{pmatrix} 0 & \boldsymbol{\sigma} \\ \boldsymbol{\sigma} & 0 \end{pmatrix}$ ,  $\beta = \begin{pmatrix} \mathbf{I}_{2 \times 2} & 0 \\ 0 & -\mathbf{I}_{2 \times 2} \end{pmatrix}$  and  $\boldsymbol{\sigma}$  is the vector of Pauli matrices

$$\boldsymbol{\sigma} = \begin{pmatrix} \sigma_x \\ \sigma_y \\ \sigma_z \end{pmatrix} \text{ with } \sigma_x = \begin{pmatrix} 0 & 1 \\ 1 & 0 \end{pmatrix}, \sigma_y = \begin{pmatrix} 0 & -i \\ i & 0 \end{pmatrix}, \sigma_z = \begin{pmatrix} 1 & 0 \\ 0 & -1 \end{pmatrix}$$

and  $\mathbf{I}_{2 \times 2}$  is a unitary  $2 \times 2$  matrix.

The  $4 \times 4$  Dirac Hamiltonian can be expanded in terms of  $(v/c)^2$ . The terms of the leading orders give a good description if one disregards relativistic effects which become important only when  $v$  is of the order of  $c$ . After keeping the zero- and first-order terms, the non-relativistic Pauli equation emerges:

$$\left[ \frac{p^2}{2m} + V + \frac{e\hbar}{2m} \boldsymbol{\sigma} \cdot \mathbf{B} - \frac{\hbar \boldsymbol{\sigma} \cdot \mathbf{p} \times \nabla V}{4m^2 c^2} - \frac{\hbar^2}{8m^2 c^2} \nabla \cdot \nabla V - \frac{p^4}{8m^3 c^2} \nabla \cdot \nabla V - \frac{p^4}{8m^3 c^2} - \frac{e\hbar p^2}{4m^3 c^2} \boldsymbol{\sigma} \cdot \mathbf{B} - \frac{(e\hbar B)^2}{8m^3 c^2} \right] \psi = E\psi \quad (2.2)$$

The first two terms are the kinetic and potential energy of the Schrödinger equation ( $H_0$ ), while the third is the Zeeman term describing the response of the particles on an external magnetic field. The fourth term is the Pauli SO coupling and the fifth the so-called Darwin term due to the electron's zitterbewegung (i.e. rapid small-scale fluctuations). The last four terms represent higher-order corrections.  $\nabla V$  is the magnitude of the potential gradient (i.e. electric field) which acts as an effective magnetic field in the electrons' rest frame. More details about the origin of this field will be given in the next sections.

### 2.1.2 Atomic spin-orbit coupling

Spin-orbit coupling is the interaction of the electronic magnetic moment  $\boldsymbol{\mu}$  with the magnetic field  $\mathbf{B}$  which arises from the electric field  $\mathbf{E}$  of the nucleus. The effective magnetic field  $\mathbf{B}$  appears in the rest frame of the electrons and can be written as:

$$\mathbf{B} = \frac{1}{c^2} \mathbf{E} \times \mathbf{v} \quad \text{and} \quad \mathbf{v} = \frac{\hbar \mathbf{k}}{m^*} \quad (2.3)$$

since  $\mathbf{E}$  is radial one may write:

$$\mathbf{B} = \frac{1}{c^2} \frac{E}{r} \mathbf{r} \times \mathbf{v} = \frac{1}{mc^2} \frac{E}{r} \mathbf{r} \times \mathbf{p} \quad (2.4)$$

For hydrogenoid atoms, the electrostatic potential  $V$  is spherically symmetric, hence it depends only on the radius. According to this central field approximation,  $E$  can be replaced by:

$$E = \frac{\partial V(r)}{\partial r} = \frac{1}{e} \frac{\partial U(r)}{r} \quad (2.5)$$

where  $U(r) = V(r)e$  is the potential energy of the electron. Equation (2.4) may be therefore written as:

$$\mathbf{B} = \frac{1}{mc^2} \frac{1}{r} \frac{\partial U(r)}{\partial r} \mathbf{L} \quad (2.6)$$

with  $\mathbf{L} = \mathbf{r} \times \mathbf{p}$  denoting the angular momentum of the electron.

Moreover, the electron possesses a magnetic moment  $\boldsymbol{\mu}$  which can be written as:

$$\boldsymbol{\mu} = -\frac{e}{2m} g \mathbf{S} \quad , \quad g = 2 \quad (2.7)$$

where  $g$  is the  $g$ -factor of the electron and

$$\mathbf{S} = \frac{1}{2}\hbar\boldsymbol{\sigma} \quad (2.8)$$

is the electron spin operator.

Coupling between  $\mathbf{B}$  and  $\boldsymbol{\mu}$  is captured by the following Hamiltonian:

$$H_{\text{Larmor}} = -\boldsymbol{\mu}\mathbf{B} = \frac{2\boldsymbol{\mu}}{\hbar m_e c^2} \frac{1}{r} \frac{\partial U(r)}{\partial r} \mathbf{L} \cdot \mathbf{S} \quad (2.9)$$

Due to the relativistic Thomas precession this result is reduced by a factor of 2, yielding the final expression for the atomic SO Hamiltonian:

$$H_{SO} = \frac{\boldsymbol{\mu}}{\hbar m_e c^2} \frac{1}{r} \frac{\partial U(r)}{\partial r} \mathbf{L} \cdot \mathbf{S} \quad (2.10)$$

Equation (2.10) can be alternatively derived by the SO term of (2.2) by relating the cross product to  $\mathbf{L}$  and using Eq. 2.8 for  $\mathbf{S}$ .

The total angular momentum of the electron is given by  $\mathbf{J} = \mathbf{L} + \mathbf{S}$  and the eigenstates of the full Hamiltonian (i.e.  $H_0 + H_{SO}$ ) are  $|n, l, s, j, m_j\rangle$ . SO coupling results into the energy splitting of a level with non-zero  $l$  into two levels with different  $j$  values. Nonetheless, the  $+s$  and  $-s$  spin values are not separated; i.e. the two states are not spin-polarized. On the other hand, in a low-dimensional solid, spin-orbit interaction can result in spin-polarized states even without the application of a magnetic field.

### 2.1.3 From Dirac to Rashba

In the case of solids with broken space inversion symmetry, the potential gradient which enters the Pauli SO term of (2.2) can result in spin-polarized states. In the absence of an external magnetic

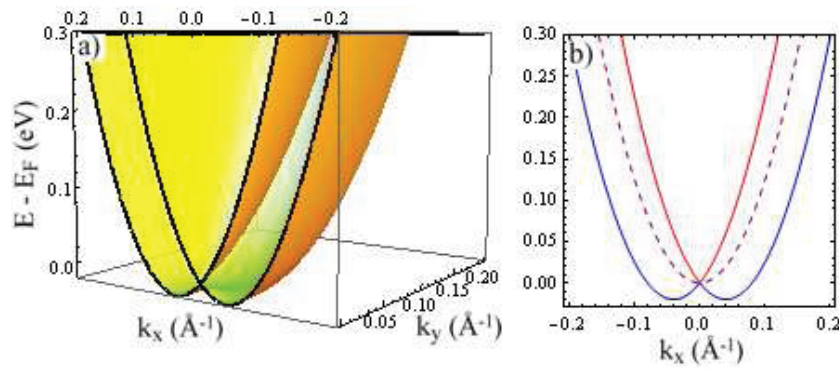


**Figure 2.1** — (a) 2D dispersion for an isotropic RB paraboloid.  $E(k_x, k_y)$  is given by the eigenvalues of the matrix (2.13). (b) Dispersion of the two spin-polarized branches (solid lines) along a high-symmetry direction. Blue and red correspond to opposite values of spin polarization. The dashed curve corresponds to the electronic dispersion without RB coupling. Simulation input:  $m^* = 0.3m_e$ ,  $\alpha_R = 1\text{eV \AA}$ .

field, this is the main correction to the Schrödinger Hamiltonian. After grouping all the constants along with the magnitude of the potential gradient, the SO term can be expressed as:

$$H_{SO} = \alpha_R(\boldsymbol{\sigma} \times \mathbf{k}) \cdot \hat{\mathbf{e}}_{\mathbf{n}} \quad (2.11)$$

In their famous work on 2D semiconductor heterostructures, Bychkov and Rashba identified the direction of the unit vector  $\hat{\mathbf{e}}_{\mathbf{n}}$  along the surface normal [28]. Assuming therefore a surface vector along  $\hat{\mathbf{e}}_{\mathbf{z}}$  one can rewrite  $H_{SO}$  as:

$$H_{SO} = \alpha_R(\hat{\mathbf{e}}_{\mathbf{z}} \times \mathbf{k}) \cdot \boldsymbol{\sigma} = \begin{vmatrix} 0 & 0 & \hat{\mathbf{e}}_{\mathbf{z}} \\ k_x & k_y & k_z \\ \sigma_x & \sigma_y & \sigma_z \end{vmatrix} \quad (2.12)$$

The last form is known as the Rashba Hamiltonian term for 2D electron gases. The combined  $H_0 + H_{SO}$  Hamiltonian has a large effect on the resulting electronic behavior. The associated electronic dispersion is represented by the eigenvalues of the following  $2 \times 2$  matrix:

$$\begin{pmatrix} \frac{\hbar^2(k_x+k_y)^2}{2m^*} & \alpha_R(-ik_x - k_y) \\ \alpha_R(ik_x - k_y) & \frac{\hbar^2(k_x+k_y)^2}{2m^*} \end{pmatrix} \quad (2.13)$$

Matrix (2.13) is written in the subspace spanned by the  $z$ -component of the spin. One may use different basis representations as explained in chapter 5. The free-electron parabola is therefore replaced by two spin-polarized branches given by:

$$E_{\pm}(k) = \frac{\hbar^2(k_x + k_y)^2}{2m^*} \pm \alpha_R k \quad (2.14)$$

and depicted in Fig. 2.1 (a), which represents the complete 2D dispersion around the center of the SBZ revealing the rotational symmetry of the Rashba-derived electronic structure. The corresponding eigenfunctions for the upper and lower branches of Figs. 2.1 (a) and 2.1 (b) are given by:

$$|\psi_{\pm, k}\rangle = \frac{e^{i(k_x x + k_y y)}}{\sqrt{2}} (|\uparrow\rangle \pm e^{i\phi(k)} |\downarrow\rangle) \quad (2.15)$$

where  $\phi(k)$  is the angle between the direction of  $\mathbf{k}$  and the  $y$  reference axis. Due to the off-diagonal terms in (2.13), the Rashba eigenfunctions mix the up and down states of the  $z$ -component of the spin. One can easily find the projection of the spins on the in-plane axes by calculating their



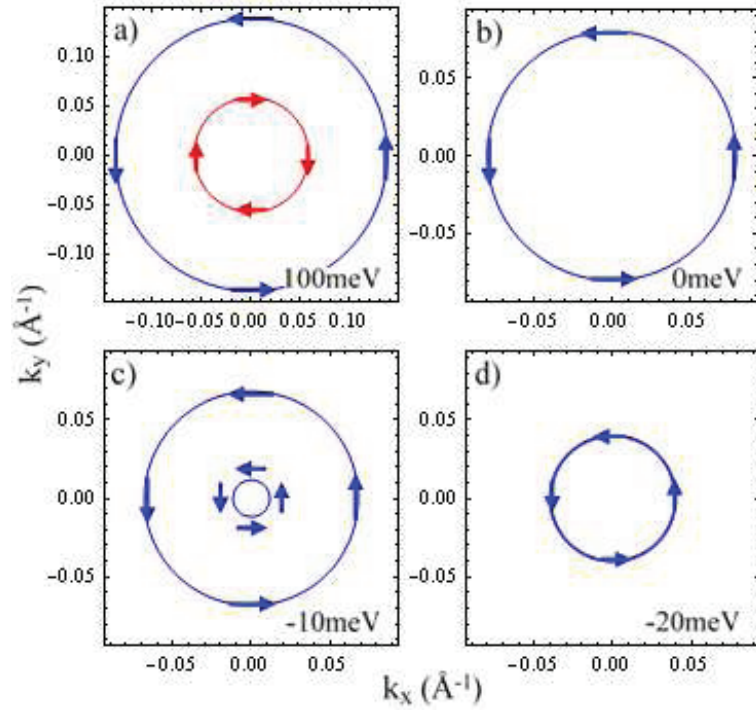


**Figure 2.2** — Constant energy (CE) contours of the bands presented in Fig. 2.1 for four different energies. The arrows represent the direction of the spin polarization. The two contours have opposite (parallel) spin polarization above (below) the spin degeneracy point.

expectation values:

$$\langle \psi_{\pm, k} | \sigma_x | \psi_{\pm, k} \rangle = \frac{1}{2} \begin{pmatrix} 1 & \pm e^{-i\phi(k)} \\ \pm e^{i\phi(k)} & 1 \end{pmatrix} \begin{pmatrix} 0 & 1 \\ 1 & 0 \end{pmatrix} \begin{pmatrix} 1 \\ \pm e^{i\phi(k)} \end{pmatrix} = \pm \cos \phi(k) = \pm \frac{k_y}{k} \quad (2.16a)$$

$$\langle \psi_{\pm, k} | \sigma_y | \psi_{\pm, k} \rangle = \frac{1}{2} \begin{pmatrix} 1 & \pm e^{i\phi(k)} \\ \pm e^{-i\phi(k)} & 1 \end{pmatrix} \begin{pmatrix} 0 & -i \\ i & 0 \end{pmatrix} \begin{pmatrix} 1 \\ \pm e^{i\phi(k)} \end{pmatrix} = \pm \sin \phi(k) = \mp \frac{k_x}{k} \quad (2.16b)$$

$$\langle \psi_{\pm, k} | \sigma_z | \psi_{\pm, k} \rangle = \frac{1}{2} \begin{pmatrix} 1 & \pm e^{i\phi(k)} \\ \pm e^{-i\phi(k)} & 1 \end{pmatrix} \begin{pmatrix} 1 & 0 \\ 0 & -1 \end{pmatrix} \begin{pmatrix} 1 \\ \pm e^{i\phi(k)} \end{pmatrix} = 0 \quad (2.16c)$$

The predicted spin polarization lies in the  $(xy)$  plane. The  $x - (y-)$  projection is maximum when the  $k$ -vector is along  $y(x)$ . Moreover, for the same value of  $k$ , the spins belonging to the upper and lower branches point towards opposite directions. These observations result into a helical spin arrangement as presented in the CE maps of Fig. 2.2. The described Rashba-Bychkov (RB) effect is isotropic and the two branches correspond to opposite values of spin polarization. The two CE contours can have either opposite (a) or identical (c) spin rotations. The spins are parallel between the crossing and the band minimum ( $m^* > 0$ ) or maximum ( $m^* < 0$ ), and antiparallel for all other energy values. As demonstrated by Cappelluti et al., the latter region is accompanied by an effective reduced dimensionality in the electronic density-of-states (DOS) and a singularity at the band minimum [29].

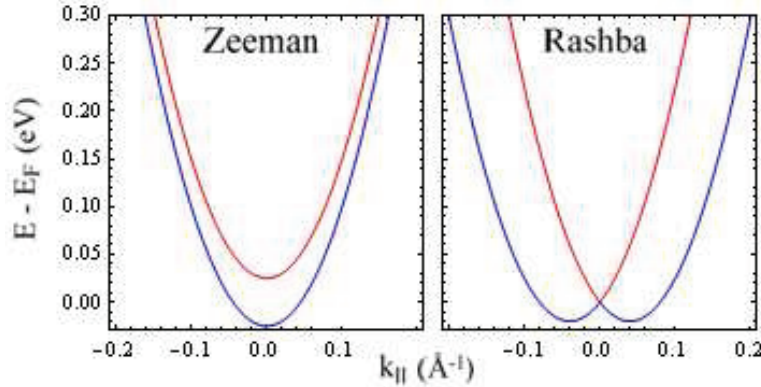


**Figure 2.3** — Simulated band dispersion along a high-symmetry direction for the two spin-polarized branches derived by the Zeeman (a) and the Rashba (b) effect. The results correspond to the eigenvalues of matrices (2.13) and (2.17). Blue and red denote opposite values of spin polarization. Simulation input:  $m^* = 0.3m_e$ ,  $\alpha_R = 1\text{eV \AA}$  and  $E_P = 0.025\text{eV}$ .

Apart from the Rashba parameter, there are two alternative ways to quantify the magnitude of the spin-splitting. One can use a wavevector scale where  $k_0 = \alpha_R m^* / \hbar^2$  describes the  $k$ -shift of the two parabolic states away from  $\bar{\Gamma}$ , as well as an energy scale by using the energy difference between the band extremum and the crossing of the two parabolas (Rashba energy  $E_R = \hbar^2 k_0^2 / (2m^*)$ ).

A more elementary but equivalent view of the RB effect can be achieved by a comparison with the Zeeman splitting. In the case of a 2DEG, an external in-plane magnetic field  $\mathbf{B}$  interacts with the electronic magnetic moment  $\boldsymbol{\mu}$  yielding a perturbation energy  $E_P = -\boldsymbol{\mu} \cdot \mathbf{B}$  which can split the free-electron parabola. In the subspace of the spin  $z$ -component, the effect can be approximated by a  $2 \times 2$  matrix:

$$\begin{pmatrix} \frac{\hbar^2(k_x+k_y)^2}{2m^*} & -iE_P \\ iE_P & \frac{\hbar^2(k_x+k_y)^2}{2m^*} \end{pmatrix} \quad (2.17)$$

where  $E_P$  is the perturbation energy introduced by the Zeeman effect. The eigenvalues are plotted in Fig. 2.3 (a) revealing a constant energy splitting of the two branches. Their spin polarizations are opposite and depend on the direction of the external magnetic field.

In the case of the Rashba effect there is no external magnetic field. In the electron's rest-frame, an out-of-plane electric field  $\mathbf{E}$  appears as an in-plane tangential magnetic field whose magnitude and direction depend on its velocity  $\mathbf{v}$  and are given by (2.4).

As before, the effective  $\mathbf{B}$  couples with the electronic magnetic moment resulting into a perturbation energy. In this case, the perturbation energy will depend on the wavevector, since the magnetic field is  $\mathbf{k}$ -dependent. This is clear in the mathematical formula of the off-diagonal terms in (2.13), whose eigenvalues yield two spin-polarized branches with a wavevector-dependent energy splitting (Fig. 2.3 (b)). As demonstrated earlier, the spin-polarization of the two branches is also  $\mathbf{k}$ -dependent in a helical arrangement.

Fig. 2.1 reveals that there are certain points of the SBZ where we observe spin degeneracy. This property is not limited to  $\bar{\Gamma}$  but it is valid for all the high-symmetry points which possess time-

reversal symmetry. In order to understand why time-reversal results into spin degeneracy according to the RB model, one has to discuss the time invariance of the Hamiltonian and the consequences of the Kramers theorem.

#### 2.1.4 The role of time-reversal symmetry

A real Hamiltonian preserves the time-reversal symmetry. For example, if one considers the complex conjugate of the time-dependent Schrödinger equation:

$$i\hbar \frac{d\psi^*}{dt} = H_0^* \psi^* \quad (2.18)$$

and replaces  $t$  by  $-t$ ,  $\psi^*$  will represent a solution of the original Schrödinger equation only because  $H_0^* = H_0$ . The Rashba  $H_{SO}$  term depends on the spin matrices which have imaginary components. One may therefore think that it is not invariant under time reversal. Nevertheless, in the absence of an external magnetic field, its special structure preserves the time invariance.

A time-reversal (i.e. motion-reversal) operator  $T$  must reverse the linear and angular momentum (orbital and spin), while leaving the position unchanged:

$$T\mathbf{x}T^{-1} = \mathbf{x} \quad , \quad T\mathbf{p}T^{-1} = -\mathbf{p} \quad , \quad T\mathbf{L}T^{-1} = -\mathbf{L} \quad \text{and} \quad T\boldsymbol{\sigma}T^{-1} = -\boldsymbol{\sigma}$$

In order to find an expression for  $T$ , one may notice that  $T\sigma_yT^{-1} = -\sigma_y$ , but also  $K_o\sigma_yK_o^{-1} = -\sigma_y$ , where  $K_o$  is the complex conjugation operator.  $T$  can be therefore expressed as the product of  $K_o$  and  $A$ , where  $A$  is an operator with the property  $A\sigma_yA^{-1} = \sigma_y$ . If  $A$  is set equal to  $-i\sigma_y$ , the time-reversal operator for spin can be written as:

$$T = -i\sigma_yK_o \quad (2.19)$$

This is an antiunitary operator which can increase the degree of degeneracy of the energy eigenstates resulting from the system Hamiltonian. In cases with space inversion symmetry, the so-called Kramers theorem yields nothing more than the degeneracy of spin-up and spin-down states. As it will be shown in the following paragraphs, its consequences become nontrivial, in the presence of a non-centrosymmetric electronic potential.

Let  $\psi$  be a solution of a time-invariant Hamiltonian  $H$ . Then:

$$H\psi = E\psi \Rightarrow TH\psi = TE\psi \Rightarrow H(T\psi) = E(T\psi) \quad (2.20)$$

and therefore  $T\psi$  is a degenerate solution of the differential equation. If  $\psi$  and  $T\psi$  are linearly independent, then they represent distinct solutions.

$$\langle \psi | T\psi \rangle = \langle T\psi | T^2\psi \rangle = -\langle T\psi | \psi \rangle \quad (2.21)$$

because  $T$  is antiunitary. By substituting the expression for  $T$ , one can also get the following:

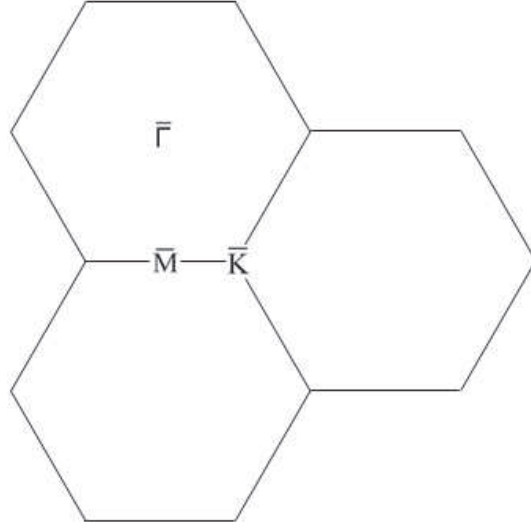


**Figure 2.4** — Schematic representation of three hexagonal unit cells in the reciprocal space with their high-symmetry points. There is no time-reversal symmetry at  $\bar{K}$  because  $T$  does not necessarily reverse the sign of  $\mathbf{k}$  between two symmetric points around it.

$$\begin{aligned} \langle \psi | T\psi \rangle &= \langle T\psi | T^2\psi \rangle = \langle (K_o(-i\sigma_y)\psi | (-i\sigma_y)K_o(T\psi) \rangle = \\ &= \langle (K_o\psi | (-i\sigma_y)(-i\sigma_y)K_o(T\psi) \rangle = \langle K_o\psi | K_o(T\psi) \rangle = \langle T\psi | \psi \rangle \end{aligned} \quad (2.22)$$

From (2.21) and (2.22),  $\langle \psi | T\psi \rangle = 0$  and hence the two solutions are degenerate but distinct.  $T\psi$  represents a solution with opposite spin and linear momentum ( $T$  contains  $K_o$ ) with respect to  $\psi$ . As a result, in the case of a Hamiltonian which is invariant under time-reversal, the Kramers degeneracy can be written as:

$$E_{k,\uparrow(\downarrow)} = E_{-k,\downarrow(\uparrow)} \quad (2.23)$$

The time-invariant points of neighboring SBZ may be also connected with a reciprocal lattice vector. Translation symmetry may therefore act in combination with time-reversal. Fig. 2.4 illustrates the results for a hexagonal SBZ where translation symmetry yields  $E_{k(\bar{\Gamma}),\uparrow\downarrow} = E_{-k(\bar{\Gamma}),\uparrow\downarrow}$ , and  $E_{k(\bar{M}),\uparrow\downarrow} = E_{-k(\bar{M}),\uparrow\downarrow}$ . In combination with the Kramers degeneracy, one arrives at  $E_{k(\bar{\Gamma}),\uparrow} = E_{k(\bar{\Gamma}),\downarrow}$  and  $E_{k(\bar{M}),\uparrow} = E_{k(\bar{M}),\downarrow}$ .

If apart from time reversal, the Hamiltonian is invariant under space inversion  $J$ , then  $J\psi$  represents a degenerate solution of the differential equation. The operator  $J$  reverses the sign of the position and linear momentum, while it does not affect the angular momentum and spin. As a result, when  $J$  acts on  $\psi$ , it yields a degenerate solution with the same spin but opposite momentum,  $E_{k,\uparrow\downarrow} = E_{-k,\uparrow\downarrow}$ . The considerations of the previous paragraph can be now extended to any arbitrary  $\mathbf{k}$ , resulting into a trivial spin-up and spin-down degeneracy for all  $k$ -values. In the case of space inversion, Kramers degeneracy can be written as  $E_{k,\uparrow} = E_{k,\downarrow}$ .

In conclusion, the trivial spin-degeneracy at an arbitrary  $k$ -point can be lifted:

- i) by an external magnetic field  $\mathbf{B}$  which breaks the time-reversal symmetry of the Hamiltonian.
- ii) in systems with broken space-inversion symmetry.

## 2.2 Unveiling the mechanism of the isotropic Rashba-Bychkov effect

Bychkov and Rashba were the first who underlined the importance of the Pauli SO coupling term as a relativistic correction of the Schrödinger Hamiltonian and examined its effect in the band dispersion [28]. They introduced the Rashba coefficient  $\alpha_R$  and calculated its numerical value for semiconductor heterojunctions by experimental data on cyclotron resonances [142, 143]. According to a NFE model,  $\alpha_R$ , and consequently  $\nabla V$ , is due to a perturbative effect associated with the surface potential gradient. It is expected to yield an energy splitting ( $E_R$ ) in the order of  $10^{-6}$  eV.

### 2.2.1 Spin splitting of noble metal surface states - early results

Although Bychkov and Rashba performed their work on semiconductor heterostructures, their predictions were experimentally verified on a different kind of 2DEG: the metallic surface state of Au(111) [89]. LaShell et al. observed a splitting which is at least three orders of magnitude larger than the estimates of Bychkov et al. and attributed this discrepancy to an artifact of the NFE (Fig. 2.5). The inconsistency stems from the fact that a NFE treatment disregards the effect of the ion cores where the potential gradient is expected to be very high. Although the qualitative behavior is well-captured by  $H_{SO}$ , the latter had to be modified in order to yield more realistic quantitative results.

A pseudopotential approach seemed to be more appropriate, since it had been already successful in calculating SO effects in the 3D electronic structure of white tin [153]. LaShell et al. followed the predictions of Animalu according to which  $H_{SO}$  could be written as  $\frac{\epsilon}{\hbar} \mathbf{L} \cdot \boldsymbol{\sigma}$  for distances from the center of the ions smaller than a given radius  $R_M$  [5].  $\epsilon$  is an energy in the order of the relevant spin-splitting, while the model radius  $R_M$  is determined by the average electronic position. Using appropriate  $\epsilon$  and  $R_M$  for the case of Au(111), LaShell et al. were able to match their novel ARPES results. Although the pseudopotential method by Animalu includes only the effects of core levels with  $p$  symmetry, their consequences are expected to be dominant in the case of  $sp$ -derived surface states, justifying the extension of this approach to the Au(111) surface. Finally, the authors proposed that due to the very small atomic  $p_{3/2} - p_{1/2}$  splitting of Ag and Cu, the RB effect on the corresponding (111) surfaces must be beyond the experimental resolution.

### 2.2.2 A combination of theory and experiment towards a better understanding

These predictions were verified after high-resolution ARPES studies by Nicolay et al. were performed on clean Au, Ag and Cu(111) surfaces [108, 124]. The experimental results were accompanied by relativistic DFT calculations which suggested that the splitting of the Ag(111) Shockley

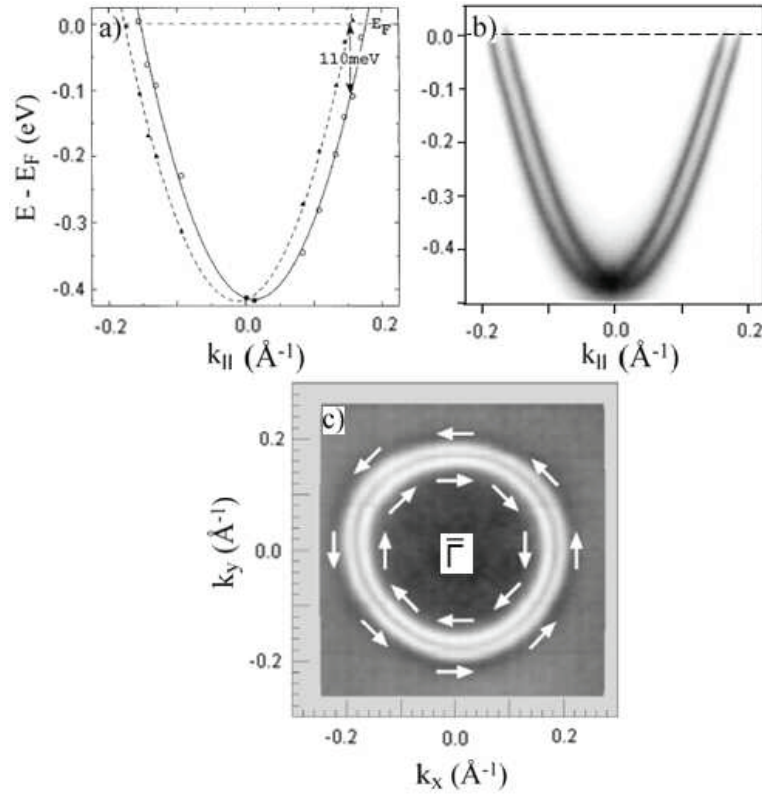


**Figure 2.5** — (a)  $E$  vs.  $k$  dispersion along  $\overline{\Gamma M}$  by LaShell et al. [89]. (b) High-resolution ARPES image along  $\overline{\Gamma M}$  (LSE-EPFL 2009). (c) The Fermi surface revealing two concentric contours in agreement with the predictions of the isotropic RB model. The white arrows indicate the orientation of the spin polarization. [89, 108]

state should be present but far too small to be experimentally resolved. However, a clear demonstration of the important role of the atomic SO coupling came from a series of experimental studies on the Ag/Au(111) system [31, 118, 30]. The authors deposited Ag films of variable thickness on a Au(111) substrate and showed that the SO splitting magnitude of the Shockley surface state exhibits a continuous transition from the parameters corresponding to the Au(111) surface to the indiscernible effect on a Ag(111) surface (Fig. 2.6). Their results were corroborated by STM images and ab-initio calculations. They concluded that the wavefunction of the surface state extends to the first five MLs and that the splitting magnitude is determined by the amount of "heavy" (i.e. Au) electrons which are probed by their wavefunction. These experimental results verified the inconsistencies of the NFE approach and the importance of the atomic term in the determination of SO-induced splitting. This was in line with a combined study on vicinal Au(111) surfaces which concluded that the surface contribution to the splitting is essentially negligible in comparison to the nuclear potential gradient [103]. An independent ARPES study on the RB splitting of  $4d$  and  $5d$  transition metal surfaces has on one hand provided another support of the important consequences of the atomic term [129]. On the other hand, the evolution of the SO splitting with Li deposition proved that the role of the surface potential gradient could be significant.

In order to get new insight into the components of the Rashba parameter  $\alpha_R$ , Petersen et al.



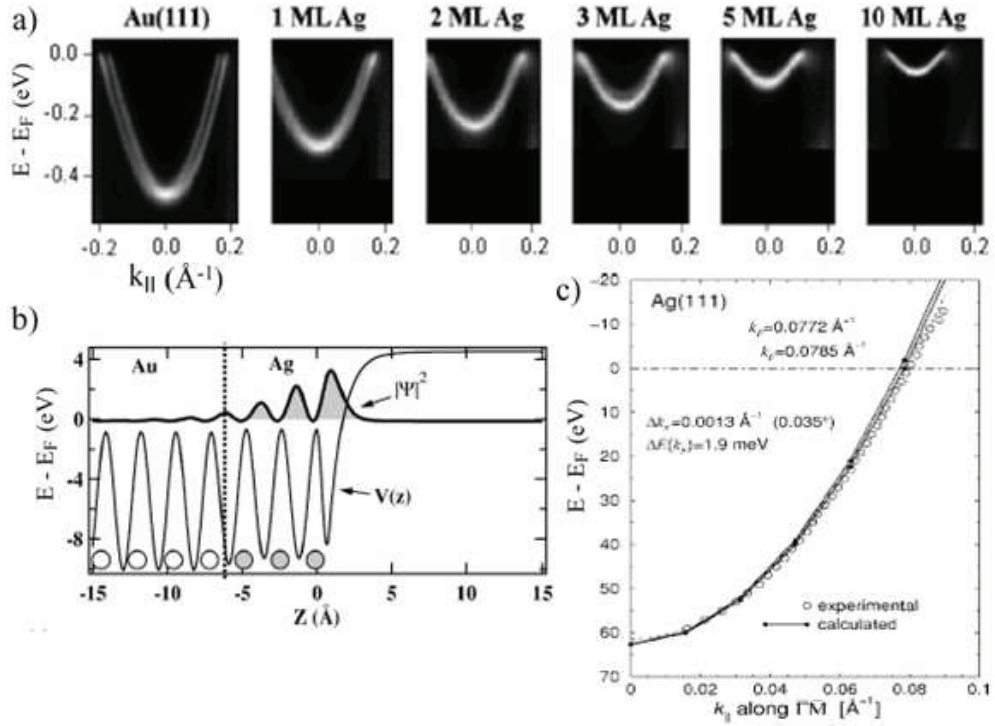


**Figure 2.6** — (a) Ag/Au(111) system: Coverage dependence of the ARPES intensity. The spin-splitting is gradually reduced with increasing  $\Theta_{\text{Ag}}$ . At the same time the surface state shifts towards lower  $E_B$ . (b) Probability density  $|\Psi|^2$  of the surface state wavefunction arising when  $\Theta_{\text{Ag}} = 3\text{ML}$ .  $V(z)$  is the potential landscape used in the corresponding Schrödinger equation [30]. (c) Experimental results and DFT calculations for the Ag(111) surface state, revealing its negligible spin splitting. [108]

developed a 2D tight-binding (TB) model on a simple hexagonal lattice [117]. They included the effect of RB splitting as a term proportional to the atomic SO coupling which is added to the conventional TB Hamiltonian. In order to develop their model, they used an atomic basis and considered the effects of  $p_x$ ,  $p_y$  and  $p_z$  orbitals. As a result, they arrived at a  $6 \times 6$  Hamiltonian matrix whose eigenvalues are a representation of the electronic band structure. The effective Hamiltonian for the  $p_z$  subspace reveals the analogies and the differences of their approach with respect to the NFE model. The authors identified  $\alpha_R$  as a term which is proportional to the product of the surface potential gradient ( $\gamma$ ) and the atomic SO coupling ( $\alpha$ ).

Based on the ratio of their atomic SO coupling terms, one would expect a splitting magnitude of the Ag(111) Shockley state around four times smaller than the one observed on Au(111) [99, 122]. Nevertheless, the aforementioned DFT calculations predicted a splitting which is far below the estimates ( $\Delta k_F(\text{Au}) = 0.028 \text{ \AA}^{-1}$  vs.  $\Delta k_F(\text{Ag}) = 0.0013 \text{ \AA}^{-1}$ ) [108, 122]. The authors attributed this discrepancy into two different factors: (i) the different degree of localization of the corresponding surface states which is reflected into their binding energies and (ii) the amount of  $p$  character in their apparent  $sp$  behavior. They invited further DFT calculations and a closer look at the electronic wavefunctions in order to gain a better understanding of the mismatch.

Bihlmayer et al. used a similar theoretical approach to discuss the origin of the RB effect

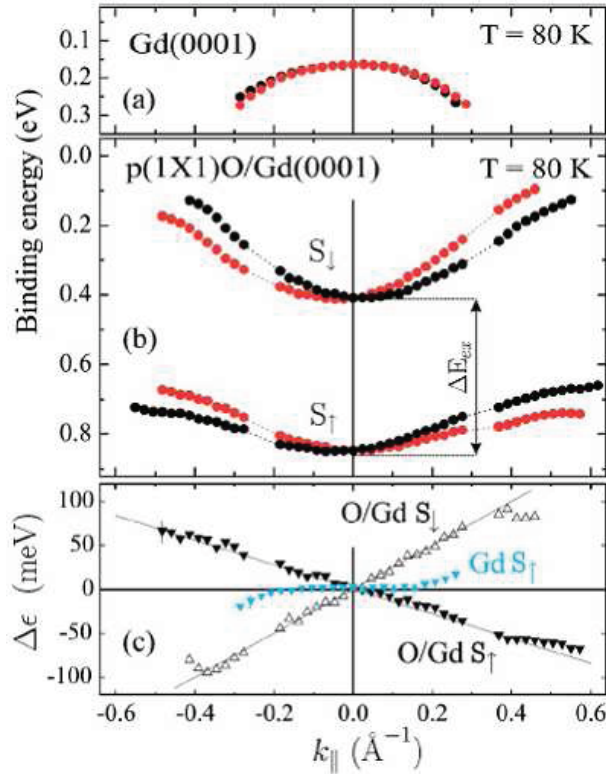


**Figure 2.7** — (a) Experimental band dispersion of the majority spin surface state of Gd(0001) along  $\bar{\Gamma}\bar{M}$ . RB splitting is negligible. (b) After oxygen deposition, RB splitting becomes substantial both at the majority ( $S_{\uparrow}$ ) and minority ( $S_{\downarrow}$ ) spin states of the  $p(1 \times 1)$ O/Gd(0001) system. The displayed dispersion is along  $\bar{\Gamma}\bar{K}$ . (c) RB splitting obtained from (a) and (b);  $\nabla$  ( $\triangle$ ) symbols refer to majority (minority) spin states. [86]

[23]. After performing DFT calculations to identify the SO coupling term of the Hamiltonian, they expanded the potential in spherical harmonics around the atom. The resulting SO Hamiltonian was given by:

$$H_{SO} = \frac{1}{4m^2c^2} \frac{1}{r} \frac{\partial V}{\partial r} (\mathbf{r} \times \mathbf{p}) \cdot \boldsymbol{\sigma} \quad (2.24)$$

where  $\mathbf{p}$  is the linear momentum operator and  $V$  the spherically symmetric potential. The authors were able to resolve the contribution of all surface and subsurface layers to the RB splitting. In the case of Au(111), they used a slab of 23 layers and concluded that more than 40% of the splitting comes from the subsurface region. This result is very important because it proves that the size of the splitting is not determined by the surface potential gradient, which should be negligible away from the surface, but by the inversion asymmetry of the surface state wavefunction. Close to the nucleus, an electronic potential gradient is realized by the formation of states with a mixed orbital character (e.g.  $p$ -states with an admixture of  $s$ - or  $d$ - character). The  $l/(l \pm 1)$  ratio is a measure of the effective gradient related to the wavefunction asymmetry and corresponds to the  $\gamma$  term introduced by Petersen et al. [117]. In analogy with the aforementioned TB model, no splitting would be expected in an isolated Au(111) ML. Electrons would pass the nuclear potential equally distributed on the upper or lower side of the layer resulting in a zero net potential gradient (i.e.



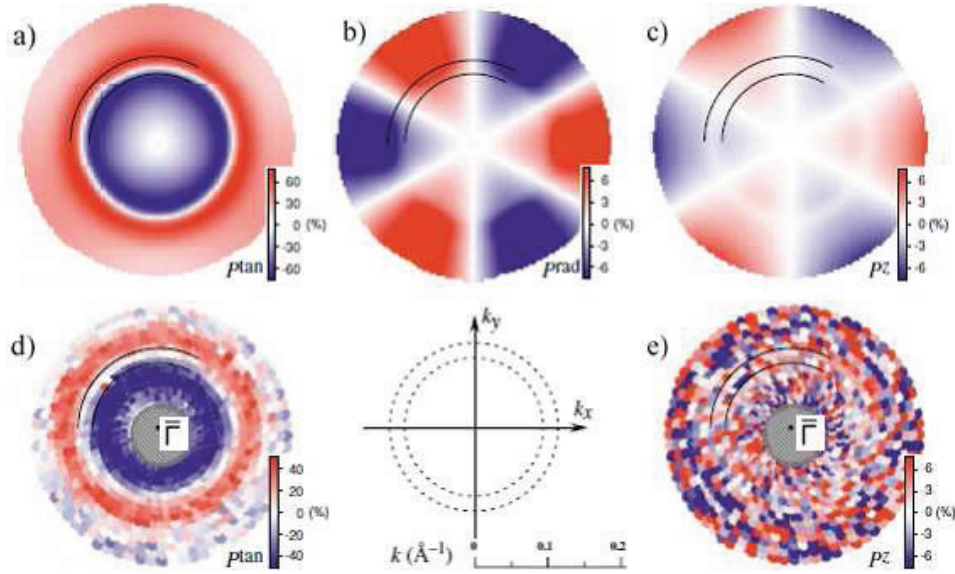


**Figure 2.8** — Theoretical (first-principles) (a)-(c) and experimental (spin-resolved ARPES) (d)-(e) CE contours at  $E_B = 0.17\text{eV}$  revealing the spin polarization of the Au(111) surface state. (a),(d) and (c),(e) refer to the in-plane tangential and out-of-plane component of  $\mathbf{P}$ . (b) denotes the theoretical prediction for the in-plane radial component and does not have any experimental counterpart. Notice that  $P_{tan}$  is dominant and opposite for the two surface state contours (black solid lines). The  $P_z$  component is very small and lies beyond the detection limit of the SARPES setup. [59]

$\langle |\psi| \frac{dV}{dr} |\psi \rangle = 0$ ). By turning on "in a way" the effect of the substrate, more electrons pass on one side than the other. At the same time the electronic wavefunction becomes asymmetric and some different orbital character mixes in. As a consequence, the electrons feel a potential gradient, which results into a finite splitting.

Observing equation (2.24), one can identify the interplay of two terms. On one hand, the surface state should lie as close as possible to the nucleus in order to enhance the weighted potential gradient (i.e.  $p$ -states are more favorable than  $d$ -states). On the other hand, the wavefunction asymmetry (or equivalently the momentum) is increased when different orbital characters contribute in a similar degree. The admixture of two different  $l$ - characters is also dependent on the atomic number  $Z$ . Their results suggest that the negligible splitting on the Ag(111) surface state is due to the high  $p : d$  ratio of its orbital character (9.5 vs. 3.3 for Au(111) ). Despite the lack of simplicity, the importance of this work lies in the fact that it reduced the number of contributions to the SO-derived splitting to one effective parameter: the surface state wavefunction asymmetry near the ion cores. Apart from the (111) surfaces of noble metals, the approach of Bihmayer et al. has successfully reproduced the Rashba effect on the (0001) surfaces of lanthanides [86, 23]. Namely, an epitaxial metal-oxide surface layer results in a significant increase of the SO-induced splitting at the magnetic Gd(0001) surface (Fig. 2.7). This was attributed to an admixture of  $p_z$  character to the almost pure  $d_{z^2}$  Gd(0001) surface state [86].

In a pair of articles Henk et al. computed the electronic properties of Au(111) using DFT calculations on a semi-infinite system [57, 58]. Spin- and angle-resolved photoemission spectra

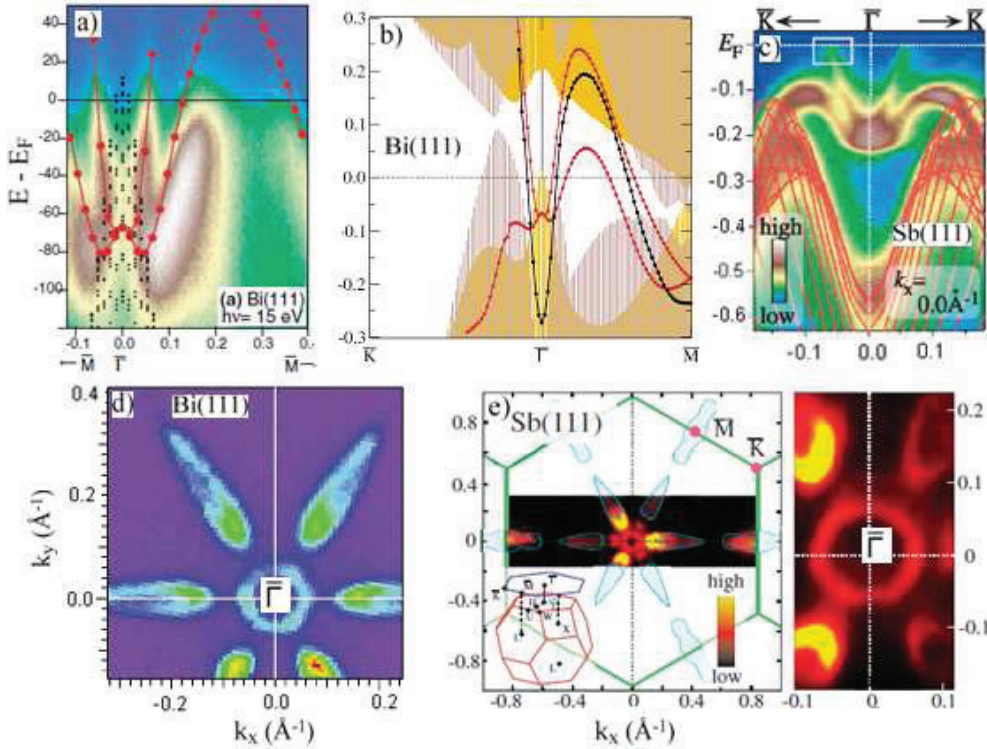


**Figure 2.9** — Anisotropic band dispersion (top row) and FS maps (bottom row) for the Bi(111) and Sb(111) surface states. (a) Experimental dispersion for Bi(111) along  $\bar{\Gamma}\bar{M}$ . The red circles are the result of relativistic calculations shown in (b). The black lines in (b) represent the surface state dispersion without the inclusion of SO coupling. The shaded areas denote the bulk band projection. (c) Experimental dispersion of the Sb(111) surface states in the vicinity of  $\bar{\Gamma}$ . Red lines represent the bulk band projection. (d), (e) Fermi surface maps for Bi(111) (d) and Sb(111) (e) measured by ARPES. The spin-split contours have strongly anisotropic momentum distributions. [8, 144, 85]

were calculated within the relativistic one-step model. Their work focused on the spin polarization of the Au(111) surface state. Interestingly, they concluded that there is a small but finite polarization component normal to the surface (i.e.  $P_z$ ) (Fig. 2.8). This effect cannot be predicted by the NFE 2DEG model with RB coupling, which was presented in section 2.1 and according to the authors it points towards a nonzero in-plane asymmetry of the surface potential. Moreover, the same work revealed the caveats one might face if the spin polarization of the surface states is to be detected by spin- and angle-resolved photoelectron spectroscopy. In fact, the polarization of the initial surface states may be obscured by the photoelectron spin polarization brought about by the photoemission process. Henk et al. suggested that best results would be obtained with an experimental setup which can produce a photoelectron spin polarization aligned along the one of the initial state.

The group of Prof. J. Osterwalder performed detailed spin-resolved measurements on the Au(111) Shockley surface state using a spin polarimeter that allows full sensitivity to all three components of the electronic spin polarization [65]. In agreement with the conclusions by LaShell et al., they reported that the split bands exhibit a high but opposite spin polarization which lies in the surface plane and is perpendicular to the momentum of the electrons [66, 104, 59]. Since the theoretically calculated magnitude of the out-of-plane component is smaller than the detection limit of

the experimental setup (5%), they were unable to verify the predictions (Fig. 2.8). A different study by Hochstrasser et al. addressed the spin polarization of the surface states of W(110)-(1x1)H [64]. Although the momentum distributions of this system deviate significantly from the isotropic contours predicted by the NFE approximation, spin-resolved data evidenced that the spin-polarization of the surface states is essentially tangential.

### 2.2.3 A quest to enhance the splitting

After the work of LaShell et al. [89], the field of RB splitting attracted a significant interest of the scientific community and many groups tried to enhance the weak splitting observed on the Au(111) surface. Surfaces of materials with higher  $Z$  and hence a stronger atomic splitting were obvious alternatives. Koroteev et al. performed ARPES measurements on three different low-index surfaces of Bi accompanied by first-principles calculations [85]. The combined study allowed them to identify spin-split branches for the Bi(111), Bi(110) and Bi(100)  $p$ -derived surface states (Fig. 2.9). In accordance with the large atomic SO coupling parameter, the observed RB splitting was by far the strongest which was reported up to that time. Their unambiguous results revised the conclusions of previous studies on the Bi(111) surface which had proposed two non-degenerate surface states around  $\bar{\Gamma}$  and the possibility of FS nesting by the formation of a CDW [8, 9]. Moreover, the authors clarified the results of an earlier work on the Bi(110) surface electronic structure. This study had suggested a SO-induced splitting, but its identification was not unambiguous due to the large splitting magnitude [4]. One important conclusion is that the spin-split states exhibit highly anisotropic behavior and the resulting CE contours are not free-electron-like (Fig. 2.5). Therefore, their topology cannot be accessed by the Rashba correction of the non-relativistic Schrödinger Hamiltonian (Eq. (2.12)).

Sb lies just one block higher than Bi in the periodic table of elements. Therefore, its low-index surfaces are the next candidates for a sizeable RB splitting. Sugawara et al. reported high-resolution ARPES results on the Sb(111) surface [144]. In the case of Sb(111), the spin-split states lie into the projected bulk gap and identification of their degeneracy point is more straightforward than for Bi(111), where one has to deal with surface resonances. The FS and RB splitting are highly anisotropic as in the case of Bi(111). Moreover, there is a strong threefold modulation of the surface state intensity due to their non-negligible decay length into the substrate of threefold symmetry (Fig. 2.9). In perfect analogy to the Bi(111) case, this study revised the conclusions of an earlier ARPES work which had suggested two non-degenerate surface states around  $\bar{\Gamma}$  [10].

As already mentioned, a couple of studies have been devoted to the RB effect on  $4d$  and  $5d$  TM surfaces. SO-induced splitting on the clean Mo(110) surface is essentially undetectable, whereas a sizeable effect was observed on the corresponding (110) surface of the heavier W element [129]. The effect was dramatically enhanced after the deposition of hydrogen or alkali metals on W(110), exemplifying the role of the surface potential gradient (Fig. 2.10 and [130, 129, 64]). A similar enhancement has been observed after the passivation of the W(110) surface by 1 ML of Au or Ag [136]. In contrast to what was observed on noble metals [31, 118, 30], the nature of the overlayer does not affect the size of the induced splitting. It is only the substrate that matters. This was verified

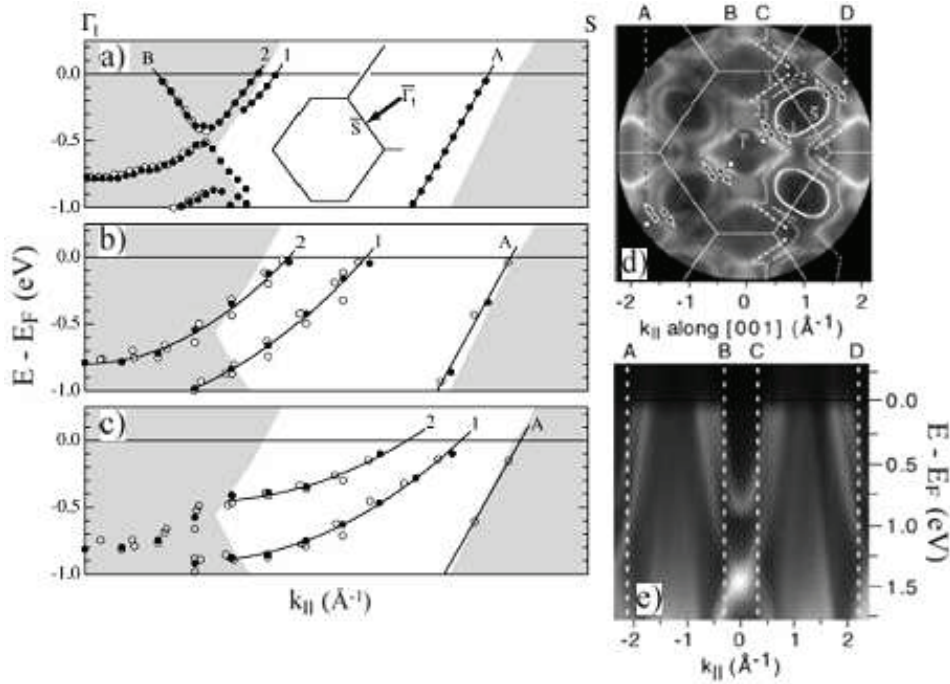


**Figure 2.10** — ARPES dispersion along  $\overline{\Gamma S}$  for (a) clean W(110), (b)W(110)-Li0.5ML and (b)W(110)-Li1.0ML. The splitting of the two spin-polarized states (labeled 1 and 2) becomes appreciable after Li deposition. The shaded region is the projection of bulk bands. (d) Experimental Fermi surface of the W(110)-(1 × 1)H system, where arrows represent the spin directions deduced from spin-ARPES measurements. (e) Corresponding band dispersion along the  $\overline{\Gamma S}$  direction. [129, 64]

by substituting W(110) with Mo(110). As a consequence, the authors claimed that the overlayer-derived states inherit their spin polarization by spin-dependent hybridization with substrate states.

Apart from moving to different systems, the splitting of the Au(111) surface state can be enhanced by the deposition of rare gases. Noble gases may alter the surface potential gradient, but they can also result into a profound spatial modification of the Shockley state wavefunction due to the Pauli repulsion caused by their filled electronic shells [44, 43]. As a consequence, the electronic density may shift closer to the nucleus, where the potential gradient is steeper, thus resulting in a larger RB splitting. In other words, noble gases deposition can affect the out-of-plane electric field seen by the electrons. The effect depends on the "nobleness" of the rare gas and is largest for Xe (Fig. 2.11).

## 2.3 The breakthrough of surface alloys and its implications

### 2.3.1 Experimental discovery and relativistic calculations

An unexpectedly large RB splitting was observed in a novel class of materials obtained after high- $Z$  metal deposition on the (111) surfaces of noble metals. Deposition of 1/3ML of Bi on a clean Ag(111) substrate results in the formation of a long-range ordered surface alloy where each Bi



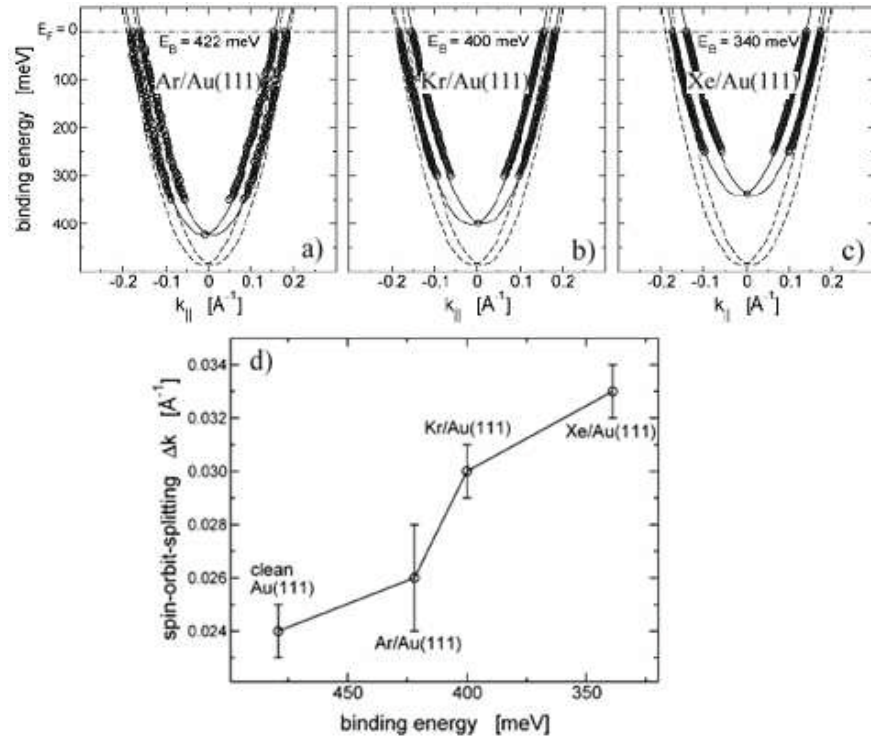


**Figure 2.11** — (a)-(c) ARPES data on the Au(111) surface covered with 1ML of different rare gases. The results are plotted along  $\bar{\Gamma}K$ . The dashed curve indicates the surface state dispersion on clean Au(111). (d) Momentum splitting ( $k_0$ ) induced by the RB effect as a function of the surface state binding energy. The effect is more pronounced with decreasing nobleness of the adsorbate. [44]

atom is surrounded by six Ag atoms (Fig. 2.12 (a) inset) [7]. A summary of the ARPES results on the BiAg<sub>2</sub> surface alloy, along with relativistic DFT calculations, is presented in Fig. 2.12. The dispersion is dominated by a pair of  $sp_z$  spin-split branches with negative dispersion. At the border of the images one can see a weak pair of  $p_{xy}$  branches which cross  $E_F$  and are also spin-split. The isostructural PbAg<sub>2</sub> surface alloy grown after the deposition of 1/3ML Pb on Ag(111) exhibits similar  $sp_z$  derived branches around  $\bar{\Gamma}$  (Fig. 2.12 (c)) [113]. A DFT calculation without the inclusion of the SO interaction cannot reproduce the observed  $k$ -shifted doublet, pointing towards its relativistic origin (Fig. 2.12 (d)). In analogy with the BiAg<sub>2</sub> surface alloy, these branches are expected to be degenerate at  $\bar{\Gamma}$  but due to the absence of one electron with respect to Bi they are partially empty and cross the Fermi level. The  $p_{xy}$  states are out of the experimental window of measurement. In the seek for enhanced RB effects, deposition of Bi on Ag single crystals was not limited to the (111) surface. The tetramer  $c(4 \times 4)$  reconstruction induced by 0.5ML of Bi on Ag(100) has been proposed to yield a pair of spin-split branches with  $\alpha_R = 8.0\text{eV \AA}$  [106]. Nevertheless, in this case one has to deal not with true 2D states but with surface resonances. As a consequence, these ARPES results are not very clear and therefore remain controversial.

The discovery of strong SO-induced splitting on surface alloys signaled a major breakthrough in the field and was in need of a theoretical explanation. According to the virtual crystal approximation proposed by Cercellier et al. [30], the SO parameters should depend on the number of heavy

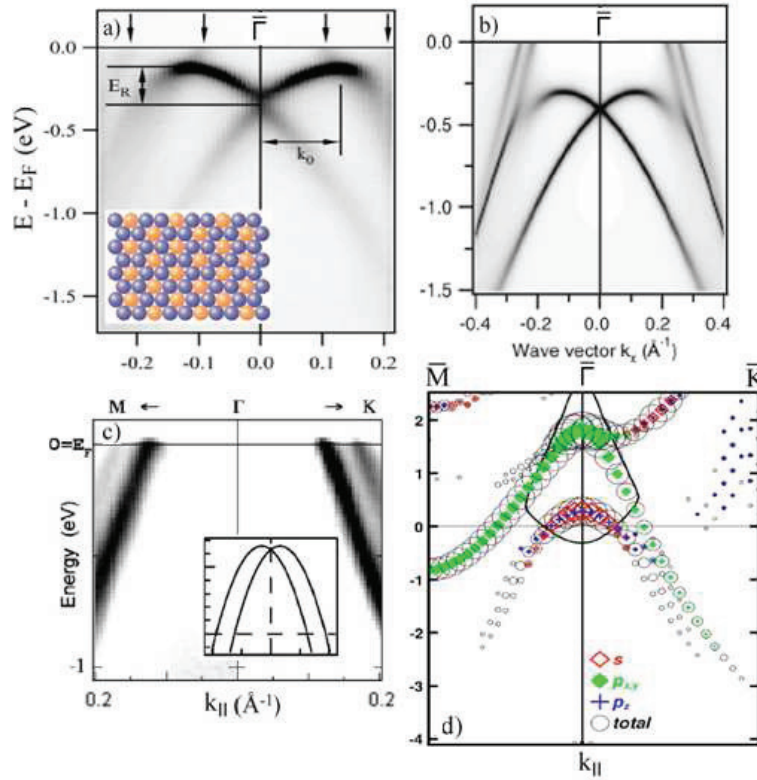


**Figure 2.12** — (top row) High-resolution ARPES results (a) and relativistic first-principles calculations (b) for the surface state dispersion of a  $\text{BiAg}_2/\text{Ag}(111)$  surface alloy. Arrows in (a) denote the  $k_F$  value of the weak  $p_{xy}$  sidebands. The inset is a schematic representation of the surface alloy structure, where one Bi atom (orange) is surrounded by six Ag atoms (purple). (bottom row) High-resolution ARPES results (c) and DFT slab calculations (without SO coupling) (d) for the surface state dispersion of a  $\text{PbAg}_2/\text{Ag}(111)$  surface alloy. The calculations cannot reproduce the weak sidebands of the central  $sp_z$  states pointing towards a relativistic origin. The  $p_{xy}$  doublet is out of the experimental window. The inset represents a fit of the experimental data which extends above the Fermi level. [113, 7]

atoms probed by the surface state wavefunction. Interestingly, this approach does not work because the surface alloy yields parameters much larger than both of its constituents (Table 2.1). A hint for an additional mechanism came from the peculiar shape of the momentum distributions. As shown in Fig. 2.13, CE contours deviate from the circular shape predicted by a simple NFE model and show a pronounced hexagonal symmetry [7]. The effect is stronger for larger wavevectors and it is clear that the states "feel" the 2D structural symmetry. The resulting 6-fold symmetry is a direct consequence of the interplay between the  $3\bar{m}$  symmetry of the studied material and the Kramers degeneracy (Eq. (2.23)). In contrast to the out-of-plane asymmetry of the potential, which yields the conventional isotropic RB effect, an additional in-plane potential asymmetry could deform the contours into the shapes presented in Fig. 2.13. Fully relativistic DFT calculations verified the hexagonal symmetry of the momentum distributions and confirmed the effect of the in-plane potential asymmetry by revealing a sizeable out-of-plane spin polarization component (Fig. 2.13) [7]. Following the considerations of section 2.1, non-zero spin polarization along the normal direction must be a consequence of a finite in-plane component of the effective electric field which

acts on the electrons.

**Table 2.1** — Spin-orbit splitting parameters of 2DEG formed at various surfaces and interfaces. The values reported are approximate and are reproduced from the corresponding Refs. The table underlines the importance of the novel surface alloys.

material	$E_R$ (meV)	$k_0$ ( $\text{\AA}^{-1}$ )	$\alpha_R$ (eV $\text{\AA}$ )	Ref.
InGaAs/InAlAs	< 1	0.028	0.07	[109]
Ag(111)	$\sim 0$	0.004	0.03	[118, 30]
Au(111)	2.1	0.012	0.33	[89, 30]
Au(111)-Xe	15	0.033	0.9	[44]
Bi(111)	14	0.05	0.6	[85]
PbAg <sub>2</sub> /Ag(111)	23	0.03	1.53	[113, 12]
BiAg <sub>2</sub> /Ag(111)	216	0.13	3.05	[7, 19]
SbAg <sub>2</sub> /Ag(111)	$\sim 0$	$\sim 0$	$\sim 0$	[102]
BiCu <sub>2</sub> /Ag(111)	13	0.032	0.82	[19, 101]

### 2.3.2 Nearly-free electron approximations of the results

The combined experimental and theoretical study on BiAg<sub>2</sub> inspired a NFE model for a 2DEG which, apart from the conventional Rashba term, includes the anisotropy effects within the confinement plane [119]. Premper et al. considered the following Hamiltonian:

$$H = \frac{p^2}{2m^*} + V(z) + V(\rho) + \frac{\hbar\boldsymbol{\sigma} \cdot (\nabla\mathbf{V}_z \times \mathbf{p})}{4m^{*2}c^2} + \frac{\hbar\boldsymbol{\sigma} \cdot (\nabla\mathbf{V}_\rho \times \mathbf{p})}{4m^{*2}c^2} \quad (2.25)$$

where the effects of the out-of-plane ( $V(z)$ ) and in-plane ( $V(\rho)$ ) potential terms have been explicitly separated.

Numerical solutions of the corresponding secular equation yield the electronic structure. In this model, each of the contributions to the RB splitting can be switched on and off independently revealing its effect on the band topology. The authors solved this anisotropic RB model for materials belonging to the  $3\bar{m}$  point group and chose their parameters in order to match the  $sp_z$  spin-split surface state of the BiAg<sub>2</sub>/Ag(111) alloy. Fig. 2.14 presents a summary of their findings. The momentum distributions are highly anisotropic in close correspondence to BiAg<sub>2</sub>. As revealed by the corresponding band dispersion, the effect is stronger as one moves away from  $\bar{\Gamma}$ , while it is negligible within a mirror plane of the system. The two hexagonal contours have an orientation offset of 90°. Moreover, there is a finite polarization component directed along the surface normal. Apart from reproducing the findings of the relativistic DFT calculations using a much simpler model, the authors commented on the relative importance of each SO contribution. The in-plane asymmetry term alone yields a very small splitting perpendicular to a mirror plane. It is only in combination with the out-of-plane asymmetry term that can result in a significant enhancement of the RB effect (Fig. 2.14).

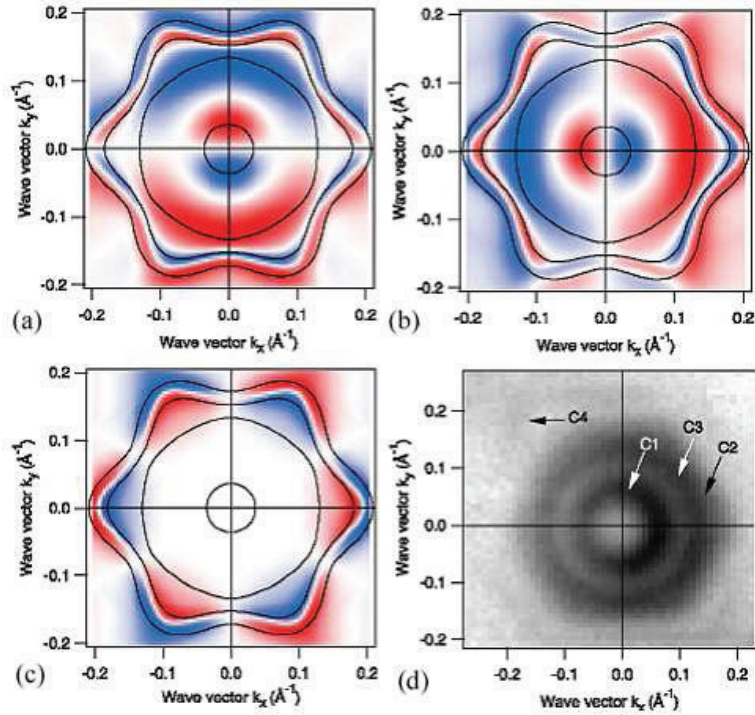


**Figure 2.13** — (a)-(c) Calculated CE contours at  $E_B = 0.55\text{eV}$  and projection of the spin polarization along the  $x$ ,  $y$  and  $z$  axis, respectively. Red (blue) colors correspond to positive (negative) values. The anisotropic momentum distributions are confirmed by ARPES results (d) at  $E_B = 0.17\text{eV}$ . [7]

Recently Fu examined the hexagonal warping effects in the edge states of 3D topological insulators [49]. He used  $\mathbf{k} \cdot \mathbf{p}$  perturbation theory to calculate higher order terms of the effective Dirac Hamiltonian. His analysis was focused on materials having  $3\bar{m}$  symmetry and therefore yielded an additional 3<sup>rd</sup>-order term which includes the effects of hexagonal warping. The same approach can be used as an alternative way to access the anisotropic RB effect. To this end, the 3<sup>rd</sup>-order warping term is added to the isotropic  $2 \times 2$  Hamiltonian matrix (Eq. (2.13)):

$$\begin{pmatrix} \frac{\hbar^2(k_x+k_y)^2}{2m^*} + \frac{c}{2}(k_+^3 + k_-^3) & \alpha_R(-ik_x - k_y) \\ \alpha_R(ik_x - k_y) & \frac{\hbar^2(k_x+k_y)^2}{2m^*} - \frac{c}{2}(k_+^3 + k_-^3) \end{pmatrix} \quad (2.26)$$

where  $k_{\pm} = k_x \pm ik_y$  and the mirror plane is along  $k_y$ . Fig. 2.15 depicts the electronic band dispersion and the spin-polarized momentum distributions given by the eigenvalues of the Hamiltonian matrix. The shape and relative orientation of the CE contours, as well as the dispersion within and perpendicular to a mirror plane are in full agreement with Premper et al. [119]. In this case, the effective Rashba term includes both the effects of the out-of-plane and in-plane asymmetry on the splitting magnitude. The warping term contains information only about the deviation of the momentum distributions from a circular shape. As a result, one cannot switch on and off the two terms independently. Nevertheless, this approach can be considered as a simpler alternative which can be easily solved analytically for every RB system with the given symmetry.



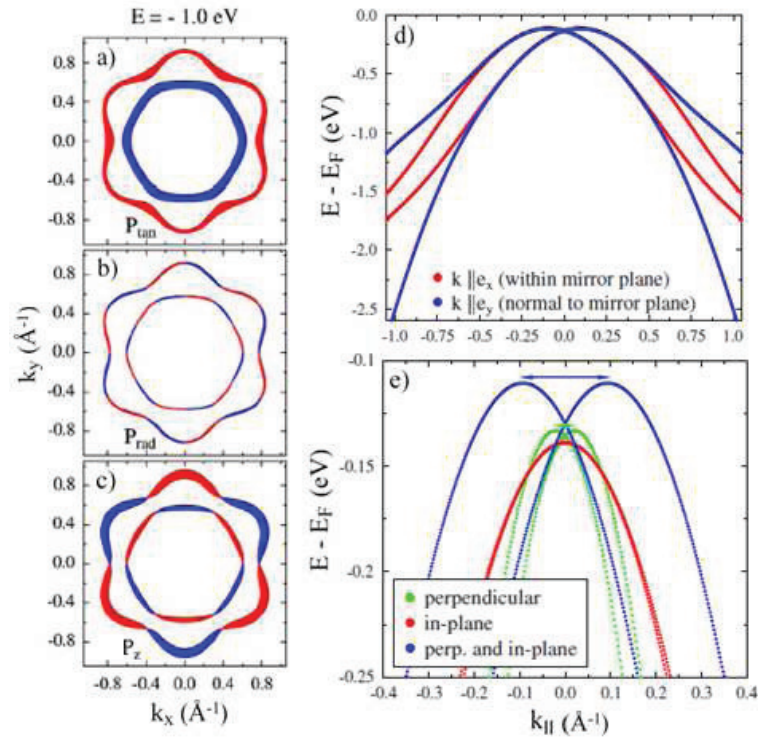


**Figure 2.14** — (a)-(c) Spin-resolved momentum distributions for an anisotropic RB 2DEG at a binding energy of 1.0eV. The parameters of the model have been chosen to fit the experimental results on the BiAg<sub>2</sub>/Ag(111) surface alloy. A hexagonal warping of the momentum distributions is accompanied by non-negligible  $P_{rad}$  and  $P_z$  components. Blue (red) symbols denote negative (positive) values of spin polarization. (d) Dispersion of the spin-split bands within and perpendicular to a mirror plane of the system. The anisotropic behavior is maximal normal to the mirror plane. (e) The effect of the in-plane potential gradient on the band dispersion (perpendicular to the mirror plane). Although, the in-plane  $\nabla V$  can dramatically enhance the splitting, the presence of an out-of-plane gradient is necessary in order to trigger the effect. [119]

### 2.3.3 An alternative view

The introduction of the in-plane potential gradient can be reconciled with the approach by Bihlmayer et al. which is based on the asymmetry of the surface state wavefunction [23]. As these authors noted in a later work, the splitting enhancement is connected to the presence of some  $p_{xy}$  character in the bands of  $sp_z$  symmetry [22]. This admixture increases the wavefunction asymmetry but also makes the electrons more sensitive to an in-plane potential gradient. This is due to the spatial orientation of the  $p_{xy}$  orbitals. The DFT calculations by Bihlmayer et al. established the connection between the splitting magnitude, the orbital character and the surface relaxation [22]. It should be stressed that according to the aforementioned experimental findings [7, 113, 94], RB splitting in BiAg<sub>2</sub> is four times higher than in PbAg<sub>2</sub>. This difference cannot be accounted for by the small increase of the  $6p$  atomic SO parameter but can find an explanation in the different orbital composition of the corresponding  $sp_z$  surface states. Nevertheless, in the case of PbAg<sub>2</sub>, it was proposed that the experimentally resolved bands may originate from two different pairs with strong RB splitting, rather than one pair with a weaker splitting (Fig. 2.16).

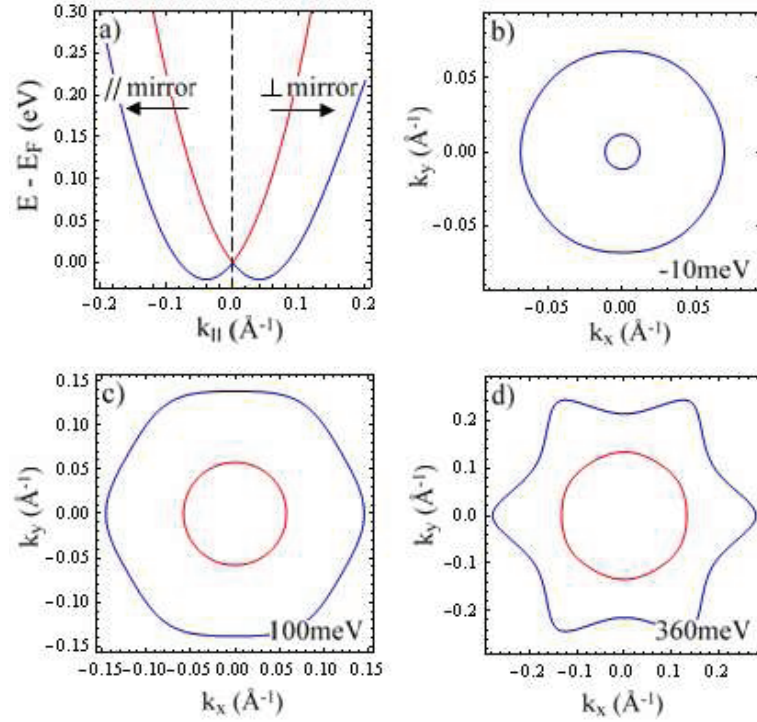


**Figure 2.15** — Simulated band dispersion (a) and CE contours (b)-(d) for an anisotropic RB 2DEG according to the Hamiltonian matrix which includes the 3<sup>rd</sup>-order correction (Eq. (2.26)). The model of the previous section (Figs. 2.1, 2.2) has been enhanced by an extra term which captures the effects of hexagonal warping. The effects are maximal normal to the mirror plane ( $k_x$ ) and become more pronounced as one moves away from  $\bar{\Gamma}$ . Simulation input:  $m^* = 0.3m_e$ ,  $\alpha_R = 1\text{eV \AA}$ ,  $c = 25\text{eV \AA}^3$ .

### 2.3.4 Tuning the spin-orbit splitting parameters

Moreschini et al. explored the possibility of further increasing the RB splitting encountered in a BiAg<sub>2</sub> surface alloy by the adsorption of rare gases [100]. They investigated the effect of Xe which gives the largest effect on the Au(111) surface state by acting on the out-of-plane potential gradient ([44] and section 2.2). As a result, they observed a strong backfolding of the bands which follows the periodicity of the induced superstructure and an increased hybridization between the  $sp_z$  and  $p_{xy}$  states. The latter is probably due to the different relaxation of the topmost layer after Xe deposition. Nevertheless, the magnitude of the splitting was not affected. Their findings can be explained if one takes into account the different predominant RB mechanisms in the cases of Au(111) and BiAg<sub>2</sub>. Therefore, their work provided an independent verification of the important role played by the in-plane potential gradient.

As briefly mentioned in section 2.1, Cappelluti et al. pointed out that the DOS of spin-split bands is considerably affected by the SO interaction in a region of width  $E_R$  between the band extremum and the spin degeneracy point [29]. In this so-called "low charge density" regime, the SO coupling cannot be considered as a perturbative correction to the electronic structure. The DOS switches from a constant value, characteristic of a parabolic 2D band, to a  $1/\sqrt{E}$  behavior typical of 1D systems, accompanied by a singularity at the band extremum. Moreover, the in-plane spin

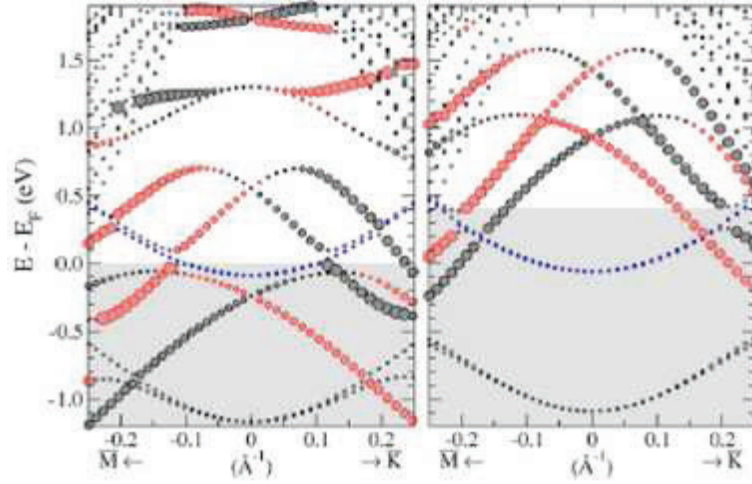


**Figure 2.16** — The band structure of a  $\text{BiAg}_2$  (left) and a  $\text{PbAg}_2$  (right) surface alloy by DFT calculations where SO coupling has been included self-consistently. The size of the circles indicates the degree of spin polarization, while the color distinguishes the opposite spin orientations. [22]

rotation of the two contours is expected to be in the same direction (Fig. 2.2). Effective interactions are strongly renormalized when the Fermi level lies in this energy range, and even enhanced superconductivity has been predicted [29]. The singularity was actually detected by scanning tunneling spectroscopy for both  $\text{BiAg}_2$  and  $\text{PbAg}_2$  as an asymmetric peak in the  $dI/dV$  spectrum [12].

The rigid band behavior of  $\text{BiAg}_2$  and  $\text{PbAg}_2$  suggests a route to attain the exotic low-charge density regime. Tuning of the Fermi level position was achieved by forming the  $\text{Bi}_x\text{Pb}_{1-x}/\text{Ag}(111)$  alloy with variable composition [11]. ARPES data supported by relativistic first-principles calculations confirmed the gradual rigid shift of the band structure, accompanied by the enhancement of the Rashba parameter between the two extreme concentrations (Fig. 2.17). The low-charge density regime is achieved for  $0.5 < x < 0.56$ . An alternative way to shift the Fermi level position is by alkali metal doping. This approach has been demonstrated for  $\text{BiAg}_2/\text{Ag}(111)$  ([45] and Fig. 2.18), as well as for the isostructural  $\text{BiCu}_2/\text{Cu}(111)$  alloy [19]. In this way, the SO parameters of the surface state do not change and one can shift the  $\text{BiAg}_2$  bands towards higher  $E_B$ .

Spin-resolved photoemission experiments provided a cast-iron confirmation of the theoretical predictions concerning the spin polarization of the split states. Meier et al. reported a non-negligible  $P_z$  component which becomes significant for the  $p_{xy}$ -derived surface states [94]. This is because the  $p_{xy}$  orbitals feel a stronger influence of the in-plane potential gradient. In agreement with the predictions by Premper et al.,  $P_z$  vanishes within a mirror plane of the system ( $\overline{\Gamma\text{M}}$ ) and is maximal in the normal direction ( $\overline{\Gamma\text{K}}$ ). According to the results of Fig. 2.15, the former corresponds to zero hexagonal warping (i.e. deviation from a circular contour) and the latter to a maximal value. A follow-up paper by the same group verified the unconventional spin topology expected in the  $\text{Bi}_x\text{Pb}_{1-x}/\text{Ag}(111)$  surface alloy when  $x$  lies in the low-charge density regime [95].

Moreschini et al. explored the interplay of the in-plane and out-of plane potential gradients by studying the isostructural  $\text{SbAg}_2$  surface alloy which is formed after the deposition of 1/3ML Sb on  $\text{Ag}(111)$  [102]. Sb has the same electronic configuration as Bi but, due to the smaller  $Z$ , it

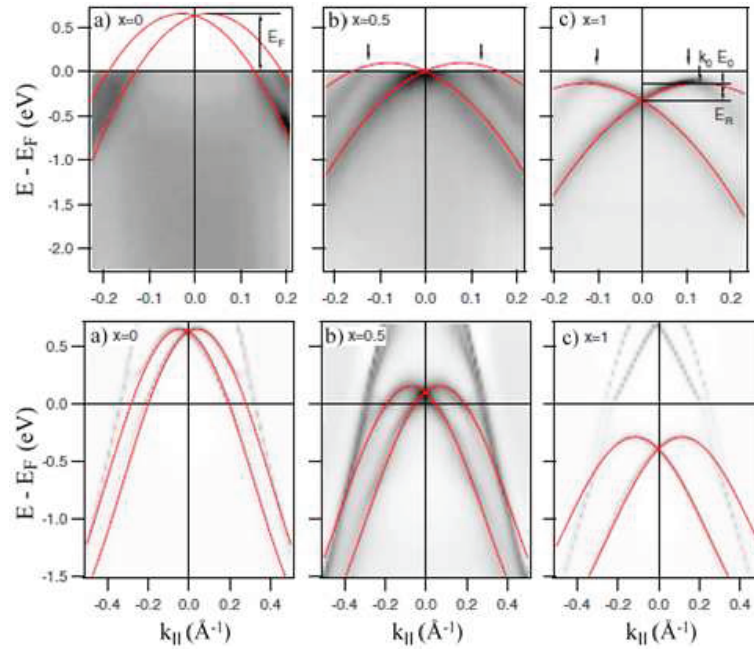


**Figure 2.17** — ARPES (top row) and relativistic first-principles (bottom row) results for the band structure of a  $\text{Bi}_x\text{Pb}_{1-x}/\text{Ag}(111)$  surface alloy. The SO parameters and the binding energy of the surface states vary continuously with increasing  $x$  from the pure  $\text{PbAg}_2$  to the pure  $\text{BiAg}_2$  case. The results are plotted along the high-symmetry  $\overline{\Gamma\text{K}}$  direction and red lines represent parabolic fits to the surface-state bands. [11]

exhibits a weaker atomic SO coupling (0.4eV for Sb vs. 1.25eV for Bi) [99]. Moreover, relativistic first-principles calculations predicted that the two alloys must have an identical orbital composition of the surface states [102]. Therefore, any difference in the magnitude of the RB splitting cannot be attributed to an in-plane potential gradient but only to the different atomic SO interaction. In fact, high-resolution ARPES results for  $\text{SbAg}_2$  were not able to distinguish between the two spin-split counterparts for most values of  $k$  revealing a strongly reduced smaller splitting [102]. Nevertheless, the anisotropic shape of the momentum distributions is still present. In agreement with the theoretical work by Prempert et al. [119], the authors concluded that a strong in-plane asymmetric potential is not by itself sufficient to generate a large splitting. It has to be accompanied by a significant atomic spin-orbit coupling, which is translated into a sizeable out-of-plane component potential gradient.

The substrate influence in determining the SO splitting in surface alloys was examined by two independent studies on the  $\text{BiCu}_2$  surface alloy [101, 19]. The atomic SO coupling is weaker in Cu due to smaller  $Z$  (0.03eV vs. 0.11eV for Ag). In line with this observation, experimental results reported a RB splitting which is four times weaker in  $\text{BiCu}_2$  than in  $\text{BiAg}_2$ . Moerschini et al. considered the observed splitting as a direct consequence of the different atomic parameters [101]. On the other hand, Bentmann et al. claimed that the main factor is the different relaxation of the Bi atoms in the two surfaces [19]. Their findings were based on the results of relativistic first-principles calculations by artificially increasing the values of the atomic constants in the Cu alloy to match those found in  $\text{BiAg}_2$ . The negligible effect on the splitting guided them to examine



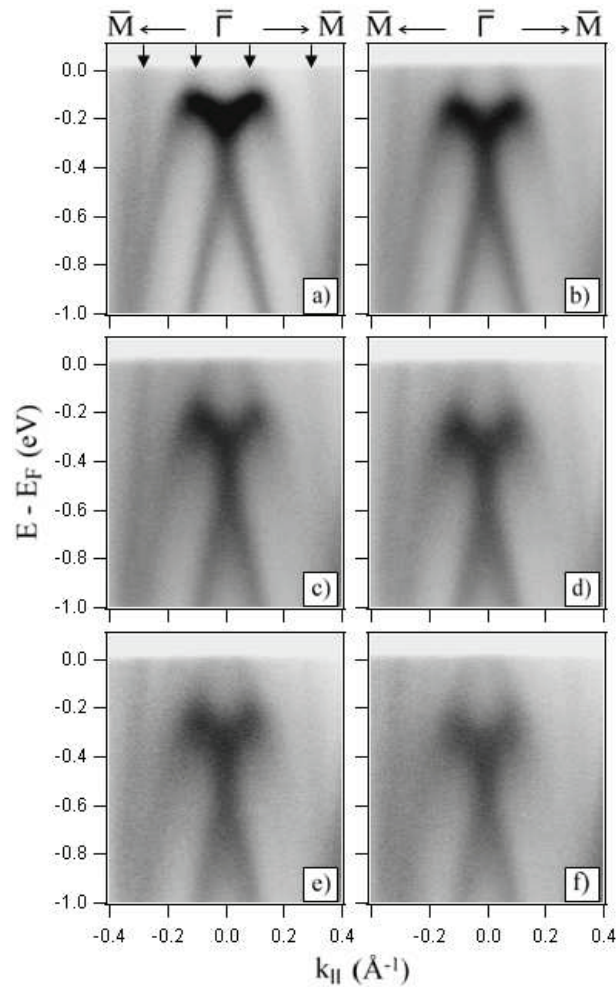


**Figure 2.18** — ARPES intensity around  $\bar{\Gamma}$  for a pure BiAg<sub>2</sub>/Ag(111) surface alloy (a) and after electron doping with increasing Na coverage (b)-(f). Each successive evaporation cycle adds 0.05ML of Na. Saturation coverage is obtained for 0.25ML Na (f) and results in a total energy shift of 230meV. (Data by A. Crepaldi) [45]

the role of structural differences. A recent quantitative LEED study examined the effect of surface relaxation on the SO-split mechanism for different surface alloys [50]. Considering each substrate individually, the authors reported the clear trend that a stronger outward relaxation leads to a larger splitting. Nevertheless, when one compares the alloys grown on Ag(111) with those grown on Cu(111), several deviations from this trend were observed. This might be related to the different orbital composition of the corresponding states.

In short, one may say that the spin splitting magnitude in surface alloys comes from the interplay of the in-plane and out-of-plane asymmetry. The latter is necessary to trigger the effect and is strongly dependent on both alloy constituents. Surface relaxation and orbital composition of the involved states may alter the size of the effect.

## 2.4 A flavor of spintronics

Spintronics (or spin-transport electronics) is an emerging technology whose main goal is the manipulation of the electronic spin degrees of freedom in solid-state systems. Three key ingredients are required in order to realize spin transport in such devices: a spin injector, a transport channel and a spin detector. The spin injector generates a current of spin polarized electrons which are electrically transferred (i.e. injected) to the sample. Manipulation of the spin during transport can be achieved by external magnetic or electric fields. The final spin orientation is detected by a spin-sensitive system (spin detector).

Metallic spintronic devices made their appearance a few years after the discovery of giant magnetoresistance (GMR) [14, 24]. The resulting spin-valve consists of two ferromagnetic layers separated by a spacer from a non-magnetic metal (Fig. 2.19 (a) and [154]). The resistivity of the system under the application of an electric potential depends on the relative spin orientation of the two layers. The latter is controlled by an external magnetic field and can be manipulated at will. A magnetic tunnel junction is the extension of the GMR-based spin-valve by replacing the non-magnetic metallic spacer with a very thin insulator (Fig. 2.19 (b)). Transport is then achieved by the quantum-mechanical tunneling effect. These technologies have already found applications in the hard disk technology as recording heads with high sensitivity, and in the development of non-volatile magnetic random access memory (MRAM).

The modern microprocessors and communication devices are based on silicon technology. In order to be able to perform all the information manipulations on a single chip, it would be therefore desirable to substitute the magnetic storage devices based on metallic spintronic elements with their semiconducting counterparts. Research on semiconductor spintronics was boosted after the measurement of extremely long room-temperature spin-coherence times in non-magnetic semiconductors [77, 76]. Although this concept is not critical for the development of the GMR and TMR-based devices, it affects the overall dynamics of the system and plays a fundamental role in the realization of novel semiconductor spin field-effect transistors (spin-FET).

Apart from their ability to integrate non-volatile storage directly into logical processors, the development of semiconductor spintronic devices could give additional advantages over the metallic spin systems. Switching within information-processing (i.e. from '1' to '0' and vice versa) could be feasible by applying a small magnetic field, either real or effective, which would be used to reorient the spins by rotating them of  $180^\circ$ . In this way, there would be no need for a minimum switching energy as in the case of metal-based systems, thereby overcoming any potential thermodynamic limitations [88]. Moreover, spin-based lasing might provide new alternatives to efficiently modulate high-power semiconductor lasers. Instead of changing the carrier density, the output intensity could be tuned by modifying the spin polarization degree of the injected current [13].

The first and most famous theoretical proposal for a device in the field of semiconductor spintronics is the spin-FET by Datta and Das in 1990 [36]. The proposed device is depicted in Figs. 2.20 and 2.21 and consists of a spin-polarizer, which corresponds to the source of a classical MOSFET

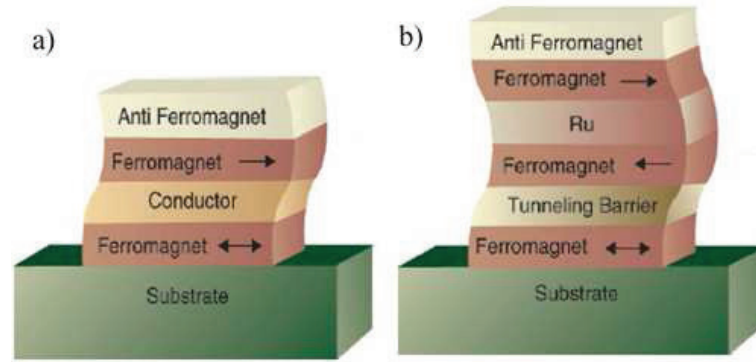


**Figure 2.19** — Spin-dependent transport devices based on metallic systems: (a) Spin valve. (b) Magnetic tunnel junction. An anti-ferromagnet is used to pin the magnetization direction of one of the ferromagnetic layers. [154]

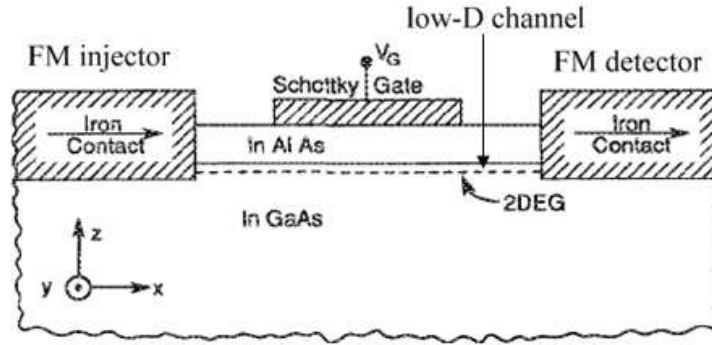


**Figure 2.20** — The proposed spin-FET proposed by Datta and Das. Electrons travel from the FM injector to the FM detector through the low-dimensional channel. Under the application of a gate voltage, the precession of their spin can be controlled. One can determine whether current passes or not by reversing the spin direction upon arrival at the detector. [36]

and a spin-analyzer as an analog of the drain. They are both made from ferromagnetic materials. Due to the non-equilibrium population of the two spins at the Fermi level, such ferromagnetic contacts can preferentially inject (polarizer) or detect (analyzer) spins with a particular orientation. After the injection, the electrons travel in a 2DEG which, according to the original proposal, is formed at a semiconductor heterojunction. The injected electrons move ballistically along this channel and they are finally collected by the detector. If their spin polarization vector points in the same direction as the one of the analyzer they can enter in the drain (ON), while if it is opposite, the electrons are scattered away (OFF). The direction of the spins is controlled by the gate voltage. Therefore, unlike the metal-based spintronic devices, there is no need for an external magnetic field. Electrically controlled spin-orbit interaction can be used as an effective magnetic field for spin coherence manipulation.

The Hamiltonian which describes the path of the electron from the source to the drain is the Rashba Hamiltonian introduced in section 2.1:

$$H_{SO} = \alpha_R(\boldsymbol{\sigma} \times \mathbf{k}) \cdot \hat{\mathbf{e}}_z \quad (2.27)$$

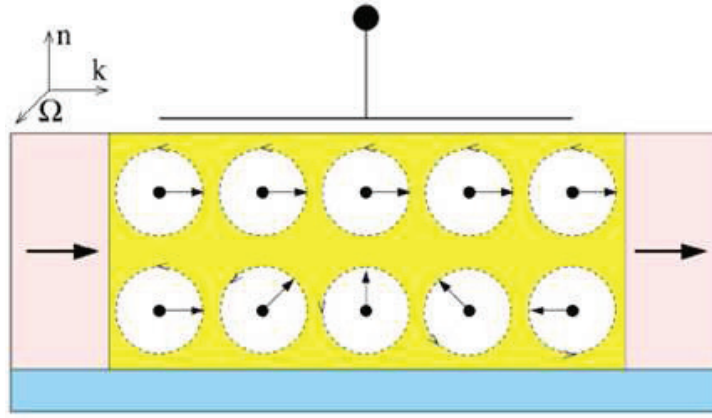


**Figure 2.21** — Another schematic representation of the Datta-Das spin-FET. During the trajectory of the spin-polarized electrons, their spins precess about the precession vector  $\Omega$ , which arises from SO coupling and can be controlled by an external gate voltage. The output current is large if the electron spin at the FM detector points in the initial direction (top) - for example, if the precession length is much larger than the source-drain separation - and small if the orientation is opposite (bottom). [157]

The effective magnetic field lies in-plane and it is always perpendicular to the momentum  $\mathbf{k}$ . The electron spin feels an effective magnetic moment and precesses in the plane perpendicular to the precession vector  $\Omega$ . The precession axis always lies in the 2D channel. The quantum mechanical evolution of the electron spin polarization vector is given by the equation of motion:

$$d\mathbf{S}/dt = \Omega \times \mathbf{S} \quad (2.28)$$

The corresponding evolution of the expectation value for the out-of-plane, ( $S_z = \mathbf{S} \cdot \mathbf{z}$ ) and the parallel to the in-plane  $\mathbf{k}$  ( $S_{\parallel} = \mathbf{S} \cdot \mathbf{k}/k$ ) components of the spin are described by:

$$dS_z/dt = 2\alpha_R k S_{\parallel} \quad , \quad dS_{\parallel}/dt = -2\alpha_R k S_z \quad (2.29)$$

On the other hand, the average spin component along  $\Omega$  ( $S_{\Omega} = \mathbf{S} \cdot (\mathbf{k} \times \mathbf{z})/k$ ) remains unchanged. Solving the above equations, one can find that the  $S_{\parallel}$  component precesses with an angular frequency  $\omega = 2\alpha_R k$ . In other words, if the initial injected spin is labeled as  $S_{0\parallel}$ , at an arbitrary wavevector  $k$ , the spin  $S_{\parallel}$  will be given by:

$$S_{\parallel} = S_{0\parallel} \cos(2\alpha_R k t) \quad (2.30)$$

Datta and Das calculated the differential shift  $\Delta\theta$  that an electron experiences after travelling in the 2DEG channel for a distance  $L$  [36]:

$$\Delta\theta = 2m^* \alpha_R L / \hbar^2 \quad (2.31)$$

which is independent of the momentum and the energy of the carriers. This is a big advantage for device applications because multiple modes can be involved in the transport without undesirable quantum interference effects.



When considering the general case with arbitrary spin polarization for the injected electrons, the results will depend on the polar angle  $\phi$  between the source-drain axis and the direction of  $\mathbf{k}$ . As a result, the probability of finding the spin in the direction of the drain magnetization will be proportional to the factor  $1 - (\cos^2 \phi)[\sin^2(\Delta\theta/2)]$ . The same factor reveals the modulation of the output current. As pointed out by Datta and Das the effect is gradually reduced to zero at  $\phi = 90^\circ$ . It would be therefore desirable to restrict the angular spectrum of the electrons by using an extra confining potential  $V(y)$ . In this way, one can obtain an effective 1D channel as a waveguide for the electron motion.

Despite its appealing advantages, there are many challenges to be faced before the experimental realization of the Datta-Das spin-FET. First of all, momentum scattering reorients the direction of the precession axis, randomizing the orientation of  $\mathbf{\Omega}$ . As a result, the electrons experience an average spin relaxation (dephasing). A large spin-splitting would be desirable in order to reduce the spin precession time, so that it is smaller than the time of relaxation. On the other hand, ballistic transport should be more easily achieved by eliminating any interface inhomogeneities. Moreover, the large impedance difference between ferromagnetic metals and semiconductors prevents the effective carrier injection into the 2DEG channel. Substituting the metallic contacts by ferromagnetic semiconductor sources [73], or using hot-electron injection [72] can be more efficient, but in any case the spin injection is a non-trivial experimental process. Finally, the modulation of  $\alpha_R$  by applying a bias voltage has only recently been demonstrated in semiconductor heterostructures [109, 97].

From the above considerations, it is obvious that materials with large  $\alpha_R$  are desirable for the experimental realization of a novel spin-FET. The Rashba parameter is inversely proportional to the precession length  $L$  (Eq. (2.31)), which must be small enough in order to allow at least half a rotation within the source-drain distance. Moreover, unwanted dephasing can be avoided only if  $L$  is smaller than the distance defined by the spin relaxation time. Nevertheless, the SO parameters for semiconductor heterojunctions are very small. Using typical values for  $\alpha_R$  and  $m^*$ , current modulation would be found at source-drain separations larger than  $1\mu\text{m}$  [109]. This value can be reduced by several orders of magnitude if one would be able to incorporate the concept of giant SO splitting observed on surface alloys into the design of a spin-FET. The first step of this experimental challenge is to observe enhanced Rashba effects on 2DEG systems formed on semiconducting substrates. This is the main motivation of the present thesis and our progress will be the subject of the following chapter.



# Chapter 3

---

## Giant spin-orbit effects on 2D systems with semiconducting substrates

---

### 3.1 Metallic surface alloys on Si(111) and thin buffer layers

#### 3.1.1 PbAg<sub>2</sub>/Ag/Si(111): An ARPES study

As noted in section 2.4, the main motivation of this work is the discovery of a semiconductor-based Rashba system with SO parameters of comparable magnitude to those of the Ag-based surface alloys (Table 2.1). To this end, a challenging route is the formation of metallic surface alloys on ultrathin films, themselves deposited on semiconducting substrates.

Hirahara et al. examined the electronic structure of Ag thin films, which are grown on a clean Si(111) substrate, both before and after the formation of a PbAg<sub>2</sub> surface alloy as a termination layer [61]. The RB splitting of the alloy-induced surface states was discussed in a subsection of their work, the latter being mainly focused on the energy shifts of the Ag quantum well states (QWS) after Pb deposition. Energy shifts are observed due to the different reflection properties at the film/vacuum interface. According to ARPES data, the Ag surface state is replaced by the alloy-derived states, while the parabolic Ag QWS persist after the formation of the alloy. Nevertheless, their dispersion is disturbed where they intersect the Pb states. At the intersections, the intensity of the QWS increases and one can follow the dispersion of the alloy states, which is otherwise masked by the strong spectral weight of the former. Following a matrix element effect argument which is based on the relative intensity of the observed surface states, the authors suggested that the spin-split states should follow the large splitting scenario proposed by Bihlmayer et al. (section 2.4 and [22]). After fitting the experimental band structure with the predictions of the corresponding theoretical study, they deduced a momentum splitting  $k_0$  equal to  $0.12 \text{ \AA}^{-1}$ , an energy splitting  $E_R$  of 120meV and a Rashba parameter  $\alpha_R$  of  $2\text{eV \AA}$ .

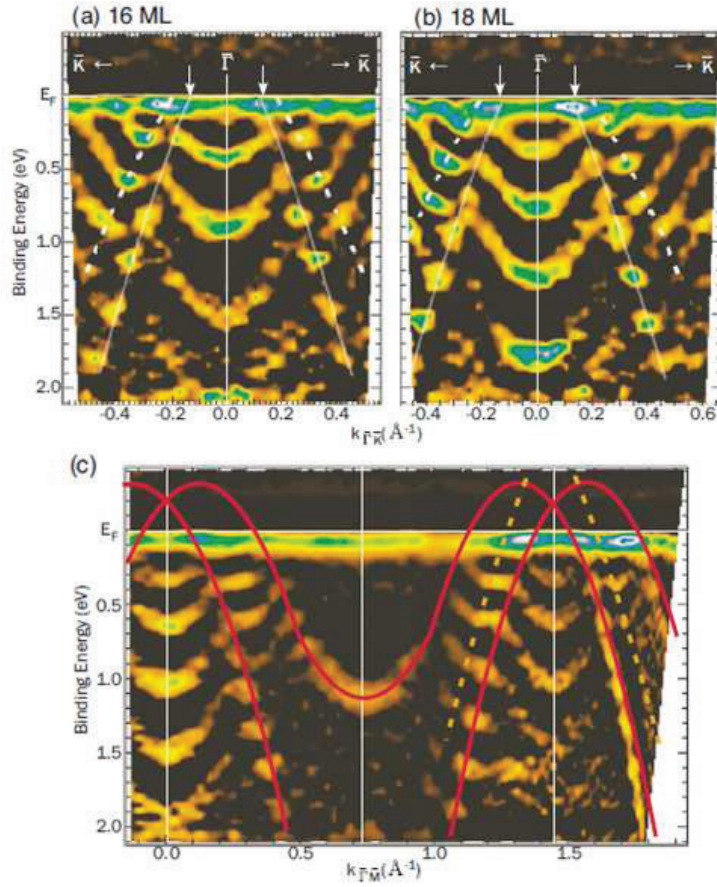


**Figure 3.1** — Electronic band dispersion of the Si(111)-Ag-PbAg<sub>2</sub> trilayer system for Ag buffer layers of three different thicknesses: (a) 16ML, (b) 18ML, (c) 24ML. The arrows point out the Fermi level crossings of the spin-polarized surface states. Solid and dotted lines refer to different pairs of spin-split counterparts following the scenario proposed in Ref. [22]. [61]

### 3.1.2 BiAg<sub>2</sub>/Ag/Si(111): An ARPES study and a NFE model

Regardless of which scenario is more accurate for describing the PbAg<sub>2</sub> band structure, the resulting RB parameters are always smaller than those of the BiAg<sub>2</sub> surface alloy (Table 2.1). Moreover, BiAg<sub>2</sub> exhibits two spin-split pairs one of which is fully occupied, thus leaving no question marks about its electronic structure. These observations make the BiAg<sub>2</sub> alloy a very attractive candidate for terminating a Si(111)-Ag *d*ML- XAg<sub>2</sub> trilayer system.

The Si(111) substrate was cleaned by direct current heating. Several flashes at 1400K were performed in order to remove the oxide layer and carbon impurities. After the surface was slowly cooled to RT, a sharp  $7 \times 7$  LEED pattern revealed its atomic order (Fig. 3.2 (a)). Ag was deposited from a Knudsen cell while keeping the substrate at 80K. The self-organization of Ag atoms deposited on a cold Si(111) substrate yields a close-packed structure after a mild annealing. Ag/Si(111) is an incommensurate interface, albeit atomically flat silver surfaces with a (111) termination plane can grow if the deposited material exceeds the amount of 6ML [69]. When the thickness of the Ag thin film is large (i.e.  $d > 40$ ML), the electronic structure before and after Bi deposition is

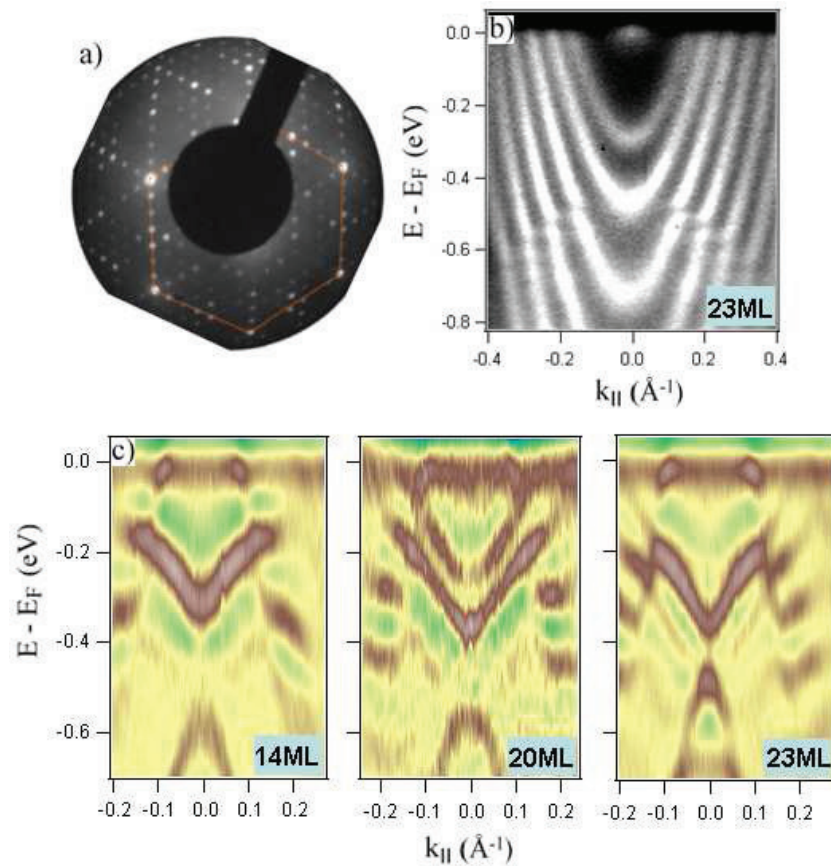


**Figure 3.2** — (a) LEED pattern of a clean Si(111) displaying a  $7 \times 7$  reconstruction. (b) QWS states arising from confinement effects after the deposition of a 23ML Ag film on a clean Si(111) substrate. (c) Electronic band dispersion of the Si(111)-Ag-BiAg<sub>2</sub> trilayer system for Ag buffer layers of three different thicknesses. The 2<sup>nd</sup> derivative of the photoemission intensity has been used to enhance the experimental features. [45]

reminiscent of the corresponding results on a Ag(111) single crystal. ARPES results on the clean film exhibit the well-studied Ag Shockley surface state. After the deposition of 1/3ML Bi and the formation of the BiAg<sub>2</sub> alloy, the experimental data is identical to the surface electronic structure of the BiAg<sub>2</sub>-Ag(111) system already discussed in a previous section (Fig. 2.12).

An interesting situation arises for thinner Ag buffer layers, where  $d$  is of the order of a few MLs. Before the deposition of Bi and the formation of the alloy, the Ag 5s states are confined within the Ag film by the vacuum potential barrier and the fundamental bandgap of the Si(111) substrate. This confinement leads to quantized wave vectors along  $z$  and to discrete energy levels in a "particle in a box" fashion. On the other hand, the electrons are nearly free in the  $xy$  plane and this yields a parabolic dispersion which is only perturbed when the energy approaches the maximum of the Si valence band [141]. The bulk continuum of the Ag 5s states is therefore replaced by the QWS which were already mentioned at the beginning of this section. QWS for the special case of 23ML are shown in an ARPES intensity plot in Fig. 3.2 (b). Their number and energy position are directly related to the thickness of the buffer layer and can be tuned at one's will.

When the BiAg<sub>2</sub> surface alloy is grown at the interface with a thin buffer layer, its surface elec-

tronic structure is significantly modified (Fig. 3.2 (c)). The spectral features are sharper than the thick-layer case because the alloy-derived states do not hybridize with the  $5s$  bulk continuum but only at their intersections with the Ag QWS. In full agreement with the PbAg<sub>2</sub> alloy, the experimental results evidence that hybridization with the quantum confined states is strong enough to alter the dispersion of the surface states in a significant way. Hybridization gaps are clearly seen in the dispersion of the branches of both the inner ( $sp_z$ ) and the outer ( $p_{xy}$ ) bands. They form at the intersections of the spin-split alloy states with the nearly spin-degenerate Ag QWS. Interestingly, the number, energy and width of the hybridization gaps can be modified by varying the value of an external parameter (i.e. the buffer layer thickness).

In order to model the interaction between the QWS and the surface states (SS), one can use a NFE Hamiltonian whose base states are  $|sp_z \uparrow\rangle$ ,  $|sp_z \downarrow\rangle$ ,  $|p_{xy} \uparrow\rangle$ ,  $|p_{xy} \downarrow\rangle$ ,  $|QW_1 \uparrow\rangle$ ,  $|QW_1 \downarrow\rangle$ ,  $|QW_2 \uparrow\rangle$ ,  $|QW_2 \downarrow\rangle$ . Spin projections refer to the  $z$  axis and for reasons of simplicity only the uppermost two QWS are considered. The corresponding Hamiltonian matrix can be then written as:

$$\begin{pmatrix} H_{SO}(sp_z) & V_{SS} & V_{(sp_z-QW_1)} & V_{(sp_z-QW_2)} \\ V_{SS}^* & H_{SO}(p_{xy}) & V_{(p_{xy}-QW_1)} & V_{(p_{xy}-QW_2)} \\ V_{(sp_z-QW_1)}^* & V_{(p_{xy}-QW_1)}^* & H_0(QW_1) & 0 \\ V_{(sp_z-QW_2)}^* & V_{(p_{xy}-QW_2)}^* & 0 & H_0(QW_2) \end{pmatrix} \quad (3.1)$$

This matrix consists of sixteen  $2 \times 2$  building blocks, each one referring to states of two different spins.  $H_{SO}$  represents the Rashba Hamiltonian matrix enhanced by the 3<sup>rd</sup>-order warping term (Eq. (??)),  $H_0$  denotes the free-electron-like dispersion of the QWS and the  $V$  building blocks refer to the hybridization between the two SS or between one QWS and one SS. The zero's point out that there is no hybridization between the two QWS. The hybridization between the QWS and the two spin-split pairs is parametrized by the corresponding potentials. These potentials are set to zero for states of opposite spins. In general, the hybridization parameters may depend on the quantum number ( $n$ ) of the QWS. This is because the SS do not have a fixed  $sp_z$  or  $p_{xy}$  character, but these relative components depend on their  $k$ -distance from the center of the SBZ [22]. Therefore, QWS of different  $n$  may interact with SS of a slightly modified character. The numerical parameters of the model are summarized in Tables 3.1 and 3.2, where  $\alpha_R$  is the Rashba parameter,  $c$  is a phenomenological constant which captures anisotropy effects (Eq. (2.26)) and the hybridization potential refers to the 1<sup>st</sup> Fourier coefficient.

**Table 3.1** — Parameters of the NFE model presented in matrix 3.1

state	$m^*$ ( $m_e$ )	$\alpha_R$ (eV Å)	$c$ (eV Å <sup>3</sup> )
$sp_z$	-0.22	4.1	23
$p_{xy}$	-0.19	3.3	21
$QW_1$	0.305	0	0
$QW_2$	0.305	0	0



**Table 3.2** — Hybridization potential between different types of electronic states as entered in matrix 3.1

Hybridization Type	Hybridization Potential (eV)
$sp_z$ - $p_{xy}$	neglected
$QW$ - $sp_z$	-0.02
$QW$ - $p_{xy}$	-0.05

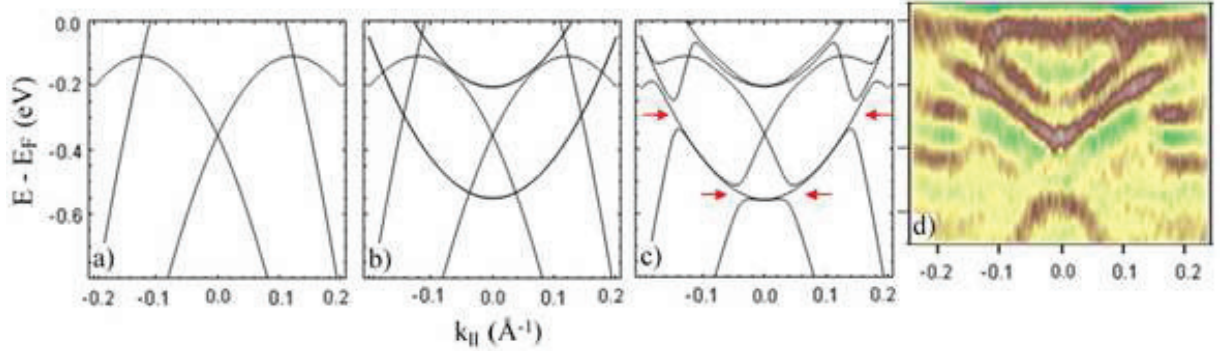


**Figure 3.3** — SS and QWS dispersion around  $\bar{\Gamma}$  for the Si(111)-Ag-BiAg<sub>2</sub> trilayer system according to a simple hybridization model: (a) Only the calculated surface states dispersion is presented. (b) Two parabolic QWS are included but their interaction with the surface states is neglected. The QWS parameters mimic the 20ML case. (c) As in (b) but the QWS interact with surface states of the same spin. The predicted discontinuities in the dispersion of the spin-split branches are pointed out by horizontal arrows. The weak hybridization of surface states has been neglected. (d) Experimental surface state and QWS dispersion for a BiAg<sub>2</sub> surface alloy grown on a 20ML buffer layer. The 2<sup>nd</sup> derivative of the photoemission intensity has been used to enhance the experimental features. [45]

The qualitative results are shown in Fig. 3.3 (c). In agreement with the experiment, the model predicts modulations in the dispersion of the spin-split branches, which are pointed out by horizontal arrows. However, these modulations do not correspond to real electronic gaps because our model assumes that SS are always 100% spin polarized. The spin-polarized SS can interact only with the QWS component of the same spin, leaving the opposite spin component unchanged. Nevertheless, inside such mini-gaps, the photoemission intensity should be dramatically decreased due to the weak signature of the QWS and the deviation from 100% spin-polarized SS. For reasons of clarity, Fig. 3.3 (b) considers the same QWS and SS but without any interaction between them. The energy positions of the QWS mimic the 20ML case (see Fig. 3.2 (d)). Interestingly, as evidenced in Fig. 3.3 (c), hybridization effects can lift the spin degeneracy of the QWS resulting into a small but finite splitting.

Relativistic first-principles calculations provide a more sophisticated means to verify the ARPES results. Extensive experimental data on the Si(111)-Ag *d*ML- BiAg<sub>2</sub> trilayer system along with the predictions of relativistic calculations are described in the following paper.

### 3.1.3 Tunable spin-gaps in a quantum-confined geometry (Phys. Rev. Lett. 101, 196805 (2008))

*We have studied the interplay of a giant spin-orbit splitting and of quantum confinement in artificial Bi-Ag-Si trilayer structures. Angle-resolved photoelectron spectroscopy (ARPES) reveals the formation of a complex spin-dependent gap structure, which can be tuned by varying the thickness of the Ag buffer layer. This provides a means to tailor the electronic structure at the Fermi energy, with potential applications for silicon-compatible spintronic devices.*

In nonmagnetic centrosymmetric bulk solids like silicon, electronic states of opposite spin have the same energy. A surface or an interface breaks the translational invariance of a three-dimensional crystal. Thus, as predicted by Bychkov and Rashba [28], the spin-orbit (SO) interaction can lead to spin-split electronic states in two-dimensional electron gases (2DEG), in asymmetric quantum wells [82], at a surface or at an interface [89, 129]. The size of the splitting is related to the strength of the atomic SO coupling (i.e. to the gradient of the atomic potential [93]) and to the potential gradient perpendicular to the confinement [44]. An unexpectedly large splitting was recently reported for a BiAg<sub>2</sub> surface alloy grown on a Ag(111) single crystal [7]. It is attributed to an additional in-plane gradient of the surface potential, hence being a direct consequence of the chemical alloy configuration [7, 119].

The spin-orbit interaction could be used to control via a gate voltage the dynamics of spins injected into a semiconductor [36, 13, 82, 109]. Moreover, the spin Hall effect - also induced by the SO interaction - could find applications in new spintronic devices [75, 148] which rely neither on magnetic materials nor on optical pumping. Interfaces between silicon and materials exhibiting large spin-orbit splitting are therefore expected to open novel vista for spintronics. The challenge is to control the electronic states and spin polarization at the Fermi level which determine the electron and spin transport through interfaces [52, 147] and nanostructures. Among the heavy metals which exhibit strong spin-orbit interactions, bismuth may be favored for environmental considerations. Experiments on thin layers of bismuth on silicon have evidenced a SO splitting in the Bi surface states, but not of their bulk counterparts [63, 62]. Moreover, it was observed that the splitting is removed by the hybridization between surface and bulk states.

In this Letter we explore a different approach. We fabricated trilayer systems composed of a BiAg<sub>2</sub> surface alloy [7], a thin Ag buffer layer of variable thickness ( $d$ ), and a Si(111) substrate (Fig. 3.4 (a)). Along the  $z$  direction, the vacuum/BiAg<sub>2</sub>/Ag/Si related potential is asymmetric and SO splitting of delocalized electronic states is expected. The good interfacial adhesion of the silver film makes the system stable at room temperature (RT) and results in a sharp interface. We investigated the complex interface by angle-resolved photoelectron spectroscopy (ARPES) experiment, supported by first-principles electronic-structure calculations. We find that the SO splitting is large. We also find that, due to quantum confinement in the buffer layer, the electronic structure exhibits patches of highly spin-polarized spectral density. The spin-dependent density of states close to the Fermi energy can be tuned by the thickness of the Ag buffer.



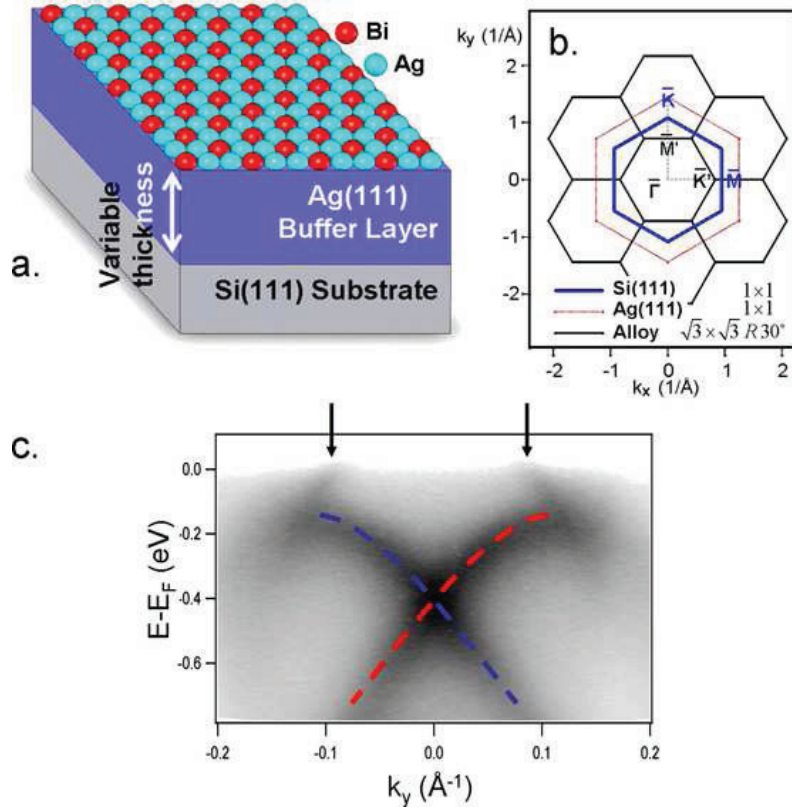


**Figure 3.4** — (a) Schematic view of a trilayer sample. The  $\sqrt{3} \times \sqrt{3} R30^\circ$  BiAg<sub>2</sub> alloy is grown on a Ag buffer - whose thickness can be varied - deposited on a silicon substrate. (b) First Brillouin zones of the surface structures. The symmetry lines  $\overline{\Gamma K M}$  and  $\overline{\Gamma K' M'}$  refer to Si(111) and to the alloy, respectively. (c) ARPES intensity of the surface states of a BiAg<sub>2</sub> alloy grown on a thick Ag layer deposited on Si(111) along  $\overline{\Gamma K' M'}$ . This system is similar to the alloy grown on a Ag(111) single crystal. Dashed lines indicate the branches of opposite spins of the  $sp_z$  surface state. Arrows point out bands of  $p_{xy}$  symmetry. Close to  $\overline{\Gamma}$  all bands exhibit a rotational symmetry around the surface normal.

The experiments were performed with a multi-chamber set-up under ultra-high vacuum. During preparation, Si(111) (highly phosphorus doped, resistivity 0.009 – 0.011  $\Omega$  cm) was flashed at 1200°C by direct current injection. After the flashes, the substrate was cooled slowly in order to obtain a sharp  $7 \times 7$  signature in low-energy electron diffraction (LEED). The Ag films were deposited with a home made Knudsen cell while the sample was kept at 80K and then annealed at 400K. The quality of the silver thin film was checked by LEED. Ag grows in the [111] direction [141]. The  $\sqrt{3} \times \sqrt{3} R30^\circ$  BiAg<sub>2</sub> surface alloy was obtained by depositing 1/3ML of Bi with an EFM3 Omicron source on the sample at RT followed by a soft annealing. Angle-resolved photoemission spectroscopy (ARPES) spectra were acquired at RT and 55K with a PHOIBOS 150 Specs Analyser. We used a monochromatized and partially polarized GammaData VUV 5000 high brightness source of 21.2eV photons.

The first-principles electronic-structure calculations are based on the local spin-density approximation to density functional theory, as implemented in relativistic multiple-scattering theory (Korringa-Kohn-Rostoker and layer-Korringa-Kohn-Rostoker methods; for details, see refs.

[7, 11]). Spin-orbit coupling is taken into account by solving the Dirac equation. The used computer codes consider the boundary conditions present in experiment, that is the semi-infinite substrate, a buffer of finite thickness, the surface, and the semi-infinite vacuum. The potentials of all sites (atoms) are computed self-consistently, except for the Si substrate which is mimicked by spherical repulsive potentials of 1 Hartree height. This so-called hard-sphere substrate follows the face-centered cubic structure of the Ag buffer. The electronic structure is addressed in terms of the spectral density which is obtained from the imaginary part of the Green function of the entire system. The latter can be resolved with respect to wavevector, site, spin and angular momentum, thus allowing a detailed analysis of the local electronic structure.

The surface electronic properties of the alloy grown on top of a thick Ag film ( $d = 80$  monolayers (ML)), as obtained by ARPES (Fig. 3.4 (c)), agree with those of the alloy grown on a Ag(111) single crystal [7]. The spin-split bands which belong to electronic states with  $sp_z$  character cross at  $\bar{\Gamma}$  (in-plane wavevector  $k_{\parallel} = \mathbf{0}$ ). They are well described by parabolas (effective mass  $m^* = -0.35m_e$ ) which are offset by  $\Delta k = \pm 0.13\text{\AA}^{-1}$ . This shift in wavevector is a signature of the aforementioned Rashba effect. Two sets of side bands stems from electronic states of mainly  $p_{xy}$  character which are also spin-polarized but less split [7, 119, 94]. The  $p_{xy}$  bands cross the Fermi level at  $k_F^{\text{inner}} \approx \pm 0.09\text{\AA}^{-1}$  and  $k_F^{\text{outer}} \approx \pm 0.21\text{\AA}^{-1}$ . Electronic-structure calculations[7] show that the BiAg<sub>2</sub> surface states are much more strongly localized in the top layer than the Ag(111) or Au(111) Shockley surface states. Thus, the spin-split bands and the giant SO splitting are not directly affected by the Ag/Si interface for Ag film thickness larger than a few monolayers. This implies that prior results for BiAg<sub>2</sub>/Ag(111) [7] can be transferred to silicon technology (i.e. to BiAg<sub>2</sub>/Ag/Si(111)) at RT.

A new and interesting situation arises for thinner Ag buffer layers, where  $d$  is of the order of the attenuation length of the electronic states. The Ag  $sp$  states are confined to the Ag film by the potential barrier (image-potential barrier) on the vacuum side (surface) and by the fundamental band gap of Si on the substrate side. This confinement leads to quantized wavevectors along  $z$  and to discrete energy levels [34]. These so-called quantum well states (QWS's) play a central role in transport properties [71] and in the coupling of magnetic layers in superlattices[111, 112, 27]. Ag/Si(111) QWS's, in particular, have been extensively studied by ARPES [141, 150, 133]. For Ag(111) films, their in-plane dispersion consists of a set of parabolic bands centered at  $\bar{\Gamma}$ , with energies determined by the film thickness (Fig. 3.5 (a);  $d = 17\text{ML}$ ). The electronic fringe structure with a negative parabolic dispersion appears due to the accumulation of QWS's near the  $k$ -dependent valence band edge of Si. This is an indirect manifestation of the heavily-doped n-type character of the Si(111) substrates used here [141]. The narrow lineshapes of the energy distribution curves (EDC's; Fig. 3.5 (b)) and momentum distribution curves (MDC's; Fig. 3.5 (c)), and the observation of the electronic fringes reflect the uniformity of the Ag buffers and the high resolution of the experiment.

We now consider the interaction of the spin-split alloy surface states and the QWS's in a BiAg<sub>2</sub>/Ag/Si trilayer, focusing first on a 17ML thick Ag buffer (Fig. 3.5 (d); i.e. the sample of Fig. 3.5 (a) covered by the BiAg<sub>2</sub> alloy). The Ag Shockley surface state disappears and the re-

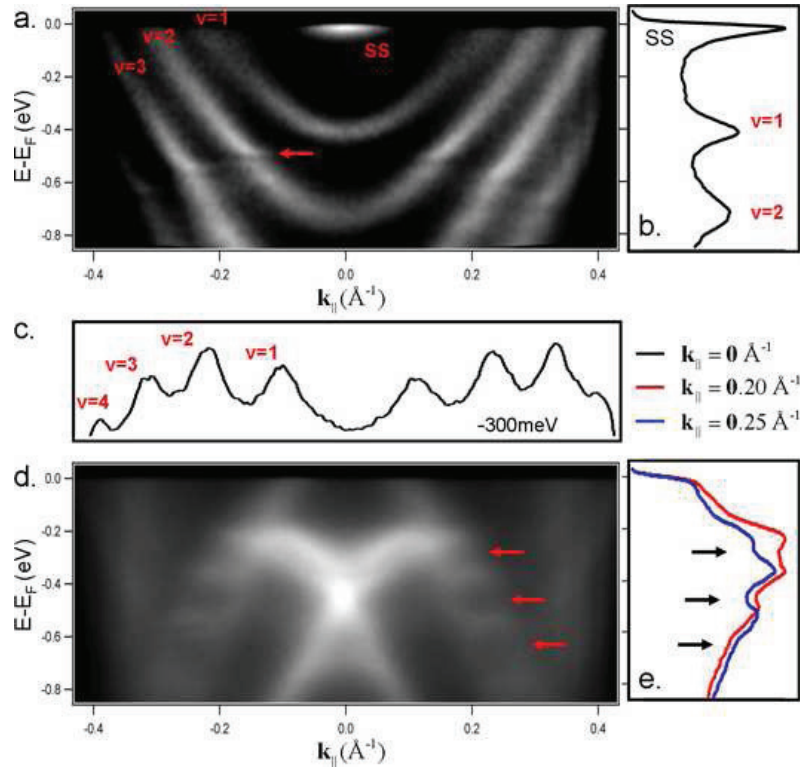


**Figure 3.5** — (a) Raw ARPES data along  $\bar{\Gamma}\bar{K}$  at 55K. QWS's in a 17ML bare Ag buffer deposited on Si(111). These parabolic states are numbered  $\nu = 1 \dots n$ . Kinks in the dispersion (arrow) are due to the hybridization of the QWS with the  $p$  bands of silicon. SS stands for the Shockley surface state of Ag(111). (b) EDC extracted from Fig. 3.5 (a) at  $\bar{\Gamma}$ , i.e.  $k_{\parallel} = 0.0 \text{\AA}^{-1}$ . The 1<sup>st</sup> and 2<sup>nd</sup> QWS signatures and the SS are indicated. (c) MDC extracted from Fig. 3.5 (a) at  $-300\text{meV}$  shows the successive branches of the QWS. (d) raw ARPES intensity along  $\bar{\Gamma}\bar{M}$  at 55K of the BiAg<sub>2</sub> alloy grown on 17ML of Ag. (e) EDC extracted from Fig. 3.5 (d) for  $k_{\parallel} = 0.20 \text{\AA}^{-1}$  and  $k_{\parallel} = 0.25 \text{\AA}^{-1}$ . Arrows indicate gaps of 100 – 200meV in the dispersion of the  $p_{xy}$  bands.

sulting surface electronic structure agrees in general with that of the system without Si substrate (BiAg<sub>2</sub>/Ag(111); no QWS's) but shows intensity modulations in both the  $sp_z$  and  $p_{xy}$  bands. The energy distribution curves, extracted from the raw data, clearly evidence band gaps (Fig. 3.5 (e)).

The remaining signature of the Ag QWS's (at large  $k$  values) and the gaps in BiAg<sub>2</sub> surface states are clearly seen even at RT in the second derivative of the ARPES intensities ( $d^2 I(E, \mathbf{k}_{\parallel})/dE^2$ ) for samples with selected Ag film thicknesses ( $d = 19, 16,$  and  $10\text{ML}$ ) in Fig. 3.6. The parabolic in-plane dispersion of the QWS's (circles in Fig. 3.6) is obtained from MDC's of Ag/Si(111) with the corresponding Ag thicknesses (as presented in Fig. 3.5 (c)). Agreement between the parabolic fits (uncovered Ag buffer) and the QWS's of the alloyed sample is obtained after shifting rigidly the parabolas by 50 – 150meV to lower binding energies. These shifts can be attributed to the different reflection properties of the bare Ag surface and of the BiAg<sub>2</sub> surface alloy [61]. However, the effective masses of the QWS's may also change. Therefore, these fits are to be considered as guides to the eye. Band gaps are found at the intersection of the QWS parabola with both branches of the surface-alloy bands regardless of their symmetry or spin, providing strong

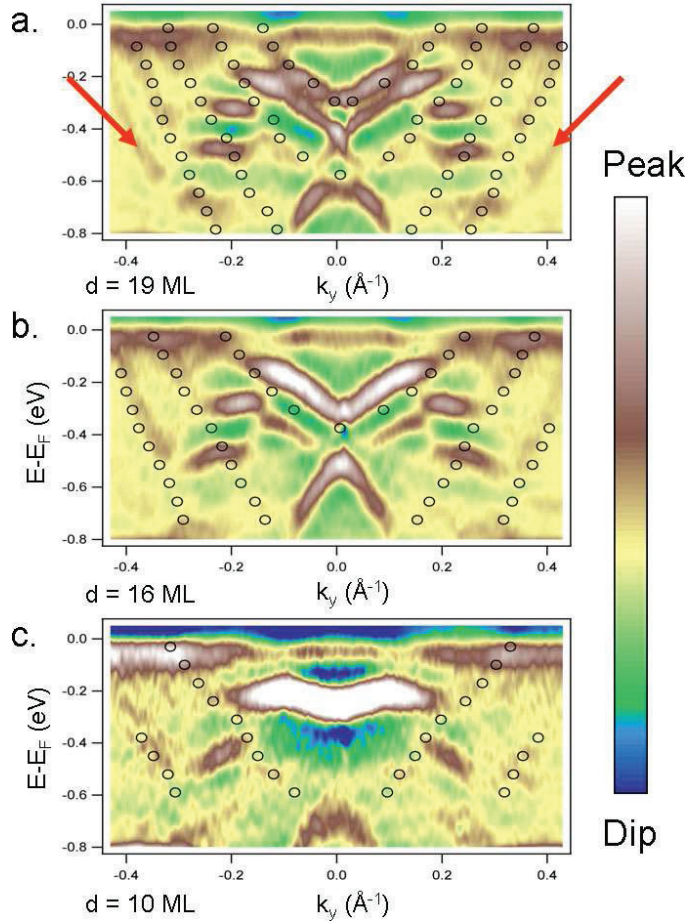


**Figure 3.6** — (a), (b) and (c): Second derivative of the ARPES intensity along  $\bar{\Gamma}\bar{M}$  for three alloy-covered samples at RT with different Ag film thicknesses, respectively 19, 16 and 10ML. Circles correspond to MDC fits of the QWS observed on the bare Ag thin films of the corresponding thicknesses shifted by 50 – 150meV upwards in order to match the remaining parts of the QWS at large  $k$  values after Bi deposition (e.g. red arrows).

evidence of their hybridization. The hybridization is spin-selective [39, 15] thus we can consider in a first approximation that the QWS are spin-degenerate or their spin-splitting is small. For thinner Ag buffers (10ML; Fig. 3.6 (c)), the number of QWS's is reduced. As a result, the number of band gaps is also decreased but their widths are larger, in particular for the  $p_{xy}$  states.

To further corroborate the above interpretation of the band gaps, first-principles electronic structure calculations for  $\text{BiAg}_2/\text{Ag}(111)$  reported in [7, 11] were extended. Since the  $\text{Ag}/\text{Si}(111)$  interface is incommensurate [141], we are forced to approximate the Si substrate. Therefore, the confinement of the Ag QWS's by the Si(111) substrate is mimicked by replacing Ag bulk layers by repulsive potentials. The latter provide the complete reflection of the Ag states at the  $\text{Ag}/\text{Si}(111)$  interface. Note that by this means details of the  $\text{Ag}/\text{Si}$  interface are roughly approximated and the binding energies of the theoretical quantum well states may differ from experiment. However, the essential features are well captured, as will be clear from the agreement of experiment and theory discussed below. The systems investigated comprise the  $\text{BiAg}_2$  surface alloy, Ag lay-



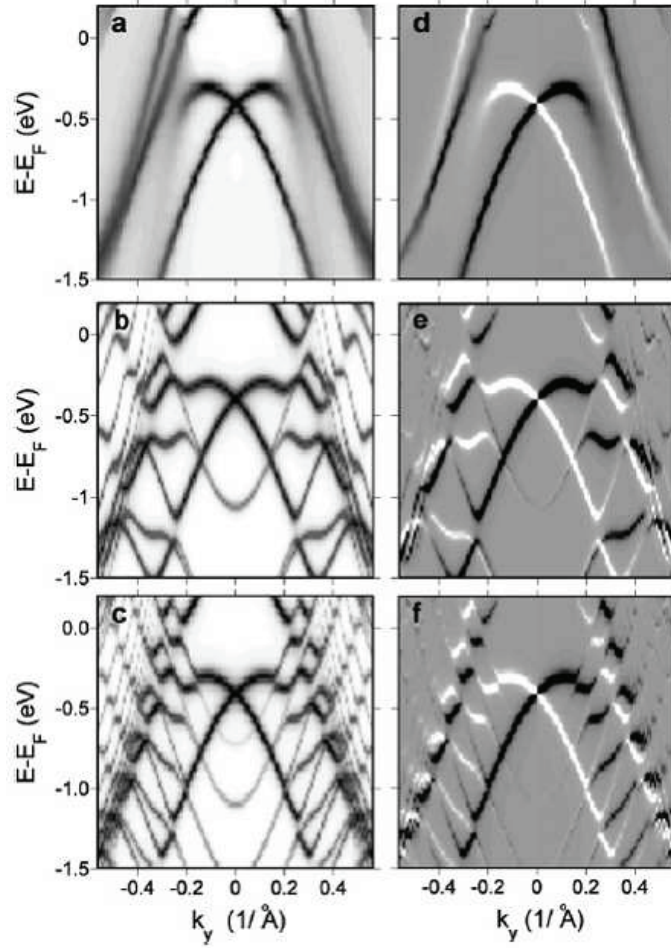


**Figure 3.7** — Effect of QWS's on the spin-split electronic structure of the  $\text{BiAg}_2$  surface alloy, as obtained from first-principles electronic-structure calculations. (a)-(c): The spectral density at the Bi site is displayed as gray scale (with white indicating vanishing spectral weight) for  $\text{BiAg}/\text{Ag}(111)$  (a) and  $\text{BiAg}_2/\text{Ag}/\text{Si}(111)$  for Ag buffer thicknesses  $d = 10$  (b) and  $d = 19$  (c). The wavevector is chosen as in the experiment (Fig. 3.6). (d)-(f): The spin polarization of the electronic states is visualized by  $\Delta N(E, \mathbf{k})$ , i.e. the difference of the spin-up and the spin-down spectral density. White and black indicate positive and negative values, respectively, whereas gray is for zero  $\Delta N$ .

ers, and the substrate built from hard spheres (HS; i. e.  $\text{BiAg}_2/\text{Ag}_{d-1}/\text{HS}(111)$ ). The theoretical analysis focuses on the wavevector- and spin-resolved spectral density  $N(E, \mathbf{k}; \sigma)$  at a Bi site ( $\sigma = \uparrow$  or  $\downarrow$  is the spin quantum number). Spin-dependent band gaps are visualized by displaying  $\Delta N(E, \mathbf{k}) = N(E, \mathbf{k}; \uparrow) - N(E, \mathbf{k}; \downarrow)$ .

For  $\text{BiAg}_2/\text{Ag}(111)$ , the Bi surface states hybridize with Ag bulk states, resulting in a rather blurred spectral density (Fig. 3.7 (a); compare Fig. 3.4 (c) for the experiment). For the systems with Si substrate, focusing here on exemplary results for  $d = 10$  (Fig. 3.7 (b)) and 19 (Fig. 3.7 (c)), quantum well states show up as parabolas centered at  $\bar{\Gamma}$ . The most striking difference to  $\text{BiAg}_2/\text{Ag}(111)$  is, however, spin-dependent band gaps at  $(E, \mathbf{k})$  points at which the QWS's would cross the Bi bands. With increasing thickness of the Ag buffer, the number of gaps (or QWS's) increases and the width of the gaps decreases. The spectral densities of the Bi states are slightly

less blurred than for BiAg<sub>2</sub>/Ag(111) because hybridization with Ag states occurs only at the band gaps, due to quantization. Eventually, we find a shift of the QWS's energies upon covering the Ag buffer with the BiAg<sub>2</sub> alloy, as observed by the experiment.

We now focus on the agreement of the experimental findings and the present theoretical approach. Apart from the similar trends concerning the number and the width of the gaps with varying the buffer layer thickness, theory predicts the experimentally-observed strong spectral weight of the remaining ungapped parts of the alloy states. Moreover, it points towards the association of the ungapped parts of the sidebands both with the  $p_{xy}$  bands and the continuation of the  $sp_z$  band at large wavevectors. The finite experimental resolution prevents us from identifying each single contribution. Nevertheless, both in the experimental (Fig. 3.6) and the theoretical data (Fig. 3.7 (e), 3.7 (f)), the overall shape of each ungapped structure of the sidebands exhibits a continuously changing curvature from positive to negative with decreasing  $d$ .

By contrast with what has been observed in Bi thin layers on silicon [63, 62], the theoretical results of Figs. 3.7 (e) and (f) clearly show that the Ag quantum well states are spin-polarized due to the Rashba effect. Close to  $\bar{\Gamma}$ , the branches of opposite spins of the QWS follow a parabolic dispersion and their momentum separation decreases with the Ag thickness. This feature is evident in figures that show spin polarization of the electron states. We now address in particular the electronic structure at the Fermi level. For  $d = 10\text{ML}$  (Fig. 3.7 (e)), highly spin-polarized states show up at  $k_{\parallel} = k_{\parallel} = 0.22\text{\AA}^{-1}$ , with a spin polarization of about 33%. On the contrary, a complete gap appears for  $d = 19\text{ML}$  (Fig. 3.7 (f)). These findings imply that the spin-dependent electronic structure at the Fermi level - and thus the transport properties - can be drastically modified by the Ag film thickness.

Our findings for BiAg<sub>2</sub>/Ag/Si(111) trilayers suggest that it is indeed possible to match systems with large spin-orbit splitting (here: BiAg<sub>2</sub>/Ag(111)) with a semiconductor substrate. Furthermore, interfacial properties can be custom-tailored, in the present case by a single parameter, namely the Ag buffer layer thickness. In this respect, multilayer systems which comprise semiconducting Si layers and Rashba-split subsystems (like BiAg<sub>2</sub>/Ag) may be very useful in the development of new spintronics devices. Tuning the band-gap structure at the Fermi level could also be achieved by chemical means, as was demonstrated for Bi <sub>$x$</sub> Pb <sub>$1-x$</sub> Ag<sub>2</sub> mixed alloys grown on Ag(111) [11]. Peculiar transport properties and spin Hall effects can be anticipated based on this interface, namely in nanostructured systems or (Bi-Ag-Si) superlattices.

*E.F. acknowledges the Alexander S. Onassis Public Benefit Foundation for the award of a scholarship. This research was supported in part by the Swiss NSF and the NCCR MaNEP.*

In comparison to the CE of the  $\text{BiAg}_2/\text{Ag}(111)$  alloy (Fig. 2.13), the CE maps of the trilayer system are expected to be significantly modified due to the hybridization with the QWS. Fig. 3.8 compares the CE contours for a surface alloy grown on a thick Ag layer with the corresponding 2D band topology when  $d$  is equal to 16ML. Apart from the additional circular contour due to the Ag QWS, the hexagonal Bi-derived  $p_{xy}$  state appears gapped at six points. In a simplistic picture, these gaps are expected since they arise from the interaction of a hexagonal contour ( $p_{xy}$  alloy state) with a state of circular in-plane symmetry (Ag QWS). Modifications of a sixfold symmetry are also expected for the  $sp_z$   $\text{BiAg}_2$  states.

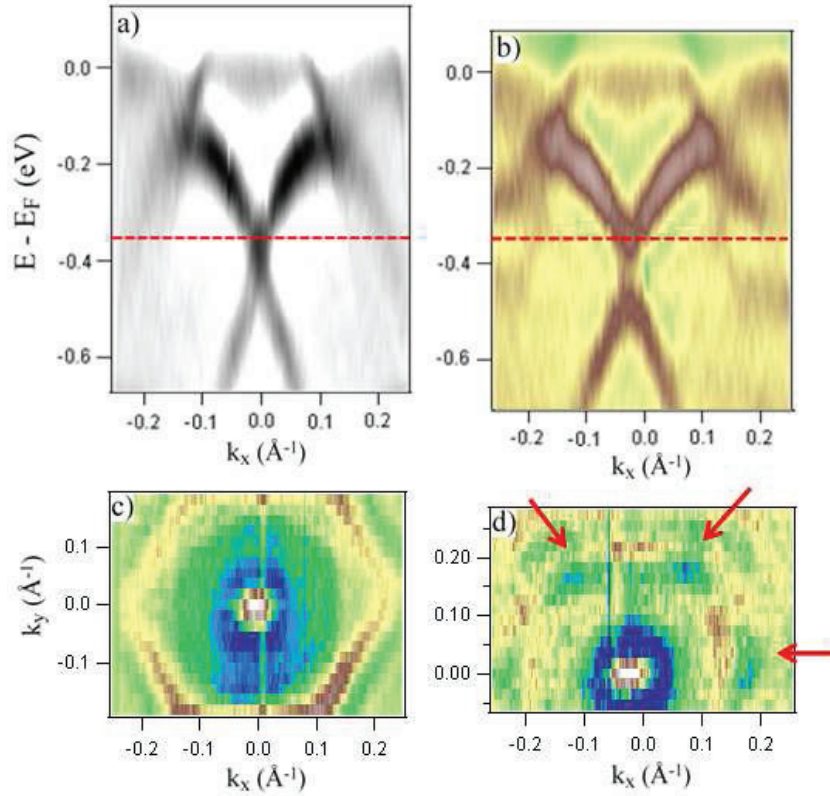


**Figure 3.8** — Comparison of the electronic band dispersion and a CE map  $E_B = 380\text{meV}$  for  $\text{BiAg}_2$  surface alloys grown on a thick  $\text{Ag}(111)$  film (a), (c) and on a thin buffer layer of 16ML (b), (d). The red arrows point out three of the six expected gaps on the hexagonal contour coming from the  $p_{xy}$  sidebands. These gaps are a consequence of the interaction with the parabolic QWS. The measurement has been performed at ambient temperature in order to increase the sample lifetime. The 2<sup>nd</sup> derivative of the photoemission intensity has been used to enhance the experimental features.

### 3.1.4 BiAg<sub>2</sub>/Ag/Si(111): A parallel ARPES study

At the same time as the work at the LSE [48, 46, 45], the Si(111)-*d*ML Ag-BiAg<sub>2</sub> system was studied in the group of Prof. Matsuda at the University of Tokyo. In this parallel study He et al. presented their ARPES data, agreeing that the observed band structure gaps arise from the hybridization between the spin-polarized surface states and the spin-degenerate QWS [55]. Their work is not accompanied by relativistic calculations but they use a simple hybridization model which is very similar to the one presented in Eq. (3.1). The authors point out the fact that spin-selective hybridization may induce spin-splitting in the QWS which is in agreement with the conclusions of our work. After measuring the gap width for different buffer layer thicknesses, they concluded that it increases with increasing QWS quantum number and decreasing film thickness (Fig. 3.9 (d)). They moreover used their phenomenological model in order to calculate the matrix elements which correspond to the gap values. The calculation results demonstrate that the experimental trends are best captured by using a film-vacuum phase-shift of  $\pi$  (Fig. 3.9 (c)).

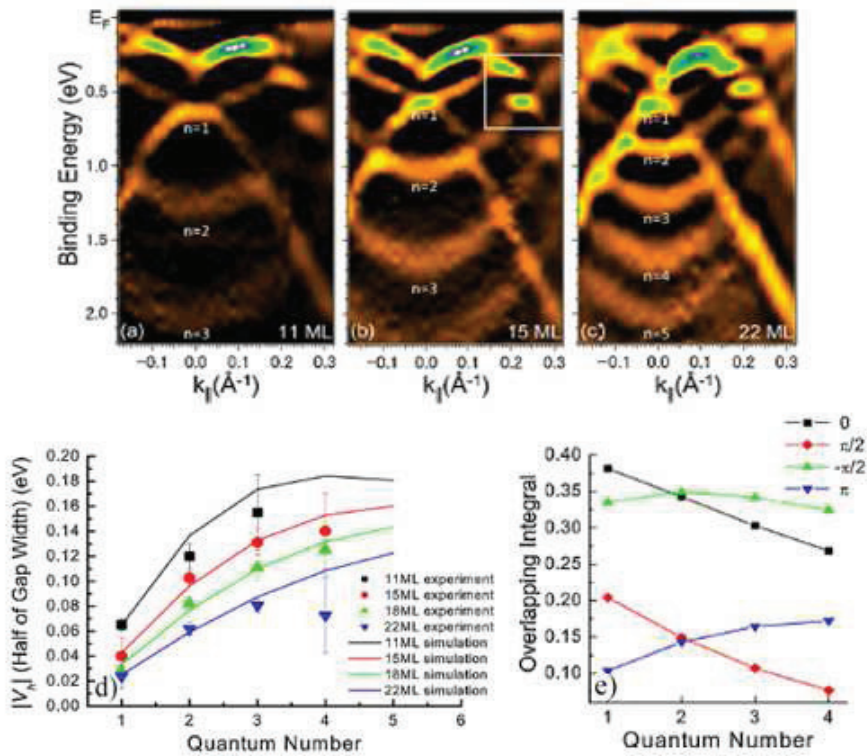


**Figure 3.9** — (a)-(c) Electronic band dispersion of a BiAg<sub>2</sub> surface alloy grown on buffer layers of 11 (a), 15 (b) and 22ML (c). (d) Evolution of the gap width as a function of the QWS quantum number and the thickness of the buffer layer. Solid lines are a result of a matrix elements calculation, while symbols denote the experimental values. (e) The matrix elements calculation for a thin film of 15ML is extended to different film-vacuum phase shifts. The experimental trend points towards a phase shift of  $\pi$ . The dotted box highlights a portion of the  $E - k$  space where spin-selective hybridization occurs. [55]



### 3.1.5 BiAg<sub>2</sub>/Ag/Si(111): A spin-resolved ARPES experiment

In a later publication He et al. used SARPES to directly probe the spin character of the electronic states [56]. Their experimental results are shown in Fig. 3.10. Panels (a) and (b) represent the measured intensity maps for the two different spin orientations, while panel (c) summarizes the band dispersion for negative  $k$ -values. In agreement with the predictions by the aforementioned hybridization models and first-principles calculations, the bands form energy gaps only when spins of the QWS and SS are identical. After a character analysis of the QWS and SS, the authors concluded that the emergence of energy gaps does not only depend on the relative spin orientation but also on the relative orbital symmetry of the involved states.

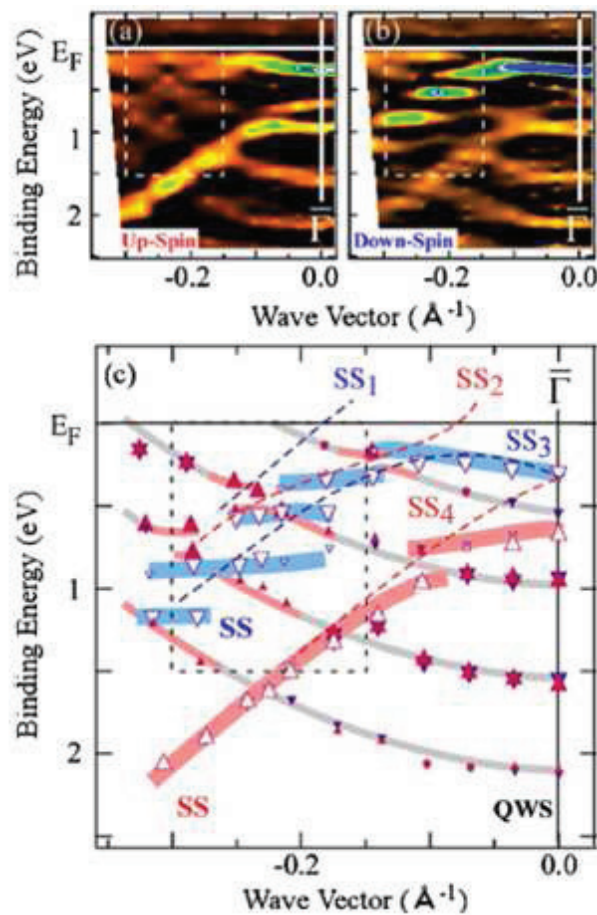


**Figure 3.10** — (a), (b) Second derivative of spin-resolved ARPES spectra displayed as a function of  $E_B$  and  $k_{\parallel}$ . Panel (a) reports the spin-up component, while panel (b) the spin-down component. A schematic representation of the spin-ARPES results. Red (blue) triangles denote the peak positions for the spin-up (spin-down) spectra. Dashed and thick lines are guides to the eye following the surface state dispersion before and after the interaction with the QWS. [56]

## 3.2 SO effects on semiconducting interfaces

### 3.2.1 Bi/Si(111): Structural characteristics

Bi deposition on a clean Si(111)- $7 \times 7$  substrate yields two stable reconstructions in the submonolayer range both of which follow the same symmetry ( $\sqrt{3} \times \sqrt{3}R30^\circ$ ). This characteristic attracted a considerable interest of the scientific community in the late 80s and the 90s. The low coverage Si(111)-Bi  $\sqrt{3} \times \sqrt{3}$  reconstruction was measured by a variety of structural probes with a view to determine the structural properties of the two phases. In specific, quantitative LEED [151, 152, 115], X-Ray diffraction [145, 107], STM [137, 114, 115] and Photoelectron Holography [128] were used to acquire new experimental evidence. As a result, there is a general consensus that at  $\Theta_{Ag} = 1/3\text{ML}$ , atoms occupy  $T_4$  sites yielding the so-called monomer reconstruction (or  $\alpha$ -phase), while at  $\Theta_{Ag} = 1\text{ML}$  one arrives at a milkstool trimer reconstruction with each trimer centered at a  $T_4$  site (or equivalently above a 2<sup>nd</sup>-layer substrate atom). The trimer reconstruction

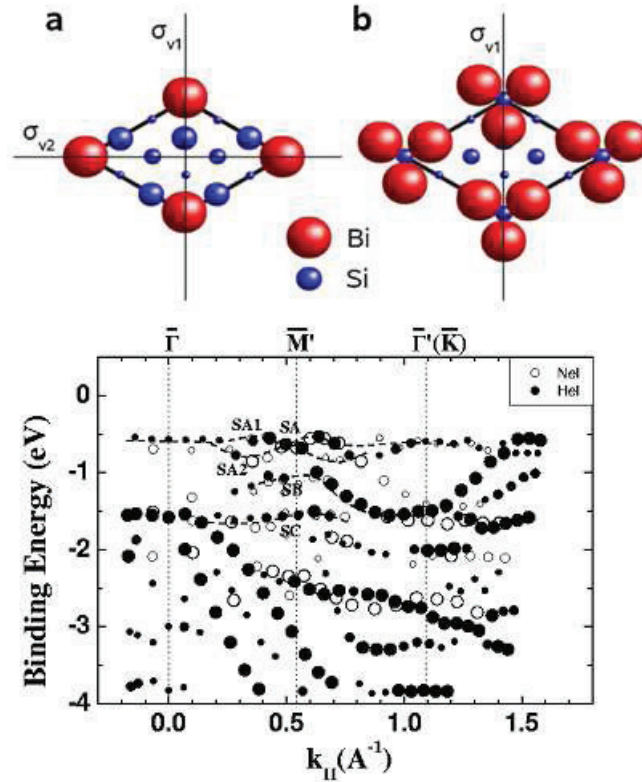


**Figure 3.11** — (top) Structural models of the monomer (a) and trimer (b) Si(111)-Bi  $\sqrt{3} \times \sqrt{3}R30^\circ$  phases. The size of the spheres indicates the distance of the atoms from the top layer. The mirror planes of the topmost layer are indicated by vertical and horizontal lines. The trimer formation enhances the in-plane  $\nabla V$  by breaking the  $\sigma_{v2}$  mirror symmetry. (bottom) Experimental band dispersion for the trimer phase along the  $\bar{\Gamma}\bar{M}$  high-symmetry direction of the reconstruction. Black (white) circles have been acquired with a photon energy of 21.2eV (16.85eV). The size of the data points reflects the intensity of the corresponding EDC peaks. [51, 79]

is also known as  $\beta$  phase. Theoretical studies verified the experimental findings and concluded that the  $T_4$  and milkstool models are the only thermodynamically stable Bi-induced reconstructions on Si(111) [33, 98, 135]. A very recent LEED study verified the aforementioned structural propositions by reporting  $I - V$  curves for single-phase high-quality samples [87]. Both structural arrangements are presented in Fig. 3.11.

### 3.2.2 Bi/Si(111): Early ARPES studies

The extensive amount of work on its structural properties initiated the scientific interest about the electronic structure of the Si(111)-Bi interface. The first ARPES study was performed by Kinoshita et al. without being able to state whether their investigation was related to the monomer or trimer phase [81]. Interestingly, they observed surface states at the border of the SBZ which seem to be split. They attributed the splitting to a strong SO interaction arising from the large atomic SO parameter of Bi. In a later study, Kim et al. confirmed that the previous authors were investigating the trimer phase by observing an identical splitting of a surface-derived feature around  $\bar{M}$  (Fig. 3.11 and [79]). The authors attributed this interesting surface state to Bi intra-trimer bonds but found no evidence to support the SO scenario by Kinoshita et al. An ARPES investigation of the monomer phase reported three prominent surface-derived bands without any sign of splitting [80]. All studies confirmed the semiconducting character of the two phases by observing no surface or bulk feature crossing the Fermi level.

### 3.2.3 Bi/Si(111): Silicon surface with giant spin splitting (full text published at Phys. Rev. Lett. 103, 046803 (2009))

According to the above findings, the Si(111)-Bi trimer phase is an ideal candidate for further investigations of sizeable RB effects on semiconducting surfaces and interfaces. In collaboration with the group of K. Kern (MPI-Stuttgart), we performed an extensive experimental study of the electronic properties of the system. This work is supported by spin-resolved band structure calculations performed by the research team of Dr. J. Henk (MPI-Halle). The combined studied has been recently published [51], and a summary of the results will be given in the following paragraphs.

An n-doped Si(111) substrate was cleaned by direct current annealing at 1100°C and cooled down slowly to 800°C until a sharp  $7 \times 7$  LEED pattern was observed. 1ML of Bi was deposited at a warm substrate (470°C) using electron beam assisted evaporation. A sharp  $\sqrt{3} \times \sqrt{3}$  LEED pattern revealed the uniformity and atomic order of the reconstruction. Quantitative LEED measurements and STM topographic imaging were used to discriminate between the monomer and trimer phases. For the LEED studies we used as a reference the calculations by Wan et al. [152] and measured the integrated intensity of the (10) and (01) spots. Fig. 3.12 presents the intensity profiles for the two reconstructions.

Long-range ARPES band structure maps are presented in Figs. 3.13 (a) and (b). Three surface-derived features ( $S_1$ ,  $S_2$  and  $S_3$ ) are observed along both directions.  $S_1$  is the counterpart of the split-state observed by earlier ARPES studies and appears as a parabolic band with negative effective mass and a band maximum located at about  $-1.3\text{eV}$  at the  $\bar{M}$  point. Along the  $\bar{\Gamma}\bar{K}\bar{M}$  direction no splitting of the state is observed revealing a strongly anisotropic band topology. The whole band structure appears shifted to higher binding energies in comparison to previous ARPES studies (for

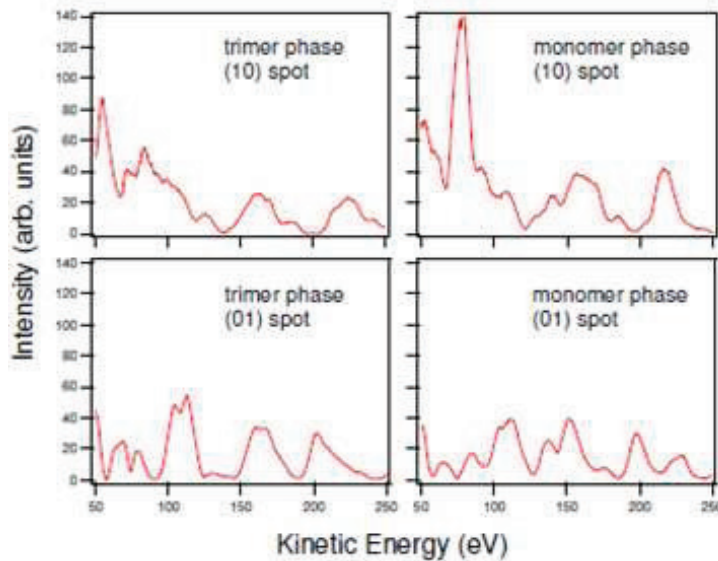


**Figure 3.12** — Comparison of the intensity profiles acquired by quantitative LEED for the trimer (left) and monomer (right) Si(111)-Bi  $\sqrt{3} \times \sqrt{3}$  phases. The corresponding integrated intensities are shown as a function of the electron energy for the (10) and (01) spots. [51]

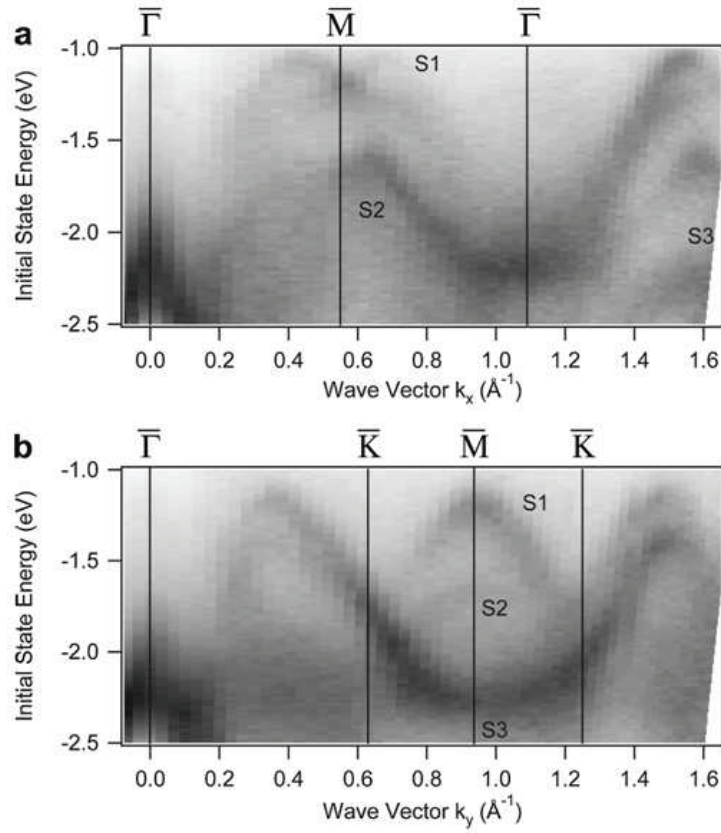


**Figure 3.13** — Electronic band dispersion along the high-symmetry directions of the  $\sqrt{3} \times \sqrt{3}$  SBZ. ARPES images have been acquired with a photon energy of 21.2eV, while the sample was kept at 90K.  $S_1$  exhibits a splitting around  $\bar{M}$  in panel (a). [51]

example Fig. 3.11). This is due to band bending arising from the highly-doped Si(111) substrate [60].

Fig. 3.14 is a close-up of the band topology around the  $\bar{M}$  point. If we assume a RB-type splitting in Fig. 3.14 (a), we can then extract an effective mass  $m^* = 0.7m_e$ , the momentum offset  $k_0 = 0.126\text{\AA}^{-1}$  and the Rashba energy  $E_R = 140\text{meV}$ . One can then calculate a Rashba parameter  $\alpha_R$  equal to  $1.37\text{eV \AA}$ . No splitting can be experimentally resolved along the  $\bar{K}\bar{M}\bar{K}$  direction. These numbers are of the same order of magnitude as the corresponding parameters for the metallic BiAg<sub>2</sub>/Ag(111) surface alloy (Table 2.1). Using Eq. (2.31), we can calculate that a phase shift of the spin precession angle  $\Delta\theta = \pi$  can be obtained after a length  $L$  of only 1.3nm. This is a great improvement in comparison to the value of 400nm which has been estimated for InGaAs/InAlAs heterostructures. Moreover, the energy separation of the spin-split counterparts in Fig. 3.14 (a) is larger than the lifetime broadening (220meV vs. 190meV), and thus it may allow distinguishing the extrinsic and intrinsic spin Hall effects. These experimental findings reveal the large potential of the system for spintronics applications and the need for theoretical confirmation.

To support our interpretation for the observed splitting, spin-resolved first-principles band structure calculations were performed. The surface geometry of the trimer structure is determined from first-principles using the Vienna ab initio simulation package (VASP). The Bi trimers (milkstool



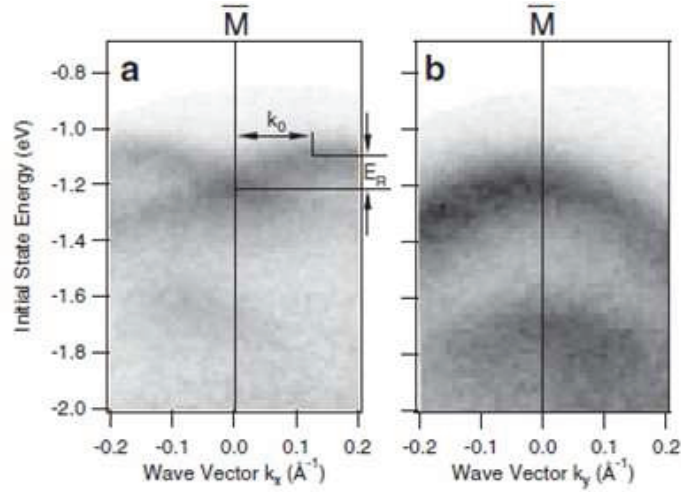


**Figure 3.14** — A close-up of the electronic band dispersion around the  $\bar{M}$  point of the  $\sqrt{3} \times \sqrt{3}$  SBZ. The experimental results along  $\bar{\Gamma}\bar{M}\bar{\Gamma}$  (a) and  $\bar{K}\bar{M}\bar{K}$  (b) reveal the anisotropy of the splitting and the band topology. [51]

structure) are relaxed outward by 13% from the ideal positions (100% corresponds to the Si bulk interlayer distances, lattice constant  $5.403\text{\AA}$ ). The subsurface relaxations are small ( $< 0.5\%$ ) and neglected in the Korringa-Kohn-Rostocker (KKR) calculations. The in-plane displacement of the Bi-trimer atoms  $\delta$  is 0.3 with  $\delta = 0$  indicating Bi atoms on top of the first layer Si atoms and  $\delta = 1$  coinciding Bi-trimer atoms on  $T_4$  sites. This value is similar to the one predicted by structural studies [152, 151, 87]. The subsequent KKR and relativistic layer-KKR calculations use the structural data from VASP as input. The spectral density  $n_{\pm}(E, \mathbf{k}_{\parallel})$  is obtained from the imaginary part of the site-dependent Green function. Resolved with respect to spin orientation (index  $\pm$ ) and angular momentum, it allows a detailed analysis of the electronic structure. The difference  $n_{+}(E, \mathbf{k}_{\parallel}) - n_{-}(E, \mathbf{k}_{\parallel})$  reveals the characteristic spin splitting of RB-split bands.

The calculation results are presented in Fig. 3.15 for the two high-symmetry directions. The intensity scale shows the total spectral density ( $n_{+}(E, \mathbf{k}_{\parallel}) + n_{-}(E, \mathbf{k}_{\parallel})$ ) of the states multiplied by the sign of the spin polarization  $\text{sgn}(n_{+}(E, \mathbf{k}_{\parallel}) - n_{-}(E, \mathbf{k}_{\parallel}))$ ; i.e. blue and red colors correspond to opposite spin polarizations. The Fermi level of the maps has been fitted to the experimental findings. As observed in Fig. 3.15 (a), the  $S_1$  splitting around  $\bar{M}$  is confirmed. The two branches show opposite spin polarization, verifying that the giant splitting has a relativistic origin. In complete agreement with the experimental data, Fig. 3.15 (b) reveals that there is a negligible splitting along  $\bar{K}\bar{M}\bar{K}$ . The calculation results predict that about 83% of the spin-split bands at the  $\bar{M}$  point are localized in the Bi adlayer and about 16% in the first Si layer, thus confirming the surface origin of the  $S_1$  state.

The giant spin-splitting in the Bi/Si(111) surface alloy is related to the additional inversion symmetry breaking in the plane of the surface. As presented in Fig. 3.11, in both monomer and trimer phases the threefold symmetry of the Si(111) substrate breaks the in-plane mirror symmetry with respect to  $\sigma_{v2}$ . Nevertheless, if one considers only the Bi layer, the trimer formation enhances



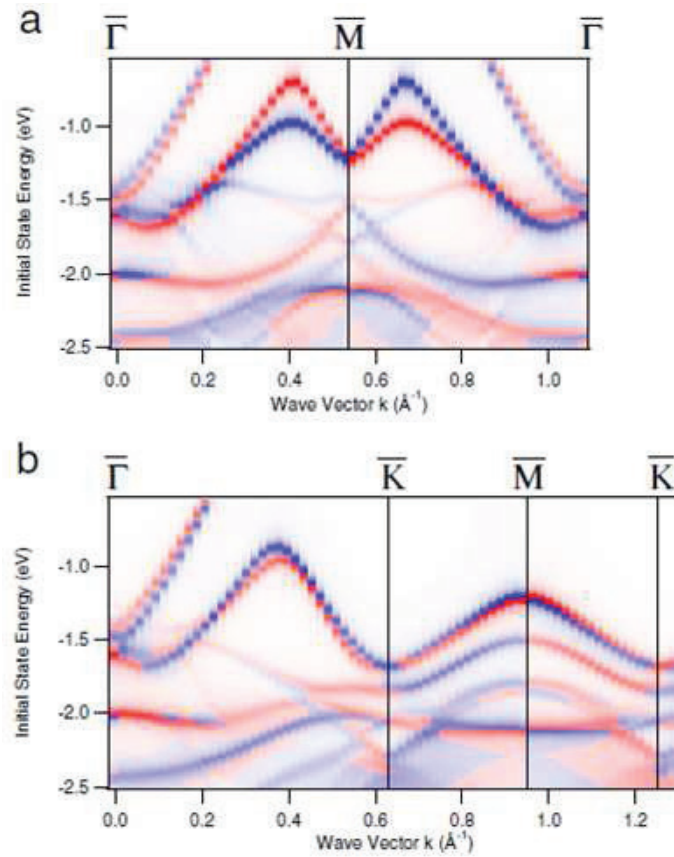


**Figure 3.15** — Calculated band dispersion along the high-symmetry directions of the  $\sqrt{3} \times \sqrt{3}$  SBZ. Blue and red colors represent the two opposite spin polarizations. Panel (a) reproduces the experimental splitting around  $\bar{M}$  and confirms that the latter is related to the RB effect. [51]

the symmetry breaking, which may lead to an increase of the in-plane potential gradient and the RB splitting. The strongly anisotropic topology around  $\bar{M}$  may be attributed to the lower symmetry of wavevectors  $\mathbf{k}_{\parallel}$  within  $\bar{\Gamma}\bar{K}\bar{M}$  or perpendicular ( $\bar{\Gamma}\bar{M}$ ) to a mirror plane of the system. Calculations with larger intra-trimer distances indicate an even smaller splitting along  $\bar{\Gamma}\bar{K}\bar{M}$ .

### 3.2.4 Bi/Si(111): A combined angle- and spin-resolved photoemission study

A parallel study, led by Prof. K. Sakamoto confirmed the major findings of our work [132]. The authors claimed a spin splitting not only for  $S_1$  ( $\alpha_R \sim 2.3\text{eV \AA}$ ), but also for  $S_2$  ( $\alpha_R \sim 1.7\text{eV \AA}$ ) and  $S_3$  ( $\alpha_R \sim 1.5\text{eV \AA}$ ) (Fig. 3.16). Their work is supported by first-principles calculations and spin-resolved ARPES measurements. Using experimental CE maps and group theory arguments, Sakamoto et al. reported a vortical spin arrangement around  $\bar{K}$  despite the lack of time-reversal symmetry around this point (Fig. 3.16). However, the combination of the vortical spin structures around the  $\bar{\Gamma}$  and  $\bar{K}$  points gives rise to a peculiar non-vortical splitting around  $\bar{M}$ , demonstrating that its time-reversal symmetry is not a sufficient condition to obtain a normal RB splitting. This study exemplifies the role of the 2D spatial symmetry in determining the effects of the RB coupling. The non-vorticity around the  $\bar{M}$  point has been confirmed by a first-principles study [105].

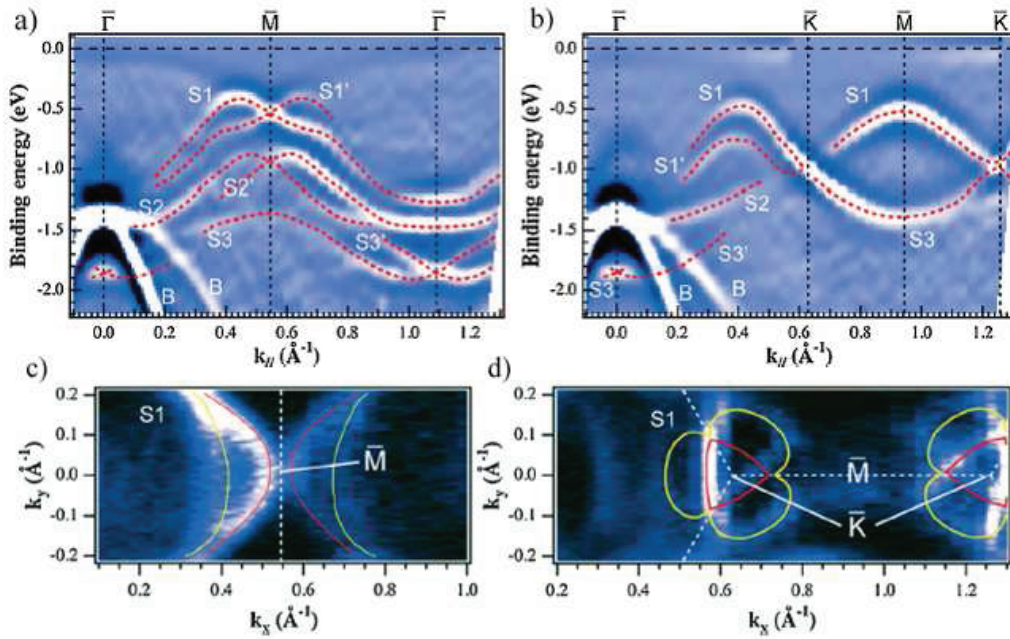


**Figure 3.16** — (a), (b) Experimental band dispersion along the high-symmetry directions of the  $\sqrt{3} \times \sqrt{3}$  SBZ. The dashed curves are obtained by tracing the corresponding features of the energy distribution curves. (c) A CE map at  $E_B = 0.45\text{eV}$  evidences spin-polarized contours which do not close around  $\bar{M}$ . This is an indication of a non-vortical spin structure. (d) A CE map at  $E_B = 0.85\text{eV}$  evidences a vortical (albeit distorted) spin arrangement around  $\bar{K}$ . Dashed lines represent the borders of the  $\sqrt{3} \times \sqrt{3}$  SBZ. [132]

The previous studies have either addressed the origin of giant splitting qualitatively [51] or stressed the role of the spatial symmetry in determining the spin arrangement [132]. There is, however, no direct link between the surface symmetry and the magnitude of the splitting. This issue is the main motivation of the following paper.

### 3.2.5 Band structure scenario for the giant spin-orbit splitting observed at the Bi/Si(111) interface (Phys. Rev. B 82, 085440)

*The Bi/Si(111) ( $\sqrt{3} \times \sqrt{3}$ )R30° trimer phase offers a prime example of a giant spin-orbit splitting of the electronic states at the interface with a semiconducting substrate. We have performed a detailed angle-resolved photoemission (ARPES) study to clarify the complex topology of the hybrid interface bands. The analysis of the ARPES data, guided by a model tight-binding calculation, reveals a previously unexplored mechanism at the origin of the giant spin-orbit splitting, which relies primarily on the underlying band structure. We anticipate that other similar interfaces characterized by trimer structures could also exhibit a large effect.*

The normal spin degeneracy of the electronic states of non-magnetic solids is lifted by the spin-orbit (SO) interaction in crystals lacking an inversion center (Dresselhaus effect) [41, 83]. A similar effect was predicted theoretically by Rashba and Bychkov (RB) for a two-dimensional electron gas (2DEG) at a surface or an interface which exhibits a structural surface asymmetry (SSA) [28]. Although the model was originally motivated by semiconductor heterojunctions, split bands were first observed by angle-resolved photoemission spectroscopy (ARPES) on metal surfaces [89, 129, 64, 122, 85, 59, 93]. Like its atomic counterpart, the RB effect has a relativistic origin, namely the coupling of the spin to the magnetic field which appears in the rest frame of the electron. In the free-electron limit considered by RB, the parabolic dispersion is split, as in Fig. 3.17, into two branches of opposite spin:

$$E^{\pm}(k) = \frac{\hbar^2 k^2}{2m^*} \pm \alpha_R k, \quad (3.2)$$

where  $k$  is the magnitude of the electron momentum in the plane of the surface, and  $m^*$  the effective mass. The Rashba parameter  $\alpha_R$  is proportional to the gradient of the surface electric potential, and defines the strength of the RB effect. The SO-splitting of the two branches can be quantified by their momentum offset  $2k_0 = 2\alpha_R m^* / \hbar^2$  or, equivalently, by the Rashba energy

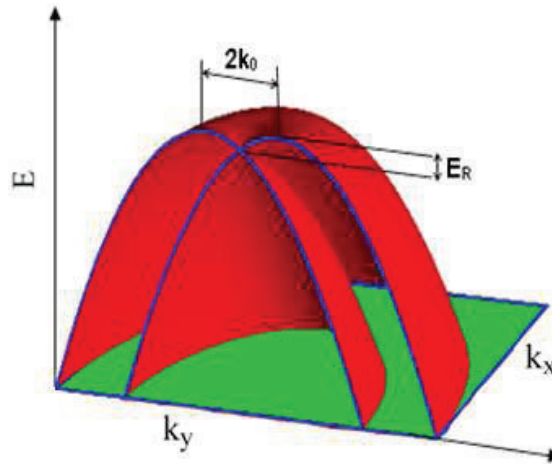


**Figure 3.17** — Schematics of the RB SO split bands for a 2D free electron gas.

$E_R = \hbar^2 k_0^2 / (2m^*)$ , the difference between the band minimum ( $m^* > 0$ ) or maximum ( $m^* < 0$ ) and the crossing point of the two branches at  $k = 0$ . In a more realistic approach, the band splitting depends not only on the surface potential gradient, but also on the atomic SO parameter, and on the asymmetry of the electron wavefunctions [117, 23, 105, 93].

Interest in the RB effect has been revamped by observations of a *giant* SO-splitting in surface alloys formed by a high-Z element – Bi or Pb – at the Ag(111) surface [7, 94]. The unusual strength of the effect has prompted a reassessment of the various factors contributing to the effect. It has been suggested that additional components of the surface potential gradient *within* the surface, reflecting the anisotropic charge distribution, are probably important [119]. Independent studies have stressed structural aspects, namely the role of relaxation and buckling of the topmost layer in defining the hybrid states [22].

Metallic surface alloys with a giant SO splitting are potentially interesting for spintronics applications. The present challenge is to make them compatible with semiconductor technology [36, 84]. There has been encouraging progress in this direction, and several attempts have been made to grow, on Si(111) substrates, thin buffer layers which support SO-split bands at their surface [48, 63, 55, 40, 45]. Recently, a giant spin-splitting with no buffer layers was demonstrated for the isostructural Bi/Si(111) [51, 132] and Bi/Ge(111) [54] interfaces. In the same line, metallic spin-split surface states were observed in the related Pb/Ge(111) system [155]. In all cases, the electronic structure of these interfaces is more complex than that predicted by the simple RB model. Although first-principles calculations reproduce the experimental results, they suffer from a certain lack of transparency. This leaves room for a simpler but more direct approach which can help in the interpretation of the experimental data, and thus contribute to clarify the unconventional properties of the electronic states. This was the motivation of the present work, which compares the results of a detailed experimental band mapping of the Bi/Si(111) interface by ARPES, with simple models of the band structure in the presence of a RB-like interaction. In particular, a parametric tight-binding scheme provides a satisfactory qualitative description of the data, and suggests a possible new mechanism to achieve a large spin polarization, which is closely connected with a characteristic feature of the band structure of the interface.

## II. Experimental Details

The Si(111) substrate (Sb-doped, resistivity  $0.01\Omega\cdot\text{cm}$ ) was flashed at  $1200^\circ\text{C}$  by direct current injection, and then cooled slowly in order to obtain a sharp low-energy electron diffraction (LEED)  $(7\times 7)$  pattern. The  $(\sqrt{3}\times\sqrt{3})R30^\circ$  Bi/Si(111) interface was prepared by deposition of 1 monolayer (ML) of Bi from a calibrated EFM3 Omicron source on the the substrate at RT followed by a mild annealing. ARPES spectra were acquired at 70K and 21.2eV photon energy, with a PHOIBOS 150 SPECS Analyzer equipped with a monochromatized GammaData VUV 5000 high brightness source. The Fermi level position was determined from the Fermi edge of a polycrystalline Au sample.

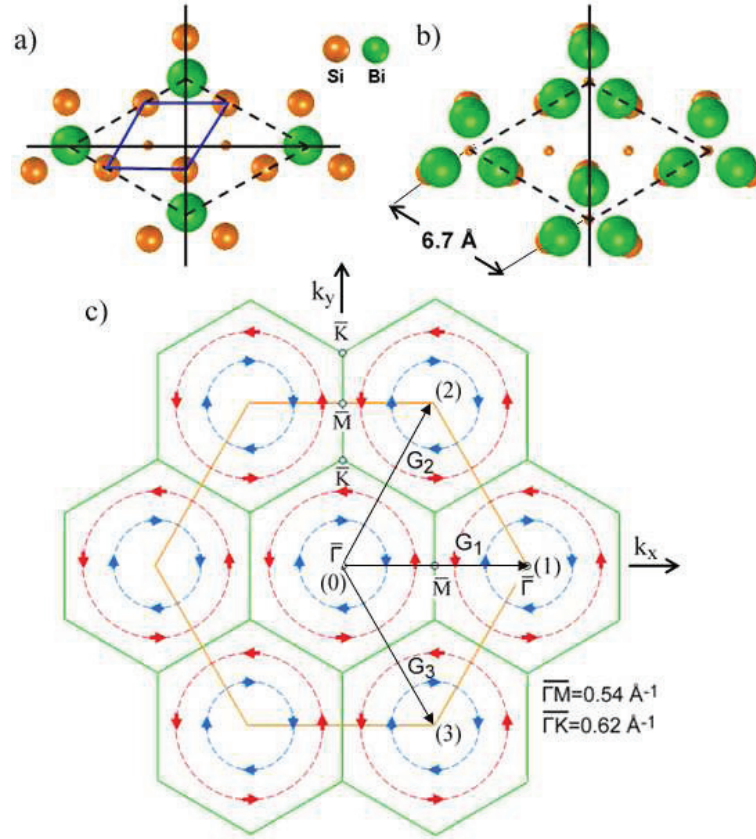


**Figure 3.18** — The structure of (a) the monomer ( $\alpha$ -) and (b) the trimer ( $\beta - \sqrt{3} \times \sqrt{3}$ ) $R30^\circ$  Bi/Si(111) phases. The size of the Si atoms indicates their distance from the surface. Solid (dashed) lines indicate the  $1 \times 1$  ( $\sqrt{3} \times \sqrt{3}$ ) primitive unit cell. The horizontal and vertical black lines follow the mirror planes of the overlayers. (c) The  $1 \times 1$  (large hexagon) and  $(\sqrt{3} \times \sqrt{3})R30^\circ$  (small hexagons) SBZs. The circles are constant-energy contours for RB paraboloids centered at each equivalent  $\bar{\Gamma}$  point of the latter, and the arrows indicate the spin polarization. The reciprocal lattice vectors  $\bar{G}_1$ ,  $\bar{G}_2$  and  $\bar{G}_3 = \bar{G}_1 - \bar{G}_2$  are those considered in the NFE model of subsections III (B) and (C).

### III. Results and Model Calculations

#### A. ARPES Measurements

The Bi/Si(111) interface exhibits two different structures with the same  $(\sqrt{3} \times \sqrt{3})R30^\circ$  Bi/Si(111) periodicity: a monomer structure ( $\alpha$ -phase) for a coverage of  $1/3\text{ML}$ , and a trimer structure ( $\beta$ -phase) for  $1\text{ML}$  coverage. They are illustrated in Fig. 3.18 (a) and (b). According to the widely accepted  $T_4$  model [107], both monomers and trimers are centered above the  $2^{\text{nd}}$  layer Si substrate atoms. Figure 2(c) shows the surface Brillouin zones (SBZ) of the unreconstructed Si(111) surface, and of the  $(\sqrt{3} \times \sqrt{3})R30^\circ$  superstructure. In the following we will always refer to the latter. The  $\alpha$  and  $\beta$  phases have quite different band structures, and can be easily distinguished. This is illustrated in Fig. 3.19, where (second derivative) ARPES intensity maps of the two phases are compared around the  $\bar{M}$  point. In agreement with previous studies, the  $\alpha$ -phase shows a rather flat surface state with a broad minimum at  $\bar{M}$  [80], while the  $\beta$ -phase shows two symmetrically dispersing fea-



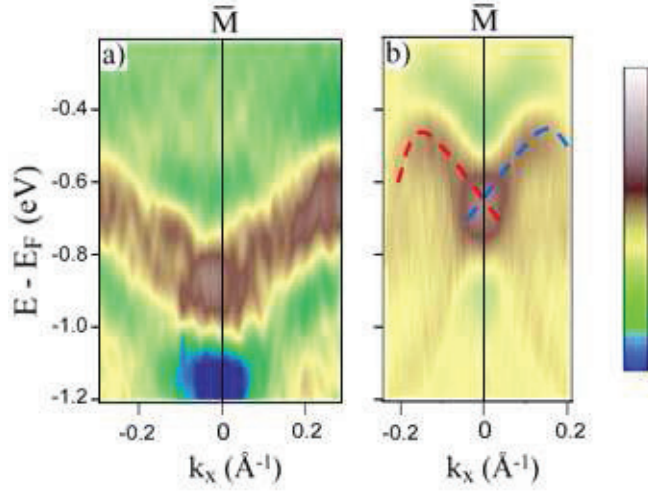


**Figure 3.19** — 2<sup>nd</sup> derivative ARPES intensity map along the  $\bar{\Gamma}\bar{M}\bar{\Gamma}$  direction for the monomer (a) and the trimer (b) phases of Bi/Si(111).

tures crossing at  $\bar{M}$  [81, 79]. In the rest of the paper we only consider the trimer  $\beta$ -phase, which is the most interesting in the present context. The system has a threefold rotation axis, and three mirror planes perpendicular to the surface. One of these mirror planes is parallel to the  $[11\bar{2}]$  direction, and also to the  $\bar{\Gamma}\bar{K}\bar{M}$  direction of the SBZ ( $k_y$  axis in Fig. 3.18 (c)). The other mirror planes are rotated by  $120^\circ$  around the  $z$  axis. The overlayer symmetry is identical to the one of the substrate and corresponds to the plane group  $p31m$ . The characteristic band crossing at  $\bar{M}$  is the signature of a peculiar RB-type SO-splitting with a momentum offset  $k_0$  of  $0.126\text{\AA}^{-1}$  and a Rashba energy of  $140\text{meV}$  [51, 132]. The large splitting has been previously associated with the inversion asymmetry induced by the trimers. We will see later that a somewhat different interpretation is possible.

The ARPES intensity maps of Fig. 3.20 illustrate the dispersion of three surface states – labelled  $S_1$  to  $S_3$  as in Ref. [132] –. All three states are predicted to be spin-polarized [132].  $S_1$  exhibits a large splitting around  $\bar{M}$ , as already shown by Fig. 3.19, and a peculiar anisotropic dispersion around that point. The experimental dispersion along the  $\bar{\Gamma}\bar{M}\bar{\Gamma}$  line (Fig. 3.20 (a)) shows a hint of the two branches predicted by theory [51, 132], which split away from the crossing point at  $\bar{M}$ . The dispersion is highlighted by dashed guides to the eye, which are consistent with the results of Synchrotron Radiation (SR) studies, where the individual  $S_1$  components could be more clearly resolved along  $\bar{\Gamma}\bar{M}\bar{\Gamma}$ . The two  $S_1$  branches merge again approaching the  $\bar{\Gamma}$  point, where they cannot be resolved from  $S_2$ . The energy splitting of the two branches increases away from the  $\bar{\Gamma}\bar{M}\bar{\Gamma}$  high-symmetry line, as shown by Fig. 3.20 (b) which shows the dispersion along the parallel cut (b) of Fig. 3.20 (d) (i.e.  $k_y \neq 0$ ). In support of our previous discussion on the experimental results of Figs. 3.20 (a) and (b), the  $S_1$  split branches are easily identified in Fig. 3.20 (c), which shows a cut parallel to the  $\bar{K}\bar{M}\bar{K}$  line. Along this line the intensity of  $S_2$  is very small due to ARPES matrix elements. The images of Fig. 3.20 (a) and (b) intersect the perpendicular cut (c) along respectively the vertical black dashed and the red solid lines.

Figure 3.21 illustrates the unusual topology of surface band  $S_1$  around the  $\bar{M}$  point, in a region



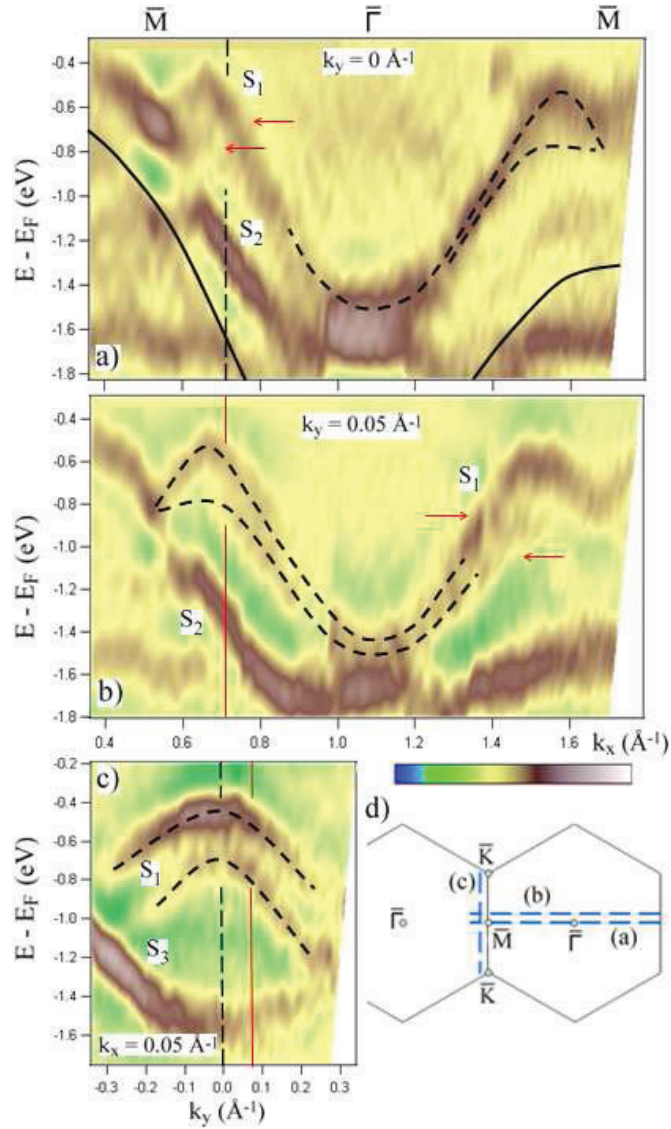


**Figure 3.20** — (a) to (c) Second-derivative ARPES intensity maps showing the band structure along the  $k$ -space cuts (a) to (c) of panel (d). The dashed curves and arrows are guides to the eye, inspired by results obtained in Refs. [51, 132], and highlight the dispersion of the  $S_1$  split branches. The thick solid line marks the edge of the projected Si bulk gap. Images (a) and (b) intersect image (c) respectively along the vertical dashed and solid lines.

of  $k$ -space where it is well separated from other surface or bulk-derived features. Panels 1 to 4 of Fig. 3.21 (a) show constant-energy (CE) cuts taken at increasing binding energies between 0.53 and 1.02 eV, corresponding to the horizontal dashed lines in the intensity maps along the  $\overline{KMK}$  and  $\overline{\Gamma M\Gamma}$  directions of panels (b) and (c). Starting at the highest binding energy, the CE maps show two intersections along  $\overline{KMK}$ , symmetrically located with respect to  $\overline{M}$ . They get closer at lower binding energy, following the negative-mass dispersion of Fig. 3.21 (b). The two intersections finally merge at  $\overline{M}$  for  $E_B \sim 0.68$  eV. This is the maximum of the dispersion along  $\overline{KMK}$ , and the crossing point of the two SO-split branches along the perpendicular  $\overline{\Gamma M\Gamma}$  direction. Panel 1, taken

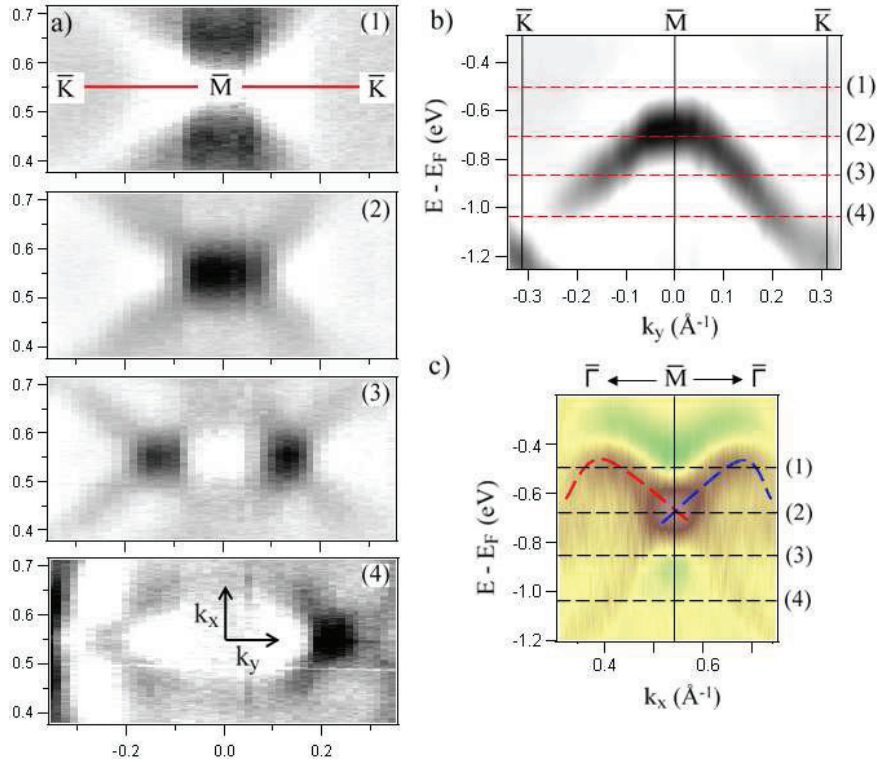


**Figure 3.21** — (a) Experimental CE maps around  $\bar{M}$ . The corresponding binding energies are 0.53, 0.68, 0.84, and 1.02 eV for panels (1) to (4). They are indicated by horizontal dashed lines in the intensity maps of panels (b) and (c), taken along the  $\bar{K}\bar{M}\bar{K}$  and  $\bar{\Gamma}\bar{M}\bar{\Gamma}$  directions. In the gray-scale plots, highest intensity is black.

above this energy, indeed shows non-intersecting CE contours.

The data of Fig. 3.21 reveals that the topology of  $S_1$  is quite different from that of Fig. 3.17, predicted by the usual Rashba model for a free-electron band centered at the  $\bar{\Gamma}$  point. The degeneracy of the SO-split branches at  $\bar{M}$  is required by a combination of time-reversal and translational symmetry. On the other hand, the line of (near) spin degeneracy of Fig. 3.21 (b) finds no correspondence in the simple Rashba model. The experimentally observed large difference of the energy splitting along the two high-symmetry directions is well captured by first-principles calculations [51, 132].

### B. An Isotropic Nearly-Free Electron Model

We will now attempt a comparison of the experimental data using simple theoretical models, to gain further insight in the unusual dispersion of the SO-split bands. The minimal requirement for any model is that it should include both the Rashba-type interaction and translational invariance. The simplest approach satisfying this condition is an isotropic nearly-free electron (NFE) model. This model is schematically illustrated in Fig. 3.18 (c). RB paraboloids ( $m^* > 0$ ) are centered at all equivalent  $\bar{\Gamma}$  points, and the CE lines are concentric circles representing the inner and outer SO-split branches. The spins exhibit a vortical structure around the  $\bar{\Gamma}$  points. Two paraboloids centered at

two adjacent SBZ intersect in the common  $\overline{\text{KMK}}$  Bragg plane along two parabolas, one at lower energy for the outer SO branch, and a second at higher energy for the inner.

The Rashba hamiltonian for a free-electron is [28]:

$$H_{\text{RB}}(\mathbf{k}) = \alpha_R(\boldsymbol{\sigma} \times \mathbf{k})_z \quad , \quad (3.3)$$

where  $\boldsymbol{\sigma}$  is the vector of Pauli matrices. In a representation where the basis states are  $|\mathbf{k} \uparrow\rangle$ ,  $|\mathbf{k} \downarrow\rangle$ , and spin projections refer to the  $z$  axis, the corresponding matrix is:

$$H_{\text{RB}}(\mathbf{k}) = \begin{pmatrix} \hbar^2 k^2/2m & \alpha_R(k_y + ik_x) \\ \alpha_R(k_y - ik_x) & \hbar^2 k^2/2m \end{pmatrix}. \quad (3.4)$$

Diagonalization of this hamiltonian generates SO-split paraboloids centered at  $\overline{\Gamma}$  as in Fig. 3.16. The corresponding ‘spin-up’ and ‘spin-down’ eigenstates refer to a quantization axis  $\mathbf{e}_\theta = \mathbf{e}_z \times \mathbf{k}/k$ , which is always perpendicular to  $\mathbf{k}$ , i.e. tangential to the constant-energy circles. These states are therefore 100% in-plane polarized, with a purely tangential spin polarization  $\mathbf{P}$  – opposite on the two branches – rotating around  $\overline{\Gamma}$ . This is easily generalized to include the lattice periodicity. Since we are mainly interested in the band structure near  $E_F$  around the  $\overline{\text{M}}$  point, it is a good approximation, to consider only the first SBZ and three adjacent zones centered at the lattice vectors  $\mathbf{G}_1 = (1, 0)$ ,  $\mathbf{G}_2 = (0, 1)$  and  $\mathbf{G}_3 = \mathbf{G}_1 - \mathbf{G}_2$ , as in Fig. 3.18 (c). The basis vectors, again referred to the  $z$  axis, are  $|\mathbf{k} \uparrow\rangle$ ,  $|\mathbf{k} \downarrow\rangle$ ,  $|(\mathbf{k} + \mathbf{G}_1) \uparrow\rangle$ ,  $|(\mathbf{k} + \mathbf{G}_1) \downarrow\rangle$ ,  $|(\mathbf{k} + \mathbf{G}_2) \uparrow\rangle$ ,  $|(\mathbf{k} + \mathbf{G}_2) \downarrow\rangle$ ,  $|(\mathbf{k} + \mathbf{G}_3) \uparrow\rangle$ ,  $|(\mathbf{k} + \mathbf{G}_3) \downarrow\rangle$ . The truncated NFE hamiltonian matrix is then:

$$H_{\text{NFE}} = \begin{pmatrix} H_{\text{RB}}(\mathbf{k}) & V_{01} & V_{02} & V_{03} \\ V_{01}^* & H_{\text{RB}}(\mathbf{k} + \mathbf{G}_1) & V_{12} & V_{13} \\ V_{02}^* & V_{12}^* & H_{\text{RB}}(\mathbf{k} + \mathbf{G}_2) & V_{23} \\ V_{03}^* & V_{13}^* & V_{23}^* & H_{\text{RB}}(\mathbf{k} + \mathbf{G}_3) \end{pmatrix}. \quad (3.5)$$

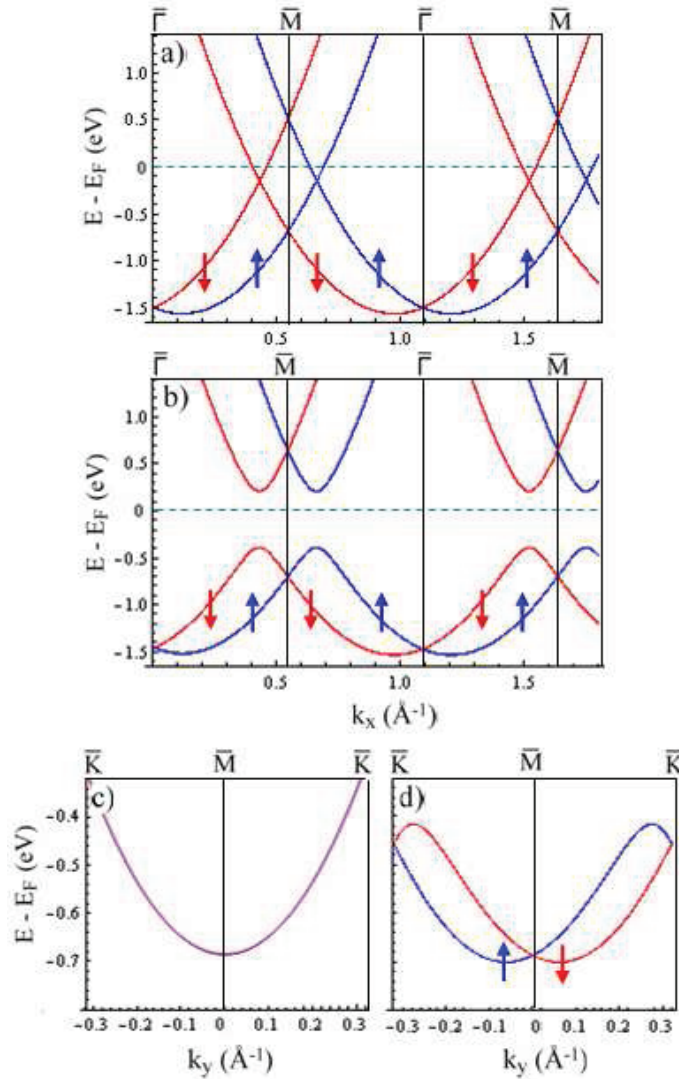
The diagonal  $2 \times 2$  building blocks now generate SO-split paraboloids centered at  $\overline{\Gamma}$ , and at  $\mathbf{G}_1$ ,  $\mathbf{G}_2$  and  $\mathbf{G}_3$ . The off-diagonal  $2 \times 2$  blocks describe the interaction between states of equal spin on the various paraboloids [39]. The hybridization strength is, as usual, the corresponding Fourier component of the crystal potential  $V(r)$  defined by:

$$V(r) = \sum_i V_{G_i} e^{i\mathbf{G}_i \cdot \mathbf{r}} \quad . \quad (3.6)$$

For instance:

$$V_{01} = \begin{pmatrix} V_{G_1} & 0 \\ 0 & V_{G_1} \end{pmatrix} \quad . \quad (3.7)$$

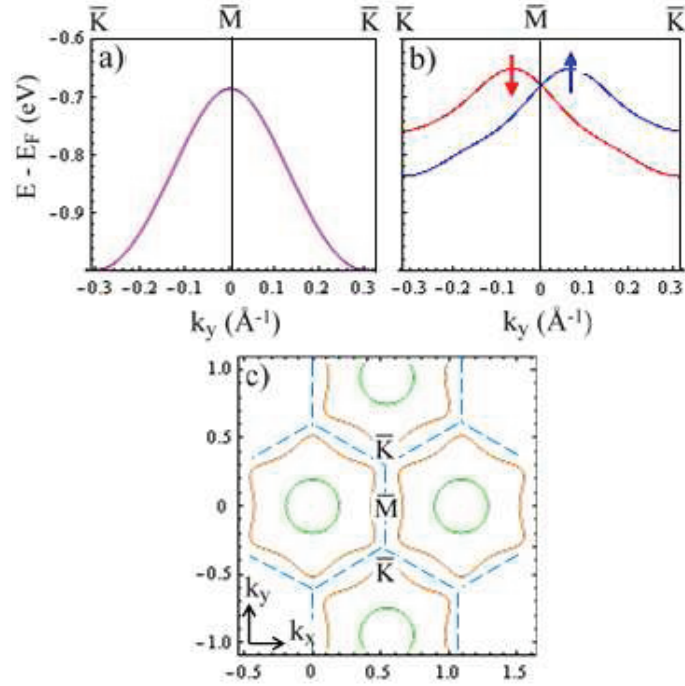
It is easy to show that (3.7) is equivalent to an interaction of the form  $V(\mathbf{k}, \mathbf{k} + \mathbf{G}_1) = V_{G_1} \cos(\delta/2)$ , where  $\delta$  is the angle between the two polarization vectors. In our case all hybridization terms are equal:  $V_{G_i} = V_G$ , and  $H_{\text{NFE}}$  contains only the two parameters  $\alpha_R$  and  $V_G$ . The



**Figure 3.22** — (a), (b) Band dispersion of the isotropic NFE model along the  $\bar{\Gamma}\bar{M}\bar{\Gamma}$  for  $|V_G| = 0$  and  $|V_G| = 0.3$  eV. Arrows indicate the opposite (in-plane) spin polarization of the two branches. (c), (d) Same for the  $\bar{K}\bar{M}\bar{K}$  high-symmetry direction. The two spin states are degenerate along the SBZ boundary for  $|V_G| = 0$ . Notice the different scales in (a), (b) and (c), (d).

binding energy of the paraboloids at  $\bar{\Gamma}$ , or equivalently the Fermi level position, are adjusted to fit the experimental data of Fig. 3.20.

Figure 3.22 (a) illustrates the predictions of the NFE model along the  $\bar{\Gamma}\bar{M}\bar{\Gamma}$  direction, in the limit  $|V_G| = 0$ . The outer branches cross at the  $\bar{M}$  point, with opposite spin polarization. Along the perpendicular  $\bar{K}\bar{M}\bar{K}$  direction (Fig. 3.22 (c)), their intersection is a parabola dispersing upwards from  $\bar{M}$ . The inner branches of the paraboloids similarly cross above  $E_F$ . The model yields a constant momentum separation between the SO-split branches of each paraboloid, and does not capture the experimentally observed  $k$ -dependent splitting. Moreover, the sign of the dispersion along the SBZ boundary is opposite to that of Fig. 3.21 (b), and the opposite spin states are strictly degenerate, for any value of  $\alpha_R$ .



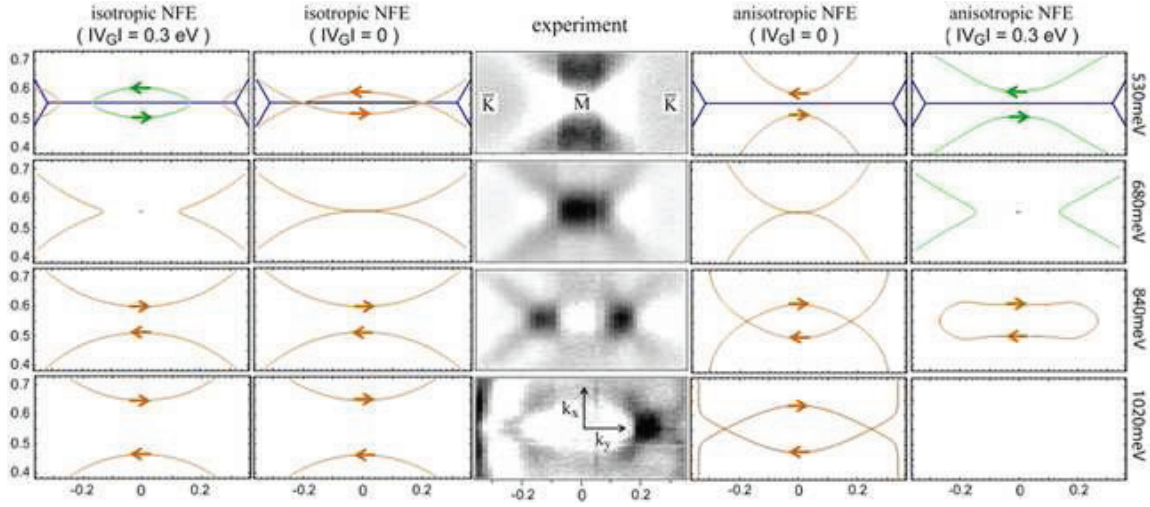
**Figure 3.23** — (a), (b) Band dispersion of the anisotropic NFE model along the  $\overline{KMK}$  SBZ boundary for  $|V_G| = 0$  and  $|V_G| = 0.3$  eV. (c) Constant energy contours for a binding energy of 1.1 eV showing the anisotropic shape of the spin-split states. Green (light gray) and brown (dark gray) colors indicate positive and negative values of tangential spin polarization.

Figure 3.22 (b) shows that the main effect of a finite lattice potential is the opening of energy gaps at the crossing of bands with parallel spins, i.e. at the crossing of the outer branch of one paraboloid with the inner branch of the paraboloid centered at an adjacent SBZ. No gap opens when either the outer or the inner branches cross at the  $\overline{M}$  point, because their spins are opposite there. This is consistent with the requirements of time-reversal symmetry. At the other crossing points along the SBZ boundary the spins are not strictly opposite, but they are nonetheless rather antiparallel, and the hybridization is therefore small. Therefore, as shown in Fig. 3.22 (d), the two spin states are not degenerate as in the case  $|V_G| = 0$ , but their energy separation is small along this direction. The model again yields a positive effective mass  $\overline{KMK}$ , in contrast with the experiment. The momentum splitting along  $\overline{KMK}$  scales with  $|V_G|$  and  $\alpha^{1/2}$ , confirming the unconventional character of the underlying mechanism. It should also be noted that although the  $\overline{M}$  spin degeneracy is fundamental, the degeneracy predicted at  $\overline{K}$  is accidental. It is lifted when further reciprocal lattice points are included.

### C. An Anisotropic Nearly-Free Electron Model

The positive effective mass along the Bragg planes predicted in Fig. 3.22 (c), (d) is a direct consequence of the simple circular CE contours of the isotropic NFE model. More complex contours are however possible in anisotropic 2D systems. Blossom-like contours have been predicted for Rashba systems [119, 7], and experimentally observed for the BiAg<sub>2</sub> [51] and SbAg<sub>2</sub> [102] surface alloys.





**Figure 3.24** — Constant energy maps as measured by ARPES (middle panel) and according to the predictions of the isotropic (left panels) and the anisotropic (right panels) NFE models described in the text. Both models are presented for  $|V_G| = 0$  and  $|V_G| = 0.3$  eV. Green (light gray) and brown (dark gray) colors indicate positive and negative values of tangential spin polarization. The arrows are a sketch of the predicted in-plane projection of the spin polarization around the  $\overline{M}$  point.

Concave CE contours are a generic effect of an in-plane anisotropy of the potential and they are not limited to surface alloys. For example, a 2D Dirac fermion state at the surface of the topological insulator  $\text{Bi}_2\text{Te}_3$  has been shown to exhibit a snow-flake-like Fermi surface [49].

$\mathbf{k} \cdot \mathbf{p}$  theory has been used to calculate higher-order terms in the effective Hamiltonian of a topological insulator with  $R3\overline{m}$  symmetry [49]. Following these results we introduce an anisotropy in  $H_{\text{NFE}}(k)$  as:

$$H_{\text{an}}(k) = H_{\text{NFE}}(k) + H'(k) , \quad (3.8)$$

with

$$H'(k) = \frac{c}{2}((k_y + ik_x)^3 + (k_y - ik_x)^3)\sigma_z . \quad (3.9)$$

This yields:

$$E^\pm(k) = \frac{\hbar^2 k^2}{2m^*} \pm \sqrt{(\alpha_R)^2 k^2 + c^2 k^6 \cos^2(3\theta)} , \quad (3.10)$$

where  $c$  is an anisotropy parameter, and  $\theta$  is the in-plane angle from the  $\overline{\Gamma M}$  direction. For small values of  $c$  this expression reduces to the free-electron case with RB splitting (Eq. (3.2)). The in-plane asymmetry could be self-consistently included starting from Eq. (3.6), but Eq. (3.8) provides a minimal alternative model with the single parameter  $c$ . The resulting band dispersion agrees well that of the anisotropic 2DEG proposed by Premper et al. [119]. It is shown in Fig. 3.23 (a) for  $|V_G| = 0$ , and (b) for  $|V_G| = 0.3$  eV. The corresponding parameters are summarized in the Appendix. The model correctly predicts a negative effective mass along  $\overline{KMK}$ . Again, the crystal potential induces a weak RB splitting. The dispersion along  $\overline{\Gamma M\Gamma}$  is essentially identical to the isotropic case, and is not shown. The CE contours evolve continuously with increasing energy from circular to blossom-like, as in Fig. 3.23 (c). The sixfold symmetry is the result of the threefold rotational symmetry and time-reversal. It should be noted that the spin polarization has only an



in-plane tangential component for an isotropic 2DEG, whereas a sizeable out-of-plane and a small radial component are present for the anisotropic case [119]. Figure 3.24 compares the experimental CE contours around  $\bar{M}$  with the predictions of the isotropic (left panels) and the anisotropic (right panels) NFE models. The latter describes reasonably well the data for  $|V_G| = 0$ , but fails to reproduce the dispersion (Fig. 3.22 (a)) due to the overestimation of the momentum splitting at  $k$ -points far from  $\bar{M}$ . A finite lattice potential does open an energy gap, but it perturbs the band structure and the agreement is completely spoiled by a finite lattice potential.

A closer examination of the CE contours reveals another subtler inaccuracy of the anisotropic NFE model. The spin polarization symmetry, determined by the mirror plane of the trimer configuration [1], is not in agreement with the tip orientation of the outer CE contour of Fig. 3.23 (c). This inconsistency is removed by the tight-binding model considered in the following subsection.

#### D. An Empirical Tight-Binding Model

The covalent character of the bonds and the semiconducting nature of the Bi-Si(111) interface suggest that local orbitals may be a better starting point. We have performed an empirical tight binding (TB) calculation which is able to reproduce the main experimental features. In order to limit the complexity of the calculation, the model considers a single orbital per atomic site with  $sp_z$  symmetry. While this is an approximation, we expect contributions from other orbital symmetries to be small in the energy range of interest. This is supported by recent results for the isostructural Bi-Ge(111) interface [54]. The primitive unit cell contains three Bi atoms, labelled a, b and c in Fig. 3.25. In the same figure the five inequivalent hopping terms are indicated by arrows. All the other terms can be generated by symmetry. The Si(111) substrate is only indirectly taken into account through the effective hopping parameters. A calculation of the transfer integrals is a non trivial computational task, which clearly goes beyond the scope of this work. Therefore we defined them in a purely phenomenological way, assuming an inverse power-law dependence of the distance  $d$  between two centers:  $V(d) = ad^{-b}$ . The prefactor  $a$  determines the bandwidths, while the exponent  $b$  determines details of the dispersion. There is obviously no angular dependence for  $sp_z$  states. The Bi-Bi distance within a single trimer was set to 2.6 Å, which is very close to literature values [152, 51]. In the actual calculation we included interactions up to 4<sup>th</sup> nearest neighbors. The required overall resemblance with the experimental dispersion significantly limits the acceptable parameter space. The chosen values are summarized in Table II of the Appendix.

Figure 3.26 illustrates the results of the TB model before the inclusion of a RB interaction. The calculation yields three bands, corresponding to the three orbitals per unit cell. The two higher lying states are shown for the  $\bar{\Gamma}\bar{M}\bar{\Gamma}$  (a) and  $\bar{\Gamma}\bar{K}\bar{M}$  (b) directions in Fig. 3.26. They can be associated to the experimental features of Fig. 3.20. The model correctly predicts a double degeneracy at the  $\bar{\Gamma}$  and  $\bar{K}$  points, independent of the parameter values. A double degeneracy is imposed by the  $C_{3v}$  symmetry of these points for the trimer structure. The  $\bar{M}$  point has a lower symmetry ( $C_{1h}$ ) and therefore no degeneracy is expected there. An interesting result is the presence of two maxima for  $S_1$  on both sides of  $\bar{M}$  along  $\bar{\Gamma}\bar{M}\bar{\Gamma}$ . This hallmark of the trimer structure, which is not observed in simple hexagonal structures, has been reported for other similar systems [78, 90]. We shall see below that

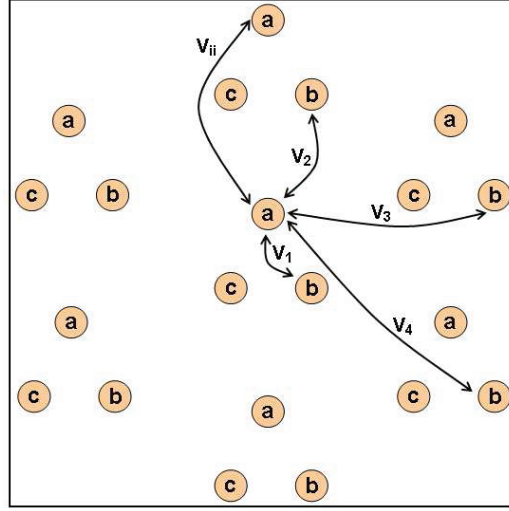


**Figure 3.25** — Schematics of the cell used for the TB calculation, with the definition of the inequivalent transfer integrals.

it plays a potentially important role in the appearance of a *giant* SO splitting in Bi-Si(111).

We consider next the effect of the SO interaction, by adding a RB term to the TB hamiltonian [74, 92, 91, 131]:

$$H_{\text{TB}} = \sum_{\langle i,j \rangle} V_{ij} c_{is}^\dagger c_{js} + \imath \sum_{\langle i,j \rangle_{s,s'}} \lambda_{ij} c_{is}^\dagger (\boldsymbol{\sigma} \times \hat{\mathbf{d}}_{ij})_z c_{js'} \quad (3.11)$$

The first term is the usual spin-independent TB hamiltonian, while the second term is the appropriate TB form for the Rashba interaction.  $c_{is}^\dagger(c_{is})$  is the creation (annihilation) operator of an electron with spin  $s$  ( $\uparrow$  or  $\downarrow$ ) on atomic site  $i$ ,  $V_{ij}$  and  $\lambda_{ij}$  are the transfer integrals and the SO coefficients. The latter are generated by a similar power-law function of the distance, but with independent parameters (see Table II of the Appendix).  $\boldsymbol{\sigma}$  is the vector of the Pauli matrices and  $\hat{\mathbf{d}}_{ij}$  is the vector connecting site  $j$  to site  $i$ .

The six basis vectors of a site-spin representation are, with obvious notation,  $|a \uparrow\rangle$ ,  $|b \uparrow\rangle$ ,  $|c \uparrow\rangle$ ,  $|a \downarrow\rangle$ ,  $|b \downarrow\rangle$ ,  $|c \downarrow\rangle$ . In this representation, the hamiltonian matrix has the form:

$$H_{\text{TB}} = \begin{pmatrix} H_0 & H_{\text{R}} \\ H_{\text{R}}^* & H_0 \end{pmatrix}. \quad (3.12)$$

$H_0$  is the  $3 \times 3$  spin-independent TB hamiltonian which describes states of equal spin.  $H_{\text{R}}$  is a  $3 \times 3$  matrix generated by the second term of  $H_{\text{TB}}$ , which describes the coupling of electrons with opposite spins. Our method is essentially akin to the TB model of Ref. [117] and can qualitatively describe the SO split bands, namely their topology.

Figure 3.27 shows the band structure of the TB model with RB interaction, for the parameters which best reproduce the experimental results [2]. The first obvious effect of the RB interaction is that all states are now split. Both  $S_1$  and  $S_2$  are doubly-degenerate at  $\bar{\Gamma}$ , and exhibit an isotropic dispersion around this point (Fig. 3.27 (a)). By moving out of the high-symmetry line (Fig. 3.27

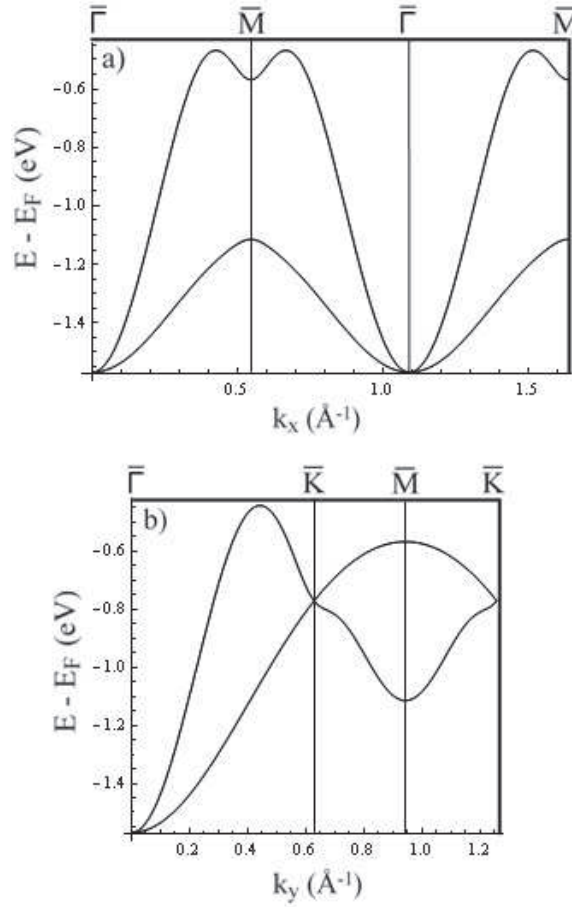


**Figure 3.26** — Calculated band dispersion of the two higher lying states according to the TB model without RB interaction, along the  $\overline{\Gamma M\bar{M}}$  (a) and the  $\overline{\Gamma KM\bar{M}}$  (b) high-symmetry directions.

(b)) the degeneracy is lifted, as expected for the usual RB scenario of Fig. 3.17. The spin-split branches cross again at  $\overline{M}$ , as required by time-reversal symmetry. Here, the dispersion of  $S_1$  is strongly anisotropic. The splitting of  $S_1$  along the  $\overline{\Gamma M\bar{M}}$  direction is much larger than that of  $S_2$ . It is also much larger than the splitting of  $S_1$  around  $\overline{\Gamma}$ . By contrast, it is small along the SBZ boundary  $\overline{KM\bar{K}}$  (Fig. 3.27 (c)). All these features of the band structure agree with the ARPES results, and also with the results of first-principles calculations [51, 132]. The calculated energy difference  $E_R(\overline{M})$  between the band crossing at  $\overline{M}$  and the band maximum is nonetheless smaller than the experimental one.

A comparison of Fig. 3.26 (a) and Fig. 3.27 (a) shows that the large SO splitting of  $S_1$  is a consequence of the split maxima on opposite sides of  $\overline{M}$ , rather than the result of a large SO coupling. In a way, the conditions for a large momentum splitting are already present in the band structure, and the main effect of the SO interaction is to split in energy the two subbands. Indeed for  $S_2$ , which has a maximum at  $\overline{M}$  in the parent structure, the Rashba splitting is small. The origin of the large momentum separation is therefore rather different from that of the 'giant' splitting observed at metallic interfaces like BiAg<sub>2</sub>/Ag(111) [7]. In the TB framework, it is due to the second term of the Hamiltonian (Eq. (3.11)), i.e. the way the trimer arrangement determines the

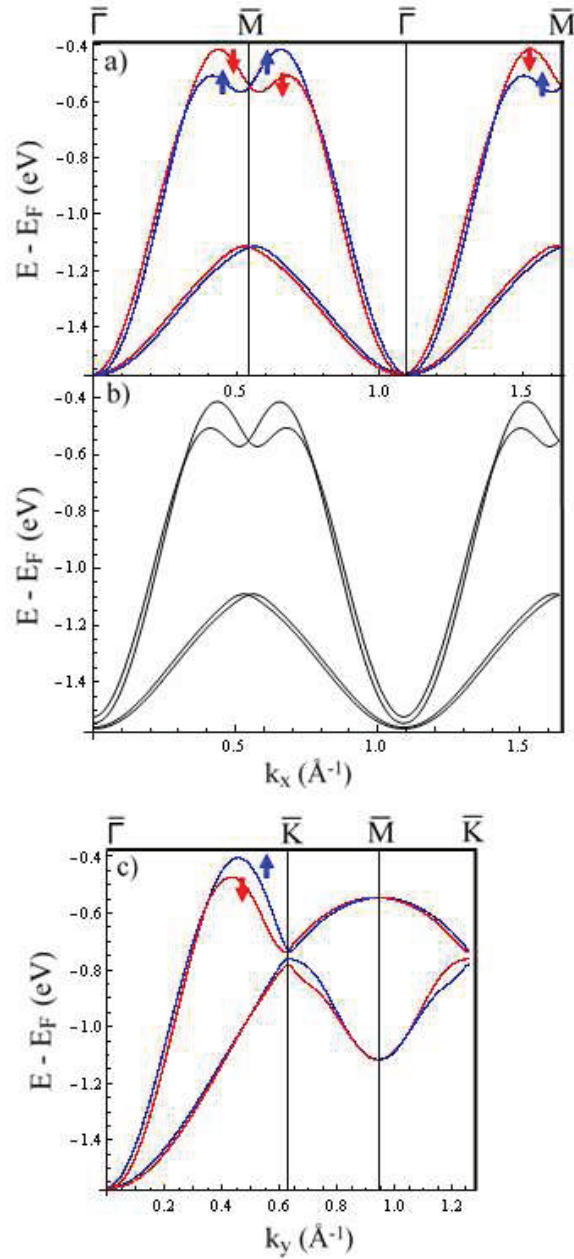


**Figure 3.27** — Calculated bands for the TB model with SO (see Table II of the Appendix for the parameters) for: (a) the  $\bar{\Gamma}\bar{M}\bar{\Gamma}$  direction; (b) the parallel cut  $b$  of Fig. 3.20 (d) ( $k_y = 0.05 \text{ \AA}^{-1}$ ) (b); (c) the  $\bar{\Gamma}\bar{K}\bar{M}$  direction. Arrows denote the main component of the spin polarization of the SO-split branches. The polarization difference is not 100% due to additional radial and out-of-plane components.

hybridization of Bi orbitals with unlike spins.

Figure 3.28 illustrates the energy evolution of the calculated CE contours near  $\bar{M}$ , across the spin-degeneracy point. The experimental contours are reproduced here for a qualitative comparison. A fully quantitative comparison is not possible due to the already mentioned difference in  $E_R(\bar{M})$ . The energies of the calculated contours were therefore adjusted to correspond to the experimental energies of the ARPES contours. The model yields open contours around  $\bar{M}$ , which are in good

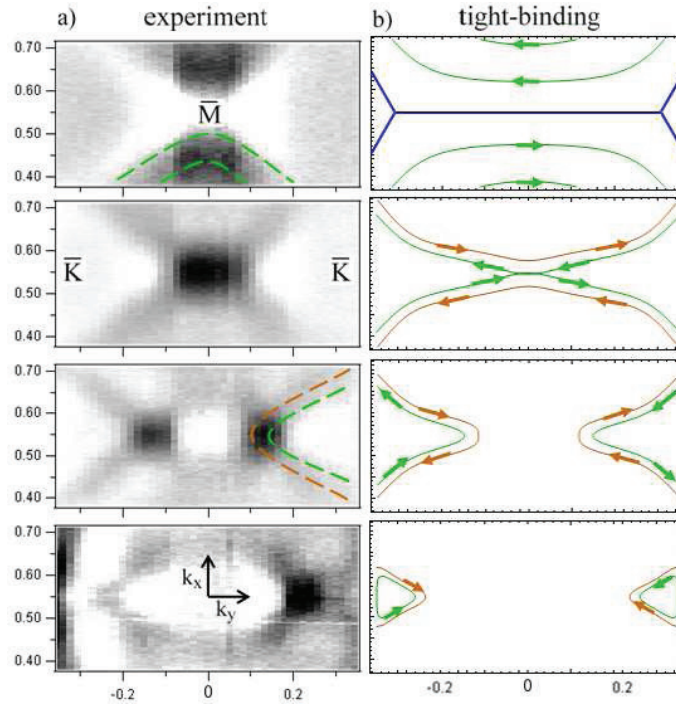


**Figure 3.28** — (a) CE ARPES contours. The dashed curves on the experimental maps are guides to the eye. Green (light gray) and brown (dark gray) colors indicate positive and negative values of tangential spin polarization. (b) CE contours for the TB model. The arrows indicate the in-plane projection of the spin polarization. The energies were adjusted to correspond to the experimental values.

agreement with the topology of the experimental bands. The CE contours are shown on a broader momentum range in Fig. 3.29 (a) and (b) for two energies above, and in Fig. 3.29 (c) for an energy well below the crossing point. The shape of the contours is nearly circular near the bottom of the band at  $\bar{\Gamma}$  (Fig. 3.29 (c)), and it evolves to a hexagonal and finally blossom-like shape at larger energy. The sixfold symmetry is the result of the threefold rotational symmetry and time-reversal symmetry. This is seen more clearly in Fig. 3.29 (d), where the SO parameters were artificially increased to enhance the splitting of the two subbands. Interestingly, the blossom-like shape of Fig. 3.29 (d) is identical to the one predicted by the anisotropic NFE model (see subsection III (C) and Ref. [119]) but the tips now point along the  $\bar{\Gamma}\bar{M}\bar{\Gamma}$  direction.

#### IV. Conclusions and Outlook

We performed a detailed ARPES study of the SO-split electronic states in the 1ML trimer phase of the Bi-Si(111) interface. We paid special attention to the region of  $k$ -space close to the  $\bar{M}$  point, where the topmost  $S_1$  hybrid surface state is both not degenerate with bulk states and distinct from other surface-related features. This region is of particular interest because there  $S_1$  exhibits a large and non-conventional Rashba-type splitting. Energy-dependent constant energy contours clarify the complex topology of the SO-split states, and underline the differences with a standard RB scenario. The ARPES data show that the interface has an insulating character, but the Fermi level could be moved into the SO-split bands by applying an external electric potential in a back-gated structure.



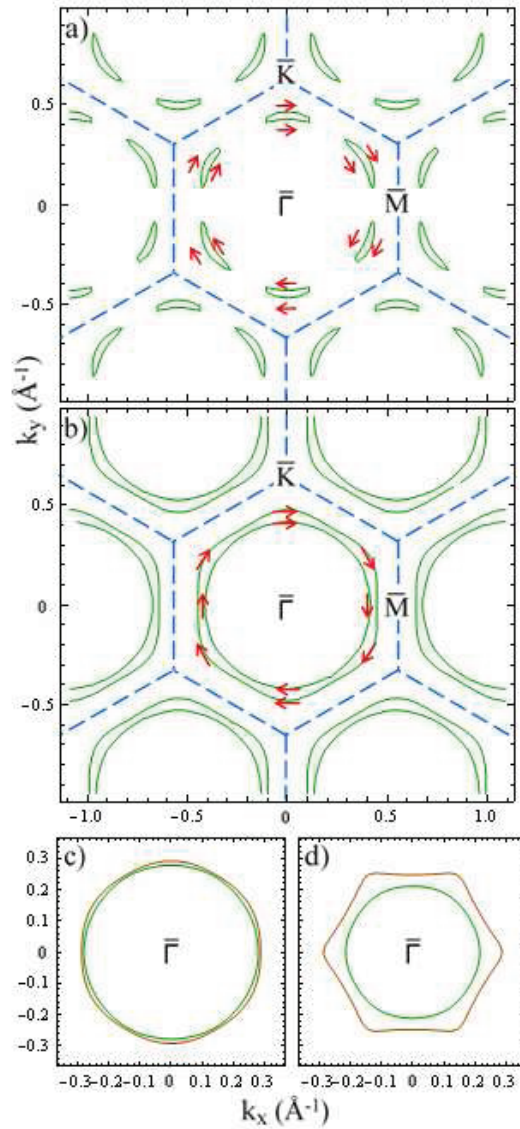


**Figure 3.29** — CE contours of the TB model for energies above (a), (b) and well below (c) the spin degenerate point at  $\bar{M}$ . Arrows indicate the in-plane projection of the spin polarization. (d) is the same as (c) for an eightfold increase in the SO parameters. Green (light gray) and brown (dark gray) colors indicate positive and negative values of tangential spin polarization.

It should then be possible to advantageously exploit the large momentum separation of the two spin-polarized subbands in a spin field-effect transistor [36, 84].

We have used the predictions of three simple models for a 2DEG in the presence of SO interaction as guidelines for the interpretation of the experimental results. The comparison of the NFE and local-orbital schemes, which proceed from opposite starting points, has a certain didactic value. Moreover we were able to assess the limits of the various approaches applied to the Bi-Si(111) case. The ARPES results and CE contours are well described by a NFE RB effect in a sufficiently small region around the  $\bar{\Gamma}$  point. Further away from  $\bar{\Gamma}$  the isotropic NFE model must be refined to include an in-plane asymmetry. Near the SZB, the specific symmetry properties of the interface determine



the characteristics of the SO splitting [110], and only the empirical TB model captures the salient features of the electronic structure. The same model predicts a peculiar spin texture (Fig. 3.29 (a)). Hole pockets with a non-vortical spin arrangement are reminiscent of the teardrop Fermi surface contours of the topological insulator  $\text{Bi}_{1-x}\text{Sb}_x$  [68]. Within a few meV the pockets develop into two connected concentric contours with the same spin polarization (Fig. 3.29 (b)). This new prediction calls for an experimental verification by spin-resolved ARPES.

Our TB approximation obviously cannot reproduce all the details of the complicated electronic structure. More elaborate TB schemes could be implemented by extending the set of local orbitals, by treating in an explicit way the hybridization with the substrate, and by deriving the relevant transfer integrals from a direct calculation. However, the actual merit of such schemes would be dubious, since the computational complexity would approach that of first principles calculations, and since the immediate simplicity of the model would be lost.

The main insight from our analysis of the new experimental data is the realization that the *giant* SO splitting at this interface is not primarily controlled by a large atomic SO parameter, as in the case of  $\text{BiAg}_2/\text{Ag}(111)$  and other metallic surface alloys [7]. On the contrary, the effect is largely due to a peculiar feature in the band structure, namely the presence of symmetrically split maxima around the  $\bar{M}$  point. This is a new, unexpected mechanism to achieve large spin separation at an interface. The underlying band feature is characteristic of the trimer structure, and it has been identified at other similar interfaces [78, 90]. We may therefore anticipate that similar large "Rashba"-type effects could be discovered in other systems characterized by moderate SO parameters.

*It is a pleasure to acknowledge fruitful discussions with A. Baldereschi, J. Henk, I. Rouschatzakis and K. Sakamoto. We also thank L. Moreschini and L. Casanellas for help during the early stage of this work. E.F. acknowledges the financial support of the Alexander S. Onassis Public Benefit Foundation. This research was supported by the Swiss NSF and the NCCR MaNEP.*

## Appendix

The phenomenological parameters of the models are summarized in the following tables:

**Table 3.3** — Parameters of the NFE modes. The potential value refers to the 1st Fourier coefficient of the crystal potential  $V(\mathbf{r})$ .

parameter	isotropic NFE	anisotropic NFE
$m^*$ ( $m_e$ )	0.8	0.8
$c$ ( $\text{eV}\cdot\text{\AA}^3$ )	0	4.8
$\alpha_R$ ( $\text{eV}\cdot\text{\AA}$ )	1.1	1.1
$ V_G $ (eV)	0.3	0.3

**Table 3.4** — Parameters of the TB model. The hopping and SO parameters are generated by power law functions of the distance  $d$  (i.e.  $ad^{-b}$ ).

	$V_{ij}$	$\lambda_{ij}$
prefactor $a$	-2.94	0.15 (1.20 in Fig. 3.29 (d))
exponent $b$	1.13	0.80

### 3.2.6 RB effects on Bi and Pb thin films

A few recent studies have addressed the RB-type splitting of thin film systems grown on Si(111). Nonetheless, with a view to the design of a small precession length spin-FET, the results are not as promising as the Bi-trimer adlayer discussed in the previous pages. Hirahara et al. investigated the electronic properties of ultrathin Bi(001) films deposited on Si(111) substrates [63]. Using a combination of ARPES and first-principles calculations, they were able to identify RB-split surface states at  $E_F$  in full agreement with a previous study on cleaved Bi surfaces [85]. Surprisingly, these surface states lose their spin-polarization at higher  $E_B$  due to interaction with spin-degenerate Bi QWS. Dil et al. deposited Pb thin films on Si(111) [40]. They used spin-resolved ARPES to report a RB-splitting of the Pb QWS of a magnitude comparable to InGaAs/InAlAs heterostructures. The splitting is too small to be observed by spin-integrated techniques and its origin can be explained by competing effects at the two boundaries of the Pb layer.

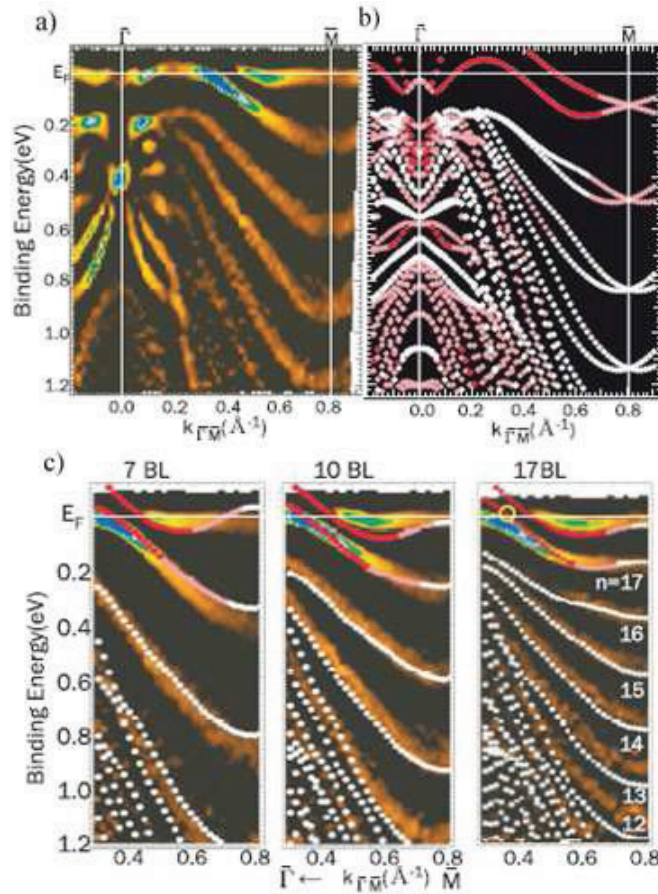


**Figure 3.30** — Experimental (a) and theoretical (b) band dispersion for a 10 bilayer (BL) Bi film on a Si(111) substrate. The space-inversion asymmetry in (b) stems from terminating one side of the slab with H. The spin-split states around  $\bar{M}$  are not reproduced by the experimental data. (c) Calculated band dispersion for free-standing Bi films (i.e. no termination with foreign atoms) is overlaid on the experimental results. All the calculated bands are now spin-degenerate and show a much better agreement with the experiment around  $\bar{M}$ . Red pink and white circles represent surface states, states close to the surface and the rest, respectively. The white numbers in the last figure refer to the quantum number of the QWS. [63, 40]

### 3.2.7 RB effects on Ge-based systems

Hatta et al. examined the electronic structure of the Ge(111)-Bi( $\sqrt{3} \times \sqrt{3}$ )R30° trimer phase [54]. The structural parameters resemble the ones reported for the Si(111)-Bi beta-phase. Therefore, it is not surprising that the authors reported a very similar RB splitting around the  $\bar{M}$  point of the reconstruction ( $\alpha_R = 1.8\text{eV \AA}$ ). By an orbital character analysis of the spin-split states, they identified the crucial role of the hybridized  $sp_z$  character in determining the wavefunction asymmetry and the giant RB effect. Band structure calculations on the Ge(111)-Tl( $3 \times 1$ ) interface predict a RB splitting of both occupied and unoccupied states, which was not reproduced by the experiment due to limited energy resolution [53]. A recent breakthrough study of the same research groups identified a metallic spin-split surface state after Pb deposition (4/3ML) on Ge(111) [155]. Spin-resolved ARPES measurements accompanied by theoretical calculations confirmed the RB-origin of the splitting, while charge density analysis suggested that it is due to an asymmetric charge distribution in proximity to Pb nuclei. The energy splitting of the RB-counterparts at  $E_F$  is as high as 200meV. Despite these impressive results, the main disadvantage of these systems is that they are not Si-compatible.

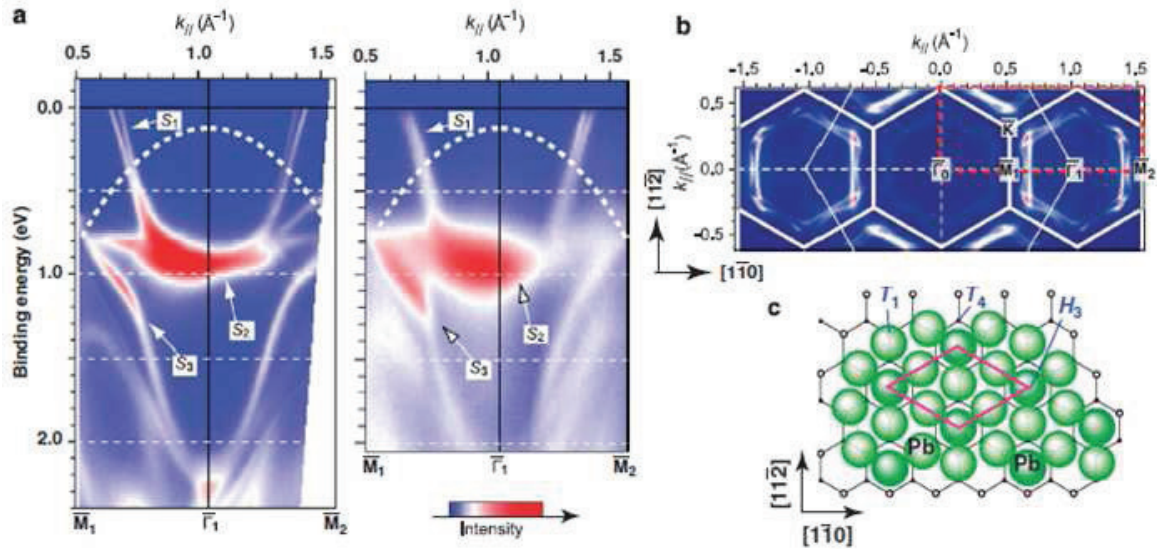


**Figure 3.31** — (a) High-resolution ARPES dispersion of surface- and bulk-derived features of the Ge(111)-Pb(4/3ML) phase. The measurements were performed at 30K (left) and RT (right).  $S_1$  is a metallic surface state and exhibit a clear splitting. (b) Fermi surface map of the band structure presented in (a). The bold red rectangle denotes the region which was actually measured. The high-symmetry points refer to the Pb-induced reconstruction. (c) Top view of the Pb-induced reconstruction on Ge(111) at a nominal coverage of 4/3ML. The solid parallelogram denotes the unit cell. [155]

# Chapter 4

---

## The Pt(111)-Ag-Bi interface: Band topology by ARPES

---

### 4.1 Pt(111)-Ag-Bi: Surface alloying on stressed monolayers

As explained in chapter 2, theory predicts that the size of Rashba-Bychkov (RB) splitting scales with the magnitude of the out-of-plane potential gradient. This observation finds experimental confirmation in the adsorption of noble gases on Au(111), which results into a spatial modification of the Shockley surface state [44, 43]. In consequence, the out-of-plane potential gradient is affected and the RB splitting can change. As expected, the same approach has given null results on the Xe-BiAg<sub>2</sub> surface alloy because the key parameter is not any more the out-of-plane potential gradient but its in-plane counterpart [100]. Introducing in-plane stress on the substrate might be a promising approach to act directly on the in-plane spatial asymmetry of the wavefunction.

Such an in-plane stress is inherent within the first Ag(111) monolayer deposited on a Pt(111) substrate. The formation of a BiAg<sub>2</sub> alloy on this interface might exhibit different SO parameters with respect to its relaxed counterpart. This was the original motivation for the study described in the following paper, albeit one observed a robust low-energy reconstruction with different symmetry from what is expected on a clean Ag(111) layer. Interestingly, by modifying the thickness of the Ag film, ARPES can track the electronic signatures of a structural transition proposed by STM and photoelectron diffraction studies [26, 121].



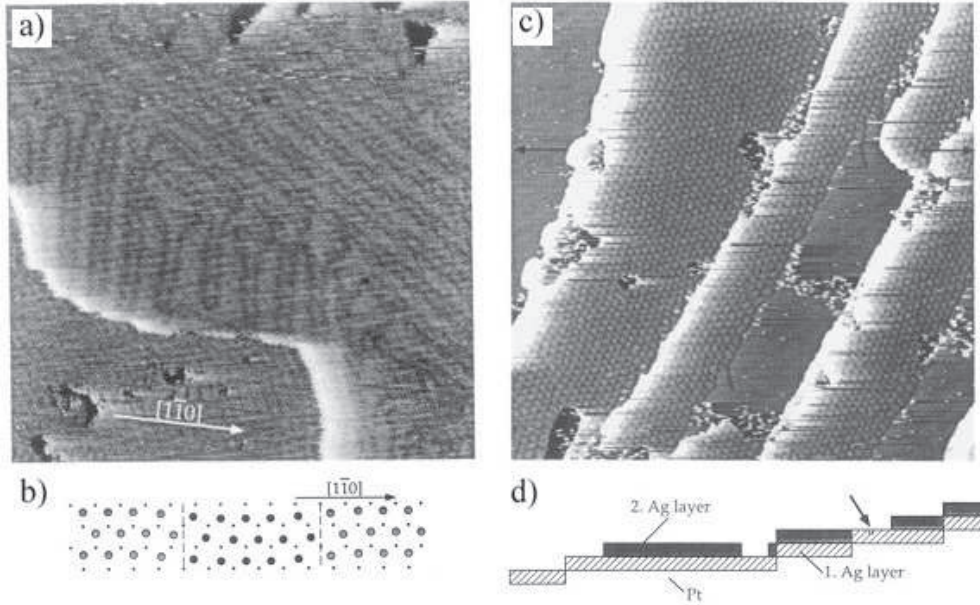


**Figure 4.1** — (a) STM image of the 2<sup>nd</sup> Ag ML on Pt(111) at 340K. The stress is relaxed by the formation of a unidirectional striped incommensurate (SI) phase. (b) Atomic model for the SI phase (black dots 1<sup>st</sup> layer Ag atoms; bright (dark) spheres: 2<sup>nd</sup> layer Ag atoms on fcc and hcp positions). (c) STM image showing the 1<sup>st</sup> and 2<sup>nd</sup> Ag ML on Pt(111) after annealing at 800K. The 2<sup>nd</sup> ML forms a long-range trigonal dislocation pattern at this temperature. (d) Schematic horizontal profile at the positions of the black arrows revealing the stacking of atomic layers. [26]

#### 4.1.1 A structural transition reflected into the band topology of the Pt(111)-Ag-Bi interface (to be submitted to Phys. Rev. B)

*We have studied the electronic band topology of the novel Bi-induced  $p(2 \times 2)$  reconstruction observed on the trilayer system Pt(111)- $x$ MLAg-Bi. The symmetry properties of the involved interface states are discussed. Interestingly, by varying the Ag coverage, our high-resolution ARPES results present the electronic signature of a strain-related structural transition which was previously reported by STM and photoelectron diffraction studies.*

##### I. Introduction

Lattice mismatch at heteroepitaxial systems either gives rise to pseudomorphic strained layers or is accommodated by the formation of incommensurate phases containing misfit dislocations where the strain is locally relieved. The Au(111) surface is a paradigm of the latter, where the 4% strain of the topmost layer is relieved by the formation of a pairwise dislocation network resulting into the well-studied  $\sqrt{3} \times 22$  herringbone reconstruction (for example [146, 16]).

The Pt(111)-Ag interface is a well-studied example for the structural manifestations of strain relief in heteroepitaxy [26, 125]. Moreover, the high-temperature phase of the Pt(111)-2ML Ag strain relief pattern has been used as a scaffold for the self-organized nucleation of nanoparticles [25], following the early STM results obtained for ordered islands on the Au(111) herringbone reconstruction [32].



Despite numerous structural investigations of these interfaces, there are limited studies devoted to their electronic structure and the symmetry of the involved states. In this article, we explore the band topology of a Bi-Ag alloy formed on heteroepitaxial Ag(111) layers which are themselves grown on a Pt(111) substrate. By modifying the thickness of the Ag film, we can track the electronic signatures of a strain-related structural transition proposed by STM and photoelectron diffraction studies [26, 121].

## II. Experimental Details

The Pt(111) substrate underwent many cycles of Ar sputtering and annealing at 1200K. The crystal was then exposed to O<sub>2</sub> partial pressure  $P=10^{-7}$ mbar (at 900K), in order to desorb the carbon impurities which had segregated from the bulk. After a final annealing at 1000K without O<sub>2</sub>, the cleanliness of the substrate was verified by means of LEED and ARPES.

Ag was deposited using a home-made Knudsen cell accurately calibrated during previous studies [48, 45]. Bi was deposited by electron-beam-assisted evaporation using a commercial EFM3 Omicron source. Both sources are well calibrated (details are given in Section III). The sample was kept at room temperature (RT) during the time of deposition. After a mild post-annealing, sharp  $p(2 \times 2)$  LEED spots revealed the symmetry of the induced reconstruction and the atomic order of the interface. The deposition order of Ag and Bi may be interchanged without any effect on the symmetry and the electronic structure of the interface as it was repeatedly verified by LEED and ARPES.

ARPES spectra were acquired at RT and 21.2eV photon energy using a Phoibos 150 Specs Analyzer equipped with a monochromatized GammaData VUV 5000 high brightness source. The base pressure was in the low  $10^{-10}$ mbar range and increased to  $3 \times 10^{-9}$ mbar during the ARPES measurements due to helium leakage from the discharge cavity.

## III. Results

Fig. 4.2 summarizes the ARPES results obtained on a clean Pt(111) substrate. The Pt 5*d* states are straddling the Fermi level, unlike the (111) surfaces of Au, Ag and Cu [6]. Therefore, there is no real gap near  $E_F$  which could permit the existence of true surface states [38]. The electronic structure near the Fermi energy is dominated by a band ( $B_1$ ) with a hexagonal contour (Fig. 4.2 (a)), which has been previously attributed to a resonant enhancement of the sixth bulk band edge near the surface plane [38, 37]. As one moves down in energy,  $B_1$  shrinks and different bulk features appear.  $B_2$  disperses along  $\overline{\Gamma M}$  but, unlike  $B_1$ , it does not cross the Fermi level. Along  $\overline{\Gamma K}$ , there is a degeneracy point at around  $1.3\text{\AA}^{-1}$  due to the apparent crossing of the  $B_2$  feature with other bulk states. This bulk-derived crossing results into a strong peak in the photoemission spectrum and is labelled  $B_C$ . Our results are in good agreement with previous studies on the clean Pt(111) surface [120, 38, 37].

Ag deposition on clean Pt(111) was calibrated by LEED and ARPES. The second Ag ML on Pt(111) forms a well-studied striped incommensurate (SI) phase characterized by a  $\sqrt{3} \times 14$  unit

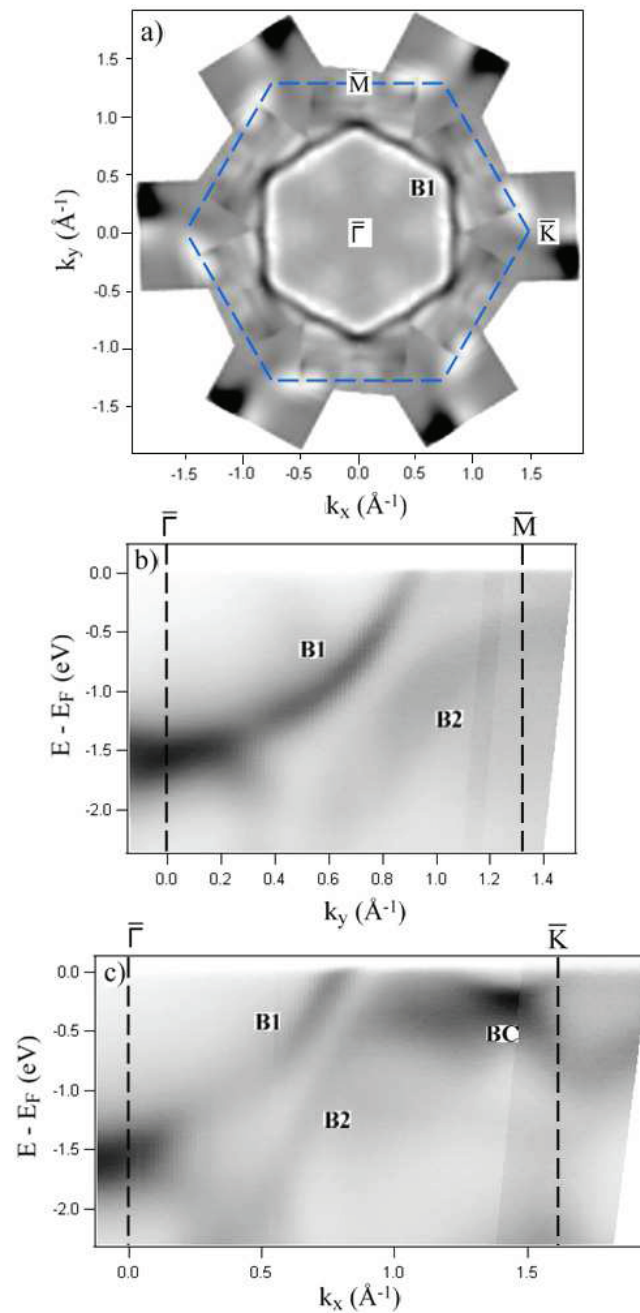


**Figure 4.2** — (color online) ARPES results on the Pt(111) substrate. (a) Measured Fermi surface dominated by a bulk-derived hexagonal contour. The 2<sup>nd</sup> derivative of the photoemission intensity has been used to enhance the experimental features. The dashed hexagon denotes the borders of the Pt(111) (i.e.  $1 \times 1$ ) surface Brillouin zone (BZ). Data has been symmetrized around a sixfold axis. (b), (c) Electronic band dispersion along the  $\bar{\Gamma}\bar{M}$  (b) and  $\bar{\Gamma}\bar{K}$  (c) high-symmetry directions. Labels of the different states are explained in the text.

cell [26]. Moreover, when the deposited amount is of the order of 2-3ML, the spectrum around  $\bar{\Gamma}$  exhibits a peculiar "x-like" feature near  $E_F$  (Fig. 4.3 (a)). This structure has been also observed by other groups and was attributed to a giant Rashba-type spin-orbit splitting [18]. At lower coverages

there is no shallow interface band, while when  $\Theta_{\text{Ag}} > 4\text{ML}$  one can observe the Ag(111) Shockley surface state (Fig. 4.3 (b)). We verified that  $\sqrt{3} \times 14$  reconstruction spots start appearing in the LEED pattern for deposition times which correspond to the threshold of the "x-like" feature. In this way, one can have two independent experimental means - i.e. LEED and ARPES - for calibrating the deposition parameters. Different Ag coverages were obtained by scaling the deposition time. Apart from the aforementioned "x-like" feature, 2-3ML Ag deposition yielded no major modification of the electronic structure presented in Fig. 4.2.

Bi deposition on the Pt(111)-Ag interface induced significant changes in the LEED and ARPES signatures. The evaporation source was calibrated after determining the deposition parameters for 1ML coverage by the characteristic LEED spots of its Moiré-type superstructure. At a coverage of around 0.25ML a sharp  $p(2 \times 2)$  LEED pattern characterizes the symmetry of the Pt(111)- $x\text{MLAg}$ -Bi interface. By varying the amount of deposited Bi, the quality of the pattern decreased, but there was no sign of a different reconstruction. One can therefore conclude that the studied  $p(2 \times 2)$  structure is a robust phase which lies well into the submonolayer Bi range. The LEED spots were sharp pointing towards good atomic order, no matter if the starting Bi-free system was a simple

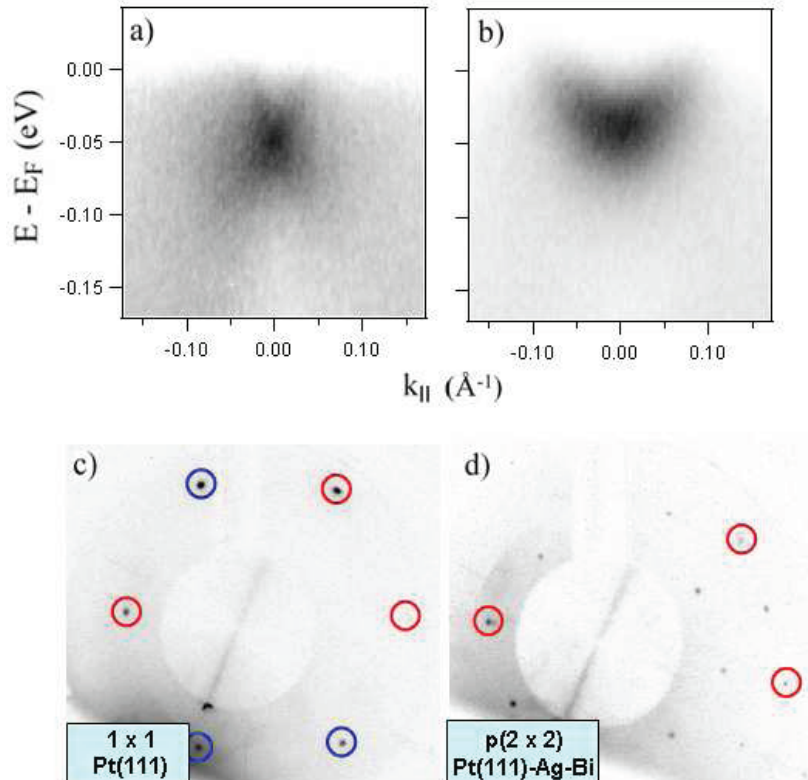


**Figure 4.3** — (a), (b) Pt(111)-Ag: Band dispersion around  $\bar{\Gamma}$  when  $x$  is around 3ML (a) and 5ML (b). The x-like feature in (a) is very different than the parabolic Shockley Ag(111) surface state in (b) and marks the 2ML coverage. (c) LEED pattern at 90eV for a clean Pt(111) substrate. The red (light gray) circles denote  $1 \times 1$  spots which can be also seen in (d). The blue (dark gray) circles denote  $1 \times 1$  spots which are hidden by the electron gun or the borders of the images in (d). (d) LEED pattern at 92eV after the deposition of Ag and Bi revealing a sharp  $p(2 \times 2)$  reconstruction. The red (light gray) circles denote  $1 \times 1$  spots.

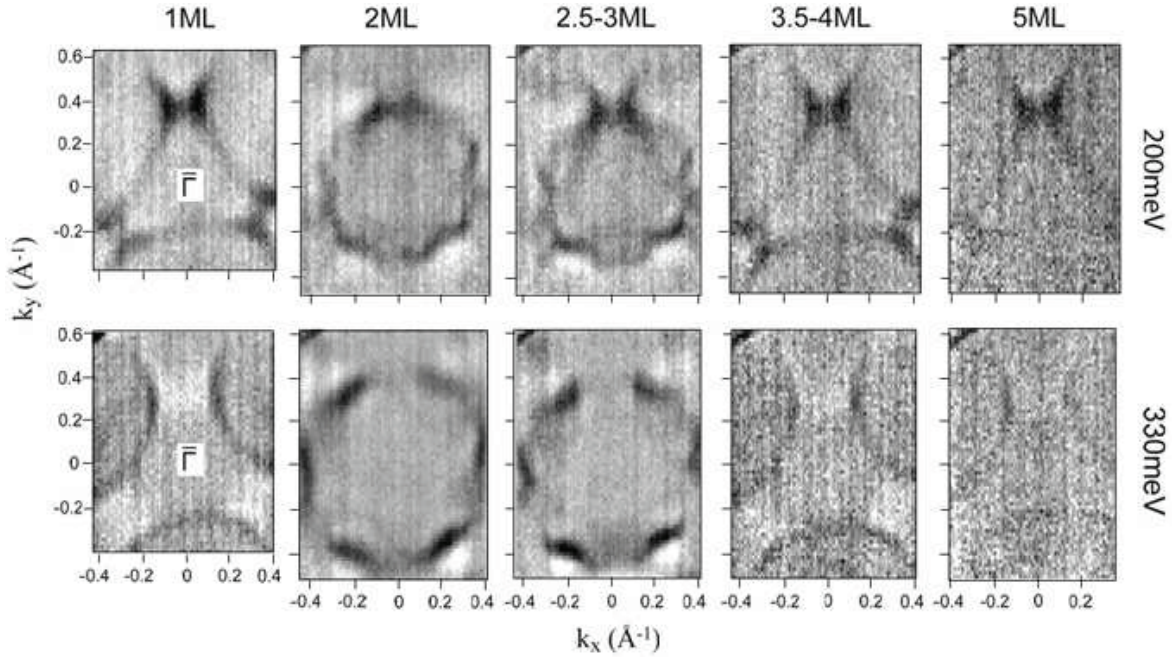


**Figure 4.4** — Pt(111)-Ag-Bi: Constant-energy maps for different Ag coverages limited to  $k$ -values around  $\bar{\Gamma}$ . A strong triangular contour is observed which is dominated by an additional interface state with sixfold symmetry when Ag coverage is around 2ML. The 2<sup>nd</sup> derivative of the photoemission intensity has been used to enhance the experimental features. Data has not been symmetrized.

$1 \times 1$  (i.e.  $x < 1\text{ML}$ ) or a reconstructed  $\sqrt{3} \times 14$  (i.e.  $x \sim 2\text{ML}$ ) Pt(111)-Ag surface. As noted in the previous section, identical LEED and ARPES results were obtained even if the deposition order of Ag and Bi was inverted (i.e. Bi evaporation followed by Ag evaporation), thus verifying the robustness of the reconstruction.

Fig. 4.4 summarizes the ARPES data after Bi deposition for various coverages of the Ag buffer layer. The results are the non-symmetrized 2<sup>nd</sup> derivative of the photoemission intensity presented at two different binding energies. The constant-energy (CE) maps show the band topology around the  $\bar{\Gamma}$  point where we evidenced the most interesting experimental features. When  $x = 1\text{ML}$  (left panel), one can observe an interface contour with an apparent threefold symmetry. This contour has no counterpart on the clean Pt(111) surface or the Pt(111)-Ag interface, thus revealing that it is related to Bi. At higher binding energies, it evolves into three arcs. When Ag coverage is around 2ML, the topology of the corresponding contours is clearly different. The triangular state is still visible, but there is a new interface band which completely dominates the photoemission spectra at 330meV. The latter has an apparent sixfold symmetry. The overlap of the two contours is more clearly seen at a slightly higher coverage (middle panel) where the threefold state is more enhanced. For even higher  $x$ , the sixfold feature disappears completely and the triangular state is again the only B-related contour. At the same time, the sample disorder has been significantly increased, due to the formation of Ag islands.

Figs. 4.5 and 4.6 present extended CE maps for the Pt(111)- $x\text{ML}$ Ag-Bi system. The main surface and bulk-derived features have been labelled ( $B$  for bulk,  $S$  for surface) and their dispersion



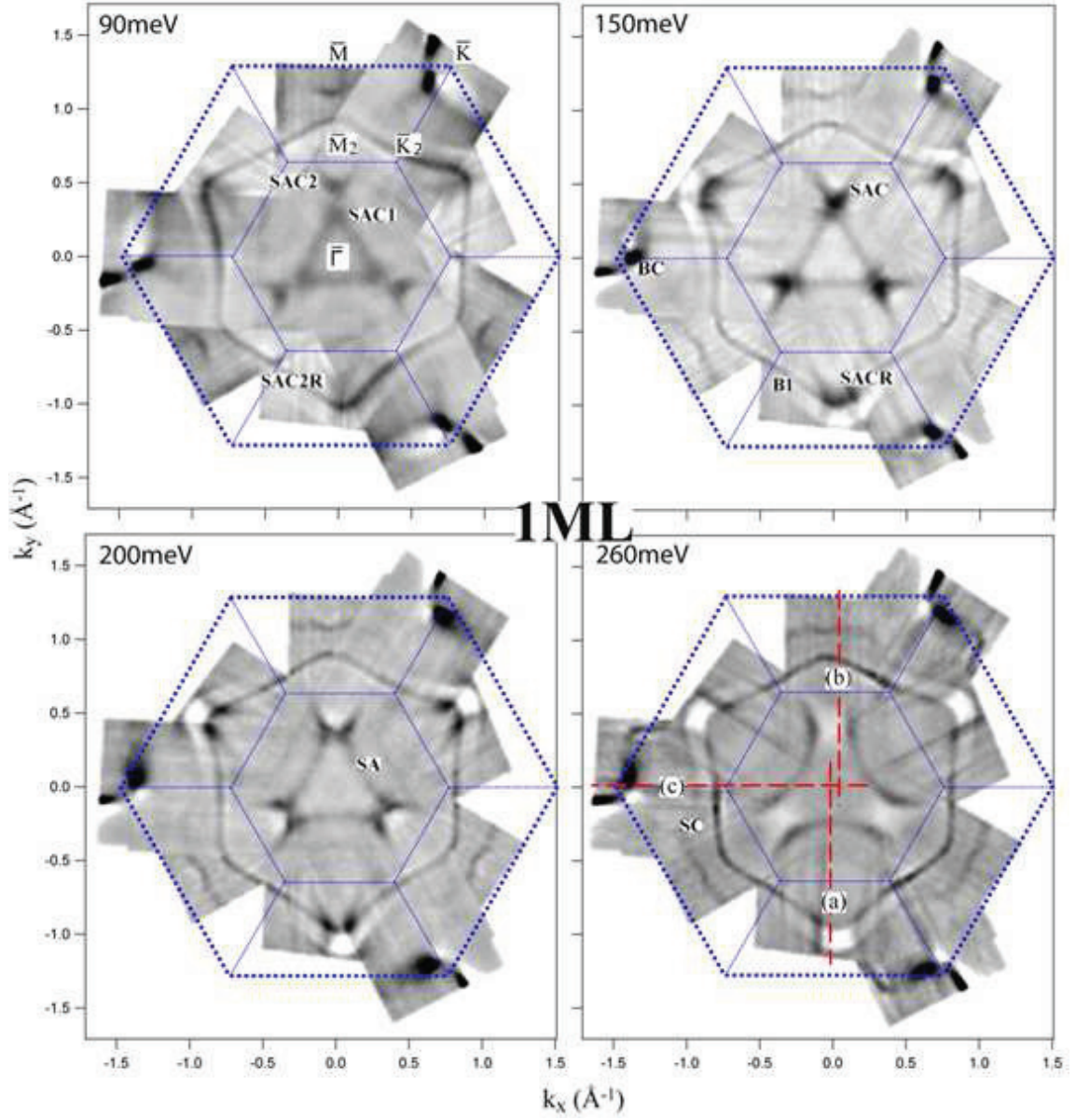


**Figure 4.5** — (Pt(111)- $x$ MLAg-Bi)- $(2 \times 2)$  interface: Long-range constant energy maps for  $x = 1$ ML. The 2<sup>nd</sup> derivative of the photoemission intensity has been used to enhance the experimental features. Data has been symmetrized using a threefold axis. Bold(light) hexagons mark the borders of the  $1 \times 1$ ( $2 \times 2$ ) surface BZ. Dashed lines correspond to the  $k$ -space paths of the images in Fig. 4.7. Arrows point out the  $(2 \times 2)$  periodicity of the triangular contour. Labels of the different states are explained in the text.

is shown in Figs. 4.7 and 4.8. The thick dashed lines in Fig. 4.5 (4.6) denote the corresponding  $k$ -space paths along which the dispersion is presented in Fig. 4.7 (4.8). Having in mind the different energy windows of Fig. 4.2 and Figs. 4.7 and 4.8, one can easily discern the bulk features  $B_1$  and  $B_C$  which were discussed earlier. The hexagonal  $B_1$  contour has nevertheless a threefold modulation and as a result it appears distorted 4.5. This is due to the interaction with the interface bands which are the main focus of our study.

Fig. 4.5 follows the topology of the interfacial triangular contour around  $\bar{\Gamma}$ . The three arcs,

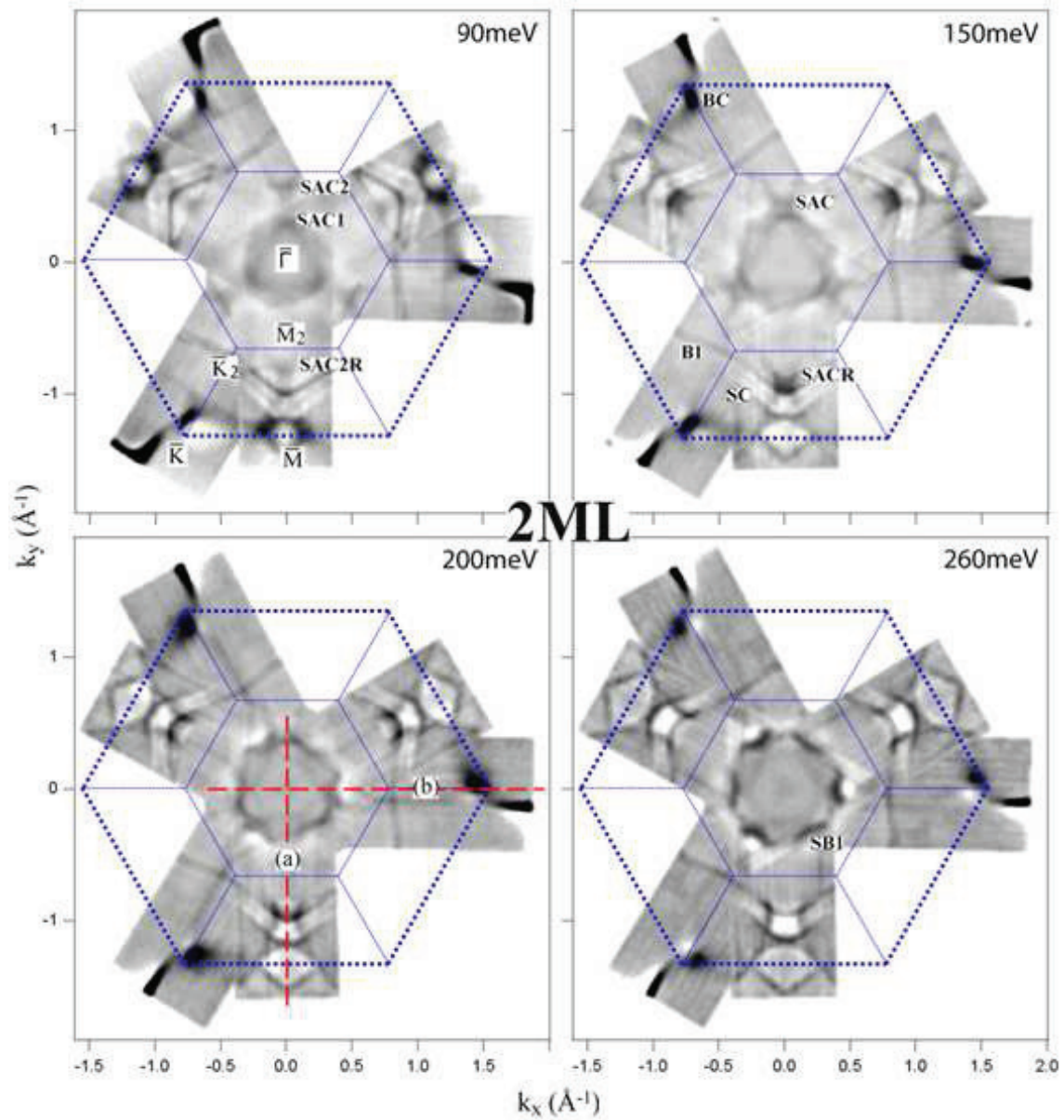


**Figure 4.6** — (Pt(111)- $x$ MLAg-Bi)- $(2 \times 2)$  interface: Long-range constant energy maps when Ag coverage for  $x = 2$ ML. The 2<sup>nd</sup> derivative of the photoemission intensity has been used to enhance the experimental features. Data has been symmetrized using a threefold axis. Bold(light) hexagons mark the borders of the  $1 \times 1(2 \times 2)$  surface BZ. Dashed lines correspond to the  $k$ -space paths of the images in Fig. 4.8. Labels of the different states are explained in the text.

labelled  $SA$ , interact in pairs resulting into two distinct crossing points for each pair.  $SAC_1$  and  $SAC_2$  denote the two crossings of the same arcs seen at a binding energy of 90meV. They reduce into a single degeneracy point ( $SAC$ ) at a slightly higher  $E_B$  (150meV). At even higher  $E_B$  no crossing point is observed. The  $p(2 \times 2)$  periodicity of these interface features is obvious by the CE maps of Fig. 4.5.  $SACR$  ( $SAC_2R$ ) denotes the  $2 \times 2$  replica of the  $SAC$  ( $SAC_2$ ) feature. The bulk  $B_1$  state dominates the photoemission spectrum at the 2<sup>nd</sup>  $2 \times 2$  surface BZ. Nevertheless, the replicas of the aforementioned surface-derived crossing points result into non-negligible photoemission



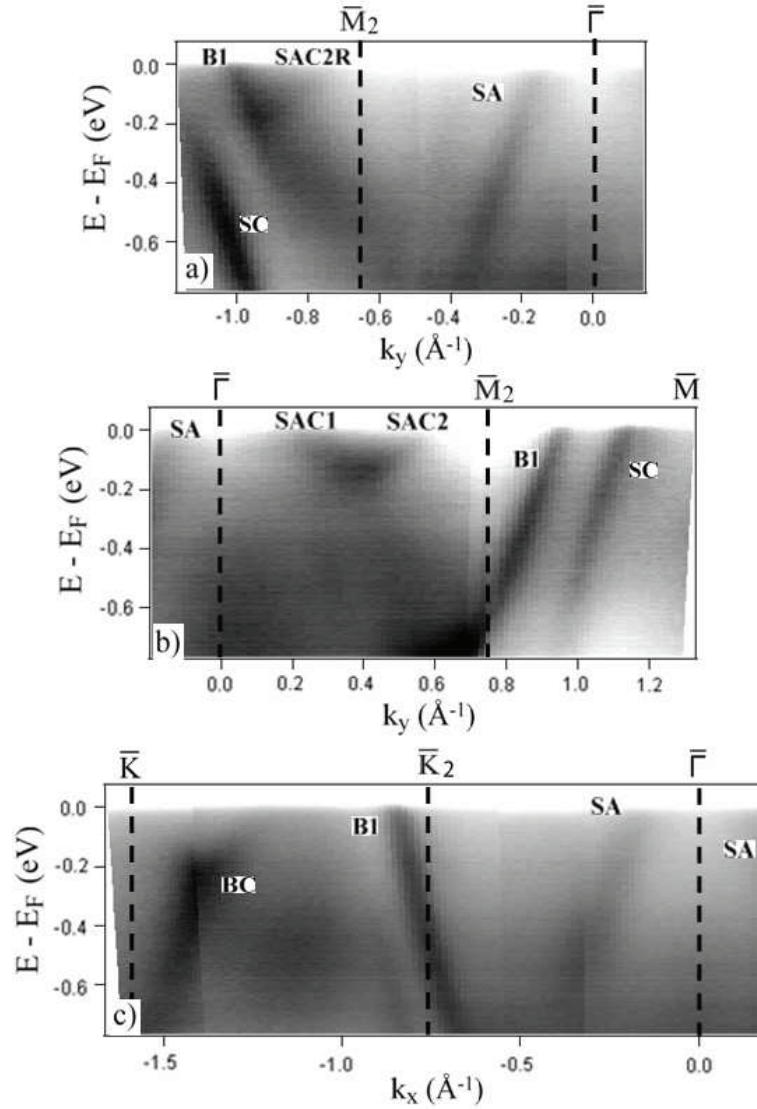


**Figure 4.7** — Pt(111)-Ag-Bi: Electronic band dispersion when Ag coverage is around 1ML. Images (a)-(c) correspond to the  $k$ -space paths of Fig. 4.5. Labels of the different states are explained in the text.

peaks. It is clear from Figs. 4.5 and 4.7 that  $B_1$  is significantly modified after its interaction with  $SAC_2R$ . Due to the triangular symmetry of the  $SA$  state, the interaction results into a threefold modulation of the hexagonal  $B_1$  contour and an asymmetry of the band dispersion for positive and negative values of  $k_y$  (Figs. 4.7 (a) and 4.7 (b)). Moreover, the metallic state  $SC$  has no counterpart in the band structure of clean Pt(111) depicted in Fig. 4.2, thus favoring a surface origin.

Figs. 4.6 and 4.8 summarize the ARPES results when Ag coverage is equal to 2ML. The observations of the previous paragraph are still valid. However, one can readily see two new interface states labelled  $SB_1$  and  $SB_2$ .  $SB_1$  dominates the electronic dispersion and CE maps for binding energies higher than 200meV rendering the identification of the  $SA$  arcs almost impossible.  $SB_2$  appears at even higher  $E_B$  and yields a weak flower-shape contour (data not shown). Both of these states are absent when  $x$  is equal to 1ML. The rest of the surface-derived features discussed in

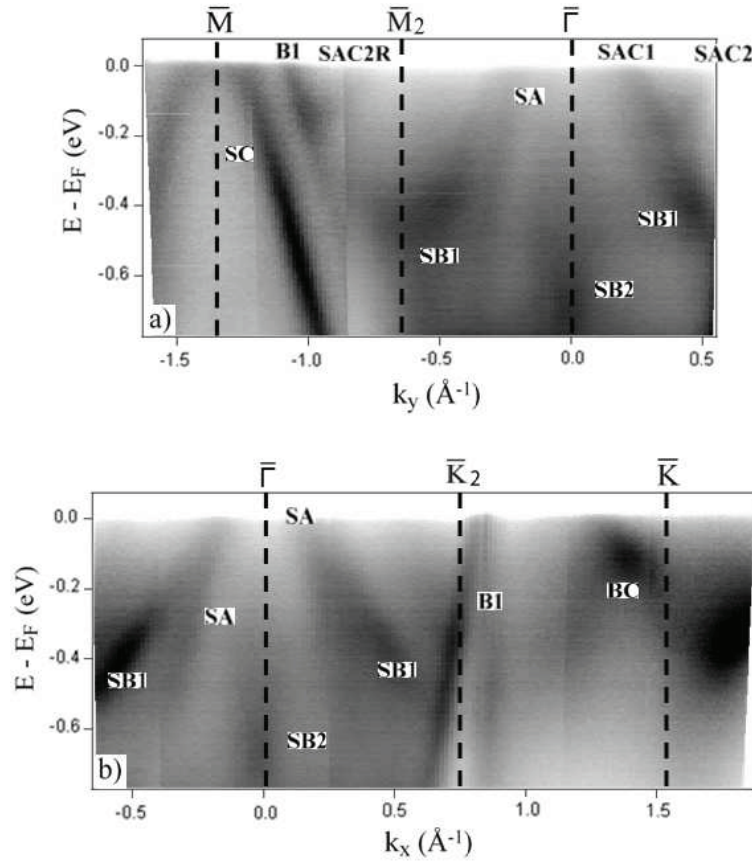


**Figure 4.8** — Pt(111)-Ag-Bi: Electronic band dispersion when Ag coverage is around 2ML. Images (a)-(b) correspond to the  $k$ -space paths of Fig. 4.6. Labels of the different states are explained in the text.

the previous paragraph are still present but their intensities are lower. One can observe their weak signatures, as well as their interaction with the hexagonal  $B_1$  state in Figs. 4.6 and 4.8.

#### IV. Discussion

In the following, we will attempt a tentative explanation of the experimental results based on previous literature for the Pt(111)-Ag system along with some basic symmetry arguments. A fundamental consequence of time-reversal (TR) symmetry is the Kramers degeneracy, which can be written as:

$$E_{k,\uparrow(\downarrow)} = E_{-k,\downarrow(\uparrow)} \quad (4.1)$$

where the arrows represent the spin-polarization of the states. In the case of negligible energy separation of the two spins, (4.1) reduces to  $E_k = E_{-k}$ . In a 2D close-packed system with a sixfold unit cell, irrespective of the magnitude of spin-separation, a spin-integrated technique such as ARPES must yield electronic contours of hexagonal in-plane symmetry satisfying (4.1). In case of a lower symmetry atomic basis which would reduce the basic symmetry operation to a threefold axis, the electronic signature would still consist of hexagonal contours due to the effect of (4.1)

[119, 47]. As a matter of fact, surface states of threefold in-plane symmetry are not in agreement with the predictions of TR as summarized in (4.1).

Bulk states are characterized by a well-defined  $k_{\perp}$ . As a result, (4.1) refers to the 3D  $k$ -vector. The combined effect of Kramers degeneracy and a threefold axis would therefore yield a 3D band topology with an overall threefold symmetry. Prime examples are the bulk electronic structures of fcc metals [6]. As expected, the shape of the corresponding fcc bulk BZ satisfies the symmetry dictated by (4.1). ARPES realizes a 2D mapping of the overall band structure. One can fix  $k_{\perp}$  by choosing  $h\nu$  and assuming a free electron final state. In this way, the threefold symmetry of the fcc bulk states can be for example reflected in the hexagonal (111) surface BZ [3, 17]. In these studies, intense threefold features on the Fermi surface maps of Cu(111) were experimentally observed. By assuming a free electron final state, they were able to identify these features as direct transitions from bulk bands. In conclusion, a threefold ARPES signature is in agreement with TR only when the involved states have a finite  $k_{\perp}$  dispersion.

As noted in section III, there are no true surface states in the energy window of interest due to the absence of a projected bulk gap. The observed interface resonances interact and hybridize significantly with the bulk continuum. As a consequence, they penetrate deeply into the crystal feeling the fcc symmetry of the bulk and this is reflected as a strong threefold intensity modulation in their momentum distributions. The hole pockets observed on the Sb(111) surface are a paradigm of this effect [144]. The fact that we nevertheless evidence interface bands with sixfold symmetry could mean that for a certain Ag coverage there is a structural modification in the bulk which results into sixfold domains. Previous work on the growth of Ag on clean Pt(111) surfaces revealed the mechanism.

The first monolayer of Ag on Pt(111) grows heteroepitaxially conserving the fcc stacking of the substrate. Due to the different lattice constants of the two materials (4.3%), Ag atoms are coherently strained resulting in a compressed commensurate overlayer [127, 126]. Upon deposition of the the second monolayer, compressive strain is relieved by the formation of either the  $\sqrt{3} \times 14$  SI phase at RT or a trigonal dislocation network upon annealing at 750-800K. The LEED signature indicates that the 2ML substrates used in this study belong to the SI phase, in agreement with the low temperature of the post-annealing ( $\sim 400$ K). The SI phase consists of regions with fcc and hcp stacking. The majority domains were attributed to fcc by STM [26] and to hcp by photoelectron diffraction [121]. Both experimental techniques agree that further Ag deposition resumes the fcc stacking of the substrate and is mainly two-dimensional at RT until a critical thickness of 6-9ML [125, 121].

An fcc stacking implies threefold symmetry, while an hcp stacking sixfold. Since the wave-functions of the surface resonances go well into the bulk they must feel at least 3ML, which are enough to distinguish between the two different stacking sequences. Hcp domains exist on the uppermost layers only after the deposition of 2ML of Ag. This could explain the coexistence of interface bands with triangular and hexagonal symmetry exactly at this thickness (Fig. 4.4). As more Ag is deposited, the fcc stacking of the uppermost layers is reflected into the electronic structure by the dominance of the triangular state. Therefore, the threefold  $\rightarrow$  threefold+sixfold  $\rightarrow$  threefold

sequence may find a natural explanation in the growth mechanism of Ag on Pt(111). ARPES has successfully mapped the symmetry of the growth domains and the strain relief pattern. Following the above line of reasoning, our ARPES results favor hcp sites as the majority domains at an Ag thickness of 2ML.

The role of Bi atoms and the structural arrangement of the Pt(111)- $x$ MLAg-Bi system remains uncertain. To this end, our ARPES and LEED data established that the presence of Bi is necessary to induce the  $p(2 \times 2)$  long-range ordered reconstruction and observe the surface resonances which not only satisfy the underlying symmetry but they also map the strain-related structural transition. The insensitivity of the reconstruction to the deposition sequence might be an indication that Bi atoms stay at the topmost layer and produce a long-range reconstruction by preferential ordering at  $2 \times 2$  sites; an issue which needs to be clarified by structural studies. We believe that the present results will motivate STM and/or diffraction experiments on this trilayer system.

## V. Conclusions

We presented detailed ARPES results on the novel  $p(2 \times 2)$  phase observed on the Pt(111)-Ag-Bi trilayer system. Despite the absence of a real gap, strong surface-derived features are observed which have no counterpart either on the clean Pt(111) substrate or on the Pt(111)-Ag interface. The surface resonances follow the symmetry of the induced reconstruction. Most interestingly, the shape of their momentum distributions is strongly-dependent on the Ag thickness. As a consequence, our ARPES results present the electronic signature and an additional proof of a strain-related structural transition proposed by STM and photoelectron diffraction.

*We thank J. Audet for experimental contributions during the early stage of this work. E.F. acknowledges the Alexander S. Onassis Public Benefit Foundation for the award of a scholarship. This research was supported by the Swiss NSF and the NCCR MaNEP.*

# Chapter 5

---

## Phenomenological simulations of the Rashba-Bychkov splitting

---

### 5.1 Introduction

This chapter is devoted to the description of simple simulations, which can be used to describe the experimental results on Rashba-Bychkov systems. The models are purely phenomenological, since parameter values are not explicitly calculated but are chosen to fit the experimental data. Therefore, they cannot be considered as alternatives to sophisticated theoretical calculations but rather as helpful tools, which can switch on and off each individual parameter, thus unravelling its effect on the electronic structure. Simulations are based on two traditional methods for approximating the electronic structure of solids; i.e. the nearly-free electron (NFE) approach and the tight-binding (TB) approximation. A few scattered results have been already presented in previous chapters. Nevertheless, a detailed summary and comparison of the two methods may be of didactic value and can serve as a robust theoretical tool in the experimentalist's hands.

Free electrons, marking a parabolic dispersion, are the starting point of the NFE approximation. Bloch theorem requires that identical free-electron parabolas should be centered at all points of the reciprocal lattice. When the lattice potential is non-negligible, two adjacent parabolas deviate from their free-electron behavior near the borders of the Brillouin zone and open hybridization gaps, whose magnitude depends on the Fourier components of the lattice potential (Fig. 5.1 (a)). Due to Bloch theorem, all  $\mathbf{k}$ -values can be represented in the 1<sup>st</sup> BZ, thus the reduced zone scheme depicts the resulting band structure, which is composed of strongly dispersing bands and numerous hybridization gaps.

The tight-binding approximation considers an opposite starting point; i.e. tightly bound electrons at atoms and non-dispersing atomic levels. When atoms are brought together in order to form a solid, the degeneracy of atomic levels is lifted and the resulting states follow appropriate linear

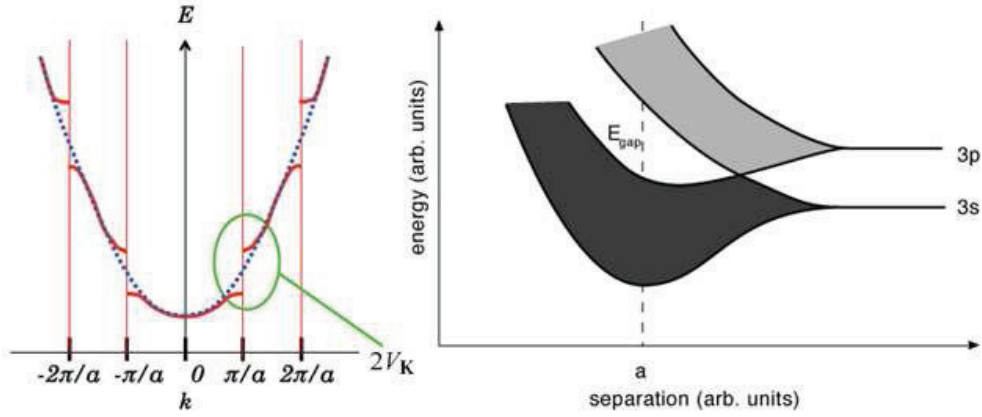


**Figure 5.1** — (left) Schematic band dispersion for a 1D solid according to the NFE model. The results are presented in the extended-zone representation for an easier comparison with the parent free-electron parabola (dashed curve). Band gaps of magnitude  $2V_K$  open at the borders of the Brillouin zone (vertical solid lines) (Figure from M. Golden). (right) The topmost atomic energy levels of Si extend into bands when the atomic distance decreases. The dashed line marks the equilibrium lattice constant of a Si crystal. Band gaps arise due to incomplete overlap of the bands. [67]

combinations of atomic orbitals (LCAO). The number of atoms is so large that one can consider the results as continuous bands of energy levels (Fig. 5.1 (b)). The band width depends on the wavefunction interaction between adjacent atoms and increases with decreasing atomic distance. Different bands may overlap and the definition of their atomic character is not anymore straightforward. The TB approach is more often used for materials with closed atomic shells and covalent solids because it generally results into weakly dispersing bands and wide gaps.

Although a detailed theoretical description of these methods is beyond the scope of this thesis, a basic mathematical formulation will be given at the introductory part of each corresponding section. In both cases, the spin-degenerate results will be discussed, and subsequently the Rashba-Bychkov interaction will be added in the model Hamiltonian.

## 5.2 Simulations based on the NFE approximation

### 5.2.1 The nearly-free electron approximation

Solutions of the Schrödinger equation for electrons in a periodic crystal potential obey the Bloch theorem:

$$\psi_{\mathbf{k}}(\mathbf{r}) = e^{i\mathbf{k}\cdot\mathbf{r}} u_{\mathbf{k}}(\mathbf{r}) \quad (5.1)$$

where  $u_{\mathbf{k}}(\mathbf{r})$  is a function which has the periodicity of the lattice (i.e.  $u_{\mathbf{k}}(\mathbf{r} + \mathbf{R}) = u_{\mathbf{k}}(\mathbf{r})$  for all



$\mathbf{R}$  in the Bravais lattice). As described in [6], the Bloch solution can be expanded in plane waves:

$$\psi_{\mathbf{k}}(\mathbf{r}) = \sum_{\mathbf{K}} a_{\mathbf{k}-\mathbf{K}} e^{i(\mathbf{k}-\mathbf{K})\cdot\mathbf{r}} \quad (5.2)$$

The plane wave coefficients  $a_{\mathbf{k}-\mathbf{K}}$  are determined by the Schrödinger equation:

$$\left[ \frac{\hbar^2}{2m^*} (\mathbf{k} - \mathbf{K})^2 - E \right] a_{\mathbf{k}-\mathbf{K}} + \sum_{\mathbf{K}'} V_{\mathbf{K}'-\mathbf{k}} a_{\mathbf{k}-\mathbf{K}} = 0 \quad (5.3)$$

where  $m^*$  is the effective mass,  $\mathbf{K}$  the reciprocal lattice vectors and  $V_{\mathbf{K}-\mathbf{k}}$  the Fourier coefficients of the crystal potential. The eigenvalues determine the energy dispersion in the presence of a weak crystal potential  $V$ . When all  $a_{\mathbf{k}-\mathbf{K}}$  are zero, the effect of crystal potential vanishes and the free-electron parabola is recovered.

For non-zero coefficients the dispersion is modified; the degree of modification depending on the value of  $\mathbf{k}$ . One can show that deviation from the free-electron predictions will be negligible (2<sup>nd</sup>-order effects) when the value of  $\mathbf{k}$  is such that there are no more than one free-electron parabolas within energy  $V$ . If, however, the value of  $\mathbf{k}$  is such that there are reciprocal lattice vectors with free-electron energies within order  $V$  of each other, a linear correction has to be included. Typically, such values of  $\mathbf{k}$  are those in the vicinity of the Brillouin zone boundaries (i.e. Bragg planes).

When only two nearly degenerate levels (i.e.  $\mathbf{K}_1, \mathbf{K}_2$ ) are involved, Eq. (5.3) is reduced to the following  $2 \times 2$  linear system of equations:

$$\begin{aligned} \left( E - \frac{\hbar^2}{2m^*} (k - K_1)^2 \right) a_{\mathbf{k}-\mathbf{K}_1} &= V_{\mathbf{K}_2-\mathbf{K}_1} a_{\mathbf{k}-\mathbf{K}_2} \\ \left( E - \frac{\hbar^2}{2m^*} (k - K_2)^2 \right) a_{\mathbf{k}-\mathbf{K}_2} &= V_{\mathbf{K}_1-\mathbf{K}_2} a_{\mathbf{k}-\mathbf{K}_1} \end{aligned} \quad (5.4)$$

A non-zero solution exists only if the eigenvalues of the following matrix determine the modified energy dispersion:

$$\begin{pmatrix} \frac{\hbar^2(\mathbf{k}-\mathbf{K}_1)^2}{2m^*} & V_{\mathbf{K}_1-\mathbf{K}_2} \\ V_{\mathbf{K}_1-\mathbf{K}_2}^* & \frac{\hbar^2(\mathbf{k}-\mathbf{K}_2)^2}{2m^*} \end{pmatrix} \quad (5.5)$$

As depicted in Fig. 5.1, the resulting dispersion exhibit band gaps of magnitude  $2V_{\mathbf{K}}$  ( $2V_{\mathbf{K}_1-\mathbf{K}_2}$  in this case) at the Brillouin zone borders.

### 5.2.2 NFE simulation - results

First we consider the interaction of two levels centered at the reciprocal lattice points  $(x_0, y_0) = (0, 0)$  and  $(x_1, y_1) = (-4\pi/(l\sqrt{3}), 0)$  with  $l = 6.65\text{\AA}$ ,  $m^* = 0.8m_e$  and  $|V_{\mathbf{K}}| = 0.3\text{eV}$ ; parameters of the Bi/Si(111) trimer phase.  $(x_0, y_0)$  and  $(x_1, y_1)$  correspond to the centers of two adjacent BZ. Electronic band dispersion in the absence of RB spin-orbit interaction is depicted in Fig. 5.2 (a).

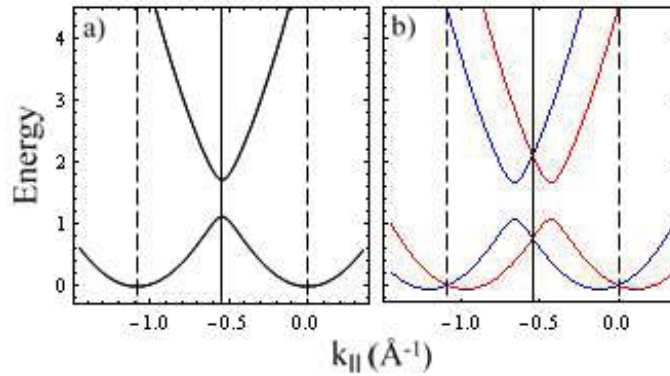


**Figure 5.2** — Calculated band dispersion for a 1D chain without (a) and after the inclusion of (b) RB coupling. Solid (dashed) vertical lines mark the center (borders) of the Brillouin zone. Two reciprocal lattice points have been used for the simulation and one has neglected the effect of all other points, which play an important role at large  $E$  and  $k$  values. Red and blue colors denote opposite directions of the spin-polarization vector. Model parameters are summarized in the text.

In the presence of RB coupling,  $H_{SO}$ , already introduced in chapter 2, has to be added in the model Hamiltonian. If  $\mathbf{K}_0$  and  $\mathbf{K}_1$  are the reciprocal lattice vectors connecting the axis origin with the corresponding center of the BZ, and one works in the subspace spanned by the  $z$ -component of the spin, the base vectors will be  $|(\mathbf{k} - \mathbf{K}_0) \uparrow\rangle$ ,  $|(\mathbf{k} - \mathbf{K}_0) \downarrow\rangle$ ,  $|(\mathbf{k} - \mathbf{K}_1) \uparrow\rangle$ ,  $|(\mathbf{k} - \mathbf{K}_1) \downarrow\rangle$ . The resulting  $4 \times 4$  matrix can be then written as:

$$\begin{pmatrix} \frac{\hbar^2(\mathbf{k}-\mathbf{K}_0)^2}{2m^*} & \alpha_R(-i(\mathbf{k}-\mathbf{K}_0)_x \dots) & V_{\mathbf{K}_0-\mathbf{K}_1} & 0 \\ \alpha_R(i(\mathbf{k}-\mathbf{K}_0)_x - (\mathbf{k}-\mathbf{K}_0)_y) & \frac{\hbar^2(\mathbf{k}-\mathbf{K}_0)^2}{2m^*} & 0 & V_{\mathbf{K}_0-\mathbf{K}_1} \\ V_{\mathbf{K}_0-\mathbf{K}_1}^* & 0 & \frac{\hbar^2(\mathbf{k}-\mathbf{K}_1)^2}{2m^*} & \alpha_R(-i(\mathbf{k}-\mathbf{K}_1)_x \dots) \\ 0 & V_{\mathbf{K}_0-\mathbf{K}_1}^* & \alpha_R(i(\mathbf{k}-\mathbf{K}_1)_x \dots) & \frac{\hbar^2(\mathbf{k}-\mathbf{K}_1)^2}{2m^*} \end{pmatrix}$$

Zero matrix elements denote that bands of opposite spins do not interact. The resulting electronic dispersion with non-negligible RB coupling ( $\alpha_R = 1.1\text{eV \AA}$ ) is depicted in Fig. 5.2 (b). The band gaps now appear at  $\mathbf{k}$ -values where states with similar spins intersect with each other, while there is a spin-degeneracy at the center and the border of the Brillouin zone in agreement with the time-reversal symmetry requirements.

One may alternatively work in the subspace of the eigenvectors  $|\mathbf{k}, \rightarrow\rangle$  and  $|\mathbf{k}, \leftarrow\rangle$  of  $H_{SO}$  (Eq. (2.15)). If  $\delta$  is the angle defined in Fig. 5.3, the  $H_{SO}$  eigenvectors can be written as  $|\mathbf{k}, \rightarrow\rangle = \frac{e^{i(k_x x + k_y y)}}{\sqrt{2}} [e^{-i\delta/2} |\uparrow\rangle + e^{i\delta/2} |\downarrow\rangle]$ . These base vectors denote positive ( $|\mathbf{k}, \rightarrow\rangle$ ) and negative ( $|\mathbf{k}, \leftarrow\rangle$ ) tangential spin polarization. In this case, the diagonal terms will correspond to the unperturbed outer and inner contours of a RB doublet and the  $H_{12}$ ,  $H_{21}$ ,  $H_{34}$  and  $H_{43}$  matrix elements will be equal to zero.

$$\begin{pmatrix} \frac{\hbar^2(\mathbf{k}-\mathbf{K}_0)^2}{2m^*} - \alpha_R(\mathbf{k}-\mathbf{K}_0) & 0 & V_{1,\rightarrow}^{0,\rightarrow} & V_{1,\leftarrow}^{0,\rightarrow} \\ 0 & \frac{\hbar^2(\mathbf{k}-\mathbf{K}_0)^2}{2m^*} + \alpha_R(\mathbf{k}-\mathbf{K}_0) & V_{1,\leftarrow}^{0,\leftarrow} & V_{1,\rightarrow}^{0,\leftarrow} \\ V_{0,\rightarrow}^{1,\rightarrow} & V_{0,\leftarrow}^{1,\rightarrow} & \frac{\hbar^2(\mathbf{k}-\mathbf{K}_1)^2}{2m^*} - \dots & 0 \\ V_{0,\rightarrow}^{1,\leftarrow} & V_{0,\leftarrow}^{1,\leftarrow} & 0 & \frac{\hbar^2(\mathbf{k}-\mathbf{K}_1)^2}{2m^*} + \dots \end{pmatrix}$$

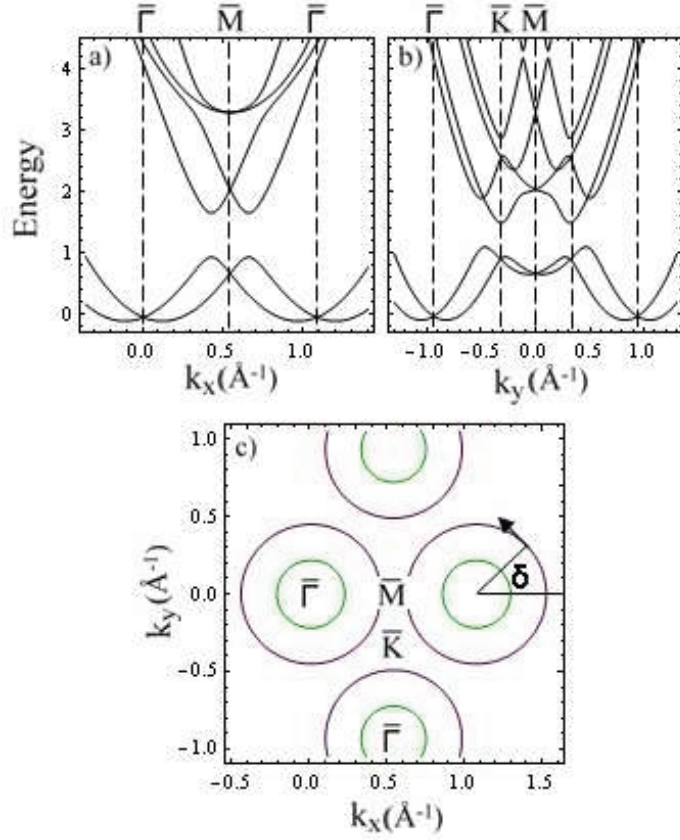


**Figure 5.3** — (a), (b) Calculated band dispersion along the high-symmetry directions for a simple 2D hexagonal lattice with RB coupling. (c) A CE map at  $E = 0.4\text{eV}$  revealing the isotropic shape of the spin-polarized contours.  $\delta$  denotes the angle which enters Eq. (5.6) and (5.7). Purple and green colors denote opposite sign of tangential spin polarization. The simulation is based on four reciprocal lattice points forming a primitive unit cell. Model parameters are summarized in the text.

Hybridization matrix elements will be now  $\mathbf{k}$ -dependent and may be calculated as in the following example:

$$H' |(\mathbf{k} - \mathbf{K}_0), \leftarrow\rangle = \frac{e^{i(k_x x + k_y y)}}{2} V [e^{-i\delta/2} | \uparrow\rangle + e^{i\delta/2} | \downarrow\rangle] \quad (5.6)$$

and

$$\mathbf{V}_{1,\leftarrow}^{0,\leftarrow} = \langle (\mathbf{k} - \mathbf{K}_1), \leftarrow | H' |(\mathbf{k} - \mathbf{K}_0), \leftarrow\rangle = V \frac{1}{2} (e^{-i\delta} - e^{i\delta}) = -\sin \delta \quad (5.7)$$

where  $\delta$  may be expressed as a function of  $\mathbf{k}$  using geometrical arguments.

The results are identical whether one works with base vectors where the spin-projections refer to the  $z$ -axis or by explicitly determining the  $\mathbf{k}$ -dependent hybridization of the tangential spin components.

One can have a reasonable description of the electronic band topology of a 2D system by increasing the number of reciprocal points. Figure 5.3 presents the results of a NFE simulation with

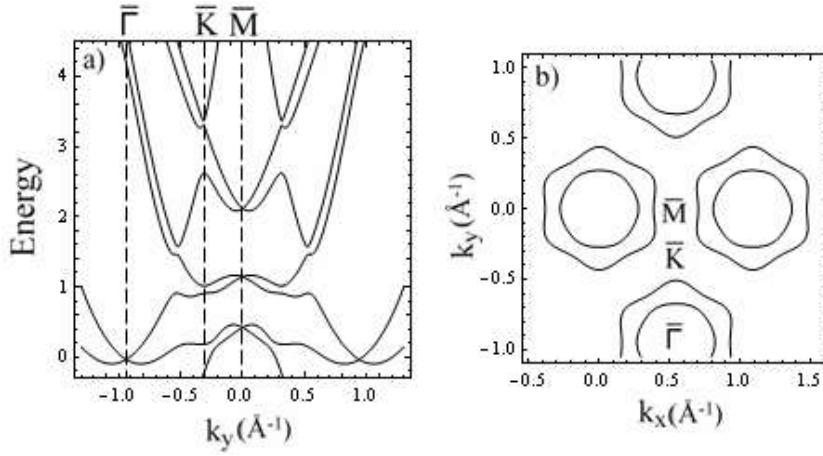


**Figure 5.4** — (a) Calculated band dispersion along the high-symmetry direction which is perpendicular to the mirror plane of a 2D hexagonal lattice with an anisotropic basis. RB coupling has been included. (b) A CE map at  $E = 0.5\text{eV}$  revealing the anisotropic shape of the spin-polarized contours. Hexagonal warping has an opposite sign for the two contours. For the CE map,  $|V| = 0.1\text{eV}$  and  $\alpha_R = 0.5\text{eV \AA}$ . The mirror plane of the system is along the direction which is perpendicular to the axis of the outer hexagon's tips. The simulation is based on four reciprocal lattice points forming a primitive unit cell. Model parameters are summarized in the text.

the same parameters as above but now four lattice points have been included:  $(x_0, y_0) = (0, 0)$ ,  $(x_2, y_2) = (4\pi/(l\sqrt{3}), 0)$ ,  $(x_3, y_3) = (2\pi/(l\sqrt{3}), 2\pi/l)$  and  $(x_4, y_4) = (2\pi/(l\sqrt{3}), -2\pi/l)$ . These points correspond to a primitive unit cell of a reciprocal lattice with hexagonal symmetry. Therefore, one may define the  $\bar{M}$  and  $\bar{K}$  high-symmetry points. The corresponding Hamiltonian matrix will consist of 64 matrix elements ( $8 \times 8$ ). Time-reversal symmetry requirements are respected at  $\bar{\Gamma}$  and  $\bar{M}$ , while spin degeneracy at  $\bar{K}$  is accidental and can be removed after the inclusion of more reciprocal-lattice points.

The above results correspond to an isotropic 2D hexagonal system; i.e. a hexagonal system with a basis of spherical symmetry. As mentioned in chapter 2, anisotropic 2D systems may be modelled by introducing a  $\mathbf{k} \cdot \mathbf{p}$  anisotropy term in the diagonal matrix elements of the matrix referring to the  $z$ -axis spin projection. This 3<sup>rd</sup>-order term captures the opposite hexagonal warping of the outer (positive warping) and inner (negative warping) spin-polarized contours. The warping magnitude is quantified by the phenomenological parameter  $c$  and the diagonal matrix elements are modified as follows:

$$\frac{\hbar^2(\mathbf{k} - \mathbf{K}_0)^2}{2m^*} \rightarrow \frac{\hbar^2(\mathbf{k} - \mathbf{K}_0)^2}{2m^*} \pm \frac{c}{2}(k_+^3 + k_-^3) \quad (5.8)$$

where  $k_{\pm} = k_{\text{perp mirror}} + ik_{\text{mirror drxn}}$  and  $+(-)$  refer to the  $H_{11}$  ( $H_{22}$ ) matrix elements. One may introduce  $k_x$  and  $k_y$  in the previous formula depending on the orientation of the mirror plane. Figure 5.4 depicts the resulting dispersion perpendicular to the mirror plane and the modified shape of the momentum distributions for an anisotropy parameter  $c = 3.8\text{eV \AA}^3$ . The shape of the CE contours is hexagonal despite the absence of any sixfold axis. It is the orientation of the 3D spin polarization

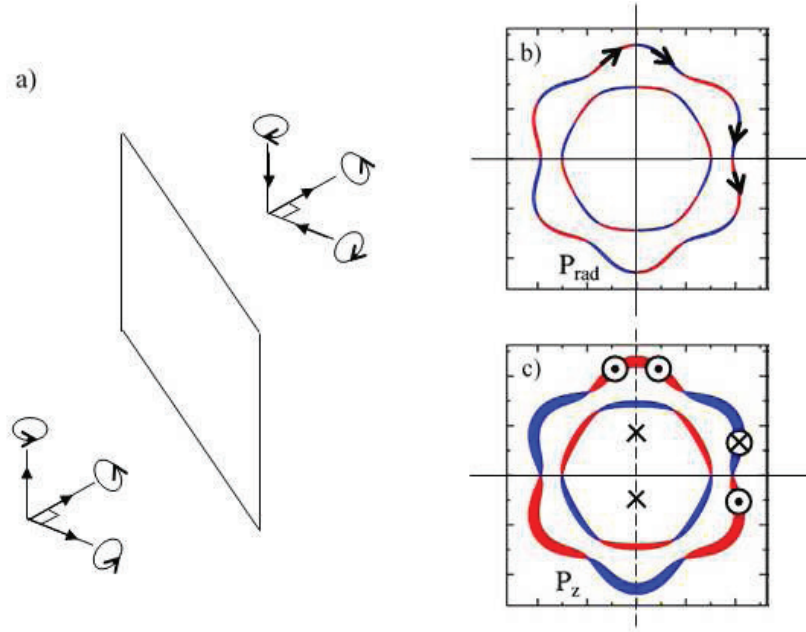


**Figure 5.5** — (a) The behavior of a pseudovector (e.g. 3D spin polarization) after mirror-plane reflection: Components parallel to the mirror plane are reversed, while the one perpendicular to the plane remains unchanged. (b) The shape of a CE contour for a system with a threefold axis and a mirror plane. Red and blue colors represent opposite values of radial spin-polarization. Arrows denote the total in-plane spin polarization after the inclusion of the dominant tangential component. Both vertical and horizontal planes satisfy the conditions determined in (a). (c) As in (b) but now red and blue colors represent opposite values of  $P_z$ . Arrows denote the total out-of-plane spin polarization. Only the horizontal plane satisfies the conditions determined in (a) and this is the only mirror plane of the system. [119]

vector which breaks the sixfold symmetry as revealed by Fig. 5.5. Following the predictions of Premper et al., the direction of  $\mathbf{P}$  is related to the tip orientation of the hexagonal in-plane contours.

### 5.2.3 NFE simulation - conclusions

One can summarize the conclusions of the NFE simulations in the following points:

NFE (1) RB spin-orbit interaction is introduced by the inclusion of  $H_{SO}$  in the model Hamiltonian.

NFE (2) In the  $z$ -axis representation, electron states carrying identical spins hybridize and their interaction is quantified by the 1<sup>st</sup> Fourier coefficient of the crystal potential.  $H_{SO}$  has no effect on their interaction. In a representation where the quantization axis is tangent, this corresponds to  $\mathbf{k}$ -dependent hybridization terms calculated as in Eq. (5.6) and (5.7).

NFE (3) The lattice constant and symmetry are introduced by using the appropriate coordinates for the reciprocal lattice points which enter the Hamiltonian.

NFE (4) In-plane asymmetry (e.g. in the case of an anisotropic basis) can be captured by a  $\mathbf{k} \cdot \mathbf{p}$  term which is added on the diagonal matrix elements. The effect is quantified by the value of the phenomenological constant  $c$ .

NFE (5) Eigenvalues correspond to positive or negative tangential spin polarization component.

NFE (6) The tip orientation of the anisotropic CE contours reveals the mirror planes of the structure.

## 5.3 Simulations based on the TB approximation

### 5.3.1 The tight-binding approximation

The TB approach for solids is a generalization of the LCAO approximation used to find the eigenvalues and eigenstates of simple molecules. The simplest system, which is often used as a textbook example is the hydrogen molecular ion  $H_2^+$ .

When the single electron is at the vicinity of nucleus  $A$ , it will feel a potential which is similar to the atomic potential (Fig. 5.6). Therefore, its wavefunction  $|\psi(\mathbf{r})\rangle$  can be approximated by the corresponding atomic wavefunction:

$$|\psi(\mathbf{r})\rangle \sim |\phi(\mathbf{r} - \mathbf{R}_A)\rangle \quad \text{for} \quad |\mathbf{r} - \mathbf{R}_A| \leq \xi \quad \text{and} \quad |\mathbf{r} - \mathbf{R}_B| \gg \xi \quad (5.9)$$

where  $\xi$  is the radius of the corresponding atomic orbital. Under the same reasoning:

$$|\psi(\mathbf{r})\rangle \sim |\phi(\mathbf{r} - \mathbf{R}_B)\rangle \quad \text{for} \quad |\mathbf{r} - \mathbf{R}_B| \leq \xi \quad \text{and} \quad |\mathbf{r} - \mathbf{R}_A| \gg \xi \quad (5.10)$$

If for all  $\mathbf{r}$ , at which  $|\psi(\mathbf{r})\rangle$  has non-negligible values, at least one of the inequalities presented in (5.9) and (5.10) is valid, one can approximate the wavefunction with a linear combination of the two atomic orbitals:

$$|\psi(\mathbf{r})\rangle \sim c_A |\phi(\mathbf{r} - \mathbf{R}_A)\rangle + c_B |\phi(\mathbf{r} - \mathbf{R}_B)\rangle \quad (5.11)$$

where  $c_A$  and  $c_B$  are the linear coefficients. Due to symmetry, these coefficients must be equal in the simple example of  $H_2^+$ . The general idea of the LCAO approach is to find the  $c_i$  values. To this end, one may start with the Schrödinger equation:

$$\begin{aligned} H|\psi(\mathbf{r})\rangle &= E|\psi(\mathbf{r})\rangle \\ \sum_i c_i H|\phi(\mathbf{r} - \mathbf{R}_i)\rangle &= E \sum_i c_i |\phi(\mathbf{r} - \mathbf{R}_i)\rangle \\ \sum_i c_i \langle \phi(\mathbf{r} - \mathbf{R}_j) | H | \phi(\mathbf{r} - \mathbf{R}_i) \rangle &= E \sum_i c_i \langle \phi(\mathbf{r} - \mathbf{R}_j) | \phi(\mathbf{r} - \mathbf{R}_i) \rangle \end{aligned}$$

$$\text{for } j = A, \quad c_A H_{AA} + c_B H_{AB} = c_A E + c_B E S \quad (5.12)$$

$$\text{for } j = B, \quad c_B H_{BB} + c_A H_{BA} = c_B E + c_A E S \quad (5.13)$$

Equations (5.12) and (5.13) form a homogeneous system of linear equations, the solution of which yields the  $c_i$  values and hence the approximation of  $|\psi(\mathbf{r})\rangle$ .  $H_{AA} = H_{BB} = \varepsilon$  is the



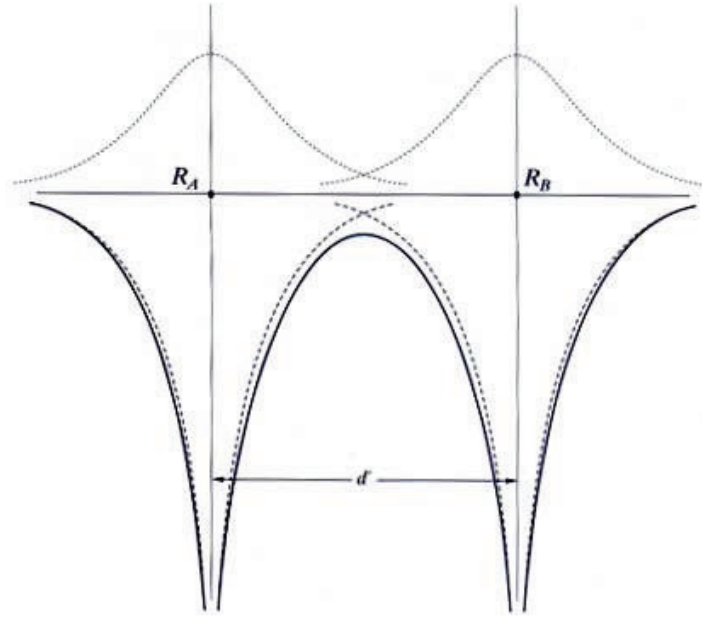


**Figure 5.6** — A schematic representation of two separate  $H$  atoms. The dashed line denotes the potential due to each individual atomic core, while the solid curve represents their sum. Dotted lines are a sketch of the  $1s$  wavefunctions of the two  $H$  atoms. [42]

common energy of the corresponding atomic orbitals,  $H_{AB} = V$  and  $H_{BA} = V^*$  denote their hybridization and  $S$  is the overlap of the atomic wavefunctions. For reasons of simplicity the latter is often neglected.

The LCAO approach will be now extended to an imaginary 1D solid, which is composed of  $N$  identical atoms and has a lattice constant of  $l$ . Following the same procedure and considering only nearest-neighbor interactions and orbitals of spherical symmetry, one will arrive at a homogeneous system consisting of  $N$  linear equations:

$$c_j \varepsilon + V(c_{j-1} + c_{j+1}) = E c_j \quad \text{with} \quad j = 1, 2, 3, \dots, N \quad (5.14)$$

Bloch theorem requires that  $c_j = c_0 e^{iklj}$ . After substituting this relationship in Eq. (5.14) and eliminating the common factors, one arrives at an expression for the band dispersion  $E(k)$ :

$$E(k) = \varepsilon + 2V \cos(kl) \quad (5.15)$$

The tight-binding approach predicts a cosinusoidal band with a mean value of energy equal to the atomic value. The band width ( $w$ ) depends on the hybridization parameter ( $w = 4V$ ). For small values of  $k$ , one may perform a Taylor expansion of (5.15) around  $k = 0$  and the band dispersion can be approximated by:

$$E(k) = \varepsilon + 2V - Vl^2 k^2 \quad (5.16)$$

The parabolic dispersion is in agreement with the NFE predictions revealing the equivalency of

the models. This point will be further considered in section 5.4. The analogy of the two approaches yields a TB expression for the effective mass:

$$m^* = -\frac{\hbar^2}{2Vl^2} \quad (5.17)$$

and  $m^*$  is positive when  $V < 0$ .

### 5.3.2 TB simulation - results

Fig. 5.7 (b) presents the TB band dispersion for a 1D linear chain ( $l = 6.65\text{\AA}$ ,  $V = -1\text{eV}$  and  $\varepsilon = 0\text{eV}$ ). A first complication arises when the solid consists of non-equivalent atoms. The simplest example is a diatomic linear chain depicted in Fig. 5.7 (a). The chain is composed of  $N$  atomic pairs (total=  $2N$  atoms). If  $|a_i\rangle$  and  $|b_i\rangle$  are the atomic wavefunctions centered on the  $a$  and  $b$  atoms of the pair with index  $j$ , the total wavefunction may be written as a linear combination:

$$|\psi\rangle = \sum_j c_j |a_j\rangle + d_j |b_j\rangle \quad (5.18)$$

Starting from the Schrödinger equation and following the same procedure as before, one arrives at a pair of homogeneous systems, each one consisting of  $N$  linear equations:

$$c_j \varepsilon_a + d_j V_{ab} + d_{j-1} V'_{ab} + c_{j+1} V_{aa} + c_{j-1} V_{aa} = E c_j \quad (5.19)$$

$$c_{j+1} V'_{ab} + c_j V_{ab} + d_j \varepsilon_b + d_{j+1} V_{bb} + d_{j-1} V_{bb} = E d_j \quad (5.20)$$

where  $\varepsilon_a$  and  $\varepsilon_b$  stand for the energies of the corresponding atomic orbitals and the  $V$  parameters denote the interactions depicted in Fig. 5.7 (a). All other hybridization parameters are neglected. The Bloch theorem yields the following pair of equations:

$$c_j = c_0 e^{iklj} \quad \text{and} \quad d_j = d_0 e^{iklj}$$

Equations 5.19 and 5.20 may be therefore simplified as:

$$c_0 \varepsilon_a + d_0 V_{ab} + d_0 e^{-ikl} V'_{ab} + 2c_0 \cos(kl) V_{aa} = E c_j \quad (5.21)$$

$$c_0 e^{ikl} V'_{ab} + c_0 V_{ab} + d_0 \varepsilon_b + 2d_0 \cos(kl) V_{bb} = E d_j \quad (5.22)$$

This is a homogenous system of linear equations in terms of  $c_0$  and  $d_0$ . Hence, there exist non-trivial solutions only if its determinant is equal to zero. Or equivalently, the energy dispersion is given by the eigenvalues of following  $2 \times 2$  TB Hamiltonian matrix:

$$\begin{pmatrix} \varepsilon_a + 2 \cos(kl) V_{aa} & V_{ab} + e^{-ikl} V'_{ab} \\ V_{ab} + e^{ikl} V'_{ab} & \varepsilon_b + 2 \cos(kl) V_{bb} \end{pmatrix} \quad (5.23)$$

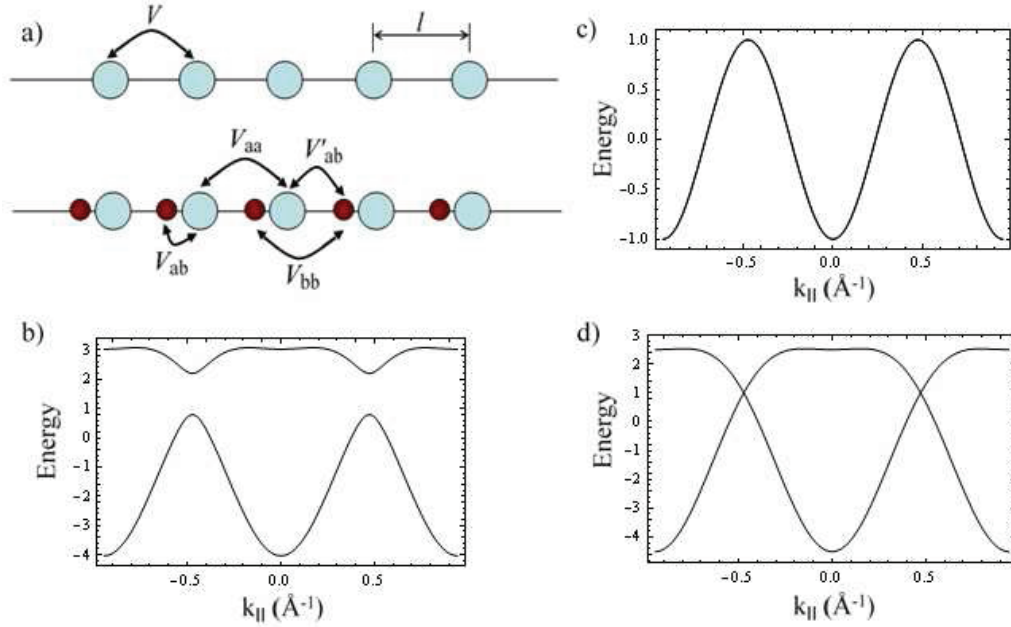


**Figure 5.7** — (a) A schematic representation of a monatomic (top) and a diatomic (bottom) 1D chain.  $V$  parameters denote the different types of interactions between spherically symmetric orbitals. (b) Electronic band dispersion for the monatomic chain with parameters summarized in the text. (c) Electronic band dispersion for the diatomic chain with parameters summarized in the text. The introduction of interactions between dissimilar atoms increases the band width of the lowest-lying band and yields another band of smaller band width at higher energy. (d) As in (c) but with  $\varepsilon_a = \varepsilon_b$  and  $V_{ab} = V'_{ab}$ . The double periodicity of the Brillouin zone reveals that this case is equivalent to a monatomic 1D chain with half periodicity.

A general compact form for the TB hamiltonian often encountered in the literature is therefore:

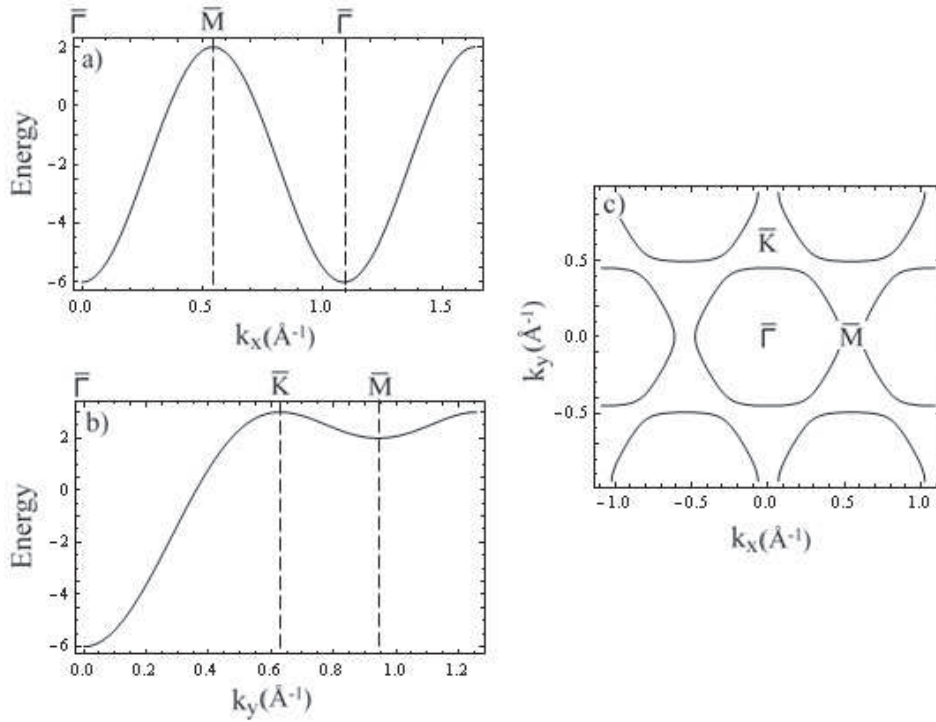
$$H_{TB} = \sum_{\langle i,j \rangle} V_{ij} c_i^\dagger c_j \quad (5.24)$$

Fig. 5.7 (c) presents the band dispersion for a diatomic chain with  $l = 6.65\text{\AA}$ ,  $\varepsilon_a = 0\text{eV}$ ,  $\varepsilon_b = 1\text{eV}$ ,  $V_{ab} = -2\text{eV}$ ,  $V'_{ab} = -1.5\text{eV}$  and  $V_{aa} = V_{bb} = -1\text{eV}$ . The number of bands (2) corresponds to the number of inequivalent atoms. When  $V_{ab} = V'_{ab} = -1.75\text{eV}$  and  $\varepsilon_a = \varepsilon_b = 0\text{eV}$ , the band gap disappears and the Brillouin zone exhibits a double periodicity (Fig. 5.7 (d)). This is because the atoms are no more inequivalent and the chain corresponds to a 1D solid with periodicity of  $l/2$ .

2D systems can be modelled using the same approach; the results being relatively simple when there is a single atom per unit cell and only spherically-symmetric orbitals are considered. Using a combination of the Schrödinger equation and the Bloch theorem, it is straightforward to find the TB band dispersion for a simple 2D hexagonal lattice:

$$E(k_x, k_y) = \varepsilon + 2V \cos(lk_y) + 2V \cos(\sqrt{3}/2lk_x + 1/2lk_y) + 2V \cos(\sqrt{3}/2lk_x - 1/2lk_y) \quad (5.25)$$

Eq. (5.25) defines a 2D band dispersion and its predictions can be plotted in the form of  $E(k)$



**Figure 5.8** — Calculated band topology for a simple 2D hexagonal lattice without RB coupling. (a), (b) Electronic dispersion along the two high-symmetry directions. (c) A CE map at  $E = 1.7\text{eV}$ . In-plane momentum distributions follow the hexagonal symmetry of the structure. Model parameters are summarized in the text. One spherically symmetric orbital per atom has been considered.

diagrams along the high-symmetry directions or CE maps at a fixed energy value. An example is presented in Fig. 5.8 for  $l = 6.65\text{\AA}$ ,  $\varepsilon = 0\text{eV}$  and  $V = -1\text{eV}$ . Fig. 5.8 (c) reveals that the in-plane contours "feel" the lattice symmetry and deviate from an isotropic circular shape.

RB spin-orbit interaction may be included by adding the TB representation of the  $H_{SO}$  Hamiltonian introduced in chapter 2 (Eq. (2.11)). In order to find the site-spin representation of  $H_{SO}$  one may successively write:

$$H_{SO} = \alpha_R(\boldsymbol{\sigma} \times \mathbf{k}) \cdot \hat{\mathbf{e}}_z = \alpha_R m^* (\boldsymbol{\sigma} \times \mathbf{k}) \cdot \hat{\mathbf{e}}_z / \hbar = \frac{\alpha_R \hbar}{2l^2 V} (\mathbf{v}_x \otimes \boldsymbol{\sigma}_y - \mathbf{v}_y \otimes \boldsymbol{\sigma}_x) \quad (5.26)$$

where the effective mass was replaced by its tight-binding representation from Eq. (5.17) and  $\otimes$  denotes the Kronecker product of two matrices. The velocity operator can be written as a matrix in the site-spin representation. For example, for two base states  $|p\rangle$  and  $|q\rangle$ :

$$\langle p | \mathbf{v}_x | q \rangle = \frac{i}{\hbar} V_{pq} (p_x - q_x) \quad (5.27)$$

All parameters can be grouped under an effective term  $\lambda_R$  which captures the RB interaction of unlike spins centered at different sites. The TB representation of the  $H_{SO}$  Hamiltonian can be then

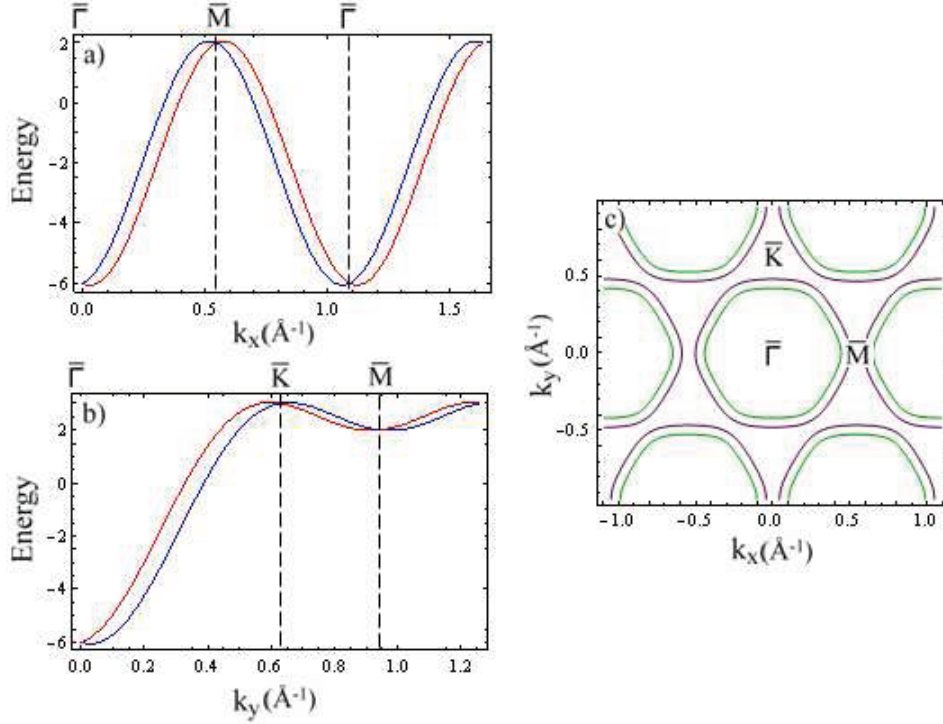


**Figure 5.9** — Calculated band topology for a simple 2D hexagonal lattice with RB coupling. (a), (b) Electronic dispersion along the two high-symmetry directions. Red and blue colors denote opposite directions of the spin-polarization vector. (c) A CE map at  $E = 1.7\text{eV}$ . In-plane momentum distributions follow the hexagonal symmetry of the structure. Purple and green colors denote opposite sign of tangential spin polarization. Model parameters are summarized in the text. One spherically symmetric orbital per atom has been considered.

written in a compact form:

$$H_{SO} = i\lambda_R \sum_{\langle p,q \rangle \alpha\beta} c_{p\alpha} (\boldsymbol{\sigma} \times \hat{\mathbf{d}}_{\mathbf{p}\mathbf{q}})_z c_{q\beta} \quad (5.28)$$

where  $\alpha, \beta$  denote spin up or spin down particles and  $\hat{\mathbf{d}}_{\mathbf{p}\mathbf{q}}$  is a unit vector along the bond that connects site  $q$  to site  $p$ . One should always bear in mind that this term is equivalent to the NFE expression of Eq. (2.11) and it must be not confused with a  $k$ -independent Zeeman on-site SO interaction, which would result in  $k$ -independent energy splitting of the bands (Fig. 2.3 (a)). The complete system Hamiltonian is a result of the combination of Eq. (5.24) and (5.28).

$$H_{TB-SO} = \sum_{\langle p,q \rangle \alpha} V_{pq} c_{p\alpha}^\dagger c_{q\alpha} + i\lambda_R \sum_{\langle p,q \rangle \alpha\beta} c_{p\alpha} (\boldsymbol{\sigma} \times \hat{\mathbf{d}}_{\mathbf{p}\mathbf{q}})_z c_{q\beta} \quad (5.29)$$

As in the case of NFE simulations, the inclusion of the SO term in the TB Hamiltonian doubles the number of base states. Hence, for the monoatomic hexagonal lattice one would arrive at a  $2 \times 2$  matrix with the following matrix elements:

$$H_{11} = H_{22} = \varepsilon + 2V \cos(lk_y) + 2V \cos\left(\frac{\sqrt{3}l}{2}k_x + \frac{l}{2}k_y\right) + 2V \cos\left(\frac{\sqrt{3}l}{2}k_x - \frac{l}{2}k_y\right)$$

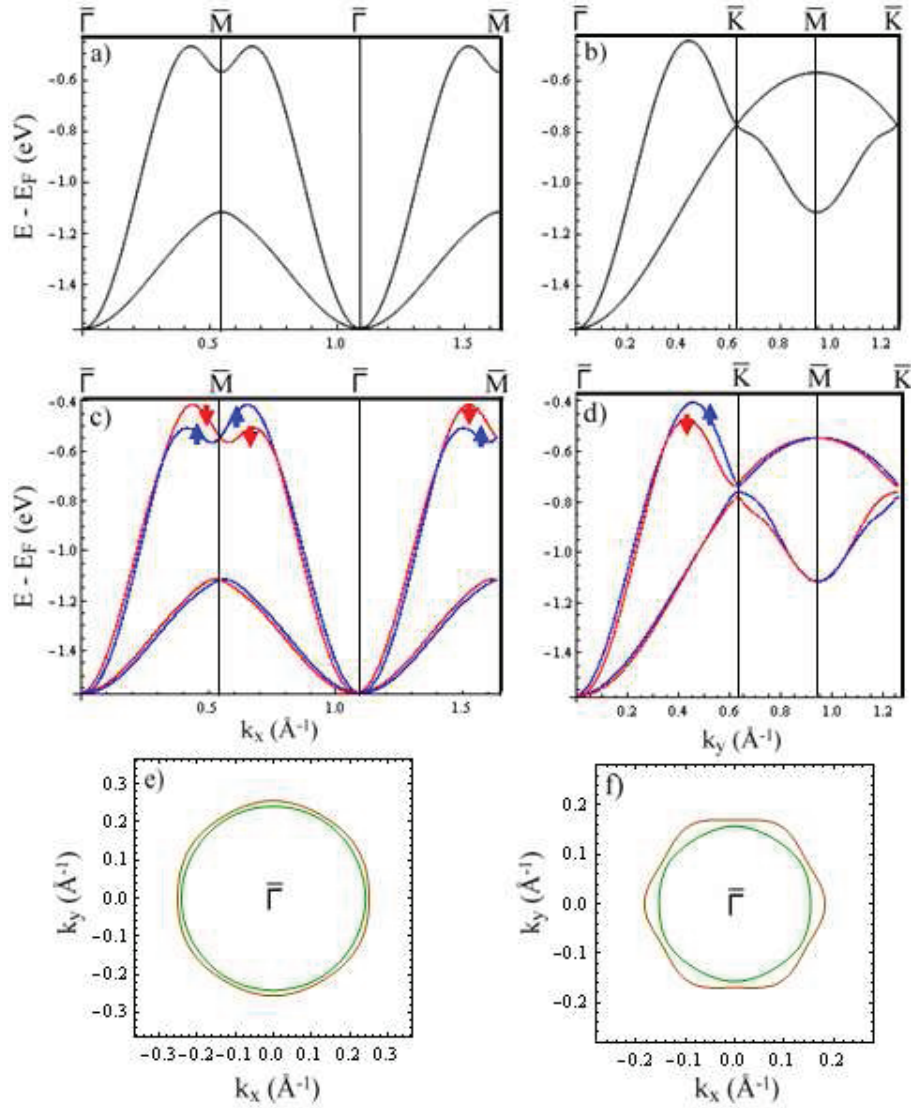


**Figure 5.10** — Calculated band topology for a 2D hexagonal lattice with a trimer basis. The simulation is based on the structural unit presented in Fig. 3.25, considers  $sp_z$ -derived orbitals and takes into account interactions up to 4<sup>th</sup>-nearest neighbors. (a), (b) Electronic band dispersion of the topmost two bands in the absence of RB coupling. (c), (d) Electronic band dispersion of the topmost two bands with RB coupling. Red and blue colors denote opposite directions of the spin-polarization vector. (e) A CE map at  $E = -0.90\text{eV}$ , revealing that the topmost band can be approximated by a RB paraboloid with negligible splitting at  $k$ -values near  $\bar{\Gamma}$ . (f) A CE map at  $E = -0.95\text{eV}$  when the SO prefactor is artificially increased by an order of magnitude. Opposite hexagonal warping of the two spin-polarized contours is a result of the system anisotropy. The in-plane orientation of the contours is consistent with the structural symmetry of the system. Brown and green colors denote opposite sign of tangential spin polarization. The values of different transfer integrals are summarized in Table 3.4.

$$H_{12} = H_{21}^* = \frac{\lambda_R}{l} \left[ 2l \sin(lk_y) + 2l \left( \frac{1}{2} + \frac{i\sqrt{3}}{2} \right) \sin \left( \frac{\sqrt{3}l}{2} k_x + \frac{l}{2} k_y \right) + 2l \left( -\frac{1}{2} + \frac{i\sqrt{3}}{2} \right) \sin \left( \frac{\sqrt{3}l}{2} k_x + \frac{l}{2} k_y \right) \right]$$

Diagonal elements are identical to Eq. (5.25) and capture the interaction of electrons with identical spins. On the other hand, off-diagonal elements represent the mathematical formulation of RB coupling. Fig. 5.9 extends the results of Fig. 5.8 by including a finite RB interaction



( $\lambda_R = 0.2$ ). The CE maps of Fig. 5.9 (b) predict that hexagonal warping has the same sign for both spin-polarized contours. This should be expected because each unit cell contains a spherically symmetric atomic basis and the system is equivalent to an isotropic NFE gas with RB interaction (Fig. 5.3). Only an atomic basis with lower symmetry can induce warping with opposite effects on the two spin-polarized contours (Fig. 5.4). In a NFE simulation this is captured by the 3<sup>rd</sup>-order  $\mathbf{k} \cdot \mathbf{p}$  perturbation term (Eq. (5.8)), while in the TB framework it must be inherent in the symmetry of  $H_{TB-SO}$  when one considers an anisotropic atomic arrangement.

In the case of a polyatomic basis in a 2D system, the degree of complexity increases substantially. The trimer arrangement of Fig. 3.25 yields a  $3 \times 3$  and  $6 \times 6$  matrix depending on whether the RB interaction has been included or not. The  $H_{TB-SO}$  Hamiltonian has to be generalized to include dissimilar  $\lambda_{pq}$  parameters:

$$H_{TB-SO} = \sum_{\langle p,q \rangle \alpha} V_{pq} c_{p\alpha}^\dagger c_{q\alpha} + i \sum_{\langle p,q \rangle \alpha\beta} \lambda_{pq} c_{p\alpha} (\boldsymbol{\sigma} \times \hat{\mathbf{d}}_{\mathbf{p}\mathbf{q}})_z c_{q\beta} \quad (5.30)$$

Analytical solutions are more challenging but still possible if interactions are restricted up to 4<sup>th</sup>-nearest neighbors. In order to diminish the number of free parameters, the values of transfer ( $V_{pq}$ ) and RB integrals ( $\lambda_{pq}$ ) can be generated by empirical power laws of the distance  $d$ :  $V(\lambda)_{pq} = ad_{pq}^{-b}$ . In this way, one arrives at two parameters for the band dispersion and two parameters for the SO splitting (prefactors  $a$  and exponents  $b$ ). Fig. 5.10 presents a comparison of the band topology for a hexagonal lattice with a trimer basis when RB coupling is turned "off" and "on". The parameter values are summarized in Table 3.4. At energies where the band dispersion can be approximated by a RB paraboloid, CE contours give indications for the opposite hexagonal warping of the two contours (Fig. 5.10 (f)). One might further notice that perfect spin degeneracy is predicted at the  $\bar{\Gamma}$  and  $\bar{M}$  points as required by time-reversal symmetry. These requirements have been respected by all levels of TB simulations presented in this section.

### 5.3.3 TB simulation - conclusions

Conclusions from the TB simulations can be summarized in the following points. TB (1) - TB (6) may be directly compared to the corresponding NFE (1) - NFE (6) points from subsection 5.2.3, thus establishing the analogies of the two approaches.

TB (1) RB spin-orbit interaction is introduced by the inclusion of the site-spin representation of  $H_{SO}$  in the model Hamiltonian.

TB (2) Electron states carrying identical spins hybridize and their interaction is captured by the first term of  $H_{TB-SO}$ . The second term (i.e.  $H_{SO}$ ), which formulates the RB effect, has no effect on their interaction.

TB (3) Lattice constant and symmetry are explicitly introduced by the form of the matrix elements.

TB (4) In-plane asymmetry is already taken into account in systems with a multiatomic basis.

TB (5) Eigenvalues correspond to positive or negative tangential spin polarization component.

TB (6) The tip orientation of the anisotropic CE contours is consistent with the structural anisotropy of the systems.

## 5.4 A comparison of the two approaches

In the present section one will attempt a comparison of the NFE and TB simulations as introduced in sections 5.2 and 5.3. The goal is to stress their equivalency despite the opposite starting points ("free" vs. "tightly-bound" electrons). Analogies and similarities have been already revealed through the concluding points of subsections 5.2.3 and 5.3.3. Therefore, in the following, a phenomenological comparison by application to a real system will be attempted.

### 5.4.1 The Au(111) surface state as a case study

The parabolic Au(111) surface state is an ideal system for this comparison. First of all, it is spin-split as has been revealed by many experimental and theoretical studies summarized in section 2.2. Secondly, it is derived from  $sp_z$  orbitals which do not require angle-dependent hybridization parameters. Finally,  $k_F$  is small compared to the size of the BZ. Therefore, the TB cosinusoidal equations maybe a good approximation at this energy range (Eq. (5.16)).

The parameters for the NFE simulation were taken from the combined experimental and theoretical study presented in Ref. [124]. These are namely  $m^* = 0.255m_e$ ,  $\alpha_R = 0.33\text{eV \AA}$  and a negative energy offset of 487meV in order to match the Fermi level position. The TB equations are those for a simple 2D hexagonal lattice with RB coupling (for example Fig. 5.9). The Au(111) lattice constant of  $2.88\text{\AA}$  was used in the simulations, while  $V$  and  $\varepsilon$  were chosen to fit the NFE results ( $V = -1.213\text{eV}$ ,  $\varepsilon = 6.792\text{eV}$ ).

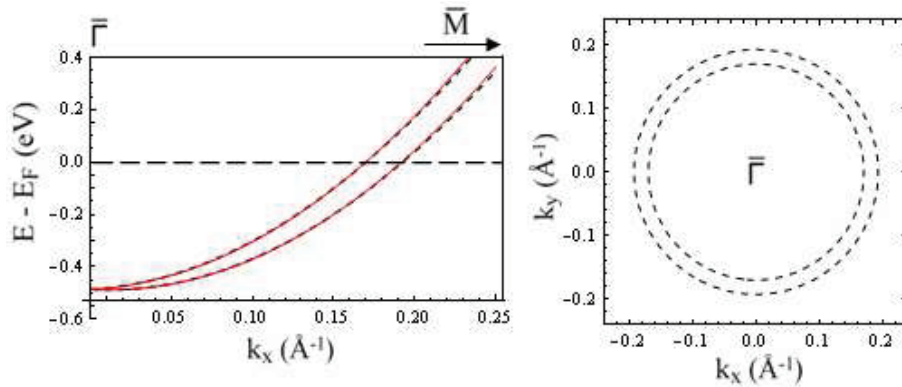


**Figure 5.11** — The  $sp_z$  surface band of Au(111) is known to be spin-orbit split due to a standard RB mechanism. (left) The TB model with  $\lambda_R = 0.039$  gives an excellent fit in the energy range of interest as shown by the perfect overlap of the TB bands (dashed curves) and a standard NFE model (solid curves) for Au(111) using the experimental values established in [124]. (right) The TB Fermi surface indicates that the hexagonal symmetry of the model does not spoil the isotropic in-plane topology of the Au surface state at small  $k$ -values.

Fig. 5.11 (a) presents a comparison of the results for a finite RB coupling (i.e.  $\lambda_R = 0.039$ ). The agreement of the two models is excellent for an energy window of around 1eV. At even higher energies, TB results are expected to deviate from the NFE parabolic behavior. Nevertheless, in the energy range of interest, TB equations with phenomenological parameters are a very good approximation for the electronic structure of the system.

$\lambda_R$  is in the order of the  $\lambda_{ij}$  parameters used for modelling the band topology of the Si(111)-Bi trimer phase (subsection 3.2.5). In the latter case, they yielded a band with giant spin-splitting. Therefore, one may conclude that the enhanced splitting in that system is indeed driven by the peculiar topology of the Si(111)-Bi spin-degenerate "parent band", rather than by the magnitude of the SO parameters.



# Chapter 6

---

## Concluding remarks

---

The conclusions of this thesis work have been already mentioned at the end of each separate chapter. Therefore, the present chapter serves merely as a summary of these remarks and aims to emphasize key points, which may have been left unnoticed even after a detailed reading.

Spin degeneracy of electronic states is the result of the combined effect of time-reversal and space inversion symmetry. An external magnetic field acts on the former (Zeeman effect). Nevertheless, it is not required in systems with broken spatial inversion. In those cases, the degeneracy is lifted by the spin-orbit interaction, termed as the Rashba-Bychkov (RB) effect. In comparison to the Zeeman effect which yields spin-polarized states with constant  $E$ -splitting, the energy separation is strongly  $\mathbf{k}$ -dependent for RB coupling. Despite these differences, RB coupling is not less important for the realization of spin-dependent transport and spintronic applications. On the contrary, it tackles the exotic question of how one can manipulate electron spins without the need of an external  $\mathbf{B}$ .

A giant RB effect has been observed in metallic surface alloys. Namely, the size of the splitting observed in a  $\text{BiAg}_2$  alloy grown on a  $\text{Ag}(111)$  surface may find important applications in the field of spintronics because it would lead to small precession lengths in a future spin FET. Despite the potential of  $\text{BiAg}_2/\text{Ag}(111)$  and related systems, the metallic character of the substrates poses serious obstacles to the observation of spin-dependent transport properties. The present thesis focused in transferring the concept of a giant RB splitting on semiconducting substrates. Two main approaches were discussed.

The first method consists of growing a  $\text{BiAg}_2$  alloy on thin silver buffers of different thicknesses, themselves deposited on a  $\text{Si}(111)$  substrate. In this way, the alloy-derived electronic states are significantly modified. Hybridization gaps were observed in the dispersion of the surface-state branches. These gaps form at the intersection of the spin-degenerate Ag quantum well states (QWS) with the spin-split alloy bands. Interestingly, the number, energy position and width of the spin-dependent hybridization gaps can be tuned by varying the thickness of the Ag buffer layer. Thereby,

the electronic structure and spin polarization near  $E_F$  can be drastically affected by a simple external parameter. This opens up the interesting possibility to modify the spin transport at one's will.

In the second method, the concept of giant RB splitting was transferred directly on a semiconducting substrate without the presence of spin-degenerate QWS which may potentially influence the transport properties of the system. The experimental realization is the 2D electronic structure formed by 1ML of Bi trimers on a Si(111) surface. As suggested by ARPES and verified by first-principles calculations, the system can be described by a RB splitting of the same order of magnitude as the Ag-based surface alloys. A phenomenological tight-binding model proposed an alternative scenario for the large spin splitting in this system; it namely revealed its intimate connection to the peculiar and highly anisotropic band topology.

The Pt(111)-Ag-Bi trilayer system has been also studied by ARPES. The complicated band structure renders spin-integrated ARPES insufficient to distinguish interface states which may exhibit RB splitting. Nevertheless, one could observe a novel surface reconstruction and use ARPES to track a strain-mediated structural transition depending on the thickness of the Ag layer.



---

## Bibliography

---

- [1] According to Prempfer et al. [119], the orientation of the finite out-of-plane component of  $\mathbf{P}$  breaks the sixfold symmetry of the underlying contours, by removing the mirror planes which point along the tips of the outer blossom-like CE contours. These generic results can be applied to our system which has the same symmetry. The orientation of the Bi trimers leaves  $\overline{\Gamma\text{KM}}$  as the only mirror plane. As a result, the symmetry-required orientation of  $\mathbf{P}$  is satisfied only if the outer hexagon tips lie within the  $\overline{\Gamma\text{M}\Gamma}$  rather than the  $\overline{\Gamma\text{KM}}$  directions as in Fig. 7 (c). 83
- [2] Notice that the TB model (Eq. (10)) with the same power-law expression for the SO parameters, would yield a momentum splitting of only  $0.012 \text{ \AA}^{-1}$  for the Au(111) surface state (see chapter 5), in agreement with the experimental results [124]. This proves that the giant splitting of the Bi/Si(111) system cannot be due to the magnitude of  $\lambda_{ij}$ . 84
- [3] P. Aebi, J. Osterwalder, R. Fasel, D. Naumović, and L. Schlapbach. Fermi surface mapping with photoelectrons at UV energies. *Surf. Sci.*, 307-309:917, 1994. 103
- [4] S. Agergaard, C. Søndergaard, H. Li, M. B. Nielsen, S. V. Hoffmann, Z. Li, and Ph. Hofmann. The effect of reduced dimensionality on a semimetal: the electronic structure of the Bi(110) surface. *New J. Phys.*, 3:15.1, 2001. 35
- [5] A. Animalu. Spin-orbit coupling effects in metals and semiconductors. *Philos. Mag.*, 13:53, 1966. 29
- [6] N. W. Ashcroft and N. D. Mermin. *Solid State Physics*. Thompson Learning, Inc., 1976. 95, 103, 107
- [7] C. R. Ast, J. Henk, A. Ernst, L. Moreschini, M. C. Falub, D. Pacilé, P. Bruno, K. Kern, and M. Grioni. Giant Spin Splitting through Surface Alloying. *Phys. Rev. Lett.*, 98:186807, 2007. 37, 38, 39, 40, 41, 56, 58, 60, 74, 81, 85, 89
- [8] C. R. Ast and H. Höchst. Fermi Surface of Bi(111) Measured by Photoemission Spectroscopy. *Phys. Rev. Lett.*, 87:177602, 2001. 34, 35
- [9] C. R. Ast and H. Höchst. Indication of Charge-Density-Wave formation in Bi(111). *Phys. Rev. Lett.*, 90:016403, 2003. 35

- [10] C. R. Ast and H. Höchst. The Fermi surfaces of thin Sb(111) films. *J. Electron Spectr. Rel. Phenom.*, 137-140:441, 2004. 35
- [11] C. R. Ast, D. Pacilé, L. Moreschini, M. C. Falub, M. Papagno, K. Kern, and M. Grioni. Spin-orbit split two-dimensional electron gas with tunable Rashba and Fermi energy. *Phys. Rev. B*, 77:081407, 2008. 43, 44, 58, 60, 62
- [12] C. R. Ast, G. Wittich, P. Wahl, R. Vogelsang, D. Pacilé, M. C. Falub, L. Moreschini, M. Papagno, M. Grioni, and K. Kern. Local detection of spin-orbit splitting by scanning tunneling spectroscopy. *Phys. Rev. B*, 75:201401, 2007. 39, 43
- [13] D. D. Awschalom and M. E. Flatté. Challenges for semiconductor spintronics. *Nature Phys.*, 3:153, 2007. 46, 56
- [14] M. N. Baibich, J. M. Broto, A. Fert, F. Nguyen Van Dau, F. Petroff, P. Etienne, G. Creuzet, A. Friederich, and J. Chazelas. Giant Magnetoresistance of (001)Fe/(001)Cr Magnetic Superlattices. *Phys. Rev. Lett.*, 61:2472, 1988. 46
- [15] I. Barke, Fan Zheng, T. K. Rügheimer, and F. J. Himpsel. Experimental Evidence for Spin-Split Bands in a One-Dimensional Chain Structure. *Phys. Rev Lett.*, 97:226405, 2006. 60
- [16] J. V. Barth, H. Brune, G. Ertl, and R. J. Behm. Scanning tunneling microscopy observations on the reconstructed Au(111) surface: Atomic structure, long-range superstructure, rotational domains, and surface defects. *Phys. Rev. B*, 42:9307, 1990. 94
- [17] F. Baumberger, A. Tamai, M. Muntwiler, T. Greber, and J. Osterwalder. The electronic structure of a surfactant layer: Pb/Cu(1 1 1). *Surf. Sci.*, 532-535:82, 2003. 103
- [18] A. Bendounan. private communication. 96
- [19] H. Bentmann, F. Forster, G. Bihlmayer, E. V. Chulkov, L. Moreschini, M. Grioni, and F. Reinert. Origin and manipulation of the Rashba splitting in surface alloys. *Europhys. Lett.*, 87:37003, 2009. 39, 43, 44
- [20] C. N. Berglund and W. E. Spicer. Photoemission Studies of Copper and Silver: Experiment. *Phys. Rev.*, 136:A1044, 1964. 6
- [21] C. N. Berglund and W. E. Spicer. Photoemission Studies of Copper and Silver: Theory. *Phys. Rev.*, 136:A1030, 1964. 6
- [22] G. Bihlmayer, S. Blügel, and E. V. Chulkov. Enhanced Rashba spin-orbit splitting in Bi/Ag(111) and Pb/Ag(111) surface alloys from first principles. *Phys. Rev. B*, 75:195414, 2007. 41, 43, 51, 52, 54, 74
- [23] G. Bihlmayer, Y. M. Koroteev, P. M. Echenique, E. V. Chulkov, and S. Blügel. The Rashba-effect at metallic surfaces. *Surf. Sci.*, 600:3888, 2006. 32, 33, 41, 74

- [24] G. Binasch, P. Grünberg, F. Saurenbach, and W. Zinn. Enhanced magnetoresistance in layered magnetic structures with antiferromagnetic interlayer exchange. *Phys. Rev. B*, 39:4828, 1989. 46
- [25] H. Brune, M. Giovannini, K. Bromann, and K. Kern. Self-organized growth of nanostructure arrays on strain-relief patterns. *Nature*, 394:451, 1998. 94
- [26] H. Brune, H. Röder, C. Boragno, and K. Kern. Strain relief at hexagonal-close-packed interfaces. *Phys. Rev. B*, 49:2997, 1994. 93, 94, 95, 96, 103
- [27] P. Bruno. Theory of interlayer magnetic coupling. *Phys. Rev. B*, 52:411, 1995. 58
- [28] Y. A. Bychkov and E. I. Rashba. Properties of a 2D electron gas with lifted spectral degeneracy. *JETP Lett.*, 39:78, 1984. 24, 29, 56, 73, 79
- [29] E. Cappelluti, C. Grimaldi, and F. Marsiglio. Topological Change of the Fermi Surface in Low-Density Rashba Gases: Applications to Superconductivity. *Phys. Rev. Lett.*, 98:167002, 2007. 25, 42, 43
- [30] H. Cercellier, C. Didiot, Y. Fagot-Revurat, B. Kierren, L. Moreau, and D. Malterre. Interplay between structural, chemical, and spectroscopic properties of Ag/Au(111) epitaxial ultrathin films: A way to tune the Rashba coupling. *Phys. Rev. B*, 73:195413, 2006. 30, 31, 35, 37, 39
- [31] H. Cercellier, Y. Fagot-Revurat, B. Kierren, F. Reinert, D. Popovic, and D. Malterre. Spin-orbit splitting of the Shockley state in the Ag/Au(111) interface. *Phys. Rev. B*, 70:193412, 2004. 30, 35
- [32] D. D. Chambliss, R. J. Wilson, and S. Chiang. Nucleation of ordered Ni island arrays on Au(111) by surface-lattice dislocations. *Phys. Rev. Lett.*, 66:1721, 1991. 94
- [33] C. Cheng and K. Kunc. Structure and stability of Bi layers on Si(111) and Ge(111) surfaces. *Phys. Rev. B*, 56:10283, 1997. 67
- [34] T.-C. Chiang. Photoemission studies of quantum well states in thin films. *Surf. Sci. Rep.*, 39:181, 2000. 58
- [35] A. Damascelli, Z. Hussain, and Z.-X. Shen. Angle-resolved photoemission studies of the cuprate superconductors. *Rev. Mod. Phys.*, 75:473, 2003. 11
- [36] S. Datta and B. Das. Electronic analog of the electro-optic modulator. *Appl. Phys. Lett.*, 56:665, 1990. 46, 47, 48, 56, 74, 88
- [37] W. Di, K. E. Smith, and S. D. Kevan. Surface Fermi contours and phonon anomalies on Pt(111). *Phys. Rev. B*, 43:12062, 1991. 95
- [38] W. Di, K. E. Smith, and S. D. Kevan. Angle-resolved photoemission study of the clean and hydrogen-covered Pt(111) surface. *Phys. Rev. B*, 45:3652, 1992. 95

- [39] C. Didiot, Y. Fagot-Revurat, S. Pons, B. Kierren, C. Chatelain, and D. Malterre. Reconstruction-induced multiple gaps in the weak coupling limit: The surface bands of Au(111) vicinal surfaces. *Phys. Rev. B*, 74:081404, 2006. 60, 79
- [40] J. Hugo Dil, F. Meier, J. Lobo-Checa, L. Patthey, G. Bihlmayer, and J. Osterwalder. Rashba-Type Spin-Orbit Splitting of Quantum Well States in Ultrathin Pb Films. *Phys. Rev Lett.*, 101:266802, 2008. 74, 91
- [41] G. Dresselhaus. Spin-Orbit Coupling Effects in Zinc Blende Structures. *Phys. Rev.*, 100:580, 1955. 73
- [42] E. N. Economou. *Solid State Physics Vol. I: Metals, Semiconductors, Insulators*. Crete University Press, 1997. 113
- [43] F. Forster, A. Bendounan, F. Reinert, V. G. Grigoryan, and M. Springborg. The Shockley-type surface state on Ar covered Au(111): High resolution photoemission results and the description by slab-layer DFT calculations. *Surf. Sci.*, 601:5595, 2007. 36, 93
- [44] F. Forster, S. Hüfner, and F. Reinert. Rare Gases on Noble-Metal Surfaces: An Angle-Resolved Photoemission Study with High Energy Resolution. *J. Phys. Chem. B*, 108:14692, 2004. 36, 37, 39, 42, 56, 93
- [45] E. Frantzeskakis, A. Crepaldi, S. Pons, K. Kern, and M. Grioni. Tuning the giant Rashba effect on a BiAg<sub>2</sub> surface alloy: Two different approaches. *J. Electron Spectr. Rel. Phenom.*, 181:88, 2010. 43, 45, 53, 55, 64, 74, 95
- [46] E. Frantzeskakis, S. Pons, and M. Grioni. Giant spin-orbit splitting in a surface alloy grown on a Si substrate: BiAg<sub>2</sub>/Ag/Si(111). *Physica B*, 404:419, 2009. 64
- [47] E. Frantzeskakis, S. Pons, and M. Grioni. Band structure scenario for the giant spin-orbit splitting observed at the Bi/Si(111) interface. *Phys. Rev B*, 82:085440, 2010. 103
- [48] E. Frantzeskakis, S. Pons, H. Mirhosseini, J. Henk, C. R. Ast, and M. Grioni. Tunable Spin Gaps in a Quantum-Confined Geometry. *Phys. Rev Lett.*, 101:196805, 2008. 64, 74, 95
- [49] L. Fu. Hexagonal Warping Effects in the Surface States of the Topological Insulator Bi<sub>2</sub>Ti<sub>3</sub>. *Phys. Rev. Lett.*, 103:266801, 2009. 40, 82
- [50] I. Gierz, B. Stadtmüller, J. Vuorinen, M. Lindroos, J. Hugo Dil, K. Kern, and C. R. Ast. The Structural Influence on the Rashba-type Spin-Splitting in Surface Alloys. *Phys. Rev. B*, 81:245430, 2010. 45
- [51] I. Gierz, T. Suzuki, E. Frantzeskakis, S. Pons, S. Ostanin, A. Ernst, J. Henk, M. Grioni, K. Kern, and C. R. Ast. Silicon Surface with Giant Spin Splitting. *Phys. Rev. Lett.*, 103:046803, 2009. 66, 68, 69, 70, 71, 72, 74, 76, 77, 78, 81, 83, 85

- [52] F. Greullet, C. Tiusan, F. Montaigne, M. Hehn, D. Halley, O. Bengone, M. Bowen, and W. Weber. Evidence of a Symmetry-Dependent Metallic Barrier in Fully Epitaxial MgO Based Magnetic Tunnel Junctions. *Phys. Rev Lett.*, 99:187202, 2007. 56
- [53] S. Hatta, T. Aruga, C. Kato, S. Takahashi, H. Okuyama, A. Harasawa, T. Okuda, and T. Kinoshita. Band structure of Tl/Ge(111)-(3 × 1): Angle-resolved photoemission and first-principles prediction of giant Rashba effect. *Phys. Rev B*, 77:245436, 2008. 92
- [54] S. Hatta, T. Aruga, Y. Ohtsubo, and H. Okuyama. Large Rashba spin splitting of surface resonance bands on semiconductor surface. *Phys. Rev. B*, 80:113309, 2009. 74, 83, 92
- [55] K. He, T. Hirahara, T. Okuda, S. Hasegawa, A. Kazikazi, and I. Matsuda. Spin Polarization of Quantum Well States in Ag Films Induced by the Rashba Effect at the Surface. *Phys. Rev Lett.*, 101:107604, 2008. 64, 74
- [56] K. He, Y. Takeichi, M. Ogawa, T. Okuda, P. Moras, D. Topwal, A. Harasawa, T. Hirahara, C. Carbone, A. Kazikazi, and I. Matsuda. Direct Spectroscopic Evidence of Spin-Dependent Hybridization between Rashba-Split Surface States and Quantum-Well States. *Phys. Rev Lett.*, 104:156805, 2010. 65
- [57] J. Henk, A. Ernst, and P. Bruno. Spin polarization of the L-gap surface states on Au(111). *Phys. Rev. B*, 68:165416, 2003. 33
- [58] J. Henk, A. Ernst, and P. Bruno. Spin polarization of the L-gap surface states on Au(111): a first-principles investigation. *Surf. Sci.*, 566:482, 2004. 33
- [59] J. Henk, M. Hoesch, J. Osterwalder, A. Ernst, and P. Bruno. Spin-orbit coupling in the L-gap surface states of Au(111): spin-resolved photoemission experiments and first-principles calculations. *J. Phys.: Condens. Matter*, 16:7581, 2004. 33, 34, 73
- [60] F. J. Himpsel, G. Hollinger, and R. A. Pollak. Determination of the Fermi-level pinning position at Si(111) surfaces. *Phys. Rev B*, 28:7014, 1983. 69
- [61] T. Hirahara, T. Komorida, A. Sato, G. Bihlmayer, E. V. Chulkov, K. He, I. Matsuda, and S. Hasegawa. Manipulating quantum-well states by surface alloying: Pb on ultrathin Ag films. *Phys. Rev B*, 78:035408, 2008. 51, 52, 59
- [62] T. Hirahara, K. Miyamoto, I. Matsuda, T. Kadono, A. Kimura, T. Nagao, G. Bihlmayer, E. V. Chulkov, S. Qiao, K. Shimada, H. Namatame, M. Taniguchi, and S. Hasegawa. Direct observation of spin splitting in bismuth surface states. *Phys. Rev B*, 76:153305, 2007. 56, 62
- [63] T. Hirahara, T. Nagao, I. Matsuda, G. Bihlmayer, E. V. Chulkov, Yu. M. Koroteev, P. M. Echenique, M. Saito, and S. Hasegawa. Role of Spin-Orbit Coupling and Hybridization Effects in the Electronic Structure of Ultrathin Bi Films. *Phys. Rev Lett.*, 97:146803, 2006. 56, 62, 74, 91

- [64] M. Hochstrasser, J. G. Tobin, E. Rotenberg, and S. D. Kevan. Spin-Resolved Photoemission of Surface States of W(110)-(1×1)H. *Phys. Rev. Lett.*, 89:216802, 2002. 35, 36, 73
- [65] M. Hoesch, T. Greber, V. N. Petrov, M. Muntwiler, M. Hengsberger, W. Auwärter, and J. Osterwalder. Spin-polarized Fermi surface mapping. *J. Electron Spectr. Rel. Phenom.*, 124:263, 2002. 34
- [66] M. Hoesch, M. Muntwiler, V. N. Petrov, M. Hengsberger, L. Patthey, M. Shi, M. Falub, T. Greber, and J. Osterwalder. Spin structure of the Shockley surface state on Au(111). *Phys. Rev. B*, 69:241401, 2004. 34
- [67] Ph. Hofmann. *Solid State Physics*. Wiley-VCH, 2008. 7, 8, 106
- [68] D. Hsieh, Y. Xia, L. Wray, D. Qian, A. Pal, J. H. Dil, J. Osterwalder, F. Meier, G. Bihlmayer, C. L. Kane, Y. S. Hor, R. J. Cava, and M. Z. Hasan. Observation of Unconventional Quantum Spin Textures in Topological Insulators. *Science*, 323:919, 2009. 89
- [69] L. Huang, S. Jay Chey, and J. H. Weaver. Metastable structure and critical thicknesses: Ag on Si(111)7×7. *Surf. Sci. Lett.*, 416:L1101, 1998. 52
- [70] S. Hüfner. *Photoelectron Spectroscopy: Principles and Applications*. Springer-Verlag, 1995. 5, 6
- [71] M. Jałochowski, E. Bauer, H. Knoppe, and G. Lilienkamp. Experimental evidence for quantum-size-effect fine structures in the resistivity of ultrathin Pb and Pb-In films. *Phys. Rev B*, 45:13607, 1992. 58
- [72] X. Jiang, R. Wang, S. van Dijken, R. Shelby, R. Macfarlane, G. S. Solomon, J. Harris, and S. S. P. Parkin. Optical Detection of Hot-Electron Spin Injection into GaAs from a Magnetic Tunnel Transistor Source. *Phys. Rev. Lett.*, 90:256603, 2003. 49
- [73] B. T. Jonker, Y. D. Park, B. R. Bennett, H. D. Cheong, G. Kioseoglou, and A. Petrou. Robust electrical spin injection into a semiconductor heterostructure. *Phys. Rev. B*, 62:8180, 2000. 49
- [74] C. L. Kane and E. J. Mele.  $Z_2$  Topological Order and the Quantum Spin Hall Effect. *Phys. Rev. Lett.*, 95:146802, 2005. 84
- [75] Y. Kato, R. C. Myers, A. C. Gossard, and D. D. Awschalom. Coherent spin manipulation without magnetic fields in strained semiconductors. *Nature*, 427:50, 2004. 56
- [76] J. M. Kikkawa and D. D. Awschalom. Resonant Spin Amplification in n-Type GaAs. *Phys. Rev. Lett.*, 80:4313, 1998. 46
- [77] J. M. Kikkawa, I. P. Shmorchkova, N. Samarth, and D. D. Awschalom. Room-Temperature Spin Memory in Two-Dimensional Electron Gases. *Science*, 277:1284, 1997. 46



- [78] J. K. Kim, K. S. Kim, J. L. McChesney, E. Rotenberg, H. N. Hwang, C. C. Hwang, and H. W. Yeom. Two-dimensional electron gas formed on the indium-adsorbed Si(111) $\sqrt{3} \times \sqrt{3}$ -Au surface. *Phys. Rev. B*, 80:075312, 2009. 83, 89
- [79] Y. K. Kim, J. S. Kim, C. C. Hwang, S. P. Shresta, K. S. An, and C. Y. Park. Electronic Structure of the  $\beta$ -Si(111)  $\sqrt{3} \times \sqrt{3}$ -Bi Surface. *J. of the Korean Phys. Soc.*, 39:1032, 2001. 66, 67, 76
- [80] Y. K. Kim, J. S. Kim, C. C. Hwang, S. P. Shresta, and C. Y. Park. Angle-resolved ultraviolet photoelectron spectroscopy study on the  $\alpha$ -Si(111) $\sqrt{3} \times \sqrt{3}$ -Bi surface. *Surf. Sci.*, 498:116, 2002. 67, 75
- [81] T. Kinoshita, S. Kono, and H. Nagayoshi. Angle-Resolved Ultraviolet Photoelectron Spectroscopy Study of the Si(111) $\sqrt{3} \times \sqrt{3}$ -Bi Surface. *J. of the Phys. Soc. of Japan*, 56:2511, 1987. 67, 76
- [82] T. Koga, J. Nitta, H. Takayanagi, and S. Datta. Spin Filter Device Based on the Rashba Effect Using a Nonmagnetic Resonant Tunneling Diode. *Phys. Rev. Lett.*, 88:126601, 2002. 56
- [83] J. Könemann, R. J. Haug, D. K. Maude, V. I. Fal'ko, and B. L. Altshuler. Spin-Orbit Coupling and Anisotropy of Spin Splitting in Quantum Dots. *Phys. Rev. Lett.*, 94:226404, 2005. 73
- [84] H. C. Koo, J. H. Kwon, J. Eom, J. Chang, S. H. Han, and M. Johnson. Control of Spin Precession in a Spin-Injected Field Effect Transistor. *Science*, 325:1515, 2009. 74, 88
- [85] Y. M. Koroteev, G. Bihlmayer, J. E. Gayone, E. V. Chulkov, S. Blügel, P. M. Echenique, and Ph. Hofmann. Strong Spin-Orbit Splitting on Bi Surfaces. *Phys. Rev. Lett.*, 93:046403, 2004. 34, 35, 39, 73, 91
- [86] O. Krupin, G. Bihlmayer, S. Gorovikov, J. E. Prieto, K. Döbrich, S. Blügel, and G. Kaindl. Rashba effect at magnetic metal surfaces. *Phys. Rev. B*, 71:201403, 2005. 32, 33
- [87] T. Kuzumaki, T. Shirasawa, S. Mizuno, N. Ueno, H. Tochiyama, and K. Sakamoto. Re-investigation of the Bi-induced Si(111)- $\sqrt{3} \times \sqrt{3}$  surfaces by low-energy electron diffraction. *Surf. Sci.*, 604:1044, 2010. 67, 70
- [88] R. Landauer. Irreversibility and heat generation in the computing process. *IBM J. Res. Dev.*, 5:183, 1961. 46
- [89] S. LaShell, B. McDougall, and E. Jensen. Spin Splitting of an Au(111) Surface State Band Observed with Angle Resolved Photoelectron Spectroscopy. *Phys. Rev. Lett.*, 77:3419, 1996. 29, 30, 35, 39, 56, 73
- [90] J. Y. Lee and M. H. Kang. Electronic Structure of the Conjugate Honeycomb-Chained-Trimer Model for the Au/Si(111)- $\sqrt{3} \times \sqrt{3}$ R30° Surface. *J. Korean Phys. Soc.*, 53:3671, 2008. 83, 89

- [91] G. Liu, Z. Wang, and S.-S. Li. Spin-Hall effect in the generalized honeycomb lattice with Rashba spin-orbit interaction. *Physics Letters A*, 373:2091, 2009. 84
- [92] G. Liu, P. Zhang, Z. Wang, and S.-S. Li. Spin Hall effect on the kagome lattice with Rashba spin-orbit interaction. *Phys. Rev. B*, 79:035323, 2009. 84
- [93] D. Malterre, B. Kierren, Y. Fagot-Revurat, S. Pons, A. Tejada, C. Didiot, H. Cercellier, and A. Bendounan. Arpes and STS investigation of Shockley states in thin metallic films and periodic nanostructures. *New J. Phys.*, 9:391, 2007. 56, 73, 74
- [94] F. Meier, H. Dil, J. Lobo-Checa, L. Patthey, and J. Osterwalder. Quantitative vectorial spin analysis in ARPES: Bi/Ag(111) and Pb/Ag(111). *Phys. Rev. B*, 77:165431, 2008. 41, 43, 58, 74
- [95] F. Meier, V. Petrov, S. Guerrero, C. Mudry, L. Patthey, J. Osterwalder, and J. Hugo Dil. Unconventional Fermi surface spin textures in the  $\text{Bi}_x\text{Pb}_{1-x}/\text{Ag}(111)$  surface alloy. *Phys. Rev. B*, 79:241408, 2009. 43
- [96] M. B. J. Meinders. PhD thesis, University of Groningen, The Netherlands, 1994. 10
- [97] J. B. Miller, D. M. Zumbühl, C. M. Marcus, Y. B. Lyanda-Geller, D. Goldhaber-Gordon, K. Campman, and A. C. Gossard. Gate-Controlled Spin-Orbit Quantum Interference Effects in Lateral Transport. *Phys. Rev. Lett.*, 90:076807, 2003. 49
- [98] R. H. Miwa, T. M. Schmidt, and G. P. Srivastava. Bi covered Si(111) surface revisited. *J. Phys.: Condens. Matter*, 15:2441, 2003. 67
- [99] C. E. Moore. *Atomic Energy Levels*. National Bureau of Standards, Washington, DC, 1949. 31, 44
- [100] L. Moreschini, A. Bendounan, C. R. Ast, F. Reinert, M. Falub, and M. Grioni. Effect of rare-gas adsorption on the spin-orbit split bands of a surface alloy: Xe on  $\text{Ag}(111)-(\sqrt{3} \times \sqrt{3})R30^\circ\text{-Bi}$ . *Phys. Rev. B*, 77:115407, 2008. 42, 93
- [101] L. Moreschini, A. Bendounan, H. Bentmann, M. Assig, K. Kern, F. Reinert, J. Henk, C. R. Ast, and M. Grioni. Influence of the substrate on the spin-orbit splitting in surface alloys on (111) noble-metal surfaces. *Phys. Rev. B*, 80:035438, 2009. 39, 44
- [102] L. Moreschini, A. Bendounan, I. Gierz, C. R. Ast, H. Mirhosseini, H. Höchst, K. Kern, J. Henk, A. Ernst, S. Ostanin, F. Reinert, and M. Grioni. Assessing the atomic contribution to the Rashba spin-orbit splitting in surface alloys: Sb/Ag(111). *Phys. Rev. B*, 79:075424, 2009. 39, 43, 44, 81
- [103] A. Mugarza, A. Mascaraque, V. Repain, S. Rousset, K. N. Altmann, F. J. Himpsel, Yu. M. Koroteev, E. V. Chulkov, F. J. Garcia de Abajo, and J. E. Ortega. Lateral quantum wells at vicinal Au(111) studied with angle-resolved photoemission. *Phys. Rev. B*, 66:245419, 2002. 30

- [104] M. Muntwiler, M. Hoesch, V. N. Petrov, M. Hengsberger, L. Patthey, M. Shi, M. Falub, T. Greber, and J. Osterwalder. Spin- and angle-resolved photoemission spectroscopy study of the Au(111) Shockley surface state. *J. Electron Spectr. Rel. Phen.*, 137-140:119, 2004. 34
- [105] M. Nagano, A. Kodama, T. Shishidou, and T. Oguchi. A first-principles study on the Rashba effect in surface systems. *J. Phys.: Condens. Matter*, 21:064239, 2009. 72, 74
- [106] T. Nakagawa, O. Ohgami, Y. Saito, H. Okuyama, M. Nishijima, and T. Aruga. Transition between tetramer and monomer phases driven by vacancy configuration entropy on Bi/Ag(001). *Phys. Rev. B*, 75:155409, 2007. 37
- [107] S. Nakatani, T. Takahashi, Y. Kuwahara, and M. Aono. Use of x-ray reflectivity for determining the Si(111) $\sqrt{3} \times \sqrt{3}$ -Bi surface structures. *Phys. Rev. B*, 52:R8711, 1995. 66, 75
- [108] G. Nicolay, F. Reinert, S. Hüfner, and P. Blaha. Spin-orbit splitting of the L-gap surface state on Au(111) and Ag(111). *Phys. Rev. B*, 65:033407, 2001. 29, 30, 31
- [109] J. Nitta, T. Akazaki, H. Takayanagi, and T. Enoki. Gate Control of Spin-Orbit Interaction in an Inverted In<sub>0.53</sub>Ga<sub>0.47</sub>As/In<sub>0.52</sub>Al<sub>0.48</sub>As Heterostructure. *Phys. Rev. Lett.*, 78:1335, 1997. 39, 49, 56
- [110] T. Oguchi and T. Shishidou. The surface Rashba effect: a  $k \cdot p$  perturbation approach. *J. Phys.: Condens. Matter*, 21:092001, 2009. 89
- [111] J. E. Ortega and F. J. Himpsel. Quantum well states as mediators of magnetic coupling in superlattices. *Phys. Rev Lett.*, 69:844, 1992. 58
- [112] J. E. Ortega, F. J. Himpsel, G. J. Mankey, and R. F. Willis. Quantum-well states and magnetic coupling between ferromagnets through a noble-metal layer. *Phys. Rev B*, 47:1540, 1993. 58
- [113] D. Pacilé, C. R. Ast, M. Papagno, C. Da Silva, L. Moreschini, M. Falub, A. P. Seitsonen, and M. Grioni. Electronic structure of an ordered Pb/Ag(111) surface alloy: Theory and experiment. *Phys. Rev. B*, 73:245429, 2006. 37, 38, 39, 41
- [114] C. Park, R. Z. Bakhtizin, T. Hashizume, and T. Sakurai. Scanning Tunneling Microscopy of  $\sqrt{3} \times \sqrt{3}$ -Bi Reconstruction on the Si(111) Surface. *Jpn. J. Appl. Phys.*, 32:L290, 1993. 66
- [115] C. Park, R. Z. Bakhtizin, T. Hashizume, and T. Sakurai. Structure of the Bi/Si(111) Surface by Field-Ion Scanning Tunneling Microscopy. *Jpn. J. Appl. Phys.*, 32:1416, 1993. 66
- [116] L. Perfetti, C. Rojas, A. Reginaldi, L. Gavioli, H. Berger, G. Margaritondo, M. Grioni, R. Gaál, L. Forró, and F. Rullier Albenque. High-resolution angle-resolved photoemission investigation of the quasiparticle scattering processes in a model Fermi liquid: 1T-TiTe<sub>2</sub>. *Phys. Rev. B*, 64:115102, 2001. 13

- [117] L. Petersen and P. Hedegård. A simple tight-binding model of spin-orbit splitting of s-derived surface states. *Surf. Sci.*, 459:49, 2000. 31, 32, 74, 84
- [118] D. Popovic, F. Reinert, S. Hüfner, V. G. Grigoryan, M. Springborg, H. Cercellier, Y. Fagot-Revurat, B. Kierren, and D. Malterre. High-resolution photoemission on Ag/Au(111): Spin-orbit splitting and electron localization of the surface state. *Phys. Rev. B*, 72:045419, 2005. 30, 35, 39
- [119] J. Prempfer, M. Trautmann, J. Henk, and P. Bruno. Spin-orbit splitting in an anisotropic two-dimensional electron gas. *Phys. Rev. B*, 76:073310, 2007. 39, 40, 41, 44, 56, 58, 74, 81, 82, 83, 87, 103, 111, 125
- [120] A. Ramstad, S. Raaen, and N. Barrett. Electronic structure of the La-Pt(111) surface alloy. *Surf. Sci.*, 448:179, 2000. 95
- [121] G. Rangelov, Th. Fauster, U. Strüber, and J. Küppers. Stacking of Ag layers on Pt(111). *Surf. Sci.*, 331-333:948, 1995. 93, 95, 103
- [122] F. Reinert. Spin-orbit interaction in the photoemission spectra of noble metal surface states. *J. Phys.: Condens. Matter*, 15:S693, 2003. 31, 73
- [123] F. Reinert, G. Nicolay, B. Eltner, S. Schmidt, S. Hüfner, U. Probst, and E. Bucher. Observation of a BCS spectral function in a conventional superconductor by photoelectron spectroscopy. *Phys. Rev. Lett.*, 85:3930, 2000. 11
- [124] F. Reinert, G. Nicolay, S. Schmidt, D. Ehm, and S. Hüfner. Direct measurements of the L-gap surface states on the (111) face of noble metals by photoelectron spectroscopy. *Phys. Rev. B*, 63:115415, 2001. 29, 120, 125
- [125] H. Röder, K. Bromann, H. Brune, and K. Kern. Strain-mediated two-dimensional growth kinetics in metal heteroepitaxy: Ag/Pt(111). *Surf. Sci.*, 376:13, 1997. 94, 103
- [126] H. Röder, H. Brune, J.-P. Bucher, and K. Kern. Changing morphology of metallic monolayers via temperature controlled heteroepitaxial growth. *Surf. Sci.*, 298:121, 1993. 103
- [127] H. Röder, R. Schuster, H. Brune, and K. Kern. Monolayer-Confined Mixing at the Ag-Pt(111) Interface. *Phys. Rev. Lett.*, 71:2086, 1993. 103
- [128] J. M. Roesler, T. Miller, and T.-C. Chiang. Photoelectron holography studies of Bi on Si(111). *Surf. Sci.*, 417:L1143, 1998. 66
- [129] E. Rotenberg, J. W. Chung, and S. D. Kevan. Spin-Orbit Coupling Induced Surface Band Splitting in Li/W(110) and Li/Mo(110). *Phys. Rev. Lett.*, 82:4066, 1999. 30, 35, 36, 56, 73
- [130] E. Rotenberg and S. D. Kevan. Evolution of Fermi Level Crossings versus H Coverage on W(110). *Phys. Rev. Lett.*, 80:2905, 1998. 35

- [131] A. Rüegg, J. Wen, and G. A. Fiete. Topological insulators on the decorated honeycomb lattice. *Phys. Rev B*, 81:205115, 2010. 84
- [132] K. Sakamoto, H. Kakuta, K. Sugawara, K. Miyamoto, A. Kimura, T. Kuzumaki, N. Ueno, E. Annese, J. Fujii, A. Kodama, T. Shishidou, H. Namatame, M. Taniguchi, T. Sato, T. Takahashi, and T. Oguchi. Peculiar Rashba Splitting Originating from the Two-Dimensional Symmetry of the Surface. *Phys. Rev. Lett.*, 103:156801, 2009. 72, 74, 76, 77, 78, 85
- [133] J. F. Sánchez-Royo, J. Avila, V. Pérez-Dieste, M. De Seta, and M. C. Asensio. Two-domains bulklike Fermi surface of Ag films deposited onto Si(111)- $7\times 7$ . *Phys. Rev B*, 66:035401, 2002. 58
- [134] G. A. Sawatzky. Testing Fermi-liquid models. *Nature*, 342:480, 1989. 10
- [135] T. M. Schmidt, R. H. Miwa, and G. P. Srivastava. STM Images and Energetics of the Bi-covered ( $\sqrt{3} \times \sqrt{3}$ ) Reconstructed Si(111) Surface. *Brazilian Journal of Physics*, 34:629, 2004. 67
- [136] A. M. Shikin, A. Varykhalov, G. V. Prudnikova, D. Usachov, V. K. Adamchuk, Y. Yamada, J. D. Riley, and O. Rader. Origin of Spin-Orbit Splitting for Monolayers of Au and Ag on W(110) and Mo(110). *Phys. Rev. Lett.*, 100:057601, 2008. 35
- [137] R. Shioda, A. Kawazu, A. A. Baski, C. F. Quate, and J. Nogami. Bi on Si(111): Two phases of the  $\sqrt{3} \times \sqrt{3}$  surface reconstruction. *Phys. Rev B*, 48:4895, 1993. 66
- [138] N. V. Smith, P. Thiry, and Y. Petroff. Photoemission linewidths and quasiparticle lifetimes. *Phys. Rev. B*, 47:15476, 1993. 13
- [139] Specs GmbH. *PHOIBOS CCD Imaging Detector*, 1.13 edition, 11 2005. 16
- [140] Specs GmbH. *PHOIBOS Hemispherical Energy Analyzer Series PHOIBOS 150 PHOIBOS 100*, 2.08 edition, 03 2006. 13
- [141] N. J. Speer, S.-T. Tang, T. Miller, and T.-C. Chiang. Coherent Electronic Fringe Structure in Incommensurate Silver-Silicon Quantum Wells. *Science*, 314:804, 2006. 53, 57, 58, 60
- [142] D. Stein, K. v. Klitzing, and G. Weimann. Electron Spin Resonance on GaAs-Al<sub>x</sub>Ga<sub>1-x</sub>As Heterostructures. *Phys. Rev. Lett.*, 51:130, 1983. 29
- [143] H. L. Stormer, Z. Schlesinger, A. Chang, D. C. Tsui, A. C. Gossard, and W. Wiegmann. Energy Structure and Quantized Hall Effect of Two-Dimensional Holes. *Phys. Rev. Lett.*, 51:126, 1983. 29
- [144] K. Sugawara, T. Sato, S. Souma, T. Takahashi, M. Arai, and T. Sasaki. Fermi Surface and Anisotropic Spin-Orbit Coupling of Sb(111) Studied by Angle-Resolved Photoemission Spectroscopy. *Phys. Rev. Lett.*, 96:046411, 2006. 34, 35, 103

- 
- [145] T. Takahashi, K. Izumi, T. Ishikawa, and S. Kikuta. Evidence for a Trimer in the  $\sqrt{3} \times \sqrt{3}$ -Bi Structure on the Si(111) surface by X-Ray Diffraction under the nearly normal Incidence Condition. *Surf. Sci.*, 183:L302, 1987. 66
- [146] Y. Tanishiro, H. Kanamori, K. Takayanagi, K. Yagi, and G. Honjo. UHV transmission electron microscopy on the reconstructed surface of (111) gold: I. general features. *Surf. Sci.*, 111:395, 1981. 94
- [147] E. Y. Tsymbal, K. D. Belaschchenko, J. P. Velev, S. S. Jaswal, M. van Schilfgaarde, I. I. Oleynik, and D. A. Stewart. Interface effects in spin-dependent tunneling. *Prog. Mater. Sci.*, 52:401, 2007. 56
- [148] S. A. Valenzuela and M. Tinkham. Direct electronic measurement of the spin Hall effect. *Nature*, 442:176, 2006. 56
- [149] VG Scienta. *High-intensity extreme UV source Scienta VUV 5000*, 1.1 edition, 08 2008. 17
- [150] A. L. Wachs, A. P. Shapiro, T. C. Hsieh, and T.-C. Chiang. Observation of film states and surface-state precursors for Ag films on Si(111). *Phys. Rev B*, 33:1460, 1986. 58
- [151] K. J. Wan, T. Guo, W. K. Ford, and J. C. Hermanson. Initial growth of Bi films on a Si(111) substrate: Two phases of  $\sqrt{3} \times \sqrt{3}$  low-energy-electron-diffraction pattern and their geometric structures. *Phys. Rev B*, 44:3471, 1991. 66, 70
- [152] K. J. Wan, T. Guo, W. K. Ford, and J. C. Hermanson. Low-energy electron diffraction studies of Si(111) $\sqrt{3} \times \sqrt{3}$ R30 $^\circ$ -Bi system: observation and structural determination of two phases. *Surf. Sci.*, 261:69, 1992. 66, 68, 70, 83
- [153] G. Weisz. Band Structure and Fermi Surface of White Tin. *Phys. Rev.*, 149:504, 1966. 29
- [154] S. A. Wolf, D. D. Awschalom, R. A. Buhrman, J. M. Daughton, S. v. Molnar, M. L. Roukes, A. Y. Chtchelkanova, and D. M. Treger. Spintronics: A Spin-Based Electronics Vision for the Future. *Science*, 294:1488, 2001. 46, 47
- [155] K. Yaji, Y. Ohtsubo, S. Hatta, H. Okuyama, K. Miyamoto, T. Okuda, A. Kimura, H. Namatame, M. Taniguchi, and T. Aruga. Large Rashba spin splitting of a metallic surface-state band on a semiconductor surface. *Nature Communications*, 1:17, 2010. 74, 92
- [156] A. Zangwill. *Physics at Surfaces*. Cambridge University Press, 1988. 5
- [157] I. Zutic, J. Fabian, and S. Das Sharma. Spintronics: Fundamentals and applications. *Rev. Mod. Phys.*, 76:323, 2004. 48



**Emmanouil Frantzeskakis**

Born on January 7th, 1981 in Athens, Greece

Greek nationality

---

## Curriculum Vitae

---

### Education

2006 – 2010 **Ph.D. in Physics at Ecole Polytechnique Fédérale de Lausanne (EPFL)**, Switzerland

Laboratoire de Spectroscopie Electronique

*Thesis:* Spectroscopic Studies on Semiconducting Interfaces with Giant Spin Splitting

*Main Experimental Techniques Used:* Angle-Resolved Photoelectron Spectroscopy, Low-Energy Electron Diffraction, Auger Electron Spectroscopy, experience with Synchrotron Radiation experiments

2004 – 2005 **M.Eng. in Materials Science and Technology, Massachusetts Institute of Technology (MIT)**, USA

*Thesis:* Analysis of Potential Applications for the Templated Dewetting of Metal Thin Films

*Degree Grade:* 4.6 out of 5.00

1998 – 2003 **M.Sc. in Metallurgy and Mining Engineering, National Technical University of Athens (NTUA)**, Greece

*Specialization:* Materials Science and Technology

*Thesis:* Structural Characterization and Optoelectronic Properties of Silicon Wafers

*Main Experimental Techniques Used:* X-Ray Diffraction, Scanning Electron Microscopy

*Degree Grade:* 8.56 out of 10.00 (ranked 1<sup>st</sup> out of 61 graduates in 2003)

### Research Visits

2005 – 2006 Ecole Polytechnique Fédérale de Lausanne (EPFL), Switzerland

Laboratoire de Nanostructures Superficielles

*Main Experimental Techniques Used:* Scanning Tunneling Microscopy, Low-energy Electron Diffraction, Auger Electron Spectroscopy

2002 AGH Technical University, Faculty of Foundry, Krakow, Poland

*Project:* Possibility of shaping micro and nano-structures with using warm modeling in precise castings from nickel superalloys: research in laboratory and verification in industrial plants.

## Teaching

Teaching Assistant at EPFL (2006-2010) in the subjects General Physics III and IV for 2<sup>nd</sup>-year B.Sc. students of mechanical engineering, electrical engineering and materials science.

**Topics Covered:** fluid statics, fluid dynamics, Bernoulli equation, Euler equation, viscosity, Reynolds number, electrostatics, dielectrics, magnetostatics, electromagnetic induction, Maxwell equations, electromagnetic radiation, interference and diffraction of waves, wave-particle duality, Schrödinger's equation, basic principles of quantum mechanics, the hydrogen atom, Pauli principle, the chemical bond, solids

**Main Tasks:** preparation of the exercises, interaction with the students (2h / week) about the solution of the exercises, correction of the tests and final exams

## Academic Prizes

**NTUA:** Dean's award for graduating with the highest GPA (2003), Greek Mining Enterprises Association (GMEA) prize (2003)

**MIT:** one-semester fellowship from the department of Materials Science and Engineering (2004)

**EPFL:** one-year fellowship from the Doctoral School (2005-2006), research and teaching award (2009)

**Public Benefit Foundations:** *Eugenides Foundation* Scholarship (2004-2005), *Onassis Public Benefit Foundation* Scholarship (2006-2009)

## Conferences

**May 2007:** International workshop on low-dimensional and statistical systems, Nancy (France)

**August 2007:** MaNEP meeting, Diablerets (Switzerland)

**March 2008:** SPS-MaNEP meeting, Geneva (Switzerland)

**August 2008:** International workshop on electronic crystals ECRYS2008, Cargèse (France)

**July 2009:** International workshop on strong correlations and angle-resolved photoelectron spectroscopy CORPES09, Zurich (Switzerland)

**June 2010:** SPS-MaNEP meeting, Basel (Switzerland)

## Languages

Greek: mother tongue

English: excellent oral and written

German: good oral and written

French: good oral and written

Polish: basic

---

## Publications

### **Tunable Spin Gaps in a Quantum-Confined Geometry**

E. Frantzeskakis, S. Pons, H. Mirhosseini, J. Henk, C.R. Ast and M. Grioni

Phys. Rev. Lett. **101**, 196805 (2008).

(selected for the Virtual J. of Nanoscale Science and Technology)

### **Silicon Surface with Giant Spin Splitting**

I. Gierz, T. Suzuki, E. Frantzeskakis, S. Pons, S. Ostanin, A. Ernst, J. Henk, M. Grioni, K. Kern and C.R. Ast

Phys. Rev. Lett. **103**, 046803 (2009).

### **Giant spin-orbit splitting in a surface alloy grown on a Si substrate : BiAg<sub>2</sub>/Ag/Si(111)**

E. Frantzeskakis, S. Pons, and M. Grioni

Physica B **404**, 419 (2009).

### **New Mechanism for Spin-Orbit Splitting of Conduction States in Surface Alloys**

E. Frantzeskakis, L. Moreschini, M.C. Falub, S. Pons, C.R. Ast, D. Pacilé, M. Papagno and M. Grioni

e-J. Surf. Sci. Nanotech. **7**, 264 (2009).

### **Band structure scenario for the giant spin-orbit splitting observed at the Bi/Si(111) interface**

E. Frantzeskakis, S. Pons and M. Grioni

Phys. Rev. B **82**, 085440 (2010).

(selected for the Virtual J. of Nanoscale Science and Technology)

### **Tuning the giant Rashba effect on a BiAg<sub>2</sub> surface alloy: Two different approaches**

E. Frantzeskakis, A. Crepaldi, S. Pons, K. Kern and M. Grioni

J. Electron Spectr. Rel. Phenom. **181**, 88 (2010).

### **A structural transition reflected into the band topology of the Pt(111)-Ag-Bi interface**

E. Frantzeskakis, S. Pons, A. Crepaldi, K. Kern and M. Grioni

(to be submitted to Phys. Rev. B)

### **not related to the Ph.D. thesis manuscript:**

### **Recent ARPES experiments on quasi-1D bulk materials and artificial structures**

M. Grioni, S. Pons and E. Frantzeskakis

J. Phys.: Condens. Matter **21**, 023201 (2009).

**Coexistence of two distinct pi states in a Graphene Monolayer on Ru(0001)**

M. Papagno, D. Pacilé, D. Topwal, P. Moras, P.M. Sheverdyaeva, F.D. Natterer, A. Lehnert, S. Rusponi, E. Frantzeskakis, S. Pons, M. Gioni, H. Brune and C. Carbone  
(in preparation)

**Alkali metal deposition as a fine tuning of the electronic properties of BiAg<sub>2</sub>-Ag/Si(111)**

A. Crepaldi, E. Frantzeskakis, S. Pons, K. Kern and M. Gioni  
(in preparation)